University of Ljubljana
Faculty of Mathematics and Physics
Department of Physics

University *of Ljubljana*
Faculty *of Mathematics and Physics*

Blaž Leban

Search for type-II seesaw mechanism processes with same charge leptons in the final states with the ATLAS detector

Doctoral thesis

Adviser: prof. dr. Borut Paul Kerševan
Co-adviser: dr. Boštjan Maček

Ljubljana, 2023

Univerza v Ljubljani
Fakulteta za Matematiko in Fiziko
Oddelek za fiziko

Univerza *v Ljubljani*
Fakulteta za *matematiko in fiziko*

Blaž Leban

Iskanje procesov gugalničnega mehanizma tipa II s pari enako nabitih leptonov v končnih stanjih z detektorjem ATLAS

Doktorska disertacija

Mentor: prof. dr. Borut Paul Kerševan
Somentor: dr. Boštjan Maček

Ljubljana, 2023

To my wife Pia
and my family

Acknowledgements

I want to express my heartfelt gratitude to my adviser, Prof. Dr. Borut Paul Kerševan, for his guidance and support throughout my PhD studies. I am sincerely grateful for the opportunities, knowledge, and insights that have not only enriched my academic experience but also prepared me for future challenges. His reassuring words when I was in a rush to finalise the paper and thesis made my life easier. He encouraged me to attend international conferences and schools, which was a great way to meet new people and exchange ideas.

I extend my sincerest appreciation to my co-adviser Dr. Boštjan Maček, colleagues, and fellow PhD students from the Department of Experimental Particle Physics at the Jožef Stefan Institute. I was truly fortunate to have the opportunity to work with such dedicated and talented individuals in the pursuit of scientific excellence. I would especially like to thank Tadej Novak for guiding me through every step of the data analysis and sharing his code, without which this thesis would have been completed much later. I am also thankful for fruitful discussions with the Doubly charged Higgs analysis team and theory colleagues, who helped me understand the studied theoretical models.

I would like to thank my family. First and foremost, I wish to express my deepest appreciation to my dear wife, Pia. Without her support, the completion of my dissertation would not have been possible. Her encouragement, patience, and unwavering belief in me have been my anchor. ⚓ Her sacrifices and constant motivation kept me going when I experienced both personal and occupational difficulties. ✝ Her love is my greatest strength. 💛 The support and guidance of my parents have shaped me into the person I am today, and I am forever grateful. Lastly, I would like to thank my extended family and friends for their invaluable patience and encouragement when I needed it most.

"I have fought the good fight, I have finished the race, I have kept the faith." (2 Timothy 4, 7)

Iskanje procesov gugalničnega mehanizma tipa II s pari enako nabitih leptonov v končnih stanjih z detektorjem ATLAS

Izvleček

V doktorskem delu je predstavljeno iskanje nastanka para dvojno nabitih Higgsovih bozonov ($H^{\pm\pm}$), izmed katerih vsak razpade na par neposrednih, izoliranih in visokoenergijskih leptonov z enakim električnim nabojem. V analizi so uporabljeni podatki, zabeleženi z detektorjem ATLAS med drugim obratovalnim ciklom (Run 2) velikega hadronskega trkalnika (LHC), kar ustreza integrirani luminoznosti 139 fb^{-1}. Zajeti so bili med trki protonov pri težiščni energiji 13 TeV. Analiza se osredotoča na razpade delca $H^{\pm\pm}$ v par leptonov z enakim nabojem, $H^{\pm\pm} \to \ell^{\pm}\ell'^{\pm}$, pri čemer je $\ell, \ell' = e, \mu, \tau$. Posebej so obravnavana končna stanja z dvema, tremi in štirimi leptoni, vendar so upoštevana le ta, ki vključujejo elektrone ali mione. Statistična obdelava podatkov ne kaže znatnih odstopanj od napovedi Standardnega modela. Ob predpostavki, da so razvejitvena razmerja v vsa možna leptonska končna stanja enaka, $\mathcal{B}(H^{\pm\pm} \to e^{\pm}e^{\pm}/e^{\pm}\mu^{\pm}/\mu^{\pm}\mu^{\pm}/e^{\pm}\tau^{\pm}/\mu^{\pm}\tau^{\pm}/\tau^{\pm}\tau^{\pm}) = 1/6$, so izpeljane ustrezne zgornje meje produkcijskih sipalnih presekov dvojno nabitih Higgsovih bozonov kot funkcija njihove mase $m_{H^{\pm\pm}}$, pri stopnji zaupanja 95%. Meje, ki so najstrožje, kar jih je doslej objavila kolaboracija ATLAS, so določene za gugalnični mehanizem tipa II znotraj levo-desno simetričnega modela. Poleg tega je to delo prvi neposredni preizkus modela Zee–Babu na LHC.

Ključne besede:

ATLAS	CERN	LHC Run 2
levo-desna simetrija	gugalnični mehanizem tipa II	model Zee–Babu
strojno učenje	pospešena odločevalna drevesa	nevronske mreže
enako nabiti leptoni	dvojno nabiti Higgsov bozon	kršitev leptonskega okusa

Search for type-II seesaw mechanism processes with same charge leptons in the final states with the ATLAS detector

Abstract

A search for pair production of doubly charged Higgs bosons ($H^{\pm\pm}$), each decaying into a pair of prompt, isolated, and highly energetic leptons with the same electric charge, is presented. The search uses a proton–proton collision data sample at a centre-of-mass energy of 13 TeV corresponding to an integrated luminosity of 139 fb^{-1} recorded by the ATLAS detector during Run 2 of the Large Hadron Collider (LHC). This analysis focuses on same-charge leptonic decays, $H^{\pm\pm} \to \ell^{\pm}\ell'^{\pm}$, where $\ell, \ell' = e, \mu, \tau$, in two-, three- and four-lepton channels but only considers final states, which include electrons or muons. No evidence of a signal is observed. Assuming that the branching ratios to each possible leptonic final state are equal, $\mathcal{B}(H^{\pm\pm} \to e^{\pm}e^{\pm}/e^{\pm}\mu^{\pm}/\mu^{\pm}\mu^{\pm}/e^{\pm}\tau^{\pm}/\mu^{\pm}\tau^{\pm}/\tau^{\pm}\tau^{\pm}) = 1/6$, the corresponding upper limits on the pair production cross-section of doubly charged Higgs bosons are derived as a function of its mass, $m_{H^{\pm\pm}}$, at a 95% confidence level. The limits, which are the strongest produced by the ATLAS Collaboration to date, are obtained for the left-right symmetric type-II seesaw model. Additionally, this work provides the first direct test of the Zee–Babu neutrino mass model at the LHC.

Keywords:

ATLAS	CERN	LHC Run 2
left-right symmetry	type-II seesaw	Zee–Babu model
machine learning	boosted decision trees	neural networks
same-charge leptons	doubly charged Higgs	lepton flavour violation

Acronyms

AFP	ATLAS Forward Proton
ALFA	Absolute Luminosity For ATLAS
ALICE	A Large Ion Collider Experiment
AOD	Analysis Object Data
ATLAS	A Toroidal LHC ApparatuS
BCM	Beam-Conditions Monitor
BDT	Boosted Decision Tree
BLM	Beam Loss Monitor
BSM	Beyond Standard Model
CB	Combined Muon
CL	Confidence Level
CERN	The European Organization for Nuclear Research (originally French: Organisation européenne pour la recherche nucléaire)
CKM	Cabibbo-Kobayashi-Maskawa
CMS	Compact Muon Solenoid
CP	Charge and Parity
CSC	Cathode Strip Chambers
EM	ElectroMagnetic
EMCAL	ElectroMagnetic CALorimeter
EMEC	LAr ElectroMagnetic End-Cap calorimeter
EW	ElectroWeak
FCal	Forward Calorimeter
FCS	Fast Calorimeter Simulation
FNP	Fake/Non-Prompt
FS	Full Simulation
GRL	Good Run List
GSF	Gaussian Sum Filter
HCAL	Hadronic CALorimeter
HEC	Hadronic End-cap Calorimeter
HEP	High-Energy Physics
HLT	High-Level Trigger
IBL	Insertable B-Layer
ID	The ATLAS Inner Detector
IP	Interaction Point
JER	Jet Energy Resolution
JES	Jet Energy Scale
L1	Level 1 trigger
LAr	Liquid Argon
LB	Luminosity Block
LEIR	Low Energy Ion Ring
LEP	Large Electron–Positron collider
Linac3(4)	Linear accelerator 3(4)

LHC	Large Hadron Collider
LHCb	Large Hadron Collider beauty
LRSM	Left-Right Symmetric Model
LS1(2)	Long Shutdown 1 (2)
LUCID	LUminosity measurement using Cerenkov Integrating Detector
MC	Monte Carlo
MDT	Monitored Drift Tubes
ME	Matrix Element
MET	Missing Transverse Energy
MIP	Minimum Ionising Particle
ML	Machine Learning
MM	MicroMegas
MS	Muon Spectrometer
MVA	MultiVAriate
(N)NLO	(Next-to-)Next-to-Leading Order
NN	Neural Network
NP	Nuisance Parameter
NSW	New Small Wheel
PS(B)	Proton Synchrotron (Booster)
PDF	Parton Distribution Function
POI	Parameter Of Interest
PS	Parton Shower
QCD	Quantum ChromoDynamics
QED	Quantum ElectroDynamics
QFT	Quantum Field Theory
RF	RadioFrequency
RMS	Root-Mean-Square
ROS	Read-Out System
RPC	Resistive Plate Chambers
SCT	Semi-Conductor Tracker
SF	Scale Factor
SM	Standard Model
SPS	Super Proton Synchrotron
SSB	Spontaneous Symmetry Breaking
sTGC	small-strip Thin Gap Chambers
TDAQ	Trigger and Data AcQuisition
TGC	Thin Gap Chambers
TileCal	Tile Calorimeter
TRT	Transition Radiation Tracker
vev	Vacuum Expectation Value
WP	Working Point
ZDC	Zero-Degree Calorimeter

Contents

List of Figures

List of Tables

Part I

INTRODUCTION

CHAPTER 1

Theoretical Motivation

This chapter motivates the search for type-II seesaw mechanism processes with the same charge leptons in the final states. Section 1.1 describes a well-established theoretical framework of elementary particles and their interactions, the Standard Model. Then, Section 1.2 addresses its shortcomings which motivate different theoretical extensions, collectively called Beyond the Standard Model or New Physics, two of which are also the type-II seesaw mechanism within the left-right symmetric model and Zee–Babu Model.

1.1 The Standard Model of Particle Physics

The Standard Model (SM) [1–4] is a well-established quantum field theory of elementary particles and their interactions with high predictive power. It has been extensively tested to high precision with the astonishing agreement between predictions and measurements. It is thus often referred to as one of the most impressive achievements of sciences. It was developed and tested in parts in the second half of the 20th century with the contributions of many scientists, both theorists and experimentalists.

The section draws inspiration from Refs. [5] and [6]. Throughout the thesis, the natural units convention is adopted, $\hbar = c = \varepsilon_0 = \mu_0 = 1$, where $\hbar$ is the reduced Planck constant, c is the speed of light, and ε_0 and μ_0 are permittivity and permeability of free space, respectively. Furthermore, the Minkowski metric $\eta_{\mu\nu}$ of metric signature (+, -, -, -) is imposed. First, we define the fundamental constituents of the universe, the *elementary particles*, and the *forces* that act between them.

1.1.1 Fundamental Forces and Particle Content

Four fundamental forces are within the SM treated mathematically as fields permeating the entire universe. Written in the order of decreasing strength, they are strong, electromagnetic, weak, and gravitational. Their relative strengths are presented in Table 1.1.

Table 1.1: The four fundamental forces of nature and their approximate relative strengths for two fundamental particles at a distance of 1 fm.

Force	Strength	Theory	Mediator
Strong	1	Chromodynamics	gluon g
Electromagnetic	10^{-3}	Electrodynamics	photon γ
Weak	10^{-8}	Flavourdynamics	W and Z bosons
Gravitational	10^{-37}	Gravity	graviton G ?

The strong force is characterised by its exceptionally short range. It is responsible for holding the protons and neutrons together in an atomic nucleus on a larger scale and quarks together to form hadrons on a smaller scale. It is assumed it generates ~ 99% of the hadron mass. It is described by the fundamental theory of strong interactions, *quantum chromodynamics* (QCD), which was given its shape by Gell-Mann, Zweig, Gross, Politzer, Wilczek [7–10] and many others.

The electromagnetic force was first mathematically formulated by Maxwell [11]. Electromagnetism plays a crucial role in the structure of atoms and molecules. It is a low-energy manifestation of the fundamental theory of electromagnetism, *quantum electrodynamics* (QED), which was perfected by Tomonaga, Feynman and Scwinger [12–14] in the 1940s.

The weak force is, for example, responsible for nuclear β-decays and the nuclear fusion processes, which were not known in classical physics before. The force got a relativistic quantum formulation right from the start by Fermi [15]. Glashow, Weinberg, and Salam [1, 3, 4, 16] put it into its present form in the 1960s.

Gravity was first described as a universal force by Newton [17]. It is extremely weak and mainly affects large objects on a long range. Later, Einstein's general theory of relativity [18] generalised it, but no adequate quantum theory of gravity exists yet. It is believed that gravity does not play a significant role in elementary particle physics.

Particles, on the other hand, manifest themselves as excitations in force fields. The SM consists of 12 matter (*fermions*) and six force carrier (*gauge bosons*) particles, as depicted in Figure 1.1 on the left and right, respectively. The fermions have spin 1/2, while bosons have spin 1. The fermions are (horizontally) divided into *quarks* and *leptons*, depending on their fundamental properties. Quarks have a fractional electric charge, q,[1] while leptons have an integer q value. In addition, the fermions can also be (vertically) split into three generations, having the same quantum numbers between each generation, except for their masses. Essentially all things encountered in nature are formed from the first generation of fermions, while to produce the rest, special conditions are required. Quarks come in six flavours, with three "up-type" quarks having a +2/3 electric charge (u, c, and t) and three "down-type" quarks with a −1/3 electric charge (d, s, and b). All quarks also carry a colour charge. Charged leptons (e, μ, and τ) have a −1 electric charge and are accompanied by their massless[2] and electrically neutral partners, neutrinos (ν_e, ν_μ, and ν_τ). Each fermion has its antiparticle with an opposite electric charge and other quantum numbers.

Each force is mediated by the exchange of gauge bosons, depicted in yellow in Figure 1.1. These are responsible for interactions of fermions. Eight massless gluons mediate a strong force. They have no electric charge and therefore do not interact electromagnetically. However, gluons carry a colour charge and couple, in addition to quarks, to other gluons. Hence three- and four-gluon vertices exist, making QCD more complicated than QED but thus richer. The QED interactions are mediated by the exchange of virtual photons. These are also electrically neutral and massless, allowing an infinite range of electromagnetic force. Since all twelve fermions

[1] The electric charge is usually expressed in units of the electron charge $q_e = -1.602 \times 10^{-19}$ C.

[2] Neutrinos are precisely massless within the SM. Experiments, however, established that neutrinos have masses, which is a clear experimental indication of physics beyond the SM, discussed in Section 1.2.

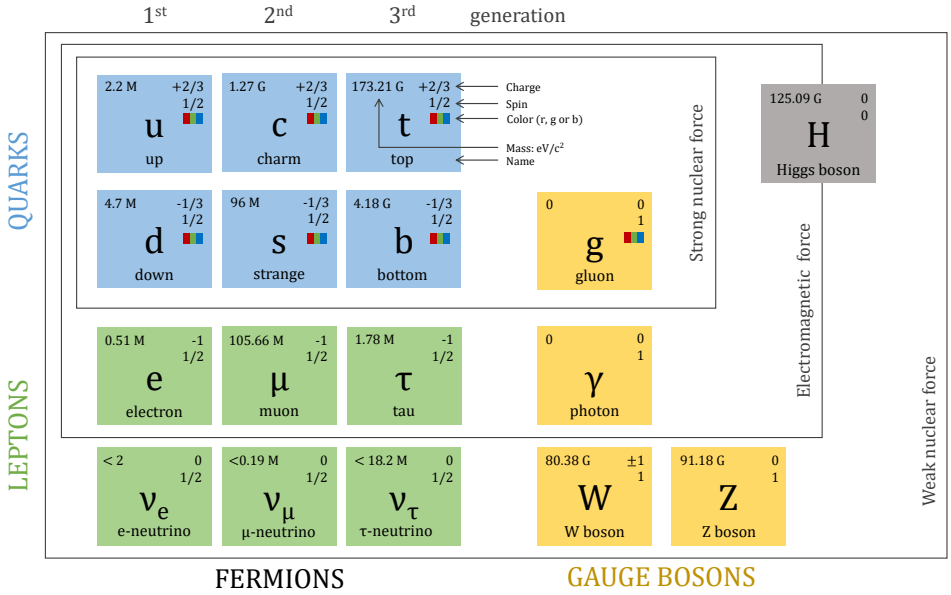

Figure 1.1: The particle content of the Standard Model, along with particle properties.

carry the charge of the weak interaction, known as weak isospin, they all participate in weak interactions. The W (Z) bosons are responsible for charged (neutral) weak interactions. The Z boson is electrically neutral, while W bosons with both ± 1 electric charges exist. They are massive, $m_W = (80\,360 \pm 16)$ MeV [19] and $m_Z = (91\,187.5 \pm 2.1)$ MeV [20], which makes the reach of the weak interaction very short. The last particle, discovered in 2012 by ATLAS [21] and CMS [22] collaborations, is the Higgs boson with mass $m_H = (124.94 \pm 0.17)$ GeV [23], which made the SM a complete and consistent theory. Unlike all other particles, it is a spin-0 scalar particle that provides a mechanism by which all other particles acquire their masses. Furthermore, it differs from all other particles in its non-zero vacuum expectation value. When initially massless particles interact with the non-zero Higgs field, they obtain their masses. Lastly, the carrier of gravity, the graviton, has not been discovered yet and is thus not presented in Figure 1.1. Contrary to the other force carriers, it is expected to have spin-2 [24].

1.1.2 Mathematical Formalism of the Standard Model

Modern physics encodes the basic laws of nature in the action, S, and then applies the principle of least action in its quantum interpretation on top. In Quantum Field Theory (QFT), the action can be written as

$$S = \int \mathrm{d}^4x \, \mathcal{L}\left[\phi_i(x),\, \partial_\mu \phi_i(x)\right], \tag{1.1}$$

and represents an integral over spacetime of the *Lagrangian density*, $\mathcal{L}$, or Lagrangian for short. Here, ϕ_i denotes the i^{th} generic quantum field and $\mathrm{d}^4x = \mathrm{d}x^0\mathrm{d}x^1\mathrm{d}x^2\mathrm{d}x^3$ is the integration measure of the four-dimensional Minkowski space. The Lagrangian is typically constructed so that it fulfils several requirements. Firstly, it must be Lorentz invariant to ensure the results

are independent of the orientation or the boost velocity of the observer. Then, the gauge invariance asserts invariance under the local group transformations. Furthermore, it must also be renormalisable to yield finite predictions. Finally, every term that is not forbidden by symmetry should be considered. The most general Lagrangian with scalar, fermion and gauge fields can be broken down into

$$\mathcal{L} = \mathcal{L}_{\text{kin}} + \mathcal{L}_{\psi} + \mathcal{L}_{\text{Yuk}} + \mathcal{L}_{\Phi}, \tag{1.2}$$

where $\mathcal{L}_{\text{kin}}$ governs the propagation of all dynamical fields in spacetime and gauge interactions, $\mathcal{L}_{\psi}$ produces the fermion mass terms, $\mathcal{L}_{\text{Yuk}}$ specifies the Yukawa interactions, and $\mathcal{L}_{\Phi}$ defines the scalar potential.

Another important concept in a QFT model building is *symmetry*. Symmetry can be thought of as a requirement that the system remains invariant after some operations are performed on it. Extremely powerful predictions can be made based on just such "weak" requirements. Multiple types of symmetries exist each having different consequences on the model, e.g. energy, momentum and angular momentum conservation laws are directly associated with the spacetime symmetry of the Lagrangian. Furthermore, exact global symmetries demand the conservation of charges. This connection between the symmetries and the conservation laws is known as *Noether's theorem* [25], which states that every symmetry of nature yields a conservation law and vice versa - every conservation law requires an underlying symmetry. The gauge symmetry of the SM is

$$\mathrm{SU}(3)_C \times \mathrm{SU}(2)_L \times \mathrm{U}(1)_Y.$$

Therefore, the resulting Lagrangian must be invariant under colour charge transformations related to the $\mathrm{SU}(3)_C$ symmetry group, with the consequence being the strong force. The electromagnetic and weak interactions are described by the unified electroweak theory, which includes the invariance under the $\mathrm{SU}(2)_L \times \mathrm{U}(1)_Y$ symmetry.[3] In this context, $\mathrm{SU}(2)_L$ represents the weak isospin group, which exclusively couples to left-handed fermions, while $\mathrm{U}(1)_Y$ represents the weak hypercharge group. Each of the abovementioned symmetries has a corresponding conserved charge, i.e. colour C, a third component of weak isospin I^3, and weak hypercharge Y, respectively.

1.1.3 Quantum Electrodynamics

Quantum electrodynamics [1, 3, 4] is the oldest, the simplest and the most successful dynamical theory [5]. It is an Abelian theory constructed in the Minkowski space and incorporates the U(1) symmetry group. Furthermore, QED is the quantum counterpart of classical Maxwell's

[3] The $\mathrm{SU}(2)_L \times \mathrm{U}(1)_Y$ symmetry group is spontaneously broken to the low-energy symmetry associated with electromagnetism, $\mathrm{U}(1)_{\text{EM}}$, when the Higgs field acquires a non-zero vacuum expectation value. See Section 1.1.6 for further details.

electrodynamics. Maxwell's equations, the basis of classical electrodynamics, read

$$\nabla \cdot \boldsymbol{E} = \rho, \tag{1.3a}$$

$$\nabla \cdot \boldsymbol{B} = 0, \tag{1.3b}$$

$$\nabla \times \boldsymbol{E} = -\frac{\partial \boldsymbol{B}}{\partial t}, \tag{1.3c}$$

$$\nabla \times \boldsymbol{B} = \boldsymbol{J} + \frac{\partial \boldsymbol{E}}{\partial t}, \tag{1.3d}$$

where $\boldsymbol{E}$ is the electric vector field, and $\boldsymbol{B}$ is the magnetic pseudovector field. The ρ and the $\boldsymbol{J}$ are the total electric charge and current densities, respectively, while ∇ is the gradient operator, defined as $\nabla = \left(\frac{\partial}{\partial x}, \frac{\partial}{\partial y}, \frac{\partial}{\partial z}\right)$. In quantum mechanics and relativity, it is often easier to work with a potential formulation of electrodynamics rather than in terms of the electric and magnetic fields. In this representation, the magnetic vector potential $\boldsymbol{A}$, and the electric scalar potential φ, are defined using gauge fixing:

$$\boldsymbol{B} = \nabla \times \boldsymbol{A}, \tag{1.4a}$$

$$\boldsymbol{E} = -\nabla\varphi - \frac{\partial \boldsymbol{A}}{\partial t}. \tag{1.4b}$$

Maxwell's equations can then be simplified and reduced by introducing another relevant quantity, the *field strength tensor*, $F^{\mu\nu}$, in the covariant notation written as

$$F_{\mu\nu} = \partial_\mu A_\nu - \partial_\nu A_\mu, \tag{1.5}$$

which represents the curvature of the gauge field. Here, a generalisation to four-dimensional Minkowski space is made, with μ and ν indices running on one time and three space coordinates. The $\partial_\mu = \left(\frac{\partial}{\partial t}, \nabla\right)$ is the four-gradient, the vector potential is given by $A_\mu = (\varphi, -\boldsymbol{A})$, and the four-current is defined as $j_\mu = \left(\rho, -\vec{j}\right)$. The $F_{\mu\nu}$ can then be expressed in matrix form as

$$F_{\mu\nu} = \begin{pmatrix} 0 & E_x & E_y & E_z \\ -E_x & 0 & -B_z & B_y \\ -E_y & B_z & 0 & -B_x \\ -E_z & -B_y & B_x & 0 \end{pmatrix} = -F_{\nu\mu} = \eta_{\alpha\nu} F^{\beta\alpha} \eta_{\mu\beta}. \tag{1.6}$$

Finally, the QED Lagrangian for a fermion field interacting with the electromagnetic field can be constructed as

$$\mathcal{L}_{\text{QED}} = -\frac{1}{4} F_{\mu\nu} F^{\mu\nu} + \sum_f \bar{\psi}_f \left(i\gamma^\mu D_\mu - m_f\right) \psi_f, \tag{1.7}$$

where the sum runs over all electrically charged fermions f with mass m_f. γ^μ are four 4×4 Dirac matrices and ψ represents the Dirac spinor, with its Hermitian adjoint operator defined as $\bar{\psi} = \psi^\dagger \gamma^0$. The gauge covariant derivative, D_μ, is introduced as

$$D_\mu = \partial_\mu + iqA_\mu \tag{1.8}$$

to ensure gauge invariance. The $\mathcal{L}_{\text{QED}}$ is invariant under U(1) global gauge transformation, $\psi \to \psi' = e^{-i\alpha}\psi$, yielding a conserved current arising from Noether's theorem, $j_\mu = \bar{\psi}\gamma_\mu\psi$.

1.1.4 Weak Interaction

As can be seen from Figure 1.1, each SM fermion is affected by a weak interaction. Enrico Fermi proposed the first theory of weak interaction in 1934 while studying β-decay [15]. It was described as a point-like four-fermion interaction. The charged-current weak interaction is invariant under the SU(2) local phase transformations

$$\psi(x) \rightarrow \psi'(x) = e^{i\frac{g_W}{2}\boldsymbol{\alpha}(x)\cdot\boldsymbol{\sigma}}\,\psi(x), \tag{1.9}$$

where g_W is the weak coupling constant, $\boldsymbol{\sigma}$ are the Pauli matrices representing the SU(2) group generators, and $\boldsymbol{\alpha}(x)$ are the three space-time dependent functions which specify the phases. Three gauge fields corresponding to three gauge bosons, W^1, W^2, and W^3, are required to ensure the gauge invariance. Furthermore, wavefunction $\psi(x)$ in Eq. 1.9 should be written in terms of two components, termed *weak isospin doublets*, differing by one unit of electric charge. Since it was observed that only left-handed chiral particle states and right-handed chiral antiparticle states participate in charged-current weak interaction, the gauge transformation from Eq. 1.9 should only affect those. For this reason, left-handed particle states and right-handed antiparticle states are assigned weak isospin $T = \frac{1}{2}$, while right-handed particle and left-handed antiparticle states have weak isospin $T = 0$ and are thus unaffected by the SU(2) gauge transformation.[4] The left-handed and right-handed components of the fermion field ψ can be extracted using the chirality projectors

$$\psi_L = P_L\,\psi = \frac{1-\gamma^5}{2}\psi, \quad \text{and} \quad \psi_R = P_R\,\psi = \frac{1+\gamma^5}{2}\psi, \tag{1.10}$$

where $\gamma^5 = i\gamma^0\gamma^1\gamma^2\gamma^3$. The SM particles are ordered into doublets and singlets:

- Left-handed fermions: $\begin{pmatrix}\nu_e\\ e^-\end{pmatrix}_L, \begin{pmatrix}\nu_\mu\\ \mu^-\end{pmatrix}_L, \begin{pmatrix}\nu_\tau\\ \tau^-\end{pmatrix}_L, \begin{pmatrix}u\\ d'\end{pmatrix}_L, \begin{pmatrix}c\\ s'\end{pmatrix}_L, \begin{pmatrix}t\\ b'\end{pmatrix}_L,$ (1.11a)
- Right-handed fermions: $e^-_R,\ \mu^-_R,\ \tau^-_R,\ u_R,\ c_R,\ t_R,\ d_R,\ s_R,\ b_R.$ (1.11b)

The weak isospin singlets are unchanged by the $\mathrm{SU}(2)_L$ local gauge transformation and do not couple to the gauge bosons of the symmetry. Since weak interaction violates parity, its interaction current requires a different form than vector interaction currents in QED and QCD. The Lorentz invariance requires writing the weak currents as a general linear combination of vector and axial vector currents. The currents for each of the three gauge fields W^a are

$$j^\mu_+ = \frac{g_W}{\sqrt{2}}\,\bar{\nu}\gamma^\mu P_L e, \tag{1.12a}$$

$$j^\mu_- = \frac{g_W}{\sqrt{2}}\,\bar{e}\gamma^\mu P_L \nu, \tag{1.12b}$$

$$j^\mu_3 = g_W\,T_3\,\bar{f}\gamma^\mu P_L f, \tag{1.12c}$$

where f represents the fermion spinor and T_3 is the third component of the weak isospin. The corresponding fundamental vertices are shown in Figure 1.2, where the physical W boson is identified as a linear combination, $W^\pm_\mu = \frac{1}{\sqrt{2}}\left(W^1_\mu \mp iW^2_\mu\right)$.

[4] Therefore, the symmetry group of the weak interaction is mainly referred to as $\mathrm{SU}(2)_L$.

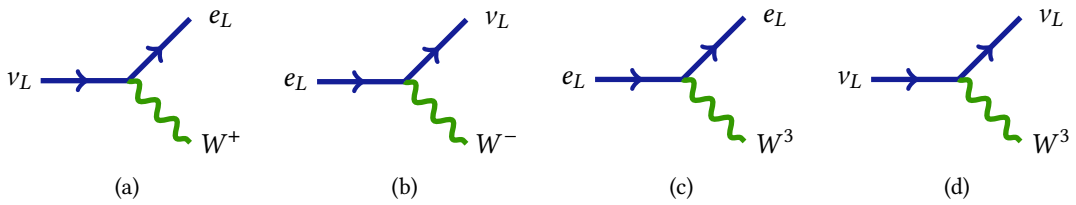

Figure 1.2: The weak interaction vertices of the e^- and ν_e weak eigenstates for (a) and (b) charged-current interaction, and (c) and (d) the neutral-current interaction.

1.1.5 Electroweak Unification

The W^3 from Figure 1.2 could be naively assigned to a physical Z boson. However, it is known from experimental observations that the Z boson also couples to right-handed fermions (and left-handed antifermions). Therefore, it is tempting to construct a physical photon and Z boson, which are both neutral, from a mix of quantum states. Glashow, Weinberg and Salam [1, 3, 4] started unifying electromagnetic and weak interaction in the 1960s. In their model, the $\mathrm{U}(1)_{\mathrm{EM}}$ is replaced with $\mathrm{U}(1)_Y$ local gauge symmetry to form the electroweak gauge group $\mathrm{SU}(2)_L \times \mathrm{U}(1)_Y$, where $\mathrm{U}(1)_Y$ transformation reads

$$\psi(x) \longrightarrow \psi'(x) = e^{ig'\frac{Y}{2}\alpha(x)}\,\psi(x), \tag{1.13}$$

and requires a new gauge field B_μ with a *weak hypercharge* Y and an additional coupling constant g'. The photon and Z boson can then be written as a linear combination of the B_μ and W^3_μ gauge fields as

$$\begin{pmatrix} A_\mu \\ Z_\mu \end{pmatrix} = \begin{pmatrix} \cos\theta_W & \sin\theta_W \\ -\sin\theta_W & \cos\theta_W \end{pmatrix} \begin{pmatrix} B_\mu \\ W^3_\mu \end{pmatrix}, \tag{1.14}$$

where θ_W is the weak mixing angle. The weak hypercharge can be expressed as a linear combination of the electromagnetic charge q and the third component of weak isospin T_3 in what is known as the Gell-Mann-Nishijima formula [26, 27]:

$$q = T_3 + \frac{Y}{2}. \tag{1.15}$$

Furthermore, the relations between coupling constants can be extracted from the known couplings and quantum numbers of different fermions:

$$e = g_W \sin\theta_W = g' \cos\theta_W \quad \text{and} \quad \theta_W = \frac{g_W}{\sqrt{g_W^2 + g'^2}}. \tag{1.16}$$

Finally, the EW Lagrangian, $\mathcal{L}_{\mathrm{EW}}$, can be constructed. The covariant derivative of the electroweak interaction is defined as

$$D_\mu = \partial_\mu - ig_W T_a W^a_\mu - ig'\frac{Y}{2}B_\mu, \tag{1.17}$$

where g_W and g' are coupling constants for $\mathrm{SU}(2)_L$ and $\mathrm{U}(1)_Y$, respectively, and T_a are the components of the weak isospin. Note that right-handed fermions (and left-handed antifermions) have $T = 0$, so no second term defining the coupling to W_μ fields exists. The field strength tensors are

$$W^a_{\mu\nu} = \partial_\mu W^a_\nu - \partial_\nu W^a_\mu - g_W \varepsilon^{abc} W^b_\mu W^c_\nu, \tag{1.18}$$

$$B_{\mu\nu} = \partial_\mu B_\nu - \partial_\nu B_\mu, \tag{1.19}$$

which yield the electroweak Lagrangian,

$$\mathcal{L}_{\mathrm{EW}} = \sum_f \bar{f} i\gamma^\mu D_\mu f - \frac{1}{4} W^a_{\mu\nu} W_a^{\mu\nu} - \frac{1}{4} B^{\mu\nu} B_{\mu\nu}. \tag{1.20}$$

1.1.6 The Higgs Mechanism

To date, every experimental observation of the electroweak interactions is consistent with a gauge theory. However, explicit mass terms for the W and Z bosons cannot be written without a mechanism external to the gauge sector. The Brout-Englert-Higgs mechanism [28–30] introduces gauge boson mass terms by adding the simplest model that satisfies the necessary four degrees of freedom, consisting of two complex scalar fields. These fields are placed into a weak isospin doublet with $Y = 1$ and one charged and one neutral component, similar to the lepton-neutrino doublet:

$$\phi = \begin{pmatrix} \phi^+ \\ \phi^0 \end{pmatrix} = \frac{1}{\sqrt{2}} \begin{pmatrix} \phi_1 + i\phi_2 \\ \phi_3 + i\phi_4 \end{pmatrix}. \tag{1.21}$$

The Lagrangian for this doublet of scalar fields is

$$\mathcal{L}_{\mathrm{Higgs}} = \left(D_\mu \phi\right)^\dagger \left(D^\mu \phi\right) \underbrace{-\mu^2 \phi^\dagger \phi - \lambda \left(\phi^\dagger \phi\right)^2}_{\text{Higgs potential } V(\phi)}, \tag{1.22}$$

with the covariant derivative defined in Eq. 1.17. The Higgs potential is gauge invariant under SU(2) symmetry and consists of μ and λ constants that are chosen to be $\mu^2 < 0$ and $\lambda > 0$ to obtain non-zero minima and an energetically bounded theory. The shape of the potential is presented in Figure 1.3.

The choice $\mu^2 < 0$ gives an infinite set of degenerate minima, shown with a dashed red curve in Figure 1.22, satisfying

$$\phi^\dagger \phi = \frac{v^2}{2} = -\frac{\mu^2}{2\lambda}, \quad \text{with} \quad \phi_0 = \langle 0|\phi|0\rangle = \frac{1}{\sqrt{2}} \begin{pmatrix} 0 \\ v \end{pmatrix}, \tag{1.23}$$

where v corresponds to a non-zero *vacuum expectation value* (vev).

A gauge transformation permits setting three out of four components in Eq. 1.21 to zero, so the Higgs doublet can be rewritten in the unitary gauge as

$$\phi(x) = \frac{1}{\sqrt{2}} \begin{pmatrix} 0 \\ v + h(x) \end{pmatrix}, \tag{1.24}$$

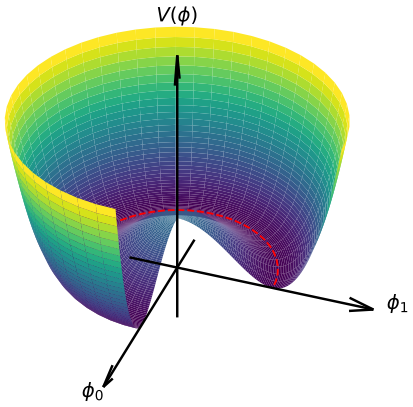

Figure 1.3: A representation of the Higgs potential, $V(\phi)$, as defined in Eq. 1.22.

where $h(x)$ corresponds to excitations of the field that represent the physically observable *Higgs boson*. The electroweak symmetry $\mathrm{SU}(2)_L \times \mathrm{U}(1)_\mathrm{Y}$ is this way spontaneously broken to $\mathrm{U}(1)_\mathrm{EM}$. A mass term for the gauge bosons appears naturally from the kinetic part of the $\mathcal{L}_\mathrm{Higgs}$, while the fermion masses are obtained from Yukawa couplings, y_ℓ, between the fermions and the Higgs field [31].

Gauge boson masses

First, we expand the kinetic part of the $\mathcal{L}_\mathrm{Higgs}$,

$$\begin{aligned}\mathcal{L}^\mathrm{kin}_\mathrm{Higgs} \supset \left(D^\mu\phi\right)^\dagger \left(D_\mu\phi\right) = \frac{1}{2}\partial^\mu h\,\partial_\mu h + \frac{1}{8}\left(h+v\right)^2 g_W^2 \left[\left(W^{\mu 1} + iW^{\mu 2}\right)\left(W^1_\mu - iW^2_\mu\right)\right] \\ + \frac{1}{8}\left(h+v\right)^2 \left[\left(g' B^\mu - g_W W^{\mu 3}\right)\left(g' B_\mu - g_W W^3_\mu\right)\right],\end{aligned} \tag{1.25}$$

and extract the mass terms, defined as $-\frac{1}{2}m_X^2 X^2$, where X is an arbitrary real scalar or vector field. Five quadratic field terms that represent real particle masses appear. One is a spin-0 scalar particle, identified as the Higgs boson, and the other four are the $W^\pm$, Z and A gauge bosons. The masses which follow from the $\mathcal{L}^\mathrm{kin}_\mathrm{Higgs}$ are:

Spin-0 particle: $\mathcal{L}^\mathrm{kin}_\mathrm{Higgs}\Big|_{s=0} = \lambda v^2 h^2$.

This term yields a Higgs boson mass, $m_h = \sqrt{2}\mu = \sqrt{2\lambda}v$.

Spin-1 particles: $\mathcal{L}^\mathrm{kin}_\mathrm{Higgs}\Big|_{s=1} = -\frac{1}{8}v^2\left[g_W^2\left(W^{\mu 1}W^1_\mu + W^{\mu 2}W^2_\mu\right) + \left(g' B^\mu - g_W W^{\mu 3}\right)^2\right]$.

The term defines masses for the W and Z bosons as $m_W = \frac{1}{2}g_W v$ and $m_Z = \frac{1}{2}\sqrt{g'^2 + g_W^2}\,v$, by using the relations from Eqs. 1.14 and 1.16. Furthermore, the W and Z boson mass relation follows, $m_Z = \frac{m_W}{\cos\theta_W}$. No mass term corresponds to the last gauge boson, identified as the massless photon, $m_A = 0$.

A summary of the gauge boson masses and relations is given below:

$$\begin{aligned} m_A &= 0, & m_h &= \sqrt{2\lambda}v, \\ m_W &= \frac{1}{2}g_W v, & m_Z &= \frac{1}{2}\sqrt{g'^2 + g_W^2}\, v = \frac{m_W}{\cos\theta_W}. \end{aligned}$$

By using the relation $m_W = \frac{1}{2}g_W v$ and the measured values of m_W and g_W, the vev of the Higgs field is found to be [32]

$$v = 246.22\,\text{GeV}. \tag{1.26}$$

Fermion masses

Since the left and right fermion chiral states have different transformation properties that break $\text{SU}(2)_L \times \text{U}(1)_Y$ invariance, there is no way of introducing fermion mass terms of the form $-m\bar{\psi}\psi = -m(\bar{\psi}_R\psi_L + \bar{\psi}_L\psi_R)$ to the SM Lagrangian. Fortunately, the Higgs mechanism can also be used to generate fermion masses. It turns out that a term of the form $-y_\ell(\bar{L}\phi R + \bar{R}\phi^\dagger L)$ respects the $\text{SU}(2)_L \times \text{U}(1)_Y$ gauge symmetry of the SM. Here, L represents a left-handed SU(2) doublet, and R stands for a right-handed SU(2) singlet. After spontaneous symmetry breaking (SSB), the Higgs acquires a vev, see Eq. 1.24, so the lepton doublet mass term in the Lagrangian looks like

$$\begin{aligned} \mathcal{L}^\ell_{mass} &= -\frac{y^\ell}{\sqrt{2}}\left[\begin{pmatrix}\bar{\nu}_\ell & \bar{\ell}\end{pmatrix}_L \begin{pmatrix}0 \\ v + h(x)\end{pmatrix} \ell_R + \bar{\ell}_R \begin{pmatrix}0 & v + h(x)\end{pmatrix} \begin{pmatrix}\nu_\ell \\ \ell\end{pmatrix}_L\right] \\ &= -\frac{y^\ell v}{\sqrt{2}}\left(\bar{\ell}_L\ell_R + \bar{\ell}_R\ell_L\right) - \frac{y^\ell h}{\sqrt{2}}\left(\bar{\ell}_L\ell_R + \bar{\ell}_R\ell_L\right). \end{aligned} \tag{1.27}$$

In the last line of Eq. 1.27, the first term represents the mass of the fermion,[5] while the last term represents the coupling between the fermion and the Higgs boson itself. The Yukawa coupling, y_ℓ, can be chosen to be compatible with the observed lepton mass, $y_\ell = \sqrt{2}\frac{m_\ell}{v}$. In this case, the Lagrangian can be simplified to

$$\mathcal{L}^\ell_{mass} = -m_\ell\bar{\ell}\ell - \frac{m_\ell}{v}\bar{\ell}\ell h. \tag{1.28}$$

Since there are no right-handed neutrinos in the SM, such mass terms can not be constructed, and neutrinos remain massless. On the other hand, Yukawa couplings of the fermions are $O(1)$, with the m_t at 173.5 GeV almost exactly matching with unity.

So far, the fermions are not interacting among themselves. The lepton number, L, is believed to be conserved, as no flavour violation has been observed in the lepton sector. On the other hand, quarks can mix flavours as the K-meson decay was experimentally detected [32]

$$K^0(d\bar{s}) \to \pi^-(d\bar{u})\ell^+\nu_\ell, \tag{1.29}$$

which implies quark interaction $\bar{s} \to \bar{u}\ell\nu_\ell$. Furthermore, it unveils the fact that the quark mass eigenstates are not the same as the weak interaction eigenstates. The mixing of states was first

[5] Note that the term is now gauge invariant.

explained for a 2×2 case by N. Cabibbo [33] and later generalised to 3×3 mixing in collaboration with M. Kobayashi and T. Maskawa [34]. The so-called unitary Cabibbo-Kobayashi-Maskawa (CKM) matrix gives the probability $|V_{ab}|^2$ that the quark changes flavour from a to b and is defined as

$$\begin{pmatrix} d' \\ s' \\ b' \end{pmatrix} = \begin{pmatrix} V_{ud} & V_{us} & V_{ub} \\ V_{cd} & V_{cs} & V_{cb} \\ V_{td} & V_{ts} & V_{tb} \end{pmatrix} \begin{pmatrix} d \\ s \\ b \end{pmatrix}. \tag{1.30}$$

Interestingly, the CKM matrix can be parametrised by just four $O(1)$ parameters λ, A, ρ, and η in the *Wolfenstein parametrisation*

$$\begin{pmatrix} 1 - \frac{1}{2}\lambda^2 & \lambda & A\lambda^3 (\rho - i\eta) \\ -\lambda & 1 - \frac{1}{2}\lambda^2 & A\lambda^2 \\ A\lambda^3 (1 - \rho - i\eta) & -A\lambda^2 & 1 \end{pmatrix}. \tag{1.31}$$

Diagonal elements of the CKM matrix have absolute values close to unity indicating that conversions mostly happen within the same generation. Since the CKM is a unitary matrix, $V_{u\alpha}V^*_{u\beta} + V_{c\alpha}V^*_{c\beta} + V_{t\alpha}V^*_{t\beta} = 0$ must hold. Here, $\{\alpha = d, \beta = s\}$ corresponds to products of elements of V found in the $K\bar{K}$ meson-mixing system, while $\{\alpha = d, \beta = b\}$ ($\{\alpha = s, \beta = b\}$) is found in the $B_d\bar{B}_d$ ($B_s\bar{B}_s$) system. Graphically, the unitary relation is represented by a *unitary triangle* in Figure 1.4.

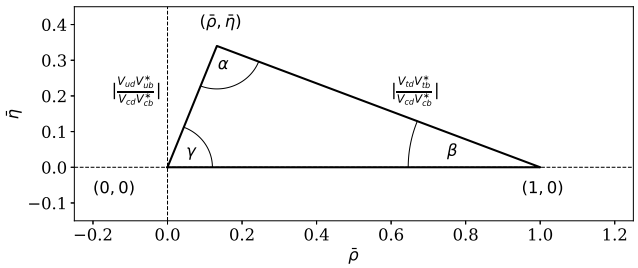

Figure 1.4: A graphical representation of the unitary triangle whose sides correspond to the three vectors in the complex plane. The $(\bar{\rho}, \bar{\eta}) = (\rho(1 - \lambda^2/2), \eta(1 - \lambda^2/2))$ are the rescaled parameters of the Wolfenstein parametrisation, and the angles can be calculated as $\alpha = \arg(V_{td}V^*_{tb}/V_{ud}V^*_{ub})$, $\beta = \arg(V_{cd}V^*_{cb}/V_{td}V^*_{tb})$, and $\gamma = \arg(V_{ud}V^*_{ub}/V_{cd}V^*_{cb})$.

1.1.7 Quantum Chromodynamics

Quantum chromodynamics (QCD) is a theory of the strong interaction between quarks and gluons. It is described by an $SU(3)_C$ symmetry group, with eight 3×3 Gell-Mann matrices, λ^a, as its generators. Thus, QCD has eight massless gauge bosons, called gluons, and three conserved *colour charges*, denoted by C. It is a non-abelian gauge theory, meaning that the generators of $SU(3)_C$ do not commute, which gives rise to gluon self-interactions. The QCD Lagrangian can be written as

$$\mathcal{L}_{\text{QCD}} = \sum_f \bar{\psi}^f_i \left(i\gamma_\mu D^\mu_{ij} - m_f \delta_{ij} \right) \psi^f_j - \frac{1}{4} G^a_{\mu\nu} G^{\mu\nu}_a, \tag{1.32}$$

where the sum over f includes all quark fields, and i and j indices run from 1 to 3. The δ_{ij} represents the Kronecker delta function, which ensures that the colour charge is conserved in the free propagation term of the Lagrangian. The ψ^f indicates a spinor triplet of a fermion, while $G^a_{\mu\nu}$ is the gluon field strength tensor. The gauge covariant derivative is defined as

$$D^{\mu}_{ij} = \partial^{\mu}\delta_{ij} - ig_s T^a_{ij} A^{\mu}_a, \tag{1.33}$$

where g_s is the $\mathrm{SU}(3)_C$ coupling constant. The $T^a = \lambda^a/2$ and A^{μ}_a $(a = 1, \ldots, 8)$ are the eight $\mathrm{SU}(3)_C$ generators and gluon fields, respectively.

The gauge invariant gluon field strength tensor is analogous to the electromagnetic field strength tensor from Eq. 1.5 and is given by

$$G^a_{\mu\nu} = \partial_{\mu}A^a_{\nu} - \partial_{\nu}A^a_{\mu} + g_s f^{abc} A^b_{\mu} A^c_{\nu}. \tag{1.34}$$

The f^{abc} represents the structure constants of the SU(3) symmetry group, and the indices a, b, and c indicate a sum over the eight colour degrees of freedom of the gluon field. Inserting the gluon field strength tensor from Eq. 1.34 to the kinetic part of the QCD Lagrangian in Eq. 1.32 yields three different types of terms, depending on the power of the gluon field, A_{μ}, two of which are also presented in Figure 1.5 in terms of Feynman diagrams:

- **quadratic term:** $\left(\partial_{\mu}A^a_{\nu}\right)\left(\partial^{\mu}A^{\nu}_a\right)$, describes the propagation of free gluons,
- **cubic term:** $g_s f_{abc}\left(\partial^{\mu}A^{\nu a} - \partial^{\nu}A^{\mu a}\right) A^b_{\mu} A^c_{\nu}$, defines the three-gluon self-interaction,
- **quartic term:** $g_s^2 f_{abc} f_{aed} A^b_{\mu} A^c_{\nu} A^{\mu e} A^{\nu d}$, specifies the four-gluon self-interaction.

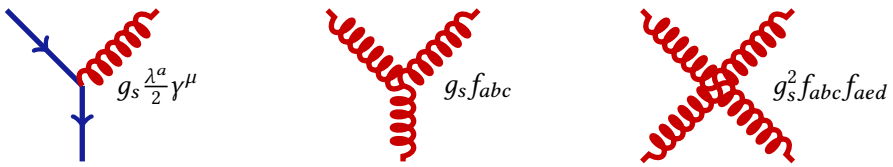

(a) (b) (c)

Figure 1.5: The strong interaction vertices depicting (a) gluon radiation, (b) gluon splitting, and (c) gluon self-interaction.

The self-interaction leads to the concepts of *asymptotic freedom* and *confinement*. At high momentum transfer or equivalently short distances, the strong coupling constant, α_s, becomes weaker contrary to the running of QED coupling, α_{EW}. This phenomenon is known as asymptotic freedom and means that quarks and gluons behave as free particles at very short distances. On the other hand, confinement refers to the interaction strength increase at high momentum transfer or large distances, which leads to the fact that colour-charged particles cannot be isolated. The energy of the gluon field between the two coloured objects that are being separated increases until, at some point, it becomes energetically favourable to form a quark-antiquark pair. As a result, when quarks are produced in particle accelerators, instead of seeing individual quarks in detectors, only jets of colour-neutral particles can be detected. This process is called hadronisation and will be discussed in Section 3.1.

1.1.8 Summary and Open Questions

The Standard Model combines insightful and profound theoretical ideas, e.g. an explanation of fermion dynamics encoded into the Dirac equation, a description of particles and their interactions by the quantum field theory, a determination of the nature of interactions by gauge principles, and the Higgs mechanism of electroweak symmetry breaking that generates particle masses. All ideas are precisely tested and supported by experimental results that often shaped the way how the SM was formed. Examples of such predictions are the discovery of the weak neutral current in 1973 with the bubble chamber at CERN [35], shortly followed by the discovery of W and Z bosons by the UA1 and UA2 collaborations [36, 37]. In 1995, the top quark was discovered by the CDF and D0 collaborations [38, 39], and the observation of τ-neutrino was made in 2000 by the DONUT collaboration [40]. Lastly, the Higgs boson was discovered in 2012 by both ATLAS [21] and CMS [22] collaborations to further strengthen the symbiosis between the theory and experiment.

The free SM parameters that need to be chosen by hand to match the observations are summarised in Table 1.2. The patterns between the different parameter values hint at a yet unknown higher theoretical principle.

Table 1.2: The 26 parameters of the Standard Model assuming neutrinos are massive Dirac fermions.

Type	Parameters	Number of parameters
Masses of fermions	m_{ν_1}, m_{ν_2}, m_{ν_3}, m_e, m_μ, m_τ m_u, m_c, m_t, m_d, m_s, m_b	12
Coupling constants	α_EM, G_F, α_s	3
Higgs potential	v, m_H	2
Mixing angles (CKM and PMNS)	λ, A, ρ, η, and θ_{12}, θ_{13}, θ_{23}, δ	8
Strong CP violation	θ_CP	1
Total number of parameters		26

Despite the success of the SM, there are many unanswered questions. Some of them are briefly discussed below.

Dark matter and dark energy. Gravitational observations indicate that approximately 27% of the matter in the universe is composed of weakly interacting, non-baryonic and non-luminous forms of matter. Furthermore, dark energy is believed to be associated with $\sim$ 68% of the universe, leaving only 5% of the universe's content for known constituents. The SM neither contains any viable dark matter candidate nor explains the relatively large energy density of the universe, responsible for the observed accelerated universe expansion [41].

Matter-Antimatter asymmetry. It is assumed that matter and antimatter were produced equally in the Big Bang. The SM can not explain why the matter prevails nowadays. The non-equal production of matter and antimatter requires violating the baryon number as well as the charge (C) and charge-parity (CP) symmetries. Although the SM involves CP

violation in the quark sector, its consequences are too small to account for the observed asymmetry [42].

Hierarchy problem is related to the Higgs boson mass value. The Higgs mass consists of its bare mass and a contribution of loop quantum corrections of all SM particles that couple to it, here denoted Δm_h^2. The radiative corrections are of the form

$$\Delta m_h^2 = \frac{y_f}{16\pi^2}\left(2\Lambda^2 + O\left[m_f^2 \ln\frac{\Lambda}{m_f}\right]\right), \tag{1.35}$$

where y_f is the Yukawa coupling to the fermions, m_f is their mass, and Λ is the ultraviolet energy scale cutoff beyond which the SM is invalid. Fine-tuning with the utmost precision is required to achieve cancellation between the bare mass and all radiative corrections and, on this wise, extract m_h, consistent with its observed value. The hierarchy problem is also related to naturalness because the fine-tuning of Higgs mass terms involves energy scales 17 orders of magnitudes higher than the m_h, which is unnatural.

Neutrino masses can not be generated within the SM as no right-handed states exist. However, it is known from neutrino oscillations that neutrinos are massive [43–45]. The current sum of neutrino masses, defined as $m_{\text{tot}} = \sum_\nu m_\nu$, is bounded between 0.06 eV and 0.12 eV [32]. Furthermore, neutrinos are the only SM particles whose Dirac versus Majorana nature is not determined yet. One of the possible solutions to the neutrino mass problem is discussed in Section 1.2.

1.2 Physics Beyond the Standard Model

Despite an accurate description of a large variety of fundamental laws of nature, the SM is still not considered the Theory of Everything due to its inability to adequately explain some physical phenomena discussed in Section 1.1.8. Due to these SM deficiencies, many theoretical Beyond the Standard Model (BSM) developments are proposed, extending the SM to be consistent with existing data. Unfortunately, no hints of any new particles were observed after 2012. Furthermore, no experimental result is accepted as definitely contradicting the SM at the 5σ level, widely considered as the threshold for discovery. That may be due to the relatively small production cross-sections or high masses of the potential BSM particles. This section focuses on SM extensions that generate neutrino masses and introduce doubly charged scalars which are the basis for the analysis presented in Part III.

1.2.1 Neutrino Masses and the Seesaw Mechanism

Multiple experimental observations of neutrino oscillations [43–45] require neutrinos to be massive. However, the SM can not explain non-zero neutrino masses at the renormalisable level due to the gauge symmetry and the absence of right-handed neutrinos.

Neutrino mass eigenstates ν_1, ν_2, and ν_3 may not be necessarily aligned with the weak eigenstates ν_e, ν_μ, and ν_τ. The two eigenstate bases can be related by a unitary matrix, analogous to the

CKM matrix from Eq. 1.30. In the lepton sector, the matrix is known as the Pontecorvo-Maki-Nakagawa-Sakata (PMNS) matrix [46] and can be parametrised as

$$U_{\text{PMNS}} = \begin{pmatrix} c_{12}c_{13} & s_{12}c_{13} & s_{13}e^{-i\delta} \\ -s_{12}c_{23} - c_{12}s_{23}s_{13}e^{i\delta} & c_{12}c_{23} - s_{12}s_{23}s_{13}e^{i\delta} & s_{23}c_{13} \\ s_{12}s_{23} - c_{12}c_{23}s_{13}e^{i\delta} & -c_{12}s_{23} - s_{12}c_{23}s_{13}e^{i\delta} & c_{23}c_{13} \end{pmatrix} \text{diag}\left(1,\, e^{i\alpha},\, e^{i\beta}\right) \tag{1.36}$$

with s_{ij} and c_{ij} representing sines and cosines of the three mixing angles θ_{12}, θ_{13}, and θ_{23}. Phase angles α, β and δ are related to charge-parity violations.

A way of generating neutrino masses is by introducing a new degree of freedom to the SM, e.g. a right-handed neutrino. In general, a Dirac mass term can be constructed in the same way as for the up-type quarks

$$\mathcal{L}_{\text{D}} = -m_D \left(\bar{\nu}_R \nu_L + \bar{\nu}_L \nu_R\right), \tag{1.37}$$

where m_D is a complex non-diagonal matrix, $(m_\nu)^{ij}_D = y^{ij}_D v/\sqrt{2}$, that can be diagonalised by using the PMNS matrix.[6]

On the other hand, the only way to generate neutrino masses without introducing right-handed neutrinos is to add a non-renormalisable neutrino mass term to the SM Lagrangian, the so-called *dimension-5 Weinberg operator*

$$\mathcal{L}_{d=5} = -y_{ij} \frac{\left(L_i^T i\tau_2 \phi\right) i\sigma_2 \left(\phi^T i\tau_2 L_j\right)}{\Lambda}, \tag{1.38}$$

where $i\tau_2$ makes the $L^T i\sigma_2 \phi$ term gauge invariant and $i\sigma_2$ Lorentz invariant. Here, both σ and τ are Pauli matrices, while L represents the left-handed lepton doublet, and Λ is the cutoff energy scale of the effective theory with effective Yukawa couplings, y_{ij}. Once the electroweak symmetry is spontaneously broken, neutrino mass can be extracted as

$$(m_\nu)^{ij}_M = y^{ij}_M \frac{v^2}{\Lambda}, \tag{1.39}$$

where M refers to the Majorana nature of neutrinos. It was in 1937 when E. Majorana [47] proposed an idea that electrically neutral half-spin particles can be described by a real-valued wave equation and would therefore be identical to their antiparticles. Neutrinos are the only SM particles that can be of Majorana type because the Majorana mass term implies direct particle-antiparticle couplings, which would allow, e.g. $e^- \leftrightarrow e^+$ transitions and, this way, violate the charge conservation. A Majorana neutrino is defined as $\nu = \nu_L + \nu_L^C$, where C represents the charge-conjugated field, $\psi^C = \hat{C}\psi = i\gamma^2\gamma^0\psi^*$. The CP conjugate field for the right-handed neutrino, ν_R^C, corresponds to a left-handed antineutrino, $\bar{\nu}_L$. The Majorana mass term is then defined as

$$\mathcal{L}_{\mathcal{M}} = -\frac{1}{2} m_M \left(\bar{\nu}_R^C \nu_R + \bar{\nu}_R \nu_R^C\right), \tag{1.40}$$

Neutrino masses are bounded to orders of magnitude below those of other SM particles [32], hinting at some other mechanism that might generate them. In terms of the *seesaw mechanism*, tiny masses can be directly attributed to the existence of heavy degrees of freedom and lepton

[6] Note that in the case of Dirac neutrinos two extra complex phases α and β are not needed in Eq. 1.36.

number violation. Extending the SM field content minimally, i.e., by only a single SM multiplet, only three models known as the type-I [2, 48, 49], type-II [49–51], and type-III [52] seesaw mechanisms are possible:

Type-I seesaw hypothesises the existence of a right-handed neutrino, ν_R, which transforms as a singlet under the SM gauge group and obtains a Majorana mass.

Type-II seesaw introduces an $\mathrm{SU}(2)_L$ scalar triplet, Δ, which couples to a left-handed lepton doublet and its charge conjugate, thus violating the lepton number by two units.

Type-III seesaw adds an $\mathrm{SU}(2)_L$ fermionic triplet, Σ. It is similar to type-I but additionally features heavy leptons that are electrically charged.

1.2.2 Left-Right Symmetric Model

Contrary to all other fundamental forces, the weak interaction is completely asymmetric between left- and right-handed fields, which even have different gauge structures. Parity violation is an experimental fact that helped shape the construction of the SM, but its origin remained unexplained. Therefore, it is natural to seek higher symmetry in a parity-conserved theory at some higher energy scale, which is at some point spontaneously broken. The idea was presented by Pati, Salam, Mohapatra, and Senjanovic in the 1970s and is known as the *left-right symmetric model* (LRSM) [53–59]. In addition to the SM symmetry group, the minimal LR symmetric theory introduces an $\mathrm{SU}(2)_R$ local symmetry, under which left-handed fields transform as singlets and right-handed fields as doublets, making the LRSM gauge group

$$\mathrm{SU}(3)_C \times \mathrm{SU}(2)_L \times \mathrm{SU}(2)_R \times \mathrm{U}(1)_{B-L}. \tag{1.41}$$

Quarks and leptons are completely symmetric and can be written with their corresponding quantum numbers as

- **left-handed quarks:** $Q_L = \begin{pmatrix} u_L \\ d_L \end{pmatrix} \sim (3_C,\ 2_L,\ 1_R,\ 1/3_{B-L})$,
- **right-handed quarks:** $Q_R = \begin{pmatrix} u_R \\ d_R \end{pmatrix} \sim (3_C,\ 1_L,\ 2_R,\ 1/3_{B-L})$,
- **left-handed leptons:** $L_L = \begin{pmatrix} \nu_L \\ e_L \end{pmatrix} \sim (1_C,\ 2_L,\ 1_R,\ -1_{B-L})$,
- **right-handed leptons:** $L_R = \begin{pmatrix} \nu_R \\ e_R \end{pmatrix} \sim (1_C,\ 1_L,\ 2_R,\ -1_{B-L})$.

The interaction Lagrangian is the same as in the SM, $\mathcal{L} = \bar{f} i\gamma^\mu D_\mu f$, but the covariant derivative now contains additional gauge symmetries introduced by the LRSM

$$D_\mu = \partial_\mu - i\left(g_S A^a_\mu T^a_{ij} + g_L W^a_{\mu L}\frac{\sigma^L_a}{2} + g_R W^a_{\mu R}\frac{\sigma^R_a}{2} + g' B_\mu \frac{B-L}{2}\right), \tag{1.42}$$

where g_S, g_L, g_R and g' are the gauge couplings, often fixed to $g = g_L = g_R$. The LRSM modifies the Gell-Mann-Nishijima formula from Eq. 1.15 to

$$q = T_{3L} + T_{3R} + \frac{B-L}{2}, \tag{1.43}$$

exchanging the SM hypercharge for $B - L$, with B representing the baryon and L the lepton number. The T_{3L} and T_{3R} are, respectively, the third components of isospin of the gauge groups $\mathrm{SU}(2)_L$ and $\mathrm{SU}(2)_R$.

There are multiple valid options for enlarging the Higgs sector of the model, but the most widely used is the addition of a bi-doublet $\Phi = (1_C, 2_L, 2_R, 0_{B-L})$, an $\mathrm{SU}(2)_L$ triplet $\Delta_L = (1_C, 3_L, 1_R, 2_{B-L})$, and an $\mathrm{SU}(2)_R$ triplet $\Delta_R = (1_C, 1_L, 3_R, 2_{B-L})$.

Symmetry requirements govern the bi-doublet and the triplets to be defined as

$$\Phi = \begin{pmatrix} \phi_1^0 & \phi_2^+ \\ \phi_1^- & \phi_2^0 \end{pmatrix}, \qquad \Delta_{L,R} = \begin{pmatrix} \Delta^+/\sqrt{2} & \Delta^{++} \\ \Delta^0 & -\Delta^+/\sqrt{2} \end{pmatrix}_{L,R}. \tag{1.44}$$

In general, the structure of the potential is quite complicated and is thoroughly presented in, e.g. Ref. [60]. In principle, all neutral components of the new Higgs fields acquire real and positive vevs, but the minimisation of the Higgs scalar potential allows us to choose the following

$$\langle \Phi \rangle = \begin{pmatrix} v_1 & 0 \\ 0 & v_2 e^{i\alpha} \end{pmatrix}, \qquad \langle \Delta_L \rangle = 0, \qquad \langle \Delta_R \rangle = \begin{pmatrix} 0 & 0 \\ v_R & 0 \end{pmatrix}, \tag{1.45}$$

where $v^2 = v_1^2 + v_2^2$. Therefore, the SSB happens in two consecutive steps. First, the extended gauge group of the LRSM breaks down into the local symmetries of the SM at high energies

$$\mathrm{SU}(3)_C \times \mathrm{SU}(2)_L \times \mathrm{SU}(2)_R \times \mathrm{U}(1)_{B-L} \rightarrow \mathrm{SU}(3)_C \times \mathrm{SU}(2)_L \times \mathrm{U}(1)_{B-L}, \tag{1.46}$$

when a neutral right-handed component of Δ_R acquires a non-vanishing vev. The right-handed counterparts of W and Z bosons arise, which acquire masses as a result of the SSB. Furthermore, the v_R also provides masses for right-handed neutrinos and all scalars except the SM Higgs doublet. Then, the Higgs mechanism explained in Section 1.1.6 occurs at the electroweak scale when Φ develops a vacuum expectation value. Hence, the SM symmetry is broken to $\mathrm{U}(1)_{\mathrm{EM}}$.

The masses of the gauge bosons are obtained from the scalar part of the Lagrangian

$$\mathcal{L}_s = \mathrm{Tr}\left(D_\mu \Delta_L\right)^\dagger \left(D^\mu \Delta_L\right) + \mathrm{Tr}\left(D_\mu \Delta_R\right)^\dagger \left(D^\mu \Delta_R\right) + \mathrm{Tr}\left(D_\mu \Phi\right)^\dagger \left(D^\mu \Phi\right) \tag{1.47}$$

$$= \begin{pmatrix} W_L^+, & W_R^+ \end{pmatrix} \begin{pmatrix} \frac{1}{2}g^2 v^2 & -g^2 v_1 v_2 e^{-i\alpha} \\ -g^2 v_1 v_2 e^{i\alpha} & g^2(v_R^2 + \frac{1}{2}v^2) \end{pmatrix} \begin{pmatrix} W_L^- \\ W_R^- \end{pmatrix}$$

$$+ \frac{1}{2} \begin{pmatrix} W_{3L}, & W_{3R}, & B \end{pmatrix} \begin{pmatrix} \frac{1}{2}g^2 v^2 & -\frac{1}{2}g^2 v^2 & 0 \\ -\frac{1}{2}g^2 v^2 & g^2(2v_R^2 + \frac{1}{2}v^2) & -2gg' v_R^2 \\ 0 & -2gg' v_R^2 & 2g'^2 v_R^2 \end{pmatrix} \begin{pmatrix} W_{3L} \\ W_{3R} \\ B \end{pmatrix}. \tag{1.48}$$

From the experimental constraints, the vev values are considered to be hierarchical, $v_L \ll v \ll v_R$, so the gauge boson masses are extracted to be

$$m_W^2 = \frac{1}{2}g^2\left(v^2 + v_R^2 - \sqrt{4v_1v_2 + v_R^4}\right) \simeq \frac{1}{2}g^2v^2, \tag{1.49}$$

$$m_{W_R}^2 = \frac{1}{2}g^2\left(v^2 + v_R^2 + \sqrt{4v_1v_2 + v_R^4}\right) \simeq g^2\left(v_R^2 + \frac{1}{2}v^2\right), \tag{1.50}$$

$$m_Z^2 = \frac{1}{2}\left[g^2v^2 + 2(g^2+g'^2)v_R^2 + \sqrt{g^4v^4 - 4g^2g'^2v^2v_R^2 + 4(g^2+g'^2)^2v_R^2}\right] \simeq \frac{1}{2}\left(g^2 + g_Y^2\right)v^2, \tag{1.51}$$

$$m_{Z'}^2 = \frac{1}{2}\left[g^2v^2 + 2(g^2+g'^2)v_R^2 - \sqrt{g^4v^4 - 4g^2g'^2v^2v_R^2 + 4(g^2+g'^2)^2v_R^2}\right] \simeq 2\left(g^2 + g'^2\right)v_R^2, \tag{1.52}$$

$$m_A^2 = 0, \tag{1.53}$$

where $g_Y^{-2} = g^{-2} + g'^{-2}$. Note that the masses of SM W and Z bosons are restored, i.e. $m_W/m_Z = \cos\theta_W$. Furthermore, not only does the LRSM restore parity, but it can also fix hypercharges that are, in principle, entirely arbitrary within the SM, explain the strong CP problem, and, paramount for this work, generate neutrino masses.

Since the LRSM introduces the right-handed neutrino for each lepton flavour, both Dirac and Majorana mass terms are possible. The Yukawa Lagrangian is given by

$$\mathcal{L}_{\text{Yuk}}^{\ell} \supset \bar{L}_L\left(y^{\ell}\Phi + \tilde{y}^{\ell}\tilde{\Phi}\right)L_R + \frac{1}{2}\left[y_L^{\ell}\,\overline{L_L^{\,c}}\,i\sigma_2\Delta_L L_L + y_R^{\ell}\,\overline{L_R^{\,c}}\,i\sigma_2\Delta_R L_R\right] + \text{h.c.}, \tag{1.54}$$

where h.c. denotes hermitian-conjugated terms. Dirac term arises from neutrino couplings to Higgs bi-doublet, Φ, while the Majorana mass term comes through Yukawa couplings between the SM leptonic doublet and the scalar triplet, $\Delta_{L,R}$. The complete mass matrix has a 6×6 structure and can be written as

$$\mathcal{L}_{mass}^{\ell} = -\frac{1}{2}\begin{pmatrix}\overline{\nu_L^{\,c}} & \overline{\nu_R}\end{pmatrix}\begin{pmatrix}M_L & M_D\\ M_D^{\mathrm{T}} & M_R\end{pmatrix}\begin{pmatrix}\nu_L\\ \nu_R^{\,c}\end{pmatrix}. \tag{1.55}$$

Here, M_D is the Dirac mass matrix and $M_{L,R}$, which are proportional to $v_{L,R}$, are the symmetric Majorana mass matrices corresponding to the neutrino-triplet couplings. Since Dirac masses must be small, one can hypothesise a hierarchy $M_L \ll M_D \ll M_R$ and diagonalise the mass matrix to obtain

$$\begin{pmatrix}\nu\\ N\end{pmatrix} = \begin{pmatrix}M_L - M_D^{\mathrm{T}}M_R^{-1}M_D & 0\\ 0 & M_R\end{pmatrix}\begin{pmatrix}\nu_L\\ \nu_R^{\,c}\end{pmatrix}. \tag{1.56}$$

The diagonal elements represent masses of three light, ν, and three heavy, N, neutrino states, respectively. The right-handed neutrino is heavy since its mass M_R is proportional to v_R, while the left-handed neutrinos remain light because the $M_L \propto v_L$ is small and $M_D^{\mathrm{T}}M_R^{-1}M_D$ is inversely proportional to v_R. This process of mass generation is known as a combined type-I and type-II seesaw mechanism since it contains both heavy right-handed neutrino and interactions with Higgs triplet fields. Furthermore, the mixing between light and heavy neutrino states can

be extracted by using $M_R = v_R/v_L M_L$ and considering the symmetricity of the Dirac mass matrix [61]:

$$M_D = M_R\sqrt{\frac{v_L}{v_R} - M_R^{-1}m_\nu}. \tag{1.57}$$

1.2.3 The Zee–Babu Model

The Zee–Babu model [62–64] is an economical extension of the SM. In addition to the usual SM Higgs doublet, two complex $\mathrm{SU}(2)_L$ scalar singlets, a singly charged $h^\pm$ and a doubly charged $k^{\pm\pm}$, are introduced. With the SM gauge group, $\mathrm{SU}(3)_C \times \mathrm{SU}(2)_L \times \mathrm{U}(1)_Y$, and the usual Gell-Mann-Nishijima formula from Eq. 1.15, their quantum numbers are

$$h^\pm \sim (1, 1, +1), \tag{1.58a}$$
$$k^{\pm\pm} \sim (1, 1, +2). \tag{1.58b}$$

Both singlets are assigned the lepton number $L = +2$. The Zee-Babu Lagrangian, $\mathcal{L}_{\mathrm{ZB}}$, consists of the SM one with a few additions

$$\mathcal{L}_{\mathrm{ZB}} = \mathcal{L}_{\mathrm{SM}} + \mathcal{L}_{\mathrm{kin}} + \mathcal{L}_{\mathrm{Yuk}} + \mathcal{L}_s, \tag{1.59}$$

where the kinetic part includes covariant derivatives with couplings to hypercharge field, B_μ:

$$\mathcal{L}_{\mathrm{kin}} = (D_\mu k)^\dagger (D^\mu k) + (D_\mu h)^\dagger (D^\mu h), \quad \text{with} \quad D_\mu = \partial_\mu + i g_Y \frac{Y}{2} B_\mu. \tag{1.60}$$

The $h^\pm$ couples to left-handed lepton doublets and $k^{\pm\pm}$ to right-handed lepton singlets, yielding a Yukawa part of the Lagrangian

$$\mathcal{L}_{\mathrm{Yuk}} = f_{ij}\overline{L^c_{L_i}} i\sigma_2 L_{L_j} h^\dagger + g_{ij}\overline{e^c_{Ri}} e_{Rj} k^\dagger + \mathrm{h.c.}, \tag{1.61}$$

where f_{ij} is a 3×3 complex anti-symmetric matrix representing Yukawa couplings to h, and g_{ij} is a 3×3 complex symmetric matrix of couplings to k. The L represents the left-handed SM lepton doublet, and the e_R is the right-handed SM lepton singlet, with index i running across three generations. From the scalar potential, $\mathcal{L}_s$, one obtains the physical masses of h and k, which are free parameters of the model. Since h and k do not mix with SM states, their gauge and mass states are aligned. The Yukawa parts, proportional to f_{ij} and g_{ij}, along with the trilinear term, $\mu_L hhk^\dagger$, from the scalar potential, violate the lepton number by two units, $\Delta L = \pm 2$. The parameter μ_L is identified as the scale of the lepton number violation.

The dominant $k^{\pm\pm}$ decay channels include $\ell^\pm\ell'^\pm$, $h^\pm h^\pm$, $h^\pm \ell^\pm \nu$, $h^\pm h^\pm + Z/H^0/\gamma$, and $\ell^\pm W^\pm \nu$. The decay of $k^{\pm\pm}$ into same-charged leptons within the Zee–Babu model is relevant to the analysis presented in Part III. Its decay width is given by

$$\Gamma(k^{\pm\pm} \to \ell^\pm \ell'^\pm) = \frac{|g_{\ell\ell'}|^2}{4\pi(1 + \delta_{\ell\ell'})} m_{k^{\pm\pm}}. \tag{1.62}$$

Since the $g_{\ell\ell'}$ couplings are free parameters, the branching ratios of the different decay modes are a priori unknown. It was shown in Ref. [65] that approximately 99% of the time k decays

into same-charge leptons for a benchmark input $m_k = 500\,\text{GeV}$, $m_h = 300\,\text{GeV}$, $\mu_L = 1\,\text{TeV}$, and $g_{\ell\ell'} = 1$. On the other hand, if $m_k > 2m_h > 200\,\text{GeV}$, it can happen that k predominantly decays into hh, which can easily escape detection [66].

There are no right-handed neutrinos in the Zee–Babu model. Therefore, Dirac mass terms can not be constructed. In addition, h and k cannot contract with lepton and Higgs doublets to generate Majorana masses at the tree level. Instead, left-handed Majorana neutrino masses are generated radiatively via two-loop diagrams, as shown in Figure 1.6.

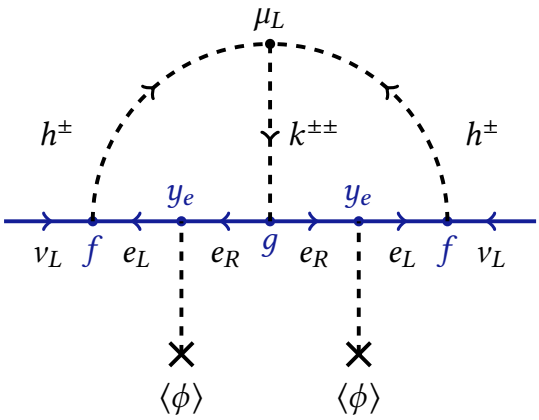

Figure 1.6: The two-loop Feynman diagram that contributes to the neutrino Majorana mass within the Zee–Babu model. In this graph, f and g are the Yukawa couplings to h and k, respectively, while y_e is the SM lepton Yukawa term, defined as $y_e H \bar{L} e_R$. The parameter μ_L, defining the trilinear coupling, is identified as the scale of the lepton number violation.

1.2.4 Doubly Charged Higgs Boson Production

No doubly charged bosons are present in the SM. However, various BSM theories, namely type-II seesaw models [49–51], LRSM [53–59], Zee–Babu neutrino mass model [62–64], 3-3-1 models [67], and the Georgi–Machacek model [68], predict the existence of doubly charged bosons. This thesis focuses on the search for doubly charged Higgs bosons within the former three, with the results presented in Part III.

In LRSM, Higgs multiplets Δ_L and Δ_R, transforming respectively as triplets under $\text{SU}(2)_L$ and $\text{SU}(2)_R$ gauge symmetries, contain doubly charged Higgs bosons, termed $H_L^{\pm\pm}$ and $H_R^{\pm\pm}$. Doubly charged Higgs particles can therefore couple to either left-handed or right-handed leptons, vector gauge bosons or scalars from the triplet.[7] The dominant production mechanism for the $H^{\pm\pm}$ at the LHC is the Drell–Yan process through an s-channel photon or a Z boson exchange. However, the two chiralities are not produced equally, as the $H_L^{++}H_L^{--}$ Drell–Yan production cross-section is a factor of about two larger than the $H_R^{++}H_R^{--}$ production due to the different couplings to the Z boson [69]. The Feynman diagram of the Drell–Yan production process is shown in Figure 1.7. At the LHC, other production mechanisms, such as vector-boson fusion,

[7] Quarks can not interact with any of the scalar triplet members due to the $\text{U}(1)_{B-L}$ symmetry.

gluon–gluon fusion, and photon-initiated [70] processes, are less significant than Drell–Yan production [69].

In the Zee–Babu case, two complex scalar $SU(2)_L$ singlets are proposed within the SM gauge group, where one is doubly charged and is usually denoted by $k^{\pm\pm}$. As it has the same quantum numbers as the $H_R^{\pm\pm}$ from LRSM, their electroweak production is the same.[8] It was recently shown that for the Drell–Yan production mechanism, cross-sections and differential scalar distributions in the Zee–Babu and type-II seesaw models differ at most by a normalisation factor when all theoretical inputs are the same [65]. If not stated explicitly, $H^{\pm\pm}$ represents any of the $H_L^{\pm\pm}$, $H_R^{\pm\pm}$, or $k^{\pm\pm}$ particles throughout the thesis.

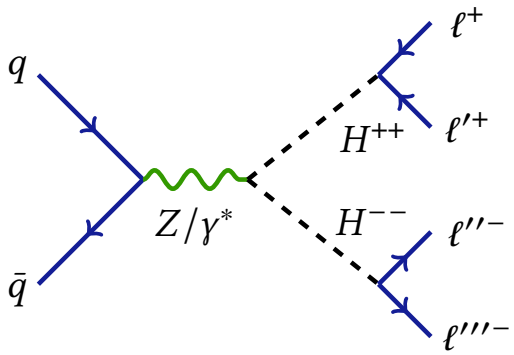

Figure 1.7: Feynman diagram of the Drell–Yan pair production process, $pp \to H^{++}H^{--}$, is presented. While the analysis presented in Part III allows for $H^{\pm\pm}$ decays into all lepton flavour combinations, it only studies electrons and muons in the final states.

The doubly charged Higgs boson can decay either to WW or $\ell\ell'$ ($\ell, \ell' = e,\ \mu,\ \tau$), depending on the vacuum expectation value of the Δ_L Higgs triplet, v_L. For low v_L values, it decays exclusively to leptons, while for larger v_L values, it predominantly decays into a pair of W bosons. The decay width for $H^{\pm\pm}$ into a pair of W bosons, assuming $m_W \ll m_{H^{\pm\pm}}$, is given by

$$\Gamma(H^{\pm\pm} \to W^{\pm}W^{\pm}) = \frac{g^4 v_L^2}{32\pi}\left(\frac{8}{m_{H^{\pm\pm}}} + \frac{m_{H^{\pm\pm}}^3}{m_W^4}\right), \tag{1.63}$$

where the first term, proportional to $m_{H^{\pm\pm}}^{-1}$, corresponds to the transverse component of the W boson, while the second term, proportional to $m_{H^{\pm\pm}}^3$, corresponds to the longitudinal component. The vacuum expectation value, v_L, smaller than 10^{-8} GeV, is studied in the analysis presented in Part III. Therefore, only leptonic decays of doubly charged Higgs bosons, $H^{\pm\pm} \to \ell^{\pm}\ell'^{\pm}$, are relevant, for which the decay width can be calculated by

$$\Gamma(H^{\pm\pm} \to \ell^{\pm}\ell'^{\pm}) = \frac{1}{1+\delta_{\ell\ell'}}\frac{h_{\ell\ell'}^2}{16\pi} m_{H^{\pm\pm}}, \tag{1.64}$$

where the Kronecker $\delta_{\ell\ell'}$ accounts for the phase space factor of $1/2!$ for identical final state leptons. Factor $h_{\ell\ell'}$ has an upper bound that depends on the flavour combination [71, 72].

[8] In principle, the $H_R^{\pm\pm}$ also couples to a Z' boson, which makes their production cross-sections distinguishable. However, the Z' boson is assumed to have a mass well beyond the energy reach of the LHC, thus making its effects negligible.

In general, there is no preference for decays into heavier leptons since the coupling is not proportional to the lepton mass as it is for the SM Higgs boson. It is worth stressing that lepton-flavour-violating decays such as $H^{\pm\pm} \to e^{\pm}\mu^{\pm}/\mu^{\pm}\tau^{\pm}/e^{\pm}\tau^{\pm}$ are also allowed by the model. This fact connects high-energy searches at LHC with low-energy neutrinoless double beta decay searches [73, 74]. The $H^{\pm\pm}$ branching ratios to $\ell^{\pm}\ell^{\pm}$ and $W^{\pm}W^{\pm}$ final states are presented in Figure 1.8.

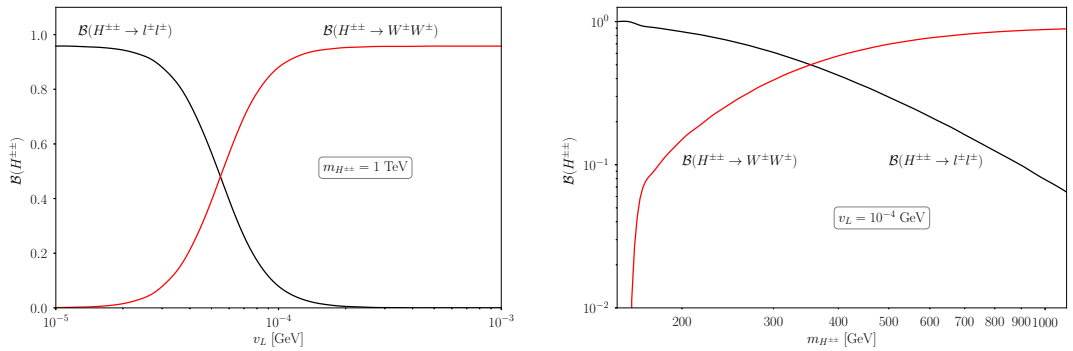

(a) (b)

Figure 1.8: Doubly charged Higgs branching ratios as a function of (a) v_L at $m_{H^{\pm\pm}} = 1$ TeV and (b) $m_{H^{\pm\pm}}$ at $v_L = 10^{-4}$ GeV. Since other decay channels represent a minor contribution to $H^{\pm\pm}$ branching ratios (below 5%), only branching ratios $\mathcal{B}(H^{\pm\pm} \to \ell^{\pm}\ell^{\pm})$ and $\mathcal{B}(H^{\pm\pm} \to W^{\pm}W^{\pm})$ are presented. The branching ratios were obtained using MadGraph5_aMC@NLO 3.5.1 [75, 76] and UFO model files from Ref. [69].

The ATLAS Collaboration previously analysed data corresponding to an integrated luminosity of 36.1 fb^{-1} from $\sqrt{s} = 13$ TeV pp collisions at the LHC during the 2015 and 2016 data-taking periods. Masses of doubly charged Higgs bosons were excluded up to 870 GeV for $H_L^{\pm\pm}$ and up to 760 GeV for $H_R^{\pm\pm}$ at 95% confidence level [77]. The CMS Collaboration performed a similar search using $\sqrt{s} = 7$ TeV pp collisions collected during Run 1 [78], establishing lower bounds on the $H^{\pm\pm}$ mass between 204 GeV and 459 GeV in the 100% branching fraction scenarios, depending on the flavour content of the two-lepton final states. A complementary analysis from the ATLAS Collaboration searched for doubly charged Higgs bosons in the $H^{\pm\pm} \to W^{\pm}W^{\pm}$ decay channel using the whole 139 fb^{-1} dataset from Run 2 of the LHC and excluded $H^{\pm\pm}$ masses up to 350 GeV [79].

1.3 Phenomenology of Proton–Proton Collisions

The analysis presented in this thesis relies on data coming from high-energy pp collisions produced at the LHC. The proton is a bound state consisting of three *valence* quarks (*uud*) that determine the quantum numbers of the proton, a cloud of virtual quark–antiquark pairs termed *sea* quarks, and gluons. These proton constituents are collectively called *partons* and can all participate in a collision. Inelastic pp collisions, in which individual partons interact with each

other, occur when there is a sufficiently high momentum transfer Q^2 available. Such processes are called hard-scattering interactions and are usually the main target of physics analyses. However, since colliding protons are not elementary particles, a complex series of QED and QCD processes happen in reality in a single proton collision, as depicted in Figure 1.9.

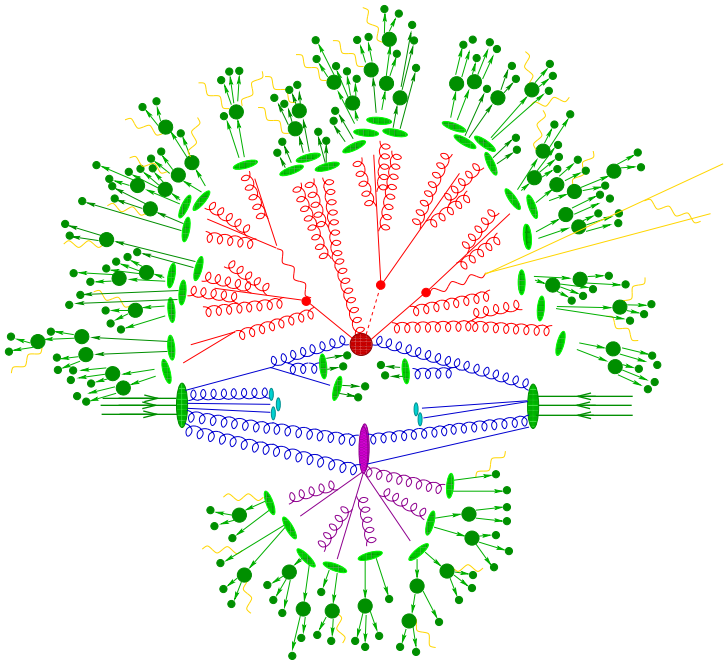

Figure 1.9: Sketch of a hadron–hadron collision. See the text for more details. Adopted from Ref. [80].

The dark green ellipses with the pointing arrows portray the protons approaching the interaction point. The blue lines represent the *initial state radiation* (ISR), with two of the partons participating in a primary hard interaction depicted with a dark red circle. The *final state radiation* (FSR) is presented with red lines, where some partons can further split according to QCD processes. Electrically charged particles also radiate soft photons, shown in yellow, in a process known as Bremsstrahlung. The light green ellipses represent hadronisation, where the quarks and gluons from hard scattering interactions, parton showers and multiple scattering interactions must be transformed into colour-neutral final states. A purple blob indicates a secondary hard scattering event. The energy scale decreases from hard scattering interactions ($\mathcal{O}(1)$ TeV) in the centre to the *parton shower* (PS) and hadronisation processes ($\mathcal{O}(1)$ GeV) in the outer shells of the sketch. Due to these large energy separations, processes must be treated differently within the QCD to get a physical observable, such as the cross-section. The asymptotic freedom allows us to perform perturbative matrix element calculations for hard interactions, while the hadronisation is dominated by non-perturbative effects and can thus only be modelled phenomenologically. Fortunately, the QCD *factorisation theorem* [81] states that one can always set a factorisation scale μ_F (energy scale that characterises the parton-parton interaction) to separate the cross-section of a high-energy pp collision from Eq. 1.65 into two parts. Depending on the parton's transverse momentum, it determines whether the individual parton participates in the hard scattering process ($p_{\mathrm{T}}^{\mathrm{parton}} > \mu_F$) or is part of the hadron structure

($p_{\mathrm{T}}^{\mathrm{parton}} < \mu_F$). If latter, the parton is absorbed in the *parton distribution functions* (PDFs) that quantify the probability of finding a parton inside a proton that carries a fraction x of the total proton's momentum. They can not be calculated using the perturbation theory but are determined experimentally at specific energy scales, usually from deep inelastic scattering measurements. An extrapolation to the energy scale relevant to the specific calculation of the physics process is then made using the DGLAP evolution equations [82–84], which unfolds the PDFs from one scale to another. An example of a NNPDF3.1NLO [85] set is shown in Figure 1.10.

The cross-section of a hard scattering pp collision can be written as a convolution of PDFs and the short-distance partonic cross-section

$$d\sigma_{pp\to f}(s,\ \mu_R,\ \mu_F) = \sum_{i,j} \int_0^1 dx_1 \int_0^1 dx_2\ f_i(x_1,\mu_F)\ f_j(x_2,\mu_F)\ d\hat{\sigma}_{ij\to f}(\hat{s},\ \mu_R,\ \mu_F), \tag{1.65}$$

where μ_R and μ_F represent the renormalisation and factorisation scales, respectively. The renormalisation scale is defined to integrate out divergences which appear in predictions beyond the LO, while the factorisation scale is introduced to regularise UV divergences which appear in partonic cross-section calculations beyond LO into a redefinition of the PDF. The sum runs over i, j partons within the colliding hadrons. f_i and f_j represent PDFs, and $d\hat{\sigma}_{ij\to f}$ denotes the partonic cross-section that can be calculated using Feynman rules. The variable s stands for the squared centre of mass energy of the collision, and $\hat{s}$ is its fraction that participates in the hard-scattering process, $\hat{s} = x_1 x_2 s$.

The partonic cross-section depends on the choice of μ_R and μ_F, but the dependence is weaker when more and more perturbative orders are included in the calculation. As a result, when computing cross sections involving QCD, it is common to incorporate higher-order loop diagrams, such as those at the next-to-leading order (NLO) or next-to-next-to-leading order (NNLO) level.

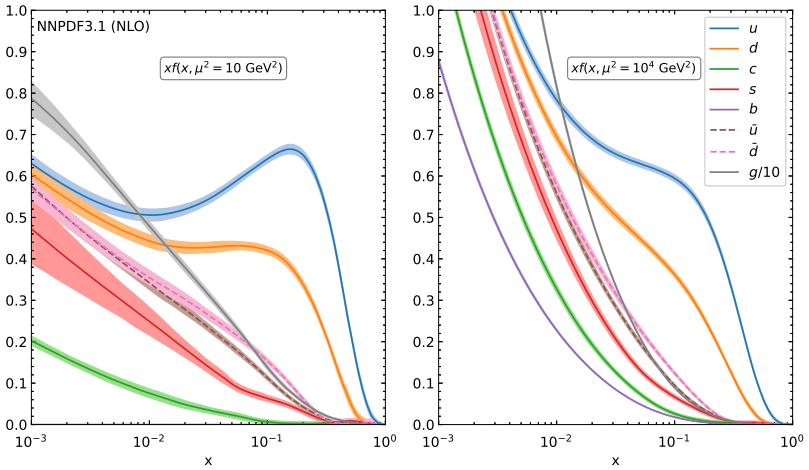

Figure 1.10: Parton distribution functions provided by the NNPDF collaboration [85] are shown as a function of x for two different factorisation scales μ_F, where x is the fraction of the total proton's momentum carried by the individual parton. The x dependence is obtained from a combined fit to data, while the scale dependence is calculated using the DGLAP evolution. The PDFs were downloaded and evaluated via the LHAPDF interface [86].

Part II

EXPERIMENTAL SETUP

CHAPTER 2

The ATLAS Detector at the CERN Large Hadron Collider

This chapter describes two technological masterpieces in high-energy physics, without which the data analysis would not be possible. First, Section 2.1 introduces the Large Hadron Collider, the world's largest and most powerful particle accelerator. Then, the ATLAS detector and its sub-detector components are outlined in Section 2.2.

2.1 The Large Hadron Collider

The Large Hadron Collider (LHC) [87] is the most powerful particle accelerator and collider ever built and is located at the European Organization for Nuclear Research (CERN) laboratory near Geneva, Switzerland. It is installed in a circular tunnel that lies between 45 m and 170 m below the surface on a plane inclined at 1.4% with a slope towards the Léman lake. The tunnel that has a circumference of 27 km was constructed between 1984 and 1989 for the LHC's lepton predecessor, the Large Electron–Positron (LEP) collider, which ended its operation in 2000. It took 8 years to finalise the hadron collider, which was first started on 10 September 2008. It can accelerate both protons and heavy ions. The scheme of the CERN complex is presented in Figure 2.1.

The first stage of the LHC acceleration is the 86 m long linear accelerator 4 (Linac4), which accelerates negative hydrogen ions (H^-) to 160 MeV to prepare them for entering the Proton Synchrotron Booster (PSB), which is the next part of the LHC injection chain. The ions are stripped of their two electrons during injection from Linac4 into the PSB to leave only protons, which are then accelerated to 2 GeV for injection into the Proton Synchrotron (PS). The PS has a circumference of 628 m and consists of 277 conventional electromagnets that squeeze and bend beams of different types of particles (including heavy ions). It is capable of accelerating them up to 26 GeV and sending them to the next stage, the so-called Super Proton Synchrotron (SPS). The SPS was commissioned in 1976 and is the second-largest machine in CERN's accelerator complex, with a circumference of almost 7 km. It consists of 1317 conventional electromagnets and operates at up to 450 GeV, providing beams of particles to different experiments, most notably to the LHC. In 1983, a Nobel-prize-winning discovery of W and Z boson particles was made with SPS [36, 37]. It was running as a proton–antiproton collider at that time.

On the other hand, the heavy ions (predominantly lead Pb, xenon Xe, and argon Ar ions) follow a slightly different set of the first few injection steps. Linear accelerator 3 (Linac3) is the starting point for the ions used in experiments at CERN. The ions are produced in Linac3's source, where electrons are removed from the atoms inside a plasma. Long pulses of bare nuclei are then sent to the Low Energy Ion Ring (LEIR), which splits the long pulses of ions into shorter and dense bunches. It takes LEIR approximately two and a half seconds to accelerate heavy ions from 4.2 GeV to 72 GeV, which is a suitable injection energy for the PS. The heavy ions follow the same acceleration steps as the protons afterwards.

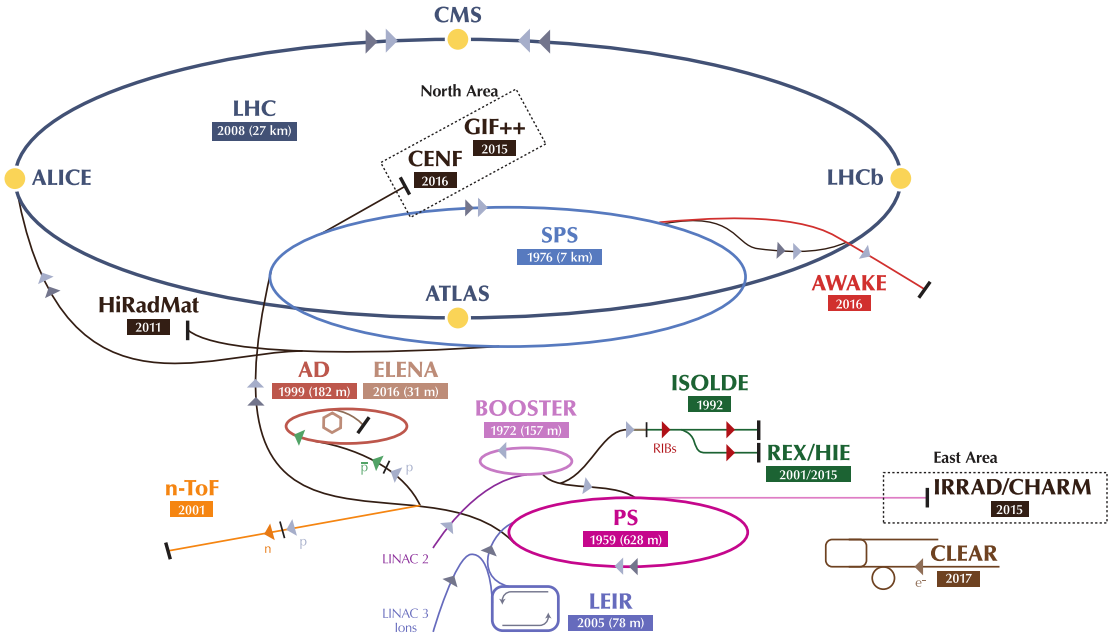

Figure 2.1: The LHC is the last ring (dark blue line) in a complex chain of particle accelerators. The smaller machines are used in a chain to help boost the particles to their final energies and provide beams to a whole set of smaller experiments, which also aim to uncover the mysteries of the Universe. Adopted from Ref. [88].

Finally, the particle bunches are injected into the last stage, namely the LHC, where the beams travel in opposite directions around the ring in two adjacent parallel beamlines called *beam pipes*. The LHC circle is split at eight equally spaced points of interest, called *Point* 1 to 8, with Point 1 being located at CERN's main site in Meyrin and others increasing in a clockwise direction. When the LHC is filled, it can contain as much as 2808 equally spaced bunches of protons (592 of heavy ions) per ring, where each bunch consists of more than 10^{11} protons (2.2×10^8 lead ions). The gap between bunches, the so-called *bunch spacing*, is usually 25 ns. Particles get further accelerated by the two independent systems of 16 MV radio-frequency (RF) cavities located at Point 4. There are 1232 superconducting niobium-titanium (Nb-Ti) dipole magnets to keep the proton (heavy ion) bunches orbiting at their maximum energy of 6.5 TeV (2.51 TeV). The dipole magnets are cooled down to an operating temperature of 1.9 K with liquid helium to make them superconducting and thus can reach the magnetic fields up to 8.3 T. Additionally, there are 392 quadrupole magnets to focus the beams in the plane, perpendicular to the beam direction, and some higher-order magnets closer to the interaction points (IP).

The LHC was designed to reach the centre-of-mass energy of proton–proton (pp) collisions $\sqrt{s} = 14$ TeV but the energy is only increasing gradually. During the first LHC run (Run 1), which lasted from 2011 to 2012, the data was recorded at the centre-of-mass energy of 7 TeV and 8 TeV with a 50 ns bunch spacing. In 2013 and 2014, the Long Shutdown 1 (LS1) period was exploited to upgrade the infrastructure. The LHC began its Run 2 in 2015 reaching a centre-of-mass energy of pp collisions $\sqrt{s} = 13$ TeV. The Run 2 ended in 2018 when the second long shutdown (LS2) started.

2.1.1 The LHC Experiments

Two particle beams collide at four interaction points where the four LHC detectors are installed. These are:

- **A Large Ion Collider Experiment (ALICE)** [89] is a heavy-ion detector that is mainly targeting Pb-Pb collisions. It is designed to study the physics of strongly interacting matter and the quark-gluon plasma in the extreme environment of heavy ion collisions, where high energy densities and temperatures are produced. In this way, the ALICE experiment is complementary to other LHC experiments and can thus address several quantum chromodynamics questions which other experiments can not. It is located at Point 2 of the LHC. Its overall dimensions are 16 m × 16 m × 26 m with a total weight of approximately 10 000 t.
- **A Toroidal LHC ApparatuS (ATLAS)** [90] is a general-purpose detector that covers a broad physics program. It was designed to detect and measure any form of new physical processes or particles. It got its name from eight large superconducting barrel loops and two smaller end-cap air toroidal magnets. The ATLAS detector is the largest volume particle detector ever constructed and lies at Point 1 of the LHC. It measures 44 m in length, has a diameter of 25 m, and weighs ~7000 t.
- **Compact Muon Solenoid (CMS)** [91] is another general-purpose detector. Although it has similar scientific goals as the ATLAS experiment, it uses different technical solutions and a different magnet-system design. The CMS detector is built around a huge solenoid magnet, which is designed to reach the 4 T magnetic fields. It is the largest superconducting solenoid ever built for a physics experiment in terms of bending power for physics, total stored energy, and stored energy per unit of cold mass. It has a length of 21 m, diameter of 15 m and weighs approximately 14 000 t. It is located at Point 5 of the LHC.
- **Large Hadron Collider beauty (LHCb)** [92] is an experiment that focuses on heavy flavour physics. Its main objective is to thoroughly examine the rare decays of beauty and charm hadrons and potentially get hints on new physics phenomena through precise charge and parity (CP) violation measurements. The studies performed could give us an answer to why there is such an imbalance between matter and antimatter in the observable universe. Contrary to the other experiments, the LHCb detector is not forward-backwards symmetric since, at high energies, both the b- and $\bar{b}$-hadrons are predominantly produced in the same forward or backward cone. It is located at Point 8 of the LHC and is 21 m long, 13 m wide, and 10 m high and weighs approximately 5600 t.

2.1.2 The LHC Beam Parameters

The number of events for a specific process collected in LHC pp collisions by an LHC experiment can be expressed with the following relation:

$$N_{events} = \sigma \cdot \mathcal{L} \cdot \varepsilon \cdot A, \tag{2.1}$$

where σ represents the cross-section for a given process, $\mathcal{L}$ is the integrated luminosity which is determined by the specifications of the machine itself, ε is the efficiency, and A the geometrical acceptance of the detector. The cross-section is a measure of the probability that a specific physics process will take place and has a different energy dependence between different processes. Formally, it is defined as the number of interactions per unit time per target particle divided by the incident flux [93] and is usually measured in barn ($1\,\mathrm{b} = 10^{-28}\,\mathrm{m}^2$). The integrated luminosity, $\mathcal{L}$, is defined as the time integral of the instantaneous luminosity L. The instantaneous luminosity only depends on the beam parameters and can be expressed for a Gaussian beam distribution as:

$$L = \frac{N_B^2 n_b f_0 \gamma}{4\pi\varepsilon_n \beta^*} F \tag{2.2}$$

where N_b is the number of particles in the bunch, n_b the number of bunches in the beam, f_0 is the revolution frequency, γ is the relativistic gamma factor, ε_n is the normalised transverse beam emittance[1], β^* is the beta function at the collision point[2], and F represents the geometric luminosity reduction factor due to the crossing angle at the IP, which is defined as:

$$F = \frac{1}{\sqrt{1 + \left(\frac{\theta_c \sigma_z}{2\sigma^*}\right)^2}}. \tag{2.3}$$

The θ_c is the full crossing angle at the collision point, σ_z is the root-mean-square (RMS) bunch length, and σ^* the transverse RMS beam size at the IP. For the LHC accelerator, these parameters are presented in Table 2.1. According to the Eq. 2.1, the LHC must reach high beam energies and

Table 2.1: Summary of the nominal design LHC parameters [87].

Variable	Value	Description
N_b	$\sim 10^{11}$	Number of particles per bunch
n_b	2808	Number of bunches per beam
f_0	11.245 kHz	Revolution frequency
γ	~ 7000	Relativistic gamma factor
ε_n	3.75 µm	Normalised transverse beam emittance
β^*	0.55 m	Beta function at the IP
F	0.84	Geometric luminosity reduction factor
θ_c	±285 µrad	Crossing angle at the IP
σ_z	7.55 cm	RMS bunch length
σ^*	16.7 µm	RMS beam size

high beam intensities to observe rare events since the relation between the number of observed events and integrated luminosity is linear. Both ATLAS and CMS require high luminosity and aim at a peak luminosity of $L = 10^{34}\,\mathrm{cm}^{-2}\,\mathrm{s}^{-1}$ for proton collisions. The ALICE experiment, however, aims at a peak luminosity of $L = 10^{27}\,\mathrm{cm}^{-2}\,\mathrm{s}^{-1}$ for nominal Pb-Pb ion operation.

[1] Emittance is the property of a particle beam that characterises its size. Roughly, emittance is an area or volume in the phase space of the particles.

[2] Beta function is related to the transverse size of the beam along the nominal beam trajectory. The value of the beta function at the IP is referred to as β^*.

Due to the instantaneous luminosity reaching such high levels, most of the time, many proton collisions occur within the same bunch crossings. The so-called mean number of interactions per bunch crossing is labelled as $\langle\mu\rangle$ and ranged between 34 and 38 in Run 2 period, see Figure 2.2(a). These additional interactions per bunch crossing are referred to as *in-time pile-up*. Fortunately, the detectors can measure the positions of particles close to the IP very accurately, so the particle tracks can be matched to a specific vertex and, this way, be distinguished from other pile-up events. On the other hand, the *out-of-time pile-up* can happen if the bunch crossing frequency is high compared to the detector recovery time, leading to signal superposition. This phenomenon can occur when an event from the next bunch crossing falls inside the detector integration time of the previous one.

During the Run 2 period, LHC provided 156 fb^{-1} of integrated luminosity to ATLAS, of which 146 fb^{-1} were successfully recorded. Finally, after additional data quality checks, 139 fb^{-1} are good to be used for physics analyses, see Figure 2.2(b).

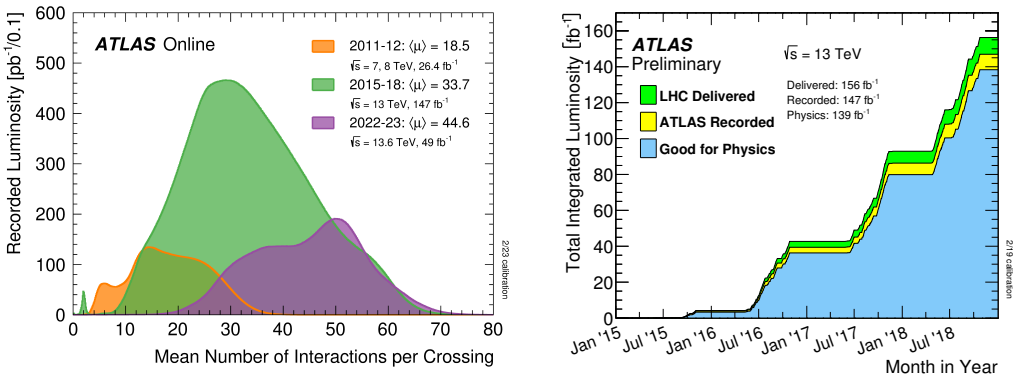

(a) (b)

Figure 2.2: (a) The average number of interactions per bunch crossing in each year of the Run 1, Run 2, and Run 3 period. The total recorded integrated luminosity and the average μ values are given in the figure. (b) Total integrated luminosity provided by the LHC to the ATLAS detector in Run 2 period for pp collisions at 13 TeV centre-of-mass energy (green), recorded by the ATLAS detector (yellow), and confirmed to be good for physics analyses (blue). Taken from Ref. [94].

2.2 The ATLAS Detector

The ATLAS (A Toroidal LHC ApparatuS) [90] detector is a general-purpose detector that was designed to exploit the full discovery potential of the LHC. The high collision rates, radiation doses, particle multiplicities, high energies and the ever-growing need for the most precise measurements have set high standards for developing this particle detector. Its construction began at individual institutes worldwide, with detector components being shipped to CERN and started being assembled in 2003. It was finished in 2008, when the first single-proton events were detected already on 10 September of the same year. In 2012, a Higgs boson discovery was announced jointly with the CMS experiment. Since it is operating at the energy frontier,

it should be able to unveil the future mysteries of the Universe, like new exotic particles, supersymmetry, hidden dimensions or even dark matter.

The ATLAS detector has a cylindrical shape of 44 m in length and 25 m in height. It is forward-backwards symmetric and thus covers nearly full 4π solid angle around the interaction point. It sits in a large cavern approximately 100 m below the ground at Point 1 of the LHC.

ATLAS is a many-layered instrument developed to detect various elementary particles with different reconstruction and identification techniques. The Inner Detector, which is thoroughly described in Section 2.2.1, is located the closest to the beam pipe and is responsible for precise charged particle momentum measurements, electron and photon identification, b-quark tagging and heavy-flavour vertex measurements. It comprises three sub-detector systems: from the inner radii out, there are the silicon pixel layers, silicon microstrip layers, and finally, at larger radii, the transition radiation tracker. A solenoid magnet, which bends the tracks of charged particles, surrounds the Inner Detector. Further out, there are electromagnetic and hadronic calorimeter systems, which complement Inner Detector tracking by accurately measuring particle energies. Both calorimeters are described in Section 2.2.2. Three toroids are situated outside the calorimeters and within the outermost detector system, the muon spectrometer. It is detailed in Section 2.2.3 and is designed to measure the position and momentum of charged muon tracks. Additionally, two end-caps are situated at both ends of the detector to improve the detector coverage in the forward region. The schematic of these ATLAS sub-detectors is illustrated in Figure 2.3.

Before proceeding to the sub-detector description, it is useful to define the coordinate system and common kinematic variables.

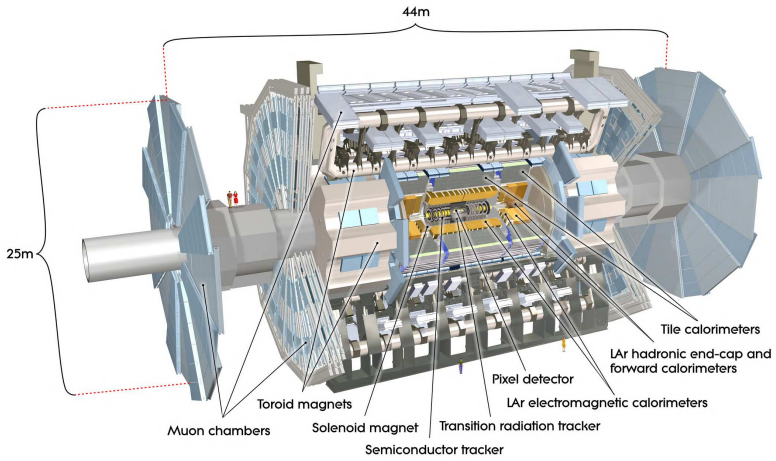

Figure 2.3: Cut-away view of the ATLAS detector showing the main detector components, namely the inner detector, the calorimeters, and the muon spectrometer alongside the magnet systems. Taken from Ref. [90].

Coordinate System and Common Kinematic Variables

The ATLAS detector uses a right-handed coordinate system with the origin defined at the interaction point in the centre of the detector. The z-axis coincides with the beam direction so the interesting physics mainly happens in the $x-y$ plane, which is perpendicular to the beam direction. The x-axis points from the IP to the centre of the LHC ring, and the y-axis points upwards. Due to the rotational symmetry of the detector around the z-axis, the cylindrical coordinate system (r, ϕ) is used in the transverse plane: the azimuthal angle ϕ measures the angle around the beam axis, and the polar angle θ is the angle from the beam axis. The pseudorapidity is defined as

$$\eta = -\ln\tan(\theta/2), \tag{2.4}$$

is often used instead of the polar angle and is equal to zero for particle trajectories perpendicular to the beam axis ($\theta = 90°$) and asymptotically approaches infinity when θ approaches zero. The pseudorapidity is equivalent to the rapidity, defined as $y = \frac{1}{2}\log\left(\frac{E+p_z}{E-p_z}\right)$, in the massless particle limit. Interesting particle collisions with high momentum transfer usually produce particles at low η. Another commonly used variable is the angular distance between two objects, defined as

$$\Delta R = \sqrt{\Delta\eta^2 + \Delta\phi^2} \tag{2.5}$$

where $\Delta\eta$ and $\Delta\phi$ are the differences between pseudorapidity and azimuthal angle between two objects, respectively. Since the momentum conservation in the $x-y$ plane implies that the vectorial sum of the transverse momentum of all the collision products must be zero, it is convenient to work with the transverse quantities, such as the transverse momentum p_{T}, the transverse energy E_{T} and the missing transverse energy $E_{\mathrm{T}}^{\mathrm{miss}}$, defined as

$$p_{\mathrm{T}} = \sqrt{p_x^2 + p_y^2}, \qquad E_{\mathrm{T}} = \sqrt{m^2 + |\vec{p}_T|^2}, \qquad \vec{E}_{\mathrm{T}}^{\mathrm{miss}} = -\sum_i \vec{p}_T(i). \tag{2.6}$$

Particle Identification

Particle identification is carried out by comparing charge and energy deposits of various types of particles in different detector layers. Particles flying out of the interaction point after the collision first hit the Inner Detector, which is responsible for measuring the tracks and momentum of charged particles. Electrons, protons and muons, for example, leave hits in the sub-detectors of the Inner Detector. Neutral particles, such as photons or neutrons, do not leave any track in the Inner Detector. Further out, the two calorimeters slow down particles and measure their energy. Photons and electrons lose all their energy within the electromagnetic calorimeter, while charged hadrons only leave a small fraction of their energy in the electromagnetic calorimeter due to ionisation energy loss but are stopped in the next layer, the so-called hadronic calorimeter. Only muons and neutrinos survive past the hadronic calorimeters. Since muons have relatively long lifetimes and do not interact with matter much, their curved tracks are determined from the Inner Detector and information provided by muon chambers in the outer layers of the ATLAS detector. Neutrinos, on the other hand, remain invisible to ATLAS and can only be reconstructed from the transverse momentum imbalance

of other detected particles. The schematic diagram of particle paths in the ATLAS detector is illustrated in Figure 2.4.

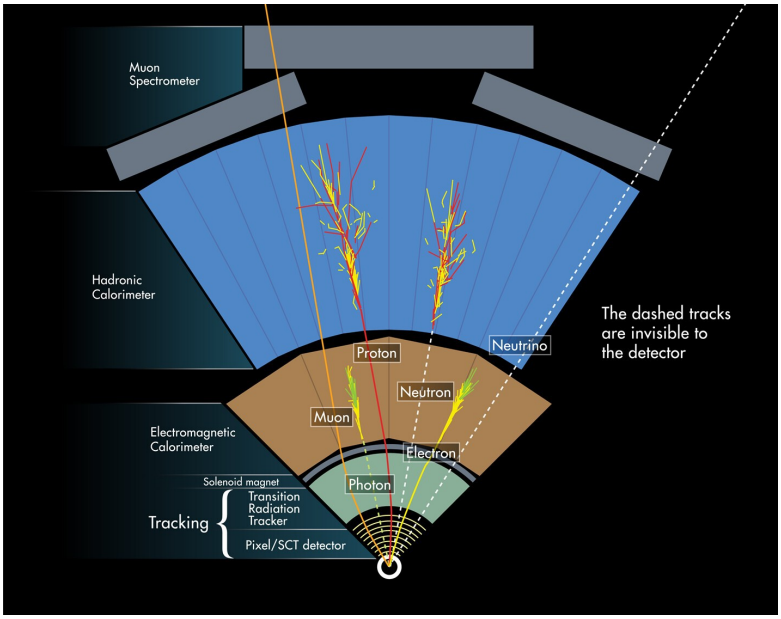

Figure 2.4: Diagram showing the particle paths inside the detector. Taken from [95].

2.2.1 Inner Detector

The objective of the ATLAS Inner Detector (ID) is to provide sturdy pattern recognition, momentum measurements, and both primary and secondary vertex determination for charged particles with p_{T} above 0.5 GeV and within the pseudorapidity range $|\eta| < 2.5$. Additionally, it contributes to electron identification on a wide range of energies for electron tracks within $|\eta| < 2.0$. Due to the large particle track density close to the beam pipe, multiple high-granularity, high-precision, and radiation-hard detectors are needed. Hence, the ID consists of four complementary sub-detectors, namely the Insertable B-Layer (IBL), silicon Pixel layers, Semi-Conductor Tracker (SCT), and Transition Radiation Tracker (TRT). The ID precisely measures 3-dimensional space points and provides excellent momentum measurements from the track curvature as it operates in a 2 T magnetic field generated by a central solenoid magnet. All sub-detectors are composed of a barrel with concentric layers and two end-caps located on each end of the Inner Detector. The layout of the Inner Detector is shown in Figure 2.5.

The ATLAS Pixel Detector [97] is the innermost element of the ID and originally contained 1744 modules that read out approximately 80 million pixels. It consisted of three barrel layers located at radii 50.5 mm (B-Layer), 88.5 mm (Layer 1), and 122.5 mm (Layer 2) and three more discs in each of the end-caps. The typical pixel size is 50 µm × 400 µm and is 250 µm thick. The output accuracy is 10 µm in the transverse direction ($R - \phi$) and 115 µm in the longitudinal direction z (R) in the barrel (end-cap).

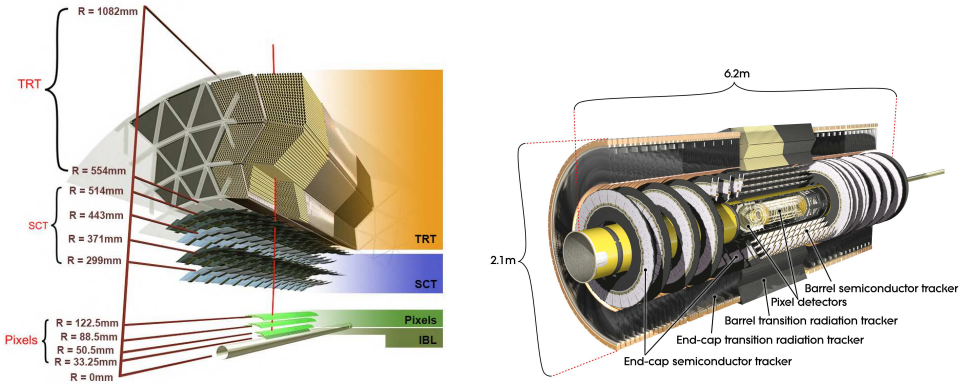

(a) (b)

Figure 2.5: (a) Cut-away illustration of the ATLAS Inner Detector barrel made up by the IBL, the three Pixel layers, the four SCT layers and straw arrangement of the TRT, and (b) the full schematic view of the Inner Detector. Taken from Refs. [96] and [90].

During the LS1, the Pixel Detector was expanded by inserting a new, innermost layer, the IBL [96, 98], located at a mean radius of 33.2 mm. It consists of 12 million pixels. The IBL improves the impact parameter and vertex reconstruction by providing additional measurement points. It assures good performance even at higher luminosity and potential radiation damage effects in the original B-layer. Furthermore, the inclusion of the IBL accounts for the majority of the 10% improvement in b-tagging efficiency [99].

The SCT [100] consists of four coaxial cylindrical layers of microstrip pairs in the barrel region and two end-caps, each containing nine disk layers. The barrel covers the range $|\eta| < 1.4$ and contains 2112 modules, while each end-cap further covers $1.4 < |\eta| < 2.5$ and contains 988, altogether amounting to 4088 SCT modules. The SCT intrinsic accuracy is 17 µm in the transverse direction ($R - \phi$) and 580 µm in the longitudinal direction both for the barrel and end-caps. Since the lower particle track density is expected in this region, silicon strips were chosen over silicon pixels. This choice allows for preserving good spatial resolution while retaining fewer readout channels.

The TRT [90] is the outermost of the three ID subsystems and consists of approximately 300 000 drift tubes that are 4 mm in diameter. The barrel region consists of 73 straw planes and the end-caps of 160, which altogether typically provide 36 hits per particle track. The tubes often referred to as straws, are 144 cm (37 cm) long in the barrel region (end-caps) and are filled with xenon gas. The carbon dioxide fills the space in between. When a charged particle passes through the TRT, it ionises the active xenon gas and produces primary ionisation bunches. The electric field, generated by the high negative voltage in the straw walls, accelerates electrons towards the central anode. Due to the second ionisation, more and more electrons are generated, producing a detectable current signal. The TRT can detect particles with $p_{\mathrm{T}} > 0.5$ GeV within $|\eta| < 2.0$, providing ($R - \phi$) information, with an accuracy of 130 µm per straw.

Ultrarelativistic charged particles passing through the polypropylene fibre emit low energy transition radiation X-rays, proportional to their Lorentz γ factor, which contributes to ionisa-

tion due to the absorption in the TRT gas mixture. Only electrons and positrons are characterised by this double contribution to ionisation, while this is not the case for heavier particles such as protons or pions, which have a lower Lorentz γ factor. Therefore, the TRT provides electron identification complementary to the calorimeter over a wide range of energies.

The combined momentum tracking resolution for a particle with transverse momentum p_{T} is given by [90]:

$$\frac{\sigma_{p_{\mathrm{T}}}}{p_{\mathrm{T}}} = 0.05\%\ p_{\mathrm{T}} \oplus 1\% \tag{2.7}$$

2.2.2 The ATLAS Calorimeters

The ATLAS calorimetric system consists of two sections: the electromagnetic (EM) calorimeter, which measures the energy of particles that interact electromagnetically, i.e. electrons and photons, and the hadronic calorimeter, which measures the energy of strongly interacting particles, i.e. protons, neutrons, pions and kaons. Both subsystems are axially symmetric and cover the range $|\eta| < 4.9$, using different techniques adapted to match the changing requirements of the physics processes of interest across the detector. All ATLAS calorimeters are sampling calorimeters built from interchanging layers of active and passive absorbing material. When a particle hits an absorber layer, it produces an electromagnetic or hadronic shower of secondary particles. These particles are then detected and their energies are measured within the active layer of the detector.

ATLAS uses Liquid Argon (LAr) and scintillating plastic as the active material. A particle can be detected via a measurement of light produced in a scintillating plastic or via the measurement of a deposited charge caused by the ionisation in a liquid. In the first case, a particle passes the scintillating material and excites the outer shell electrons which, by dropping back down to the ground state, re-emit the absorbed energy in terms of light. The scintillation light is then detected and amplified by the photomultiplier tubes. In the second case, particles that pierce through the liquid argon medium create a free charge by ionisation. The ionisation produces enough electrical signal to be read out by suitable electronics.

Dense materials such as lead are used as passive absorber materials. Electrons lose their energy by emitting bremsstrahlung, which causes further electron–positron pair production and thus EM showers. Muons, on the other hand, emit less bremsstrahlung due to their higher mass, so they pass the calorimeters as the minimum ionising particles (MIPs). Hadrons lose their energy in the strong nuclear interactions, forming hadronic showers. Figure 2.6 schematically shows the layout of the ATLAS calorimetric system.

The EM calorimeter (EMCAL) [101] is divided into a barrel part ($|\eta| < 1.475$) and two end-cap (EMEC) components ($1.375 < |\eta| < 3.2$). It is a lead-LAr detector with accordion-shaped electrodes and lead absorber plates. In a so-called precision physics region ($|\eta| < 2.5$), the EM calorimeter is segmented into three sections in depth, as depicted in Figure 2.7, while only two layers of detector modules are used in the forward region, where also the granularity is coarser than in the central part. The EM calorimeter thickness is wisely chosen to contain all the EM

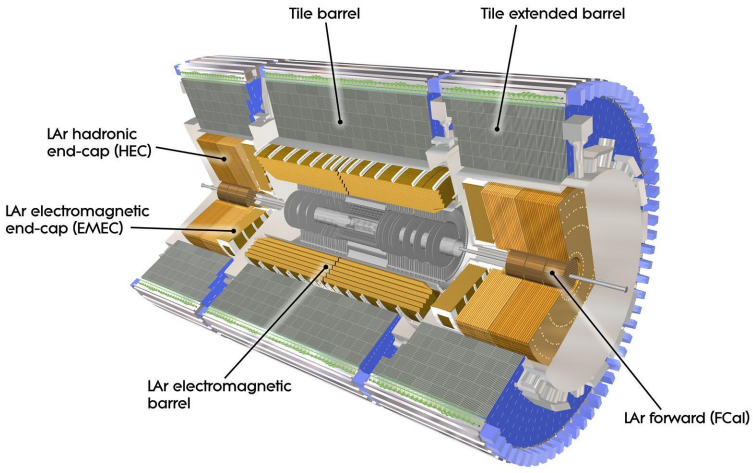

Figure 2.6: A schematic view of the ATLAS calorimeter system. Taken from Ref. [90].

showers within its volume. The total thickness of the EM calorimeter is more than 22 radiation lengths X_0[3] in the barrel part and more than 24 X_0 in the end-caps. A thin (1.1 cm in the barrel and 0.5 cm in the end-cap) presampler detector is used in $|\eta| < 1.8$ region to recover the energy lost by electrons and photons before they reach the EM subsystem.

The coarser-granularity hadronic calorimeter (HCAL) is used for the identification and measurements of jets and hadronically decaying τ particles, as well as for the $E_{\mathrm{T}}^{\mathrm{miss}}$ measurements. To contain the hadronic showers and limit the punch-through into the muon system, the total thickness of the HCAL is 11 interaction lengths λ[4] at $\eta = 0$. It is composed of three sub-parts, namely the Tile Calorimeter (TileCal), the LAr Hadronic End-cap Calorimeter (HEC), and the LAr Forward Calorimeter (FCal) [90]:

TileCal directly surrounds the EM calorimeter (as seen in Figure 2.6) and covers the range $|\eta| < 1.0$ in the central barrel part. However, two extended barrels are placed on each side of the detector to provide the coverage of the additional $0.8 < |\eta| < 1.7$ range. It uses steel as the absorber and scintillating tiles as the active material.

HEC consists of two cylinders per each side of the detector, placed directly behind the two EMECs, thus sharing the same LAr cryostats. It covers the range $1.5 < |\eta| < 3.2$. The HEC is constructed from 25 mm (50 mm further out) parallel copper plates as an absorber material, interleaved with 8.5 mm LAr gaps that provide an active medium for this sampling calorimeter.

FCal consists of three modules in each end-cap. The first is made of copper and is optimised for EM measurements, while the other two are made of tungsten (W) and are designed

[3] The radiation length X_0 is the mean distance over which the particle loses e^{-1} of its energy.
[4] Interaction length λ represents the mean distance travelled by a hadron until its energy reduces by a fraction of e^{-1} of the initial energy.

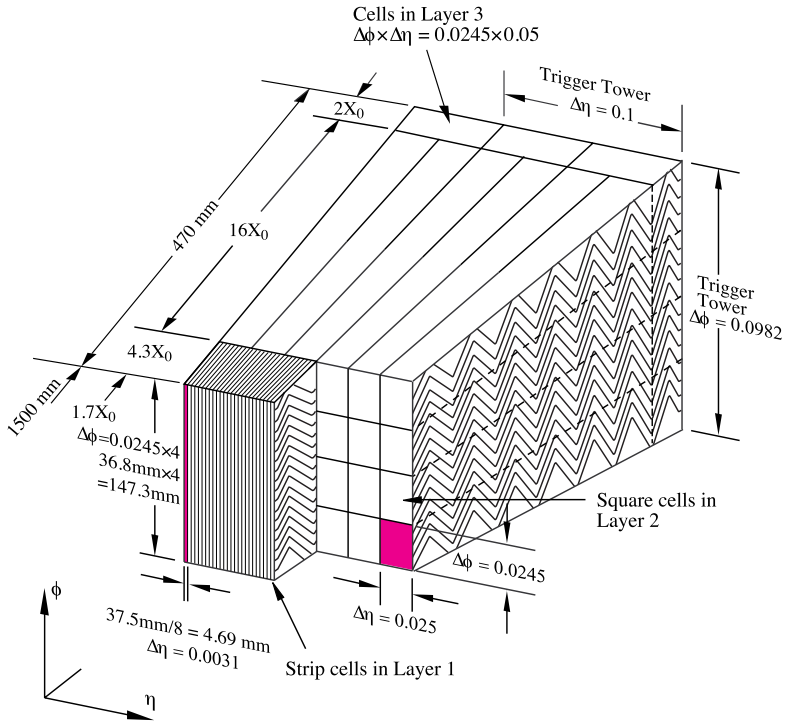

Figure 2.7: A sketch of the ATLAS EM calorimeter, where an accordion structure is visible. Taken from Ref. [101].

to measure hadronic interactions. The three layers cover the very forward region $3.1 < |\eta| < 4.9$.

Table 2.2 shows a summary of ATLAS calorimetry resolution and η coverage [90].

Table 2.2: Summary of the general performance goals of the ATLAS calorimetry subsystems.

Detector component	**Resolution**	**η coverage**
EM calorimetry	$\sigma_E/E = 10\%/\sqrt{E} \oplus 0.7\%$	± 3.2
TileCal, HEC	$\sigma_E/E = 50\%/\sqrt{E} \oplus 3\%$	± 3.2
FCal	$\sigma_E/E = 100\%/\sqrt{E} \oplus 10\%$	$3.1 < \|\eta\| < 4.9$

2.2.3 Muon Spectrometer

The muon spectrometer (MS) [102] is the outermost layer of the ATLAS detector, covering the pseudorapidity range $|\eta| < 2.7$. The MS is designed to identify muon candidates and to measure the muon momentum and charge independently from the ID. It has an outer diameter of 22 m and consists of four subsystems, i.e. Monitored Drift Tubes (MDT) and Cathode Strip Chambers (CSCs) responsible for precision muon tracking and Resistive Plate Chambers (RPCs) and Thin Gap Chambers (TGCs) for providing fast triggering information. The CSCs were replaced with

the New Small Wheel, discussed at the end of this chapter, during LS2. The schematic of the MS layout is presented in Figure 2.8, while the summary of subsystem specifications is given in Table 2.3.

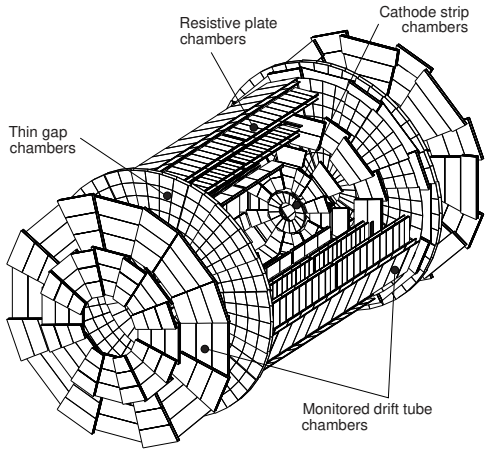

Figure 2.8: View of the muon spectrometer system indicating the areas covered by the four different chamber technologies. Taken from Ref. [102].

Muon measurements are based on the magnetic bending of tracks which is caused by the large superconducting toroid magnets described in Section 2.2.4. The magnetic field, which provides 1.5 to 5.5 T m of bending power, is perpendicular to the beam axis, hence the muons traversing it change their trajectory. This allows for an independent momentum measurement with respect to one provided by the ID. The chambers in the barrel region ($|\eta| < 1.4$) are arranged in three concentric cylindrical layers around the beam axis at radii of approximately 5 m (inner station), 7.5 m (middle station) and 10 m (outer station). In the transition ($1.4 < |\eta| < 1.6$) and two end-cap ($1.6 < |\eta| < 2.7$) regions, large muon wheels are placed perpendicular to the z-axis and are located at distances of $|z| \sim 7.4$ m, 10.8 m, 14 m, and 21.5 m from the IP.

The precision chambers are used to determine the coordinates of the track in the bending plane and are composed of the MDT in the barrel and the CSC in the end-cap region.

The MDT are aluminium drift tubes, 30 mm in diameter, operated with 93% Argon (Ar) and 7% carbon dioxide (CO_2) gas mixture at 3 bar. A central tungsten-rhenium (W-Re) wire at a potential of 3080 V attracts electrons resulting from ionisation.

The CSC are multi-wire proportional chambers with the wires oriented in the radial direction. Both cathodes are segmented with strips oriented orthogonal to each other, thus providing the precision coordinate. The whole CSC subsystem consists of two disks with eight chambers each. This layout provides four independent measurements in η and ϕ along each particle track. The CSC combine high spatial, time and double-track resolution with high-rate capability and low neutron sensitivity.

The trigger chambers are fast muon momentum measurement detectors consisting of RPC in the barrel region and TGC in the end-cap region. The subsystems provide fast trigger signals (15 to 25 ns) for muons within the $|\eta| < 2.4$ range. Furthermore, the RPC and TGC detectors are also used to measure the muon ϕ direction in the non-bending plane (x, y).

The RPC are gaseous parallel electrode-plate detectors, filled with a mixture of 94.7% tetrafluoroethane ($C_2H_2F_4$), 5% isobutane (Iso-C_4H_{10}), and 0.3% sulfur hexafluoride (SF_6). The RPC consist of three concentric cylindrical layers around the beam axis. The large lever arm between the inner and outer chambers permits the trigger to select high momentum tracks in the range from 9 to 35 GeV (high-p_T trigger), while the two inner chambers provide the low-p_T trigger in the range from 6 to 9 GeV. A track going through all three stations, for example, delivers six measurements in η and ϕ. Muons penetrating the chamber produce electrons via a primary ionisation that are then multiplied into avalanches by a 4.9 kV/mm electric field. The signal is read out via capacitive coupling to metallic strips.

TGC have two goals, namely the muon trigger capability and the determination of the second, azimuthal coordinate to complement the MDT's measurement in the bending (radial) direction. The TGC operate in a quasi-saturated mode allowed by the 55% carbon dioxide (CO_2) and 45% n-pentane (n-C_5H_{12}) gas mixture. Each TGC module is composed of a wire plane (kept at a high positive voltage) inserted between two resistive grounded cathode plates. The high electric field around the TGC wires and the small wire-to-wire distance lead to excellent time resolution for the large majority of the tracks.

Table 2.3: Summary of MS sub-detector parameters. Adopted from Ref. [102].

Feature \ MS subsystem	MDT	CSC	RPC	TGC
Coverage	$\|\eta\| < 2.7$ (innermost layer $\|\eta\| < 2.0$)	$2.0 < \|\eta\| < 2.7$	$\|\eta\| < 1.05$	$1.05 < \|\eta\| < 2.7$ (2.4 for triggering)
Number of chambers	1150	32	606	3588
Number of channels	339 000	31 000	373 000	318 000
Function	Precision tracking	Precision tracking	Triggering, second coordinate	Triggering, second coordinate
z/R resolution	35 µm (z)	40 µm (R)	10 µm (z)	2 to 6 mm (R)
ϕ resolution	–	5 mm	10 mm	3 to 7 mm
time resolution	–	7 ns	1.5 ns	4 ns

New Small Wheel (NSW) [103] is a set of precision tracking and trigger detectors capable of working at high rates with excellent real-time spatial and time resolution covering the pseudorapidity range $1.3 < |\eta| < 2.7$. It was installed in 2021 during the LS2, replacing the first station of the ATLAS muon end-cap system, to address issues such as the degraded muon track reconstruction performance and the expected increase in muon trigger rates in future LHC runs. It utilises two detector technologies: small-strip Thin Gap Chambers (sTGC) as the primary trigger and Micromegas (MM) as the primary precision tracker. Each of the 16 NSW sectors consists of a sTGC-MM-MM-sTGC multi-layer for improved track segment angular resolution at the trigger level. The sTGC consists of a grid of 50 µm gold-plated tungsten (W) wires with a 1.8 mm pitch placed between two cathode plates at a distance of 1.4 mm from the wire plane. The strips have a much smaller pitch than the strip pitch of the previous TGC technology used in

ATLAS. The sTGC operate in a quasi-saturated mode allowed by the 55% carbon dioxide (CO_2) and 45% n-pentane (n-C_5H_{12}) gas mixture. In addition to precise coordinate measurements in the η direction, it can also complement the tracking information from MM. The MM are wireless gaseous particle detectors that consist of a planar drift electrode, a gap of a few millimetres filled with a gas and used as a drift region, and a thin metallic mesh that creates the amplification region. The electric field gradient is held at a large value of $40 - 50$ kV/cm in the amplification region, while it is much lower (few hundred V/cm) in the drift region. The charged particles, penetrating the detectors' drift region, ionise the gas, and the electrons are attracted toward the mesh. The electron avalanche happens in the amplification region, placed immediately above the read-out electrode. The MM provide spatial resolution better than 100 µm independent of track incident angle.

2.2.4 Magnets

The ATLAS magnet system [104–107] consists of four superconducting magnets: a central solenoid generating the magnetic field for the central tracker, a large air-core barrel toroid, and two end-cap toroids surrounding the calorimeters, hence providing a magnetic field for the MS. The geometry of the system is shown in Figure 2.9. The purpose of the magnet system is to provide strong magnetic fields in order to bend the trajectories of charged particles within the ID and MS so that the charge and momentum of particles can be correctly measured.

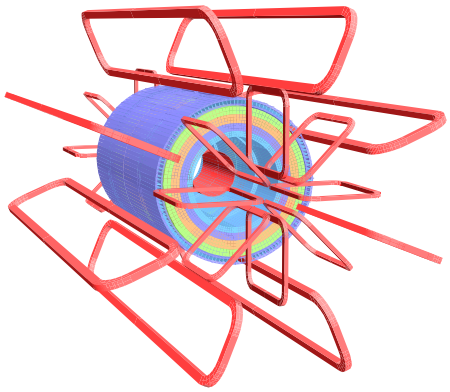

Figure 2.9: A 3-dimensional view of the bare windings of the ATLAS magnet system: the central solenoid, the 8 coils of the barrel toroid and the interleaved 2×8 coils of the end-cap toroids. Taken from Ref. [90].

The central solenoid is aligned with the beamline and generates a 2 T axial magnetic field for the ID. The solenoid's length is 5.8 m with inner and outer diameters of 2.46 m and 2.56 m. The single-layer niobium-titanium (Nb-Ti) coil is placed in front of the LAr calorimeter and was designed to be thin enough not to degrade the calorimeter performance - particles should not start showering before they hit the active calorimeter layers.

The barrel toroid consists of eight rectangular coils arranged in a cylindrical configuration that provide approximately 0.5 T magnetic field for the MS (3.9 T peak field in the windings). Being 25.3 m long and having an inner and outer diameter of 9.4 m and 20.1 m, respectively,

it surrounds the calorimeters and is placed within the muon spectrometer, thus curving the particles within $|\eta| < 1.4$. It is based on a niobium-titanium-copper (Nb/Ti/Cu) conductor and runs at a nominal current of 20.5 kA.

The end-cap toroids, similarly to the barrel toroid, consist of eight coils but provide a slightly higher ~1 T magnetic field (4.1 T peak field in the windings). The coils are rotated by 22.5° with respect to the barrel toroid. The end-cap toroids have an inner and outer diameter of 1.65 m and 10.7 m, respectively, while their length is 5 m. The end-cap toroids provide magnetic bending over $1.6 < |\eta| < 2.7$, while in the so-called transition region ($1.4 < |\eta| < 1.6$), the magnetic deflection is given by a combination of barrel and end-cap fields. Such magnet configuration generates a field that is mostly orthogonal to the muon trajectories. Furthermore, the open structure of toroids reduces the amount of material in front of the MS, therefore minimising the multiple scattering, which limits the muon momentum resolution.

2.2.5 Trigger and Data Acquisition

With the amount of data flowing from each pp collision (~1 MB/event) [108] happening every 25 ns, it is impossible to store and process all the information. Therefore, it is crucial to select only events that contain interesting characteristics that might lead to new physics discoveries. To reduce the data flow to manageable levels, ATLAS uses a Trigger and Data Acquisition (TDAQ) system, which picks approximately 1000 interesting events with distinguishing characteristics for physics analyses per second.

The ATLAS Trigger and Data Acquisition [109] system is made up of two channels: a read-out system, which reads and transmits electrical signals from the detectors, and a trigger system, which receives signals and makes a decision on which events should be stored for further offline analysis. A layout of the ATLAS TDAQ system is shown in Figure 2.10.

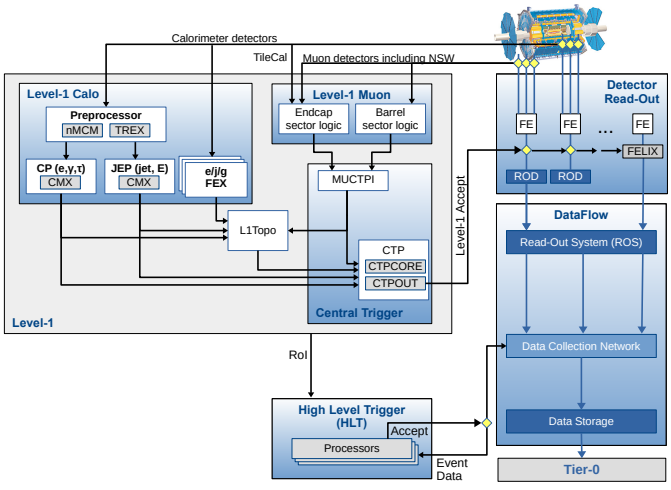

Figure 2.10: The ATLAS TDAQ system in Run 3 with emphasis on the components relevant for triggering. Taken from Ref. [110].

The trigger system consists of two consecutive levels: a first-level hardware Level 1 (L1) trigger and a software-based High-Level Trigger (HLT). The L1 trigger, constructed with custom-made electronics located on the detector, works on a subset of information from the calorimeters and the MS. The decision to keep the data from an event is made less than 2.5 µs after the event occurs. During this time, the event data is kept in storage buffers. The event rate in the L1 stage is reduced from 40 MHz to 100 kHz. If the event is accepted, it is first passed to the Read-Out System (ROS) and then to the HLT, where the event rate is further reduced to an average of 1 kHz. In each event, the L1 trigger defines one or more Regions-of-Interest (RoI), which are the η and ϕ coordinates of those regions within the detector, where its selection process has identified interesting features. This information is subsequently used by the HLT. The events that pass the HLT are stored locally at the experimental site and reconstructed at the CERN computing centre.

The main goal of the L1 trigger is to identify objects and select events as fast as possible. It targets events containing high-p_{T} muons, electrons, photons, jets, and τ leptons decaying into hadrons. Furthermore, it triggers on events with large E_{T} and $E_{\mathrm{T}}^{\mathrm{miss}}$. It uses reduced-granularity data from a subset of detectors: RPC and TGC for muons, and all the subsystems for EM clusters.

The HLT uses tracking information from the ID (which is not available at L1), finer-granularity measurements from the calorimeter, and more precise data from the MS. The HLT reconstruction can be performed only on ROIs identified by L1 or, if needed, on the whole detector.

Different thresholds and selection criteria at each of the trigger levels are specified each year of the data taking to address the requirements of the physics analysis at the ATLAS experiment. These lists of L1 and HLT triggers are called the *trigger menu*. To provide an optimal trigger menu that agrees with rate constraints at a given instantaneous luminosity, *prescale* factors can be applied to L1 and HLT triggers to disable or keep only a fraction of certain types of events. The prescale factors enable storing a fraction of events which happen often but are nevertheless useful for efficiency and performance measurements. Prescales are constant inside each *luminosity block* (LB), which is approximately a minute-long data-taking interval in which the instantaneous luminosity is approximately constant.

Since the instantaneous luminosity changes depending on the data-taking conditions, one can increase the momentum thresholds, tighten the quality of the reconstructed object at the trigger level or prescale the trigger to keep the trigger rates at a reasonable level. Trigger efficiencies are shown in Figures 2.11 and 2.12 for electrons and muons, respectively.

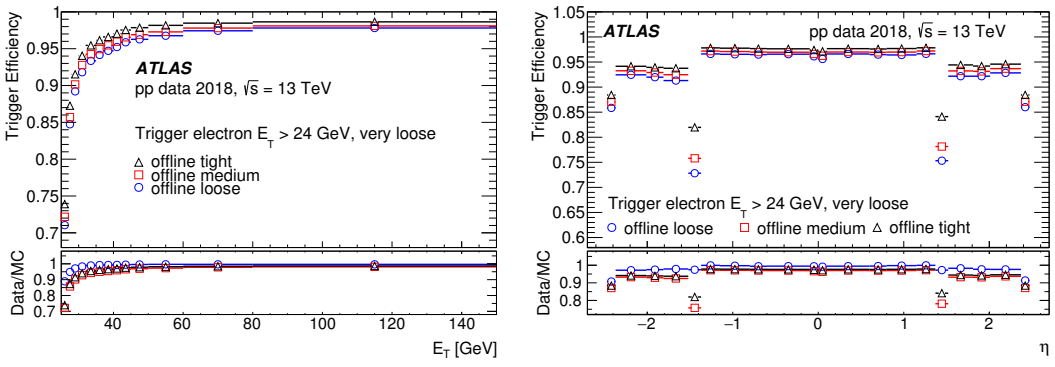

(a) (b)

Figure 2.11: Efficiencies of the `e24_lhvloose_nod0` trigger as a function of the offline electron (a) E_{T} and (b) η corresponding to offline `Tight`, `Medium` and `Loose` identification, and no isolation requirements. The efficiencies are measured in data and shown with corresponding statistical and systematic uncertainties. Also, the ratios of data to MC simulation are shown. For (b), only offline candidates with $E_{\mathrm{T}} > 25\,\mathrm{GeV}$ are used. Taken from Ref. [111].

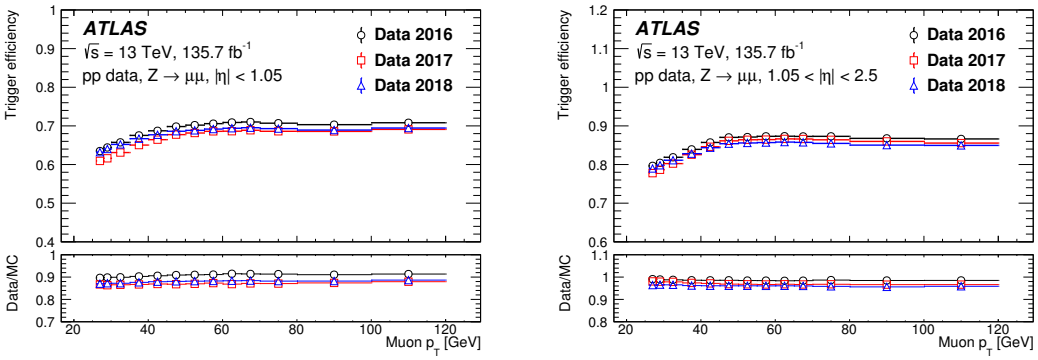

(a) (b)

Figure 2.12: Efficiency of passing either the `HLT_mu26_ivarmedium` or the `HLT_mu50` trigger in the (a) barrel and (b) endcaps as a function of the muon p_{T}, computed using data taken in 2016–2018. The error bars show the statistical uncertainties only. Taken from Ref. [112].

2.2.6 Forward Detectors

In addition to the main ATLAS detectors described in the previous chapters, a few more detector sets are located in the far forward region, i.e. close to the beamline. Only a fraction of pp collisions is inelastic scattering that gives rise to particles at high angles with respect to the beam axis. Other events can be used to determine the total cross-section by estimating the luminosity provided by the LHC.

- **LUminosity measurement using Cerenkov Integrating Detector (LUCID)** [113] is the primary online relative-luminosity and beam conditions monitor for ALTAS. At ±17 m from the IP, it detects inelastic pp scattering at high η with the help of several small Cherenkov detectors.
- **Absolute Luminosity For ATLAS (ALFA)** is located at ±240 m and consists of scintillating fibre trackers, providing alternative luminosity measurements via elastic scattering at small angles (3 µrad).
- **Zero-Degree Calorimeter (ZDC)** plays a crucial role in determining the centrality of heavy-ion collisions at very high pseudorapidity, $|\eta| > 8.2$. It is placed at 140 m and is also used to trigger on ultra-peripheral ion-ion interactions. Its modules are quartz rods and tungsten plates, making it a calorimeter.
- **ATLAS Forward Proton (AFP)** is a silicon tracker located 200 m from the IP. It is used to accurately measure the momentum and emission angle of forward protons that do not interact.
- **Beam-Conditions Monitor (BCM)** is designed to prevent proton bunches from hitting the collimators in front of the detectors, which would cause high radiation doses and potential detector damage. It is located at $z = \pm 1.9$ m and consists of several modules with radiation-hard diamond sensors. Particles from ordinary collisions hit the detectors on both sides of the IP simultaneously, while showers originating from collimators reach them with a delay. The BCM also provides a measurement of bunch-by-bunch luminosities in ATLAS by counting in-time and out-of-time collisions and can trigger the LHC beam dump in case of unwanted behaviour. A second system, the ATLAS Beam Loss Monitor (BLM), is an independent system which complements the BCM and was added as a backup.

CHAPTER 3

Simulation in ATLAS

Not much information can be extracted from observed data in particle physics until it is compared to theoretical predictions. Due to the complexity of the final states that are produced in high-energy collisions between elementary particles, Monte Carlo (MC) simulations are required to obtain quantities that can be compared to the measured data. Such simulations can be used for several purposes in HEP, as it is presented in this chapter. Event simulation is presented in Section 3.1, followed by the description of various types of detector simulation in Section 3.2.

The MC methods are a broad class of algorithms that are used for calculating integrals that may be hard to solve with standard numerical approaches by relying on repeated random sampling.

A complex ATLAS simulation chain [114], incorporated into the ATLAS software framework *Athena* [115], is used to reproduce events which occur in physics processes as close as possible to what would be observed in the detector for an actual pp collision. The simulation sequence is comprised of multiple stages. The first step is *event generation*, in which particles from hard processes and their immediate decay in the event are generated. Then the *detector simulation* propagates particles emerging from the pp collision through the detector and simulates their interactions with the detector material. The GEANT4 toolkit [116] is used to simulate the response of the ATLAS detector. Finally, the charge and energy deposited in the detector are converted into detector response as voltages and currents for direct comparison to the readout of the ATLAS detector in the *digitisation* step. The final goal is that both the simulated and real data from the detector can be run through the same ATLAS trigger and reconstruction packages, requiring the format of the MC and observed data to be the same. The only difference after the digitisation step is that the originally generated events in the MC samples, referred to as *truth*, are available alongside the reconstructed objects. The truth information thus includes a record of interactions from the generator onward for each particle. An overview of the ATLAS simulation workflow is presented in Figure 3.1.

3.1 Event Simulation

MC event generation can be split into multiple steps that need to be simulated to replicate the physics phenomena presented in Section 1.3. These include the primary hard-scattering process, generation of parton showers related to the coloured participants of the process, non-perturbative interactions that evolve the showers into final-state hadrons and connect them to the initial-state hadrons, secondary interactions that produce the underlying event, and the decays of unstable particles that do not leave the detector [117].

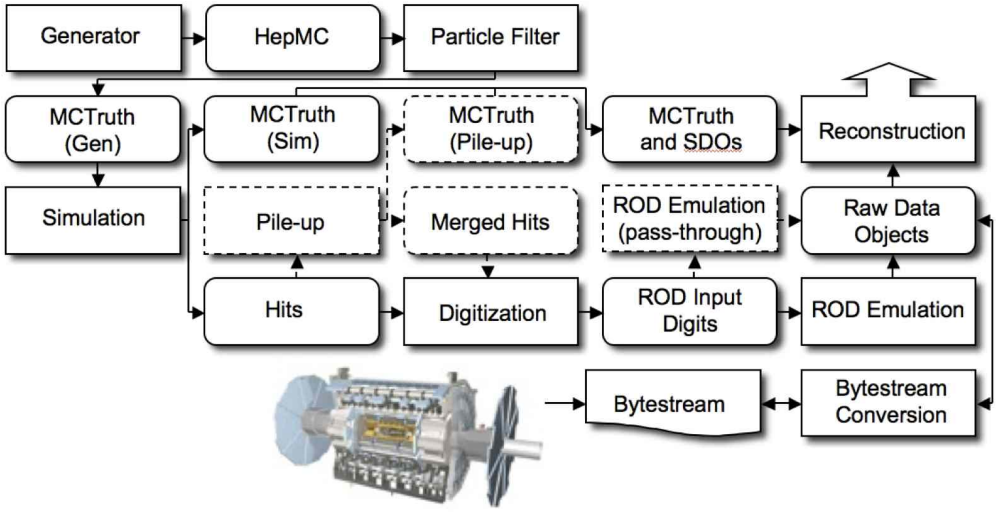

Figure 3.1: The flow of the ATLAS simulation software, from event generators (top left) through reconstruction (top right). Algorithms are placed in square-cornered boxes and persistent data objects are placed in rounded boxes. Taken from Ref. [114].

Hard subprocess: Most interesting physics happens in collisions with large momentum transfers that produce high-p_{T} particles. Since the partons are asymptotically free, such interactions can be described by perturbation theory, which makes it possible to calculate physical observables of the studied event by simply using Feynman rules. Eq. 1.65 can be rewritten as

$$d\sigma_{pp\to f} = \sum_{i,j} \int_0^1 dx_1 \int_0^1 dx_2 \; f_i(x_1, \mu_F) \; f_j(x_2, \mu_F) \times \frac{1}{2\hat{s}} \left|\mathcal{M}_{ij\to f}\right|^2 (\Phi_f, \; \mu_R, \; \mu_F) d\Phi_f, \qquad (3.1)$$

which holds to all orders of the perturbation theory. From this equation one can extract the necessary ingredients for calculating the cross-section: the parton-level *matrix element* (ME), the PDFs, and the integration over the corresponding phase space, $d\Phi_f$. There are multiple frameworks available for the matrix element evaluation that employ NLO calculations using different methods, e.g. MadGraph [75], Sherpa [118]. Sometimes LO calculations are still used when simulating complex processes, but the results are only valid for the shape of distributions in that case. The normalisation is often inaccurate due to substantial higher-order corrections and can be fixed by introducing the so-called K-factor, which is the ratio of the total NLO to LO cross-sections of the studied process, calculated by theorists in specialised studies.

The factorisation and renormalisation scales mu_F and μ_R must be determined to bypass the infrared and ultraviolet divergences that can occur during the ME calculation, and the choice is arbitrary. The scale selection impacts the simulation results, often contributing significantly to the overall systematic uncertainty in physics analyses. Usually, only one hard scale is chosen such that both scales are equal, e.g. $\mu_F = \mu_R = M^2$ in the production of an s-channel resonance with mass M or $\mu_F = \mu_R = p_{\mathrm{T}}^2$ in the case of a pair production of a massless particle with a transverse momentum p_{T}.

Parton showers: The partons participating in the hard subprocess are highly energetic and carry a colour charge. Therefore they emit QCD radiation in the form of gluons just as the accelerated electrons emit QED radiation - photons. However, contrary to the QED, the emitted radiation (gluons), which can either stem from initial or final state partons, also carries the colour charge and can thus emit additional radiation, leading to parton showers. These showers can be viewed as higher-order corrections to the hard subprocess but are unfortunately not exactly calculable.

The energy of the radiation successively decreases from the scale of the hard subprocess down to an infrared scale at which the hadronisation processes take place and splitting is terminated in the case of FSR. For the ISR simulation, a backward evolution is used in which the momentum fractions x_1 and x_2 of the incoming partons are chosen at the high energy scale of the hard-scattering using the PDFs. Then, the incoming partons are propagated backwards so that their energy increases in each emission to the low energy scale of the incoming hadrons.

Achieving an optimal description of the events involves aligning the predictions from ME generators and PS algorithms which must be done with special care and dedicated algorithms. The most commonly used methods are the matrix element (ME + PS) [119–122] or the NLO calculation (NLO + PS) [119] matching to the parton shower.

Hadronisation: The strong coupling constant α_s is not an actual constant but a scale-dependent quantity. It grows when lowering the energy scale so that the perturbation theory becomes invalid at one point during the PS evolution. In the hadronisation step (sometimes also called fragmentation), colour-neutral final-state hadrons are formed from individual partons in this non-perturbative regime due to the confining nature of QCD. The most commonly used models in event generators are the Lund string model [123], which is based on the assumption of linear confinement, and the cluster hadronisation model [124], which is grounded on the preconfinement property of parton showers [125].

Underlying event: An additional hadron production is happening in the pp collisions, which can not be entirely associated with the parton interactions of the hard subprocess. It is believed that also the proton remnants undergo QCD interactions in a process known as an *underlying event* [126].

3.2 Detector Simulation

3.2.1 Full Simulation

The event generation outputs a collection of four-vectors corresponding to each final state particle. These can be used in the so-called truth-level studies without considering any of the effects that the detector may cause. However, most of the time, analyses compare simulated events to the measured data. The detector effects must be accounted for within the simulation so that the simulated events completely mimic those measured with the ATLAS detector. The

GEANT4 toolkit is used to simulate the interactions of the generated particles with the detector material. A detailed description of the ATLAS geometry, material distribution, and the magnetic field is mandatory if interactions with the material, such as multiple scattering, energy loss or photon conversions, and decays of unstable particles, are to be simulated correctly. The description is so precise that even the support structures and cabling are added to the detector model. The output of the GEANT4 simulation, the so-called *hit*, is the position and timing information of the energy depositions in each sensitive detector part. The hits are then passed to the *digitisation* step, where they are transformed into digits, simulating the output of the electronics. Some sub-detectors give information only when the voltage or current of the signal exceeds a certain threshold, while others also output information about the signal shape over time. The digitisation step produces raw detector data, which is of the same format as the observed data and can thus be treated similarly in the reconstruction step, described in Chapter 4.

The abovementioned simulation procedure is referred to as *Full Simulation* (FS) in ATLAS. However, due to the complicated geometry of the detector and the detailed physics modelling employed in the FS, the simulation becomes computationally expensive. Collecting the necessary statistics becomes infeasible for many physics analyses and performance studies without a faster simulation approach. Consequently, various types of fast simulation programs, described in Section 3.2.2, have been developed to supplement the GEANT4 simulation.

3.2.2 Fast Simulation

An extensive fraction of time ($\sim$ 75%) in FS is spent simulating electromagnetic particles traversing the calorimeters since they produce large amounts of secondary particle showers. In this regard, the *Fast G4 Simulation* [127, 128] was introduced, which aims to speed up the calorimeter simulation by developing fast shower parameterisation and introducing pre-simulated *frozen showers*. The fast shower parameterisation technique involves tuning a parameterisation, which is subsequently used in the simulation, to single electrons. Consequently, the frozen shower technique employs pre-simulated showers which replace the low-energy particles during the simulation process. The CPU time is reduced by a factor of three by using this method in hard-scattering events (such as $t\bar{t}$ production) with minimal impact on the underlying physics.

Another approach that can be used to reduce the FS simulation time is the *ATLAS Fast Simulation II* (AtlFast-II) [129]. It is meant to provide large statistics simulating events as fast as possible while still being able to run the standard ATLAS reconstruction. The reconstructed output of the AtlFast-II includes all the properties associated with a reconstructed object. It consists of two components, namely the *Fast ATLAS Tracking Simulation* (FATRAS) [130] for the inner detector and muon system simulation and the *Fast calorimeter Simulation* (FASTCALOSIM or FCS) [131] for the calorimeter simulation:

FATRAS is a framework used for fast simulation of the ATLAS tracking systems. It is based on an MC approach, with its output holding the complete track information, including hits on tracks. FATRAS uses a simplified reconstruction geometry model instead of the

detailed full-simulation one, thus making the simulation significantly faster. An ATLAS track extrapolation engine [132] propagates the track parameters through the detector, considering the amount of pass-through material and multiple types of physics processes regarding material interactions. Events simulated using FATRAS can undergo the standard digitisation and reconstruction chain equivalent to those produced using GEANT4.

FASTCALOSIM reduces the calorimeter simulation time by an order of magnitude, to a few seconds per event, by depositing the energy of single particle showers using parameterisations of the longitudinal and lateral energy profile instead of simulating the particle interactions with the detector material. The parameterisation is based on the GEANT4 simulations of single photons, electrons, and charged pions. A fine parameterisation binning in the particle's energy, pseudorapidity, and longitudinal depth is required to adequately characterise the energy deposition in the calorimeter and correctly address the distribution of active and inactive material.

Since AtlFast-II is known to have certain limitations, particularly in the modelling of large-radius jets and their detailed substructure, a new tool, AtlFast3 (AF3) [133], is planned to be used extensively in Run 3. It has the same CPU performance as AtlFast-II but better accuracy in reproducing GEANT4. AtlFast3 combines the strengths of the updated version of FastCaloSim (V2) [134] and a machine-learning-based FastCaloGAN [135] calorimeter simulation.

3.2.3 Pile-up Simulation

As discussed in Section 2.1.2, a particular collision recorded with the ATLAS detector contains multiple events, even those that do not necessarily belong to the same bunch crossing. This phenomenon is addressed by separately simulating a large amount of inclusively generated pp events without any preselection on the physics process. Such *minimum bias events* are merged with a hard-scattering event and weighted by the *pile-up reweighting* algorithm to reproduce the distribution of the average number of interactions per bunch crossing, $\langle\mu\rangle$, observed in the data (see Figure 2.2(a)). The hits from the pile-up events are then combined with the ones produced by the hard process of interest before the digitisation step.

3.3 Data and Simulated Samples

3.3.1 Data Samples

The datasets analysed in the presented work contain proton–proton collision data recorded during the Run 2 data-taking period at a centre-of-mass energy of $\sqrt{s} = 13\,\text{TeV}$. During this period, a total integrated luminosity of $156\,\text{fb}^{-1}$ was provided by the LHC, out of which $147\,\text{fb}^{-1}$ were successfully recorded by ATLAS, as shown in Figure 2.2(b). All data had to also pass standard data-quality requirements to be labelled as *good for physics* and used in physics analyses. Therefore, the total integrated luminosity of the dataset used in this thesis was reduced to $139\,\text{fb}^{-1}$ [136] and only includes periods when the LHC provided stable beam

conditions and all ATLAS sub-detectors were fully operational. After the analysis was published, a more precise luminosity measurement was made, stating that the entire Run 2 pp data sample corresponds to an integrated luminosity of 140.1 fb^{-1} with an uncertainty of 0.83% [137].

The data recorded by the ATLAS detector is split into *runs* which usually last several hours. Runs are further divided into ~ 1 min long luminosity blocks, inside which data-taking conditions are expected to be the same, and the instantaneous luminosity is approximately constant. Finally, all LBs that pass the good-for-physics requirements are stored in the so-called Good Run Lists (GRLs). The presented analysis uses four of them, contributing $\mathcal{L} = 3.2\,\text{fb}^{-1}$ (2015), $\mathcal{L} = 33\,\text{fb}^{-1}$ (2016), $\mathcal{L} = 44.3\,\text{fb}^{-1}$ (2017), and $\mathcal{L} = 58.4\,\text{fb}^{-1}$ (2018) to the total luminosity, respectively.

3.3.2 Simulated Signal Samples

Signal events were generated at leading order with the LRSM package in Pythia 8.212 [138], which implements the $H^{\pm\pm}$ scenario described in Ref. [139] using FeynRules [140]. A set of tuned parameters called the A14 tune [141] and the NNPDF2.3lo [142] PDF set were used. The ME calculations were matched and merged with Pythia 8.212 and EvtGen 1.6.0 [143] to simulate parton showering. All samples contain a mixture of $H_L^{\pm\pm}$ and $H_R^{\pm\pm}$ particles. The value of $h_{\ell\ell'}$ in Eq. (1.64) was set to 0.02 for each leptonic decay mode to obtain a $H^{\pm\pm}$ decay width that is negligible compared to the detector resolution. Consequently, the branching ratios are assumed to be equal for all possible leptonic final states. Only Drell–Yan production of the $H^{\pm\pm}$ particles was simulated. The $H_L^{\pm\pm}$ pair production cross-sections at $\sqrt{s} = 13\,\text{TeV}$ were calculated to LO and NLO accuracies [69]. The resulting NLO-to-LO K-factor was then applied to the $H_R^{\pm\pm}$ LO production cross-section, σ_R^{LO}. The cross-sections for the Zee–Babu model were calculated using the same simulation set-up at NLO accuracy [65] and agree well with the $K \times \sigma_R^{\text{LO}}$ value, as expected. Eleven samples were simulated with different masses of the $H^{\pm\pm}$ particle decaying into light leptons, and an additional eleven with at least one τ-lepton in the final state were produced. Signal mass points considered in the analysis range from 400 GeV to 1300 GeV in steps of 100 GeV. Cross-sections and K-factors for signal samples assuming different mass hypotheses are listed in Table 3.1 for $H_L^{\pm\pm}$, $H_R^{\pm\pm}$, and k particles.

The theoretical uncertainty of the NLO cross-section for $pp \to H^{++}H^{--}$ is reported to range from a few per cent at low $H^{\pm\pm}$ masses to approximately 25% [65, 69] for the highest signal mass points studied in the analysis. The uncertainty on signal cross-section includes the renormalisation and factorisation scale dependence and the uncertainty in the parton densities. The theoretical uncertainty in the $pp \to H^{++}H^{--}$ simulation is assessed by varying the A14 parameter set in Pythia 8.186 and choosing CTEQ6L1 [144] and CT10 [145] as alternative PDFs. The impact on signal acceptance is found to be negligible. These theoretical uncertainties are considered fully correlated across the various analysis regions.

3.3.3 Simulated Background Samples

Similarly to the signal sample production described above, dedicated MC samples were simulated to model relevant SM backgrounds that impact the analysis. The Drell–Yan process depicted

Table 3.1: LO, NLO cross-sections, and K-factors for the pair-production of $H_L^{++}H_L^{--}$, $H_R^{++}H_R^{--}$, and $k^{++}k^{--}$ in pp collisions at $\sqrt{s} = 13$ TeV. The K-factors ($K = \sigma_{\text{NLO}}/\sigma_{\text{LO}}$) are identical for $H_L^{\pm\pm}$, $H_R^{\pm\pm}$, and $k^{\pm\pm}$. The values are calculated by the authors of Refs. [69] and [65] using the NNPDF2.3LO [142] and NNPDF3.1NLO [85] PDF sets.

	$H_L^{\pm\pm}$		$H_R^{\pm\pm}$ or $k^{\pm\pm}$		
$m(H^{\pm\pm})$ [GeV]	σ_{LO} [fb]	σ_{NLO} [fb]	σ_{LO} [fb]	σ_{NLO} [fb]	K-factor
300	13	18	5.6	7.6	1.35
400	3.9	5.3	1.7	2.3	1.36
500	1.4	1.9	0.60	0.82	1.36
600	0.57	0.77	0.25	0.33	1.34
700	0.26	0.34	0.11	0.15	1.33
800	0.12	0.16	0.054	0.070	1.29
900	0.063	0.079	0.027	0.035	1.26
1000	0.033	0.040	0.014	0.018	1.22
1100	0.018	0.021	0.0078	0.0092	1.18
1200	0.0098	0.011	0.0044	0.0049	1.12
1300	0.0055	0.0059	0.0025	0.0026	1.07

in Figure 1.7 enquires for an accurate description of the diboson and Drell–Yan processes which constitute a large part of the irreducible background. A small contribution of top-quark pair ($t\bar{t}$) and single-top-quark production processes is expected. The event generators used to produce the MC samples alongside the corresponding PDF set used for ME calculation, cross-section normalisation, set of tuned parameters, and frameworks to model PS are provided in Table 3.2. The scaling of main irreducible backgrounds is considered a free parameter in the final binned-likelihood fit, detailed in Chapter 8, to correct any potential normalisation mis-modelling of the MC samples.

Table 3.2: Simulated signal and background MC samples: the corresponding event generator, PDF set used for the ME calculation, cross-section normalisation, set of tuned parameters, and parton shower are shown for each sample. The generator cross-section is used where not clearly stated otherwise.

Physics process	**Event generator**	**PDF set**	**Cross-section** normalisation	**Parton shower**	**Parton shower** tune
Signal $H^{\pm\pm}$	Pythia 8.212 [138]	NNPDF2.3LO [142]	NLO	Pythia 8.212 & EvtGen 1.6.0	A14 [141]
Drell–Yan $Z/\gamma^* \to e^+e^-/\mu^+\mu^-/\tau^+\tau^-$	Sherpa 2.2.1 [118]	NNPDF3.0NNLO [146]	NNLO	Sherpa	Sherpa default
Diboson ZZ, WZ, WW	Sherpa 2.2.1 & 2.2.2	NNPDF3.0NNLO	NLO	Sherpa	Sherpa default
Multiboson WWW, WWZ, WZZ, ZZZ	Sherpa 2.2.1 & 2.2.2	NNPDF3.0NNLO	NLO	Sherpa	Sherpa default
Top-quark processes					
$t\bar{t}$	Powheg Box v2 [147–150]	NNPDF3.0NLO	NNLO + NNLL	Pythia 8.230	A14
Single t	Powheg Box v2	NNPDF3.0NLO	NLO	Pythia 8.230	A14
$3t$, $4t$	MadGraph5_aMC@NLO 2.2.2 [75]	NNPDF2.3LO	LO	Pythia 8.186	A14
$t\bar{t} + W/Z/H$	MadGraph5_aMC@NLO 2.3.3	NNPDF3.0NLO	NLO	Pythia 8.210	A14

Drell–Yan ($q\bar{q} \to Z/\gamma^* \to \ell^+\ell^-$) production was modelled with the Sherpa 2.2.1 generator [118] and the NNPDF3.0NNLO PDF set [146], using NLO matrix elements for up to two partons, and LO

matrix elements for up to four partons, calculated with the Comix [151] and OpenLoops [152–154] libraries. They were matched with the Sherpa parton shower [155] using the MEPS@NLO prescription [119–122]. The parton shower used the set of tuned parameters developed by the Sherpa authors, and the samples were normalised to a NNLO prediction [156]. Similar methods were used to simulate W+jets processes that contribute to the fake-lepton background, which is estimated in Section 6.2.

The theoretical uncertainty in the Drell–Yan background is estimated by PDF eigenvector variations of the nominal PDF set, and variations of the PDF scale, α_s, electroweak corrections, and photon-induced corrections.

Samples of diboson (VV) and multiboson (VVV) final states were simulated with the Sherpa 2.2.1 and Sherpa 2.2.2 [118] generator depending on the process. Where appropriate, off-shell effects and Higgs boson contributions were included. Fully leptonic final states and semileptonic final states, where one boson decays leptonically and the other hadronically, were generated using ME at NLO accuracy in QCD for up to one additional parton and at LO accuracy for up to three additional parton emissions. Samples for the loop-induced processes, $gg \to VV$, were generated using LO-accurate ME for up to one additional parton emission for both the fully leptonic and semileptonic final states. The ME calculations were matched and merged with the Sherpa parton showers, using Catani–Seymour dipole factorisation [151, 155] with the MEPS@NLO prescription [119–122]. The virtual QCD corrections were provided by the OpenLoops library [152–154]. The NNPDF3.0nnlo set was used [146], along with the dedicated set of tuned parton-shower parameters developed by the Sherpa authors.

For Sherpa-simulated processes (Drell–Yan, diboson and multiboson processes), uncertainties from missing higher orders are evaluated [157] using seven variations of the QCD factorisation and renormalisation scales in the matrix elements by factors of 0.5 and 2, avoiding variations in opposite directions. The effect of the PDF choice is considered using the PDF4LHC15 prescription [158]. Uncertainties in the nominal PDF set were evaluated using 100 replica variations. Additionally, the results were cross-checked using the central values of the CT14nnlo [159] and MMHT2014nnlo [160] PDF sets. The effect of the uncertainty in the strong coupling constant, α_s, was assessed by variations of ± 0.001.

The NLO Powheg Box v2 [147–150] generator was used with the NNPDF3.0nlo [146] PDF set to model the production of $t\bar{t}$ and single-top-quark Wt-channel events; the top-quark mass was set to 172.5 GeV and the h_{damp} parameter[1] was set to 1.5 m_{top} [161]. For the Wt-channel single-top events, the diagram removal scheme [162] was used to remove interference and overlap with $t\bar{t}$ production. The events were interfaced to Pythia 8.230 [138] to model the parton shower, hadronisation, and underlying event, with parameters set according to the A14 tune [141] and using the NNPDF2.3lo set of PDFs [142]. The decays of bottom and charm hadrons were performed by EvtGen 1.6.0 [143]. Additionally, top-quark spin correlations are preserved through the use of MadSpin [163]. The predicted $t\bar{t}$ production cross-section, calculated

[1] The h_{damp} parameter is a resummation damping factor and one of the parameters that controls the matching of Powheg matrix elements to the parton shower and thus effectively regulates the high-p_{T} radiation against which the $t\bar{t}$ system recoils.

with Top++ 2.0 [164] to NNLO in perturbative QCD and including soft-gluon resummation to next-to-next-to-leading-log order, is 830^{+20}_{-29} (scale) ± 35 (PDF + α_s) pb.

For $t\bar{t}$ and single-top-quark samples, the uncertainties in the cross-section due to the PDF and α_s were calculated using the PDF4LHC15 prescription [158] with the MSTW2008nnlo [165, 166], CT10nnlo [145, 167] and NNPDF2.3lo [142] PDF sets in the five-flavour scheme, and were added in quadrature to the effect of the factorisation scale uncertainty.

The MadGraph5_aMC@NLO 2.3.3 [75] generator was used with the NNPDF3.0nlo [146] PDF set to model the production of $t\bar{t} + W/Z/H$ events. The events were interfaced to Pythia 8.210 [138] using the A14 tune [141] and the NNPDF2.3lo [146] PDF set. The production of $3t$ and $4t$ events was modelled using the MadGraph5_aMC@NLO 2.2.2 [75] generator at LO with the NNPDF2.3lo [146] PDF set. The events were interfaced with Pythia 8.186 [168] using the A14 tune [141] and the NNPDF2.3lo [146] PDF set. The decays of bottom and charm hadrons were simulated using the EvtGen 1.2.0 program [143].

For $t\bar{t}V$ production and processes producing three or more top quarks, the uncertainty due to ISR was estimated by comparing the nominal event sample with two samples where the up/down variations of the A14 tune were employed.

Top-quark ($t\bar{t}$, single-top-quark, $3t$, $4t$ and $t\bar{t} + W/Z/H$) and multiboson (WWW, WWZ, WZZ, and ZZZ) processes represent minor backgrounds in the analysis and are thus joined to form the 'Other' background category.

Pile-up events from additional interactions in the same or neighbouring bunch crossings were simulated with Pythia 8.186 [168] using the NNPDF2.3lo PDFs and the A3 tune [169] and overlaid on the simulated hard-scatter events, which were then reweighted to match the pile-up distribution observed in data.

CHAPTER 4

Event Reconstruction in ATLAS

This chapter describes the process of reconstruction and identification in ATLAS, i.e. how the raw detector information is converted into final state physics objects, such as electrons, muons, jets, and missing transverse energy. Furthermore, the calibration of these objects to account for possible detector effects is presented. First, the track reconstruction is discussed in Section 4.1. Then, the reconstruction procedure for electrons, muons, and jets, which are built from track and calorimeter cluster information, is detailed in Sections 4.2, 4.3, and 4.4, respectively. Lastly, the reconstruction of missing transverse momentum that can be determined from the momentum imbalance from all other objects is outlined in Section 4.5.

The reconstruction of physics objects mainly relies on high-level information from ID tracks and vertices, MS tracks, and topological calorimeter clusters. Physics objects are identified with some uncertainty by comparing sub-detector responses to those expected for a particular type of particle. Since the signatures that different physics objects leave in the detector are not easily distinguishable, dedicated identification algorithms use a multitude of detector information to select an ensemble of object candidates that is as pure as possible. Due to the broad ATLAS physics programme and different physics analysis requirements, a few identification working points exist that achieve different predefined signal efficiency thresholds. A physics object can be rejected if a significant additional detector activity is found close to it. These so-called isolation requirements, commonly used for leptons, further enhance background suppression.

4.1 Tracks and Vertices

Reconstruction of charged particles' trajectories, henceforth referred to as *track reconstruction*, is a crucial task for most particle physics experiments as it is essential also for other physics objects reconstruction, e.g. lepton reconstruction, primary vertex finding, pile-up removal and flavour tagging. Unfortunately, finding and fitting a track is also one of the most complex and CPU-intensive parts of event reconstruction in HEP experiments due to the high luminosity and, consequently, large pile-up, especially in the hadron colliders.

The most important steps of the ALTAS Run 2 track reconstruction, thoroughly described in Ref. [170], are presented in the following paragraphs.

A charged particle (a charged lepton or a jet), produced in a pp collision, traverses the ATLAS detector and leaves charge deposits in the Pixel and SCT detectors. Hits from the TRT can also be added [171]. The first step of the track reconstruction is *clustering*, in which hits, leaving a sufficient energy deposit in a unique layer of the Pixel or SCT detectors, are grouped to form three-dimensional *space points*. In the Pixel detector, each cluster equates to one space point, while in the SCT, clusters from both sides of a strip layer must be combined. Groups of three space points with a minimum spatial separation are combined in the following *track seed* finding step. Track seeds can only be built from three Pixel or three SCT space points, but

not from combinations of both detectors. If a fourth space point, compatible with the initial seed, is found in a different detector layer, it is likely to originate from a charged particle and is therefore given higher priority. Finding the initial seeds with high efficiency is a difficult challenge in high pile-up conditions. Many possible combinations of hits must be considered, and the combinatorial possibilities increase dramatically. A combinatorial Kalman filter [172, 173] is run as a pattern recognition step on seeds to build track candidates and extract initial estimates of track parameters. These are used to extrapolate the tracks to the remaining layers of the Pixel and SCT detectors, where additional hits can be added to the track if compatible with the first estimate. The particle's trajectory is a helix as the ID is submerged in a solenoidal magnetic field. The track is parametrised by five variables: the magnitude of the transverse momentum, p_{T}, the polar angle θ, the azimuth angle ϕ, the transverse impact parameter d_0 relative to the beam direction, and the longitudinal distance z_0 from the primary vertex. The last two parameters are expressed in mm and are measured between the IP and the point of the closest approach in the transverse (d_0) and longitudinal plane (z_0). Tracks built from purely random sets of space points are discarded in this step.

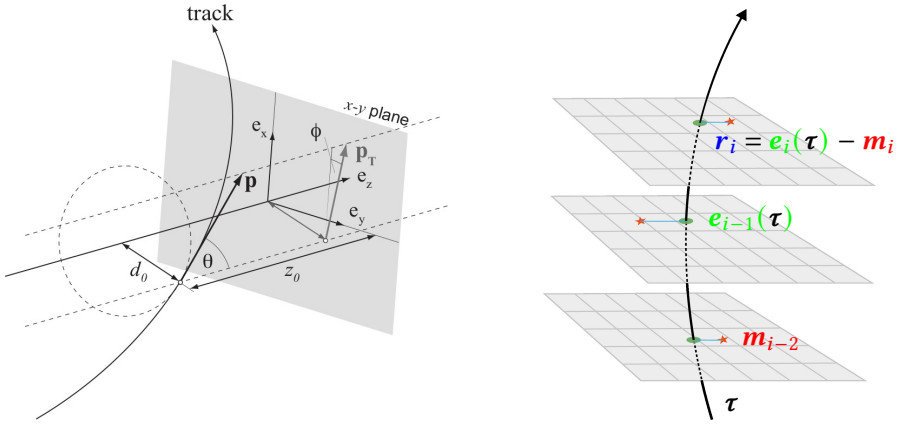

Figure 4.1: (a) Parameters used to describe particle track in a magnetic field. (b) Schematic representation of a charged particle crossing detector planes. The measurement, m_i, on each of the i^{th} layer, is indicated by a red star. Also shown are the fitted track trajectory for a given set of track parameters, τ (black line), the position of the intersection of the fitted track with the surface on which the i^{th} measurement is made, $e_i(\tau)$ (green ellipse), and the residuals, r_i (blue line). Taken from Ref. [174].

Since the Kalman filter builds multiple track candidates per seed if more than one compatible space point extension exists on the same layer, the *ambiguity-solving algorithm* is run on top. Each track is assigned a score based on the global χ^2 of the track fit, the logarithm of its momentum and the number of holes in the track.[1] Clusters can, at most, be shared by two tracks. Furthermore, each track can have no more than two shared clusters. The ambiguity solver finally rejects tracks that do not satisfy requirements, presented in Table 4.1.

Since a high-resolution fit that uses all available information is relatively CPU-intensive, it is

[1] A hole in a track is defined as a missing cluster on the intersection of the candidate track and the sensitive detector layer.

Table 4.1: Requirements that a track must fulfil to pass through the ambiguity solver and be added to the final track collection. Adopted from Ref. [175].

Requirement
$p_{\mathrm{T}} > 500\,\mathrm{MeV}$
$\lvert\eta\rvert < 2.7$
≥ 7 pixel or SCT clusters (12 are expected)
≤ 2 holes in the combined pixel and SCT detectors
≤ 2 holes in the pixel detector
$\lvert d_0\rvert < 5.0\,\mathrm{mm}$
$\lvert z_0\rvert < 200\,\mathrm{mm}$
≤ 1 shared pixel cluster or ≤ 2 shared SCT clusters on the same layer

performed only for tracks that pass through the ambiguity solver algorithm. Ultimately, such a track is added to the final track collection. For the high-resolution track fits, the position and uncertainty of each cluster are determined by neural networks [176]. Track reconstruction efficiencies of charged primary particles are presented in Figure 4.2.

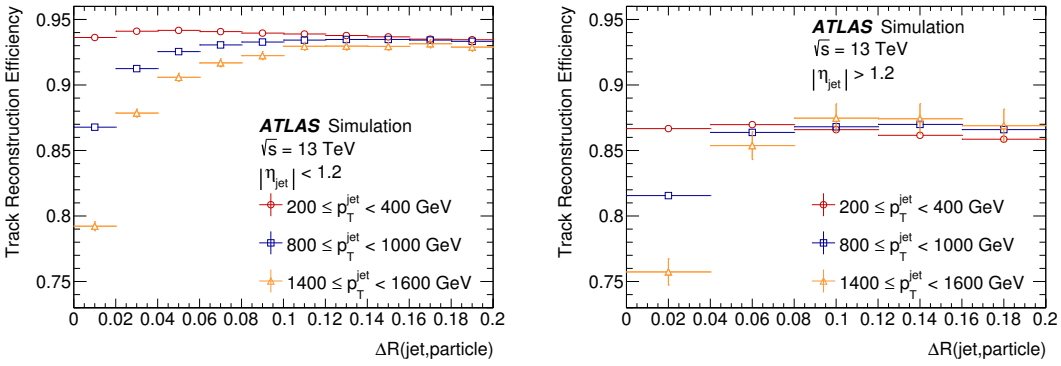

(a) (b)

Figure 4.2: Reconstruction efficiencies of charged primary particles in jets with (a) $|\eta| < 1.2$ and (b) $|\eta| > 1.2$ are shown as a function of the $\Delta R(j, \text{particle})$ for different $p_{\mathrm{T}}^{\mathrm{jet}}$ in simulated dijet MC events. Taken from Ref. [170].

Primary vertex

After all track candidates are reconstructed, the vertex positions can be determined by finding the track intersections. Generally, only one pp collision per bunch-crossing is of interest, referred to as the *primary vertex*, whose products must be isolated from the nearby pile-up. Primary vertex reconstruction is done in two stages: *vertex finding*, in which the tracks are associated with vertices, and *vertex fitting*, where the actual position of the vertex is reconstructed [177]. Firstly, a seed position for the initial vertex is estimated with high accuracy

using a Gaussian resolution model for the track impact parameter. The density of tracks along the beam axis is used to estimate the most likely position of a pp interaction vertex. Then, an iterative χ^2 minimisation for finding the optimal vertex position is done using an annealing procedure with the dedicated vertex fitting algorithm. Each track is weighted according to its compatibility with the initial vertex estimation. The vertex position is repetitively recomputed with the updated weights of the trajectories until the last iteration when the final weight of each track used in the vertex fit is evaluated. Tracks that are further than 7 σ away from the vertex are removed and serve as seeds for another vertex. This procedure is repeated until no more vertices can be found. Valid primary vertex candidates must be associated with at least two tracks with $p_{\mathrm{T}} > 0.5\,\mathrm{GeV}$, out of which the one with the highest sum of squares of transverse momenta, $\sum p_{\mathrm{T}}^2$, is defined as the primary vertex. Others are considered to be pile-up vertices.

The vertex reconstruction efficiency has been evaluated from MC simulation and exceeds 99% for all processes with at least two charged particles reconstructed within the ATLAS ID.

4.2 Electrons

Stable elementary particles such as electrons, muons or photons appear in many final states that emerge from pp collisions. They played an essential role in many of the SM and Higgs-boson physics discoveries, and precision measurements, and are likewise present in many BSM final states. In fact, electrons, besides muons, are the main target of the work presented in this thesis. Therefore, the following sections describe the keystone on which the analysis relies, i.e. being able to successfully reconstruct, efficiently identify, and also isolate electrons from other particles having a similar detector signature.

Electrons produced in the pp collisions leave tracks in the ID and deposit all their energy in the electromagnetic calorimeter.[2] The electron reconstruction algorithm [178–180] combines directional information from the tracker with the energy estimation from the EMCAL for electrons that remain in the $|\eta| < 2.47$ region. A schematic illustration of a path of an electron and the detector subsystems that provide information for its reconstruction and identification is depicted in Figure 4.3.

Electron Reconstruction

The electron reconstruction exploits three fundamental characteristics of the electron's signature within the particle detector. These are the localised energy deposits in the EMCAL, charged-particle tracks in the ID, and the close matching between these two to form the final electron candidates. Electron reconstruction starts by combining cells into topologically connected clusters, the *proto-clusters*. The cells from both the EM and hadronic calorimeters are

[2] To be precise, some can escape the detector in the very forward regions, which are not covered by the tracker but those are not used in the thesis.

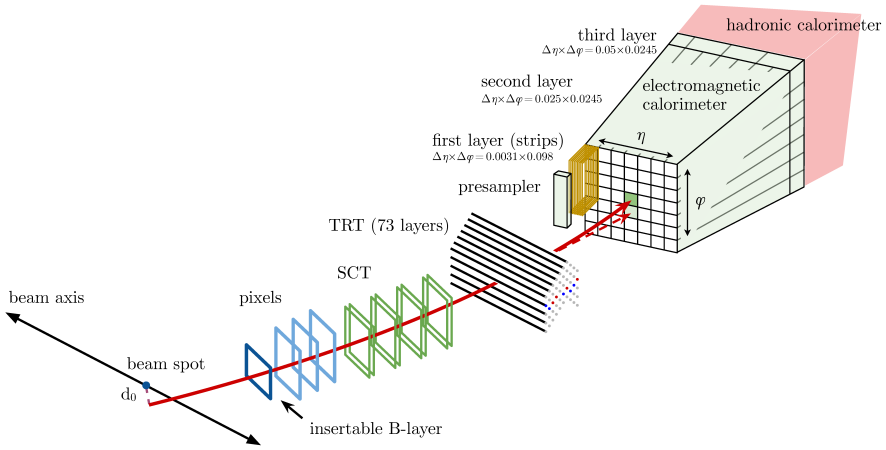

Figure 4.3: An illustration of a trajectory of an electron, shown in solid red, passing the ATLAS ID (Pixel, SCT, and TRT) and entering the electromagnetic calorimeter. The dashed red arrow represents the path of a bremsstrahlung photon, emerging from the electron's interaction with the detector material and leaving an energy deposit near that of the original electron. Taken from Ref. [178].

considered, with the only requirement being that the energy deposit within each cell is equal to or above four times the level expected from noise and pile-up:

$$|\xi^{\mathrm{EM}}_{\mathrm{cell}}| = \left| \frac{E^{\mathrm{EM}}_{\mathrm{cell}}}{\sigma^{\mathrm{EM}}_{\mathrm{noise,\,cell}}} \right| \geq 4, \tag{4.1}$$

where $E^{\mathrm{EM}}_{\mathrm{cell}}$ is the energy of the EMCAL cells, and $\sigma^{\mathrm{EM}}_{\mathrm{noise,\,cell}}$ is the expected cell noise. The proto-clusters are merged with the neighbouring cells having a significance $|\xi^{\mathrm{EM}}_{\mathrm{cell}}| \geq 2$, which become probes for probable further merging. Proto-clusters that contain the same cell with $|\xi^{\mathrm{EM}}_{\mathrm{cell}}| \geq 2$ are merged. Contrary, those that contain two or more cells with $E^{\mathrm{EM}}_{\mathrm{cell}} > 500$ MeV and have at least four neighbours that do not have a stronger signal are split into separate clusters. Then, only the cells that are in the EMCAL and belong to the original cluster are considered. Finally, the clusters with EM energy higher than 400 MeV and the ratio of the EM energy to the total cluster energy greater than 0.5 are further used in the electron reconstruction procedure and are referred to as EM *topo-clusters* [181].

Then, the topo-clusters are matched to tracks, which are reconstructed in the ID using either the standard track reconstruction, described in Section 4.1 or an alternative approach that accounts for up to 30% energy losses due to bremsstrahlung at each material intersection. Additionally, tracks with silicon hits loosely matched to clusters are re-fitted with a non-linear generalisation of the Kalman filter, the Gaussian sum filter (GSF) algorithm [182], to improve track parameter estimation and recover bremsstrahlung losses. The track-to-topo-cluster matching is done by extrapolating the track to the second EMCAL layer and requiring low separation from the cluster $|\eta_{\mathrm{track}} - \eta_{\mathrm{cluster}}| < 5\%$, and $-0.10 < q \cdot (\Phi_{\mathrm{track}} - \Phi_{\mathrm{cluster}}) < 0.05$, where q is the reconstructed charge of the trajectory. The requirement on $q \cdot (\Phi_{\mathrm{track}} - \Phi_{\mathrm{cluster}})$ is asymmetric since tracks sometimes miss some energy from radiated photons that clusters measure.

Next, the *super-clusters* are built by merging GSF tracks and topo-clusters. Matching is done by firstly sorting the list of seed EM topo-clusters in descending E_T (only considering the EM energy), removing those with $E_T < 1$ GeV, and associating them with a track that has at least four SCT hits. Then, if a neighbouring cluster is found within $\Delta\eta \times \Delta\Phi = 0.0075 \times 0.125$ of an electron, it is added to the seed. This window can be extended up to 0.125×0.3 if the best-matched track of the two clusters is the same.

Finally, the electron objects that are used in the analyses are built. Their energies are calibrated, and discriminating variables that separate electrons from the background are added. An example of electron reconstruction efficiencies obtained from $Z \to e^+e^-$ decay studies is shown in Figure 4.4.

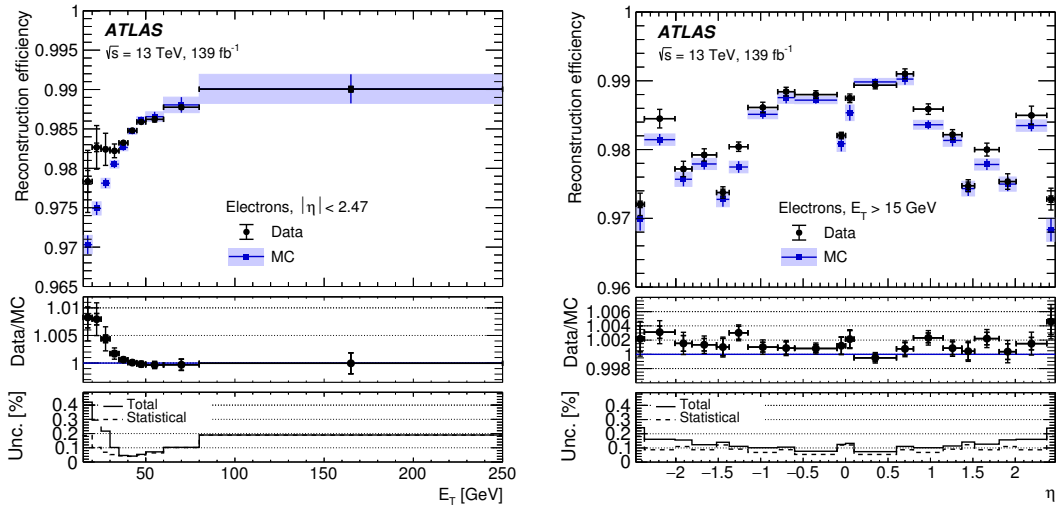

(a) (b)

Figure 4.4: Reconstruction efficiencies of electrons from $Z \to e^+e^-$ decays as a function of (a) E_T and (b) η. The top panels show the efficiencies obtained in data and simulation with the statistical and total uncertainties. The middle panels show the data/MC efficiency ratio. The bottom panels show the statistical and the total uncertainties on that ratio, which is applied as a correction factor in the analyses. Taken from Ref. [180].

Electron identification

Additional quality criteria called *electron identification* are used to further improve the purity of selected electron objects. Prompt electron candidates are selected with a multivariate likelihood discriminant, constructed from quantities measured in the ID, calorimeter and a combination of both [178]. The variables are chosen to optimise the separation of prompt electrons from the background, predominantly consisting of photon conversions and heavy-flavour hadron decays. Electron identification relies on the quality of lateral and longitudinal shower development in the calorimeter, the track-to-cluster matching, and the primary electron track. The latter, for example, requires that electron candidates produce hits at least in the two Pixel layers and

seven hits in the Pixel and SCT combined, which reduces the background originating from photon conversions.

The discriminant uses probability density functions (pdfs), P, to describe the signal, L_S, and background, L_B. In the MVA method, the electron can still pass the full selection criteria, even though it may fail the requirement on one or more specific variables. The pdfs are created by smoothing histograms of the discriminating variables with a KDE [183]:

$$L_{S(B)}(\vec{x}) = \prod_{i=1}^{n} P_{S(B),i}(x_i), \tag{4.2}$$

where $\vec{x}$ is the vector of discriminating variable values. The pdfs take for the quantity i at value x_i the values $P_{S,i}(x_i)$ and $P_{B,i}(x_i)$ for signal and background, respectively. The likelihood discriminant is defined as the natural logarithm of the ratio of L_S and L_B. Lastly, the inverse sigmoid function is used to transform the discriminant.

Electron identification is finally defined by three identification working points (WPs) in order of increasing background rejection: `Loose`, `Medium`, and `Tight`. These are mutually inclusive and are characterised by a cut optimised in multiple E_T and η bins. Each working point uses the same variables to define the likelihood discriminant, but the requirements on individual ones may differ. For a typical electroweak process, the target efficiencies are, on average, 93%, 88% and 80% for the `Loose`, `Medium`, and `Tight` working points, respectively, and gradually increase from low to high E_T.

An example of electron identification efficiencies obtained from $Z \rightarrow e^+e^-$ decay studies using the tag-and-probe method is shown in Figure 4.5 for electrons with $E_T > 15\,\text{GeV}$. For lower-energy electrons ($4.5\,\text{GeV} < E_T < 20\,\text{GeV}$), identification efficiencies are measured using $J/\psi \rightarrow e^+e^-$ events instead [180].

Electron isolation

Most ATLAS analyses implement another quality criterion, *electron isolation*, to achieve better extraction of the prompt electron production. It focuses on discriminating electrons originating from the hard-scattering vertex or heavy resonances decay from background electrons that are misidentified hadrons, converted photons, or produced in semileptonic decays of heavy quarks. Electron isolation exploits the fact that little activity is expected in a relatively small $\Delta\eta \times \Delta\Phi$ area around the signal electron both in the ID and in the calorimeter. It constructs variables (usually summing the cluster E_T in the calorimeter and the p_T-s of the tracks except the one of the candidate) to quantify the amount of activity in the $\Delta R = \sqrt{\Delta\eta^2 + \Delta\Phi^2}$ vicinity of the candidate object.

Calorimeter-based isolation sums E_T of all positive-energy topo-clusters in the EMCAL inside the electron candidate's cone with radius $\Delta R = 0.2$, with the electron energy subtracted. The fully corrected calorimeter-based isolation variable E_T^{cone20} is defined.

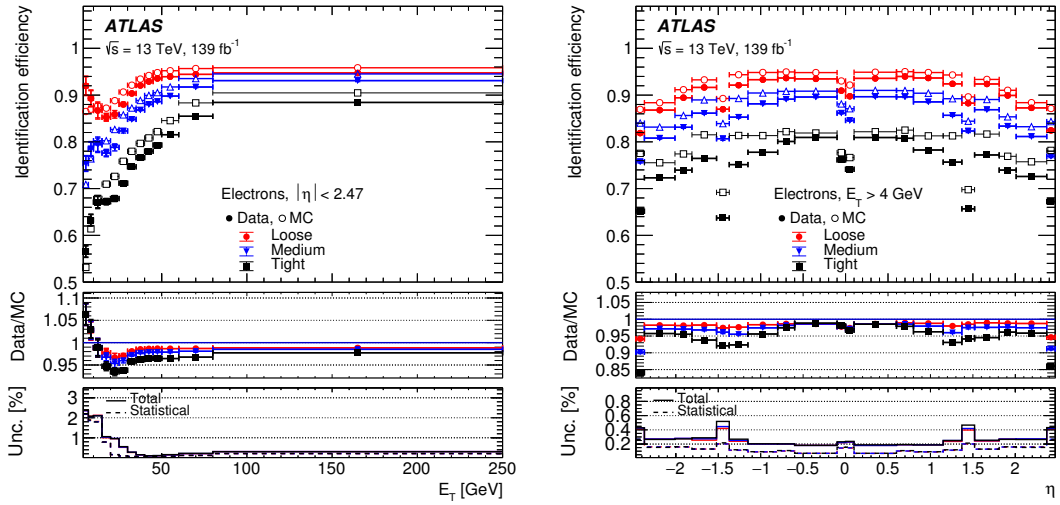

(a) (b)

Figure 4.5: Measured electron identification efficiencies in $Z \to e^+e^-$ events for various working points as a function of (a) E_T and (b) η are shown in the upper panels. The middle panels show the data/MC efficiency ratio. The bottom panels display the relative uncertainty of the combination of measurements. Taken from Ref. [180].

Track-based isolation calculates $p_T^{\text{varcone20}}$ by summing all the tracks (except the candidate's) that satisfy the $p_T > 1$ GeV, basic track-quality requirements and fall within the fiducial region of the ID ($|\eta| < 2.5$). It uses the variable-sized cone $\Delta R = \min(0.2, 10\,\text{GeV}/p_T[\text{GeV}])$, which shrinks for higher p_T^e, to define the vicinity of an electron. The track isolation variables do not depend on pile-up due to the high rejection of tacks originating from pile-up vertices.

The working points either target constant efficiency, ε_{iso}, or fixed cuts on the isolation variables. They are usually defined by the cuts on E_T^{cone20}/p_T and $p_T^{\text{varcone20}}/p_T$ ratios. The `Gradient` WP is, for example, designed to give efficiency of 90% at $p_T = 25$ GeV and 99% at $p_T = 60$ GeV, uniform in η. The summary of the electron isolation points is presented in Table 4.2.

Table 4.2: Definitions of the electron isolation working points and isolation efficiency ε_{iso} are given. All WPs use a cone size of $\Delta R = 0.2$ for calorimeter isolation and $\Delta R_{\text{max}} = 0.2$ for track isolation. Adopted from Ref. [178].

Selection criteria	Calorimeter isolation	Track isolation
`Gradient`	$\varepsilon = 0.1143 \times p_T + 92.14\%$	$0.1143 \times p_T + 92.14\%$
`HighPtCaloOnly`	$E_T^{\text{cone20}} < \max(0.015 \times p_T, 2.5\,\text{GeV})$	–
`Tight`	$E_T^{\text{cone20}}/p_T < 0.06$	$p_T^{\text{varcone20}}/p_T < 0.06$
`Loose`	$E_T^{\text{cone20}}/p_T < 0.20$	$p_T^{\text{varcone20}}/p_T < 0.15$

An example of electron isolation efficiencies obtained from inclusive 2018 data $Z \to e^+e^-$

events using the tag-and-probe method is shown in Figure 4.6. The probe electrons satisfy the `Medium` identification selection. The newer, slightly modified `Tight_VarRad` selection criterion, gives the highest background rejection below 60 GeV, while the `HighPtCaloOnly` WP gives the highest rejection in the high-E_{T} region ($E_{\mathrm{T}} > 100$ GeV) [180].

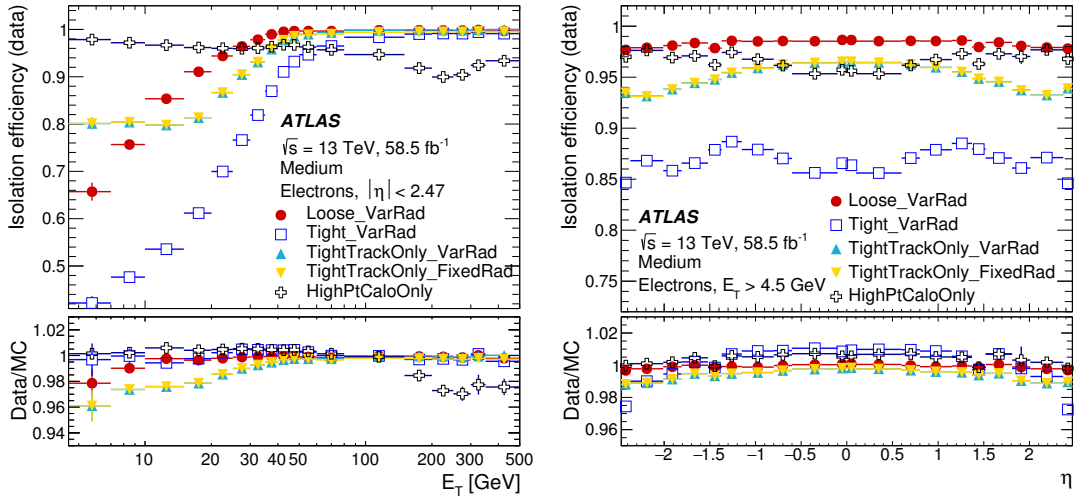

(a) (b)

Figure 4.6: Measured electron isolation efficiencies in $Z \rightarrow e^{+}e^{-}$ events for various working points as a function of (a) E_{T} and (b) η are shown in the upper panels. The electrons are required to fulfil the `Medium` selection from the likelihood-based electron identification. The bottom panels show the data/MC efficiency ratio. The uncertainty shown consists of both statistical and systematic uncertainties. Taken from Ref. [180].

The total electron selection efficiency can be factorised as a product of the abovementioned efficiency terms:

$$\varepsilon_{\mathrm{total}} = \varepsilon_{\mathrm{cluster}} \times \varepsilon_{\mathrm{reco}} \times \varepsilon_{\mathrm{id}} \times \varepsilon_{\mathrm{iso}} \times \varepsilon_{\mathrm{trigger}}. \tag{4.3}$$

The $\varepsilon_{\mathrm{cluster}}$ efficiency is the probability to reconstruct an EM cluster given a genuine electron. It is found to be above 99% for electrons with $E_{\mathrm{T}} > 10$ GeV [179] and is evaluated exclusively from MC simulation, while others are extracted from both data and simulation. Multiplicative correction factors are derived for the last four terms to correct the simulation to match what is observed in data and are defined as the ratio of efficiency measured in data and the one determined from MC events. The correction weights are typically close to unity and are furthermore assigned a systematic uncertainty by varying the requirements on the selection.

4.3 Muons

Muons are the second crucial ingredient of the final state that is searched for in the analysis presented in this work. They can be viewed as the minimum ionising particles at the LHC

energy scale. When a muon passes the ATLAS detector, it leaves hits in the inner detector, characteristic energy deposits in the calorimeters, and tracks in the muon system.

Muon Reconstruction

Usually, the muon reconstruction relies primarily on ID and MS detectors, but the calorimeter information can also be added if there is a significant loss of energy within the calorimeter [184, 185]. The muon reconstruction begins with a search for short straight-line local track segments reconstructed from hits in individual MS stations. These segments are then extrapolated across sections to form an initial muon track candidate by imposing a loose constraint on the muon to be compatible with the IP and assuming a naive parabolic track approximation. A χ^2 fit is then performed considering the muon bending in the magnetic field and accounting for the possible material effects and chamber misalignment. Then, a similar iterative fitting procedure is done as in Section 4.1, in which outlier hits are removed. On the other hand, those that are compatible with the trajectory, but were not assigned to a track before, are added.

Muon tracks within the ID are reconstructed as described in Section 4.1. Once the calorimeter information is added, the global muon reconstruction is performed. Five different types of reconstruction are defined based on which subdetectors are included. These are schematically presented in Figure 4.7 and described in the following:

`Combined (CB)` muons category, as the name suggests, joins fitted tracks from the ID and the MS. If they match, a refit on combined hits is performed by also considering the energy loss in the calorimeters. The MS hits can be added or removed in this step, in which case the fit is repeated.

`Inside-out (IO)` category uses a complementary approach which, contrary to the `Combined`, extrapolates ID tracks outwards and then searches for hits in the MS. A fit is performed considering the information from all the available subdetectors.

`MS extrapolated (ME)` muons are those for which the MS track can not be combined with any ID tracks. The track parameters are extrapolated from MS and used at the beamline position. At least two layers of MS chambers in the barrel or three layers in the forward region must be traversed. They are mainly used to extend the muon reconstruction acceptance to the part of the detector not covered by the ID.

`Segment-tagged (ST)` muons are, similarly to `ME`, extrapolated from ID to MS but with a stricter requirement to tightly match with at least one reconstructed MS segment. No refit is made. The properties of the ID tracks directly define such muons.

`Calorimeter-tagged (CT)` muons are identified by ID track extrapolation to the calorimeter. There, a signature compatible with a MIP is searched for. The muon parameters are taken from the ID track fit. This type has the lowest purity of all the abovementioned muon types.

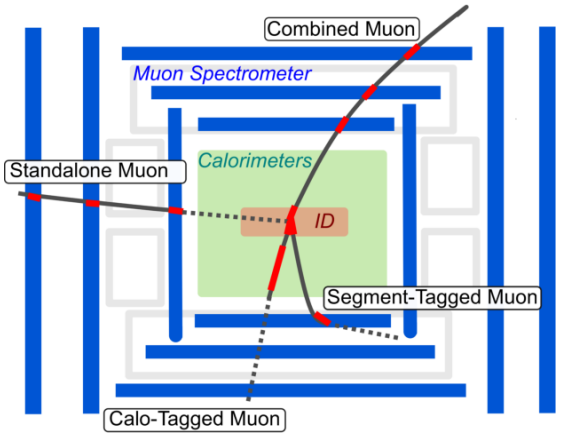

Figure 4.7: Schematic drawing of the detector parts used for muon reconstruction. Based on the detector parts used for the reconstruction, several muon types are defined. Taken from Ref. [186].

Simple rules are defined to resolve any potential overlaps between the muon reconstruction types. If different muon types share the same inner detector track, `CB` muons are preferred, then `ST`, and finally `CT`. If there is an overlap with the `ME` muons, track hits are analysed, and the track with a better fit and a higher number of hits is kept.

Muon identification

Similarly to the electron reconstruction, additional selections can be made on top of the muon reconstruction to further reject the background muons that predominantly originate from decays of kaons or pions. High-quality muon candidates can be extracted based on a collection of requirements on the number of hits in the different ID subdetectors and MS stations, on the track fit properties, and on quantities that test the compatibility between the ID and MS measurements. Such a set of requirements is referred to as a working point and is defined for each muon type described before. Three standard WPs are defined to suit the needs of different analyses and are mutually inclusive, as in the electron case. These are `Loose`, `Medium`, and `Tight`, in order of increasing purity, respectively. Furthermore, additional identification WP is constructed to cover extreme phase space regions, the `High-`p_{T} WP.

`Medium muons` are the default WP for muons in ATLAS. This WP is designed to minimise the systematic uncertainties associated with muon reconstruction and identification. Only `CB` and `IO` muons are included in the $|\eta| < 2.5$ region, which coincides with the ID coverage. These must have at least two precision stations,[3] except in the $|\eta| < 0.1$, where muons with only one precision station are allowed. A loose compatibility between the ID and MS measurements is required. More than 98% of $t\bar{t}$ events passing the `Medium` WP were found to be `CB` muons.

[3] The precision station is defined as the number of MS stations in which the muon produced at least three hits in the MDT or CSC chambers.

`Loose muons` are designed to maximise the reconstruction efficiency while providing good-quality muon tracks. All muon types are included. Compared to `Medium` WP, it has approximately 20% higher efficiency for low-p_{T} muons and 1 to 2% for higher-p_{T} ones, but it comes at the cost of a higher fake rate.

`Tight muons` minimise the fake rate to reach high purity but lose efficiency. Only `CB` and `IO` muons with at least two precision stations are accepted among the muons passing the `Medium` selection WP. More stringent requirements are set on a combined track fit. `Tight` WP achieves a background reduction of more than 50% compared to `Medium`, with a corresponding efficiency loss for prompt muons of approximately 6%.

`High-`$\boldsymbol{p}_{\mathrm{T}}$ `muons` WP is defined to optimise high-resonance searches in a $p_{\mathrm{T}} > 100$ GeV range. Only `CB` and `IO` muons that pass the `Medium` WP are accepted. Even though the reconstruction efficiency is reduced by about 20%, the p_{T} resolution above 1.5 TeV is improved by approximately 30%.

An example of muon reconstruction and identification efficiencies obtained from $J/\psi \to \mu^+\mu^-$ and $Z \to \mu^+\mu^-$ decay studies is shown in Figure 4.8.

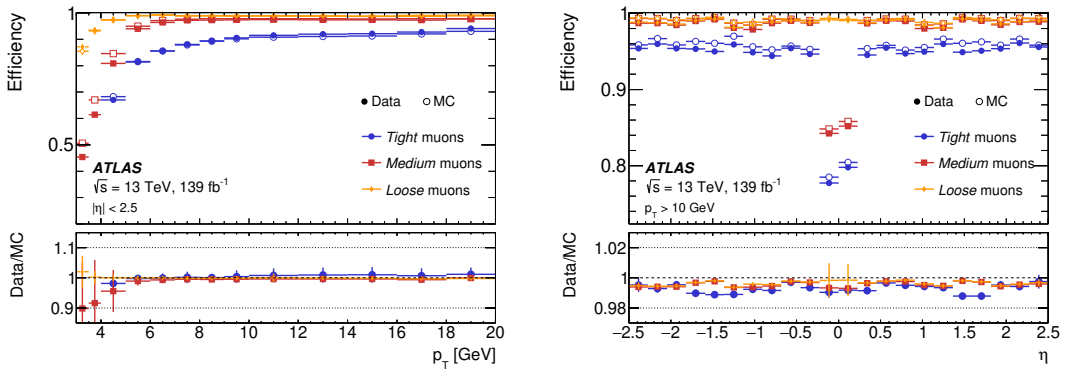

(a) (b)

Figure 4.8: Muon reconstruction and identification efficiencies (a) from $J/\psi \to \mu^+\mu^-$ decays as a function of p_{T} and (b) from $Z \to \mu^+\mu^-$ as a function of η for muons with $p_{\mathrm{T}} > 10$ GeV. The `Loose`, `Medium` and `Tight` criteria are shown. The estimated efficiencies are depicted as open markers, while the filled markers illustrate the results obtained from data. The bottom panels show the data/MC ratio with statistical and systematic uncertainties. Taken from Ref. [185].

Muon isolation

As for the electrons, targeted muons originating from prompt decays of SM or even BSM bosons are typically isolated, while those coming from semi-leptonic hadron decays are always embedded in close-by activity. Therefore, further isolation selections can be made to improve muon quality. Isolation WPs are based on track ($p_{\mathrm{T}}^{\mathrm{varcone30}}/p_{\mathrm{T}}^{\mu}$) and calorimeter isolation variables ($E_{\mathrm{T}}^{\mathrm{cone20}}/p_{\mathrm{T}}^{\mu}$). The tightest WP provides an average isolation efficiency of 36% in the p_{T} range of

3 to 5 GeV, 90% in the range from 5 to 20 GeV, 93% in 20 to 100 GeV, and 93% for $p_{\mathrm{T}} > 100$ GeV. The corresponding misidentification rates for light hadrons in the same p_{T} ranges are 0.15%, 0.38%, 0.12%, and 0.04%, respectively. It should be noted that the `Tight` WP by construction does not select any muons with $p_{\mathrm{T}} < 4$ GeV, which is reflected in the corresponding efficiency in the first mentioned p_{T} region [185].

4.4 Jets

Showers of secondary particles, predominantly quarks and gluons, are commonly produced in a pp collision. These QCD particles undergo hadronisation and fragmentation, in which they combine into colour-neutral particles, like pions and kaons, to form a collimated spray of particles if sufficiently Lorentz boosted. These sprays of particles are referred to as *jets* and are identified in the ATLAS detector from the tracks in the ID (track jet) and energy deposits in the calorimeter (calorimeter jet). The characteristics of jets highly depend on a choice of a reconstruction algorithm, which groups calorimeter energy deposits to form jets. The standard ATLAS choice is the anti-k_t [187] algorithm, which is infrared and collinear safe. Infrared safety refers to the algorithm's ability to correctly identify and count the jets in an event despite the presence of soft particles, while collinear safe algorithms accurately determine the number of jets regardless of the collinearity of the particles. An illustration of an example event, clustered by k_t and anti-k_t clustering algorithms, is shown Figure 4.9.

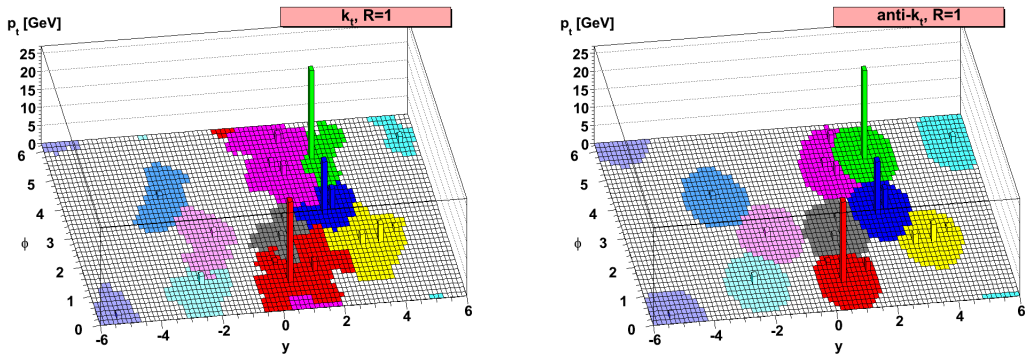

(a) (b)

Figure 4.9: Illustration of (a) k_t and (b) anti-k_t jet clustering algorithms in the $y - \Phi$ plane on an example event. Taken from Ref. [187].

A *Particle flow* [188] algorithm was introduced for Run 2 in ATLAS, combining momentum information from the tracker and energy measurements provided by the calorimeter to (ideally) form individual particles. Firstly, tracks are reconstructed as described in Section 4.1, and calorimeter topo-clusters are generated using the same methodology as for the electrons, detailed in Section 4.2. The algorithm then tries to match each track to a single topo-cluster forming a track+topo-cluster system. The energy of a particle, that created a track and deposited energy in the calorimeter is determined from the topo-cluster position and the track momentum.

However, since particles often deposit energy in multiple topo-clusters, the algorithm assigns a probability that the particle energy was deposited in more than one topo-cluster to each track+topo-cluster system. Then, based on that probability, the algorithm decides if more topo-clusters need to be added to the track+topo-cluster to recover the entire shower energy. In the next step, the energy of a particle that produced the track is subtracted cell by cell from the collection of matched topo-clusters. If the remainder is consistent with the width of the $E^{\text{clus}}/p^{\text{trk}}$ distribution (i.e. $< 1.5\sigma(E_{\text{dep}})$, where $\langle E_{\text{dep}}\rangle = p^{\text{trk}}\langle E^{\text{clus}}/p^{\text{trk}}\rangle$), the topo-cluster system is assumed to be produced by a single particle. Therefore, the remnant energy originates purely from shower fluctuations and is removed. On the other hand, if the remaining energy exceeds the defined threshold, the topo-clusters are retained, as it is likely that multiple particles deposited energy in the surrounding region.

Anti-k_t algorithm is used for particle flow jet reconstruction, considering only positive energy topo-clusters that survive the energy subtraction step described above. Additionally, $|z_0 \sin(\theta)| < 2\,\text{mm}$ is required assuring that the selected tracks match with the hard-scatter primary vertex while removing a significant fraction of pile-up tracks [189]. Anti-k_t, implemented within the FastJet package [190], uses individual objects' four-vectors representing calorimeter clusters or tracks as inputs. For each pair of objects i and j, their relative distance measure d_{ij} is defined as

$$d_{ij} = \min\left(p_{\text{T},i}^{-2}, p_{\text{T},j}^{-2}\right)\frac{\Delta R_{ij}^2}{R^2}, \tag{4.4}$$

where $p_{\text{T},i}$ and $p_{\text{T},j}$ are the transverse momenta associated with two clusters, ΔR_{ij} is their angular separation, and R is an arbitrary distance parameter. The algorithm initialises by taking the cluster with the highest p_{T} as the seed cluster i and computes the distance d_{ij} to the nearest one j. This distance is compared to the distance of a seed cluster from the beam axis, $d_{iB} = p_{\text{T},i}^{-2}$. If the d_{ij} is smaller than the d_{iB}, the two clusters are merged into a new one that takes a role of a seed in the next iteration, else the original cluster i is called a jet, and its associated clusters are removed from the collection. Clustering proceeds until all clusters are associated with a jet. The output of an anti-k_t algorithm is a conical jet with an energetic core and a soft edge which is ensured by the adoption of inverse p_{T} dependence. The radius parameter, R, defines the size of the cone and the minimum distance between two jets and is typically set to 0.4.

The jet energies are measured from the topo-cluster energy deposits and must be calibrated to correct for different experimental effects, such as different calorimeter responses for electromagnetic and hadronic interactions, energy leakage, and pile-up contamination. It guarantees that the measured jet energy scale (JES) agrees with the particle-level scale. The energy calibration is done using measurements of reference objects and consists of multiple steps, described, e.g. in Refs. [191] and [192], yielding normalisation factors derived from simulations and data. In addition to the JES calibration, the jet energy resolution (JER) [192] is measured in data using dijet balance measurements and providing important information for systematic uncertainty determination. Finally, a dedicated jet vertex tagger (JVT) [193] algorithm employs a multivariate technique that relies on jet energy and tracking variables to determine the likelihood that the jet originates from the primary vertex.

b-tagging algorithms

Flavour tagging plays an essential role in the ALTAS physics programme. Many SM precision measurements, studies of Higgs boson properties, and searches for new phenomena would not be possible without the dedicated algorithms used to identify b-quarks and c-quarks [194]. These so-called b-tagging algorithms [195] identify heavy-flavour quarks based on their long lifetime, high mass and high decay multiplicity of b- and c-hadrons. With the b-hadron's lifetime of the order of 1.5 ps, it travels a few mm from the hard-scatter IP before decaying and producing a secondary, displaced vertex.

Multiple low-level tagging algorithms are used in ATLAS, designed to reconstruct the characteristic features of b-jets. These algorithms mainly exploit the substantial impact parameters of the tracks originating from the b-hadron decays to identify b-jets and try to reconstruct the secondary vertices. The output of the low-level tagging algorithms is fed into high-level algorithms mainly constructed from deep-learning classifiers nowadays. The `DL1r` algorithm based on fully connected multi-layer feed-forward neural networks is used in this analysis. It is trained on a hybrid training sample, consisting of 70% of jets from $t\bar{t}$ events and 30% from $Z' \rightarrow q\bar{q}$ events. The `DL1r` neural network has a multidimensional output corresponding to the probabilities for a jet to be a b-jet, a c-jet or a light-flavour jet achieving much better rejection factors for both c-jet and light-flavour jets than previous `MV2c10` series algorithms [196]. The discriminant distribution of the `DL1r` algorithm output is shown in Figure 4.10(a). Different cuts can be applied to the discriminant, defining the operating points with the desired average b-tagging algorithm efficiency. Efficiency operating points commonly used in ATLAS analyses (60%, 70%, 77% or 85%) are presented in Figure 4.10(b). Normalisation factors are defined as a ratio between data and MC efficiencies to correct the discrepancies between both and are finally applied to the simulation.

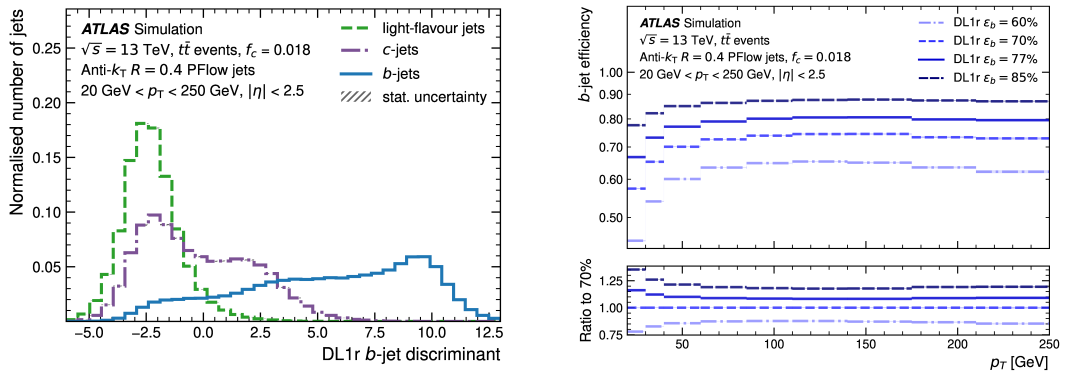

(a) (b)

Figure 4.10: (a) Distributions of the outputs of the `DL1r` b-tagging algorithm for b-jets, c-jets and light-flavour jets in $t\bar{t}$ simulated events. (b) The b-tagging efficiency for several operating points as a function of $p_{\mathrm{T}}^{\mathrm{jet}}$. Efficiency operating points commonly used in ATLAS analyses of LHC Run 2 pp data are presented. The lower panel shows the ratio of each operating point's performance to that of the 70% operating point. Taken from Ref. [195].

4.5 Missing Transverse Energy

Neutrinos escape the ATLAS detector undetected because they only interact weakly with matter, and their interaction cross-section is negligibly small. However, information about their presence can still be indirectly inferred by relying on energy and momentum conservation. In a first approximation, the incoming partons in the pp collision do not carry any transverse momentum. Therefore, the vectorial sum of all transverse momenta of outgoing particles should cancel to zero. If not, the momentum imbalance is termed *missing transverse energy* ($E_{\mathrm{T}}^{\mathrm{miss}}$) [197] and is defined as the negative vectorial sum of the transverse momenta of all reconstructed particles and energy deposits in a given event.

$$\mathbf{E}_{\mathrm{T}}^{\mathrm{miss}} = \underbrace{\underbrace{-\sum_{\substack{\text{selected}\\\text{electrons}}} \mathbf{p}_{\mathrm{T}}^{\mathrm{e}}}_{\mathbf{E}_{\mathrm{T}}^{\mathrm{miss},e}} \underbrace{-\sum_{\substack{\text{accepted}\\\text{photons}}} \mathbf{p}_{\mathrm{T}}^{\gamma}}_{\mathbf{E}_{\mathrm{T}}^{\mathrm{miss},\gamma}} \underbrace{-\sum_{\substack{\text{accepted}\\\tau\text{-leptons}}} \mathbf{p}_{\mathrm{T}}^{\tau_{\mathrm{had}}}}_{\mathbf{E}_{\mathrm{T}}^{\mathrm{miss},\tau_{\mathrm{had}}}} \underbrace{-\sum_{\substack{\text{selected}\\\text{muons}}} \mathbf{p}_{\mathrm{T}}^{\mu}}_{\mathbf{E}_{\mathrm{T}}^{\mathrm{miss},\mu}} \underbrace{-\sum_{\substack{\text{accepted}\\\text{jets}}} \mathbf{p}_{\mathrm{T}}^{\mathrm{jet}}}_{\mathbf{E}_{\mathrm{T}}^{\mathrm{miss,jet}}}}_{\text{hard term}} \underbrace{-\sum_{\substack{\text{unused}\\\text{tracks}}} \mathbf{p}_{\mathrm{T}}^{\mathrm{track}}}_{\mathbf{E}_{\mathrm{T}}^{\mathrm{miss,soft}}} .}_{\text{soft term}} \tag{4.5}$$

The $E_{\mathrm{T}}^{\mathrm{miss}}$ reconstruction strongly depends on the energy scale and resolution of all reconstructed and calibrated hard objects: electrons, muons, photons, jets and hadronically decaying τ-leptons, representing the *hard term* in Eq. 4.5. Since all these particles are well calibrated, the hard term does not depend much on pile-up. On the other hand, all signals that are not associated with any previous hard object are reconstructed from ID tracks as the $E_{\mathrm{T}}^{\mathrm{miss}}$ *soft term*. This term mainly consists of contributions from the hard scatter. Moreover, the underlying event and pile-up interactions can contribute. The addition of soft term significantly improves both $E_{\mathrm{T}}^{\mathrm{miss}}$ scale and resolution. Because $E_{\mathrm{T}}^{\mathrm{miss}}$ depends on the entire event activity, it is one of the most challenging quantities to evaluate, leading to non-negligible uncertainties of the reconstructed object.

Overlap removal

The order of $E_{\mathrm{T}}^{\mathrm{miss}}$ computation needs to be defined to achieve optimal $E_{\mathrm{T}}^{\mathrm{miss}}$ reconstruction performance. Furthermore, an ambiguity-solving procedure is implemented to avoid double-counting of the same physics objects. All electrons passing the selection described in Section 4.2 enter the $E_{\mathrm{T}}^{\mathrm{miss}}$ reconstruction as the highest priority signature. Electrons are followed by photons, τ_{had}, muons, and hadronic jets. Lastly, the soft term is added [197]. The following list, ordered by the physics objects descending in priority, provides more information:

Electrons (e): all passing the `Medium` reconstruction quality and kinematic selections. Electrons are required to have $p_{\mathrm{T}} > 10\,\mathrm{GeV}$ and $|\eta| < 2.47$ excluding the crack region ($1.37 < |\eta| < 1.52$).

Photons (γ): all passing its `Tight` reconstruction quality and kinematic selections and not overlapping with e. Photons are required to have $p_{\mathrm{T}} > 25\,\mathrm{GeV}$ and $|\eta| < 2.47$ excluding the crack region ($1.37 < |\eta| < 1.52$).

Hadronically decaying τ-leptons (τ_{had}): all passing its `Medium` reconstruction quality and kinematic selections and not overlapping with e, γ. τ_{had} are required to have $p_{\mathrm{T}} > 20\,\mathrm{GeV}$ and $|\eta| < 2.47$ excluding the crack region ($1.37 < |\eta| < 1.52$).

Muons (μ): all passing its `Medium` reconstruction quality and kinematic selections. Muons are required to have $p_{\mathrm{T}} > 10\,\mathrm{GeV}$ and $|\eta| < 2.7$.

Jets (j): all passing reconstruction quality and kinematic selections and not overlapping with e, γ, τ_{had}.[4] Jets are required to pass either ($|\eta| < 4.5$, $p_{\mathrm{T}} > 60\,\mathrm{GeV}$), or ($2.4 < |\eta| < 4.5$, $20\,\mathrm{GeV} < p_{\mathrm{T}} < 60\,\mathrm{GeV}$), or ($|\eta| < 2.4$, $20\,\mathrm{GeV} < p_{\mathrm{T}} < 60\,\mathrm{GeV}$, JVT score > 0.59).

ID track: all ID tracks from the hard-scatter vertex passing reconstruction quality and kinematic selections and not associated with e, τ_{had}, μ. ID tracks are required to have $p_{\mathrm{T}} > 400\,\mathrm{MeV}$, $|d_0| < 1.5\,\mathrm{mm}$, $|z_0 \sin(\theta)| < 1.5\,\mathrm{mm}$, $\Delta R(\mathrm{track}, e/\gamma\mathrm{cluster}) > 0.05$, $\Delta R(\mathrm{track}, \tau_{\mathrm{had}}) > 0.2$.

4.6 Derivation Framework

After the simulation and reconstruction are done, the results are written to disk in an Analysis Object Data (AOD) format for the measured data and simulated events. AODs contain lots of information and thus take up a lot of disk space, making them cumbersome to use in day-to-day analysis, where people run over their data samples frequently to optimise their analysis. The ATLAS *Derivation framework* [198] takes the petabyte-scale AOD output from the ATLAS reconstruction of real and simulated data, and reduces its size to a few terabytes, starting from Run 2 on, by introducing the following steps which are also schematically presented in Figure 4.11:

- **skimming:** removal of whole events based on preset criteria,
- **thinning:** removal of whole objects within events based on preset criteria,
- **slimming:** removal of variables within objects uniformly across events,
- **augmentation:** addition of new containers or variables of reconstructed objects.

Athena produces a new ROOT-readable format (xAOD) directly from the reconstruction step. Then, the derivation framework generates the intermediate layer from the xAOD by removing (or adding) information whilst maintaining the structure used in the original xAOD. The outputs, so-called *Derived xAODs* (DxAOD), contain final combined performance corrections, are easily configured and can be highly optimised to target specific analyses while minimising disk requirements. A given derived format usually takes around 1% (or less) of the xAOD's

[4] The overlap with muons is also considered and thoroughly described in Ref. [197].

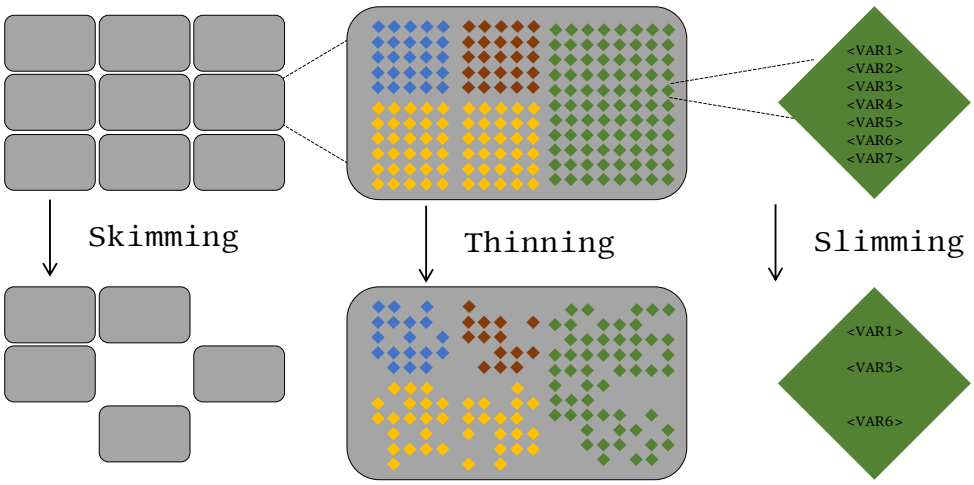

Figure 4.11: A visual representation of the ATLAS derivation framework showing the three standard operations to reduce xAOD file size and produce user-friendly DxAOD. The grey rectangles represent events, and different coloured diamonds represent different physics objects that contain information about several quantities, depicted as ⟨VAR⟩.

volume. Furthermore, the production of DxAODs is done centrally, which offloads lots of work from the individual analysers.

In the work presented in this thesis, three different kinds of derivation are used:

EXOT12: two-lepton events, regardless of their flavour or charge, are selected if individual lepton satisfies the $p_{\mathrm{T}} > 20\,\mathrm{GeV}$ requirement. Electrons (muons) must pass the `Loose` (`CB`) identification requirement. This derivation is used in the Doubly charged Higgs search, presented in Part III.

EXOT19/22: at least one light lepton with $p_{\mathrm{T}} > 20\,\mathrm{GeV}$ is required that passes the `Loose` (electron) or `Combined` (muon) identification requirement. This derivation is used in the fake lepton estimation, detailed in Section 6.2.

Part III

SEARCH FOR DOUBLY CHARGED HIGGS BOSON PRODUCTION IN MULTI-LEPTON FINAL STATES

CHAPTER 5
Analysis Strategy

A search for pair production of doubly charged Higgs bosons, ($H^{\pm\pm}$), each decaying into a pair of prompt, isolated, highly energetic leptons with the same electric charge, is presented in the following chapters. The signal is searched for in the data collected by the ATLAS detector at $\sqrt{s} = 13\,\text{TeV}$, using the total integrated luminosity of 139 fb^{-1} from Run 2 of the LHC. This chapter defines the analysis objects, describes the event selection, and outlines the analysis strategy.

5.1 Introduction

As presented in Section 1.2.4, the dominant $H^{\pm\pm}$ production mechanism is pair production via the Drell–Yan process. An analysis can detect this kind of signal by searching for its leptonic decays, $H^{\pm\pm} \to \ell^{\pm}\ell'^{\pm}$, resulting in same-charge lepton pairs in final states with two, three or four leptons. The two and three lepton categories are necessary to retrieve events in which a fourth lepton is lost due to selection acceptance. An example of invariant mass distribution of same-charge electron pairs in the simulated sample for different $H^{\pm\pm}$ mass hypotheses is shown in Figure 5.1.

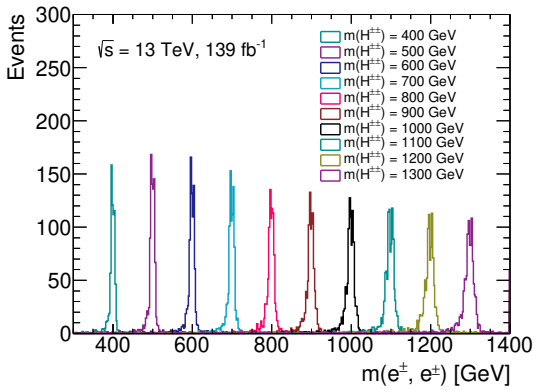

Figure 5.1: Invariant mass distribution of same-charge electron pairs in the simulated $pp \to H^{++}H^{--}$ sample is shown, where only events containing exactly two leptons are selected.

Highly energetic, same-charge lepton pairs represent a striking signature for BSM physics since such events are produced rarely in proton–proton collisions by SM processes. The SM background events differ from signal ones both in topology and their impact across the analysis regions. Events containing two leptons predominantly originate from SM Drell–Yan processes with wrongly identified charges, while background events with three or four leptons are mostly diboson events. The analysis only considers light leptons, i.e. electrons and muons, in the two-, three- and four-lepton final states, thereby including leptonic τ decays. Branching ratios to each of the possible leptonic final states, $\mathcal{B}(H^{\pm\pm} \to e^{\pm}e^{\pm}) = \mathcal{B}(H^{\pm\pm} \to e^{\pm}\mu^{\pm}) = \mathcal{B}(H^{\pm\pm} \to$

$\mu^\pm\mu^\pm) = \mathcal{B}(H^{\pm\pm} \to e^\pm\tau^\pm) = \mathcal{B}(H^{\pm\pm} \to \mu^\pm\tau^\pm) = \mathcal{B}(H^{\pm\pm} \to \tau^\pm\tau^\pm) = 1/6$, are assumed equal. To estimate the compatibility of the data with the SM expectations, as well as to extract upper limits on the $H^{\pm\pm}$ mass at a 95% confidence level (CL), a binned maximum-likelihood fit to data, described in Chapter 8, is performed. A simultaneous fit to the distribution of the invariant mass of the two same-charge light leptons with the highest p_{T} in the event, $m(\ell^\pm\ell'^\pm)_{\mathrm{lead}}$, is implemented in the two- and three-lepton regions, while a single-bin event yield is used in the four-lepton ones, merging two-lepton channels to obtain the best sensitivity.

Events are selected with a *cut-based* method, where the selection requirements on kinematic variables are chosen orthogonally. Then, preliminary studies were conducted to improve results with the *machine-learning* techniques, where a functional selection dependence on a combination of observables is implemented. The object definitions, presented in Section 5.3, are the same for both approaches. On the other hand, the analysis regions were optimised for each method individually. The results of a cut-based approach were published in Ref. [199].

5.2 Event Selection

Three distinct types of regions are defined in this search: *control regions* (CR), *validation regions* (VR), and *signal regions* (SR). The normalisation factors of the dominant backgrounds are treated as free parameters in the likelihood fit and are constrained by the control regions. Validation regions are used to cross-check the background modelling but are not included in the fit. Both the control regions and validation regions are intended to be close to the kinematic region of the expected signal but must be constructed in a way to allow only negligible signal contamination. The CRs and VRs are defined using selections orthogonal to the SRs. Signal regions are parts of phase space where a signal model predicts a significant excess of events over the expected background level. A convenient procedure called *blinding* is often considered while maximising the signal significance and optimising SRs. It is intended to avoid biasing the physics results by not looking at the measured data in the SRs until a satisfactory agreement is found between normalised background predictions and observed data in the CRs and VRs. A signal significance [32, 200] is defined as

$$\mathcal{S} = \sqrt{2\left((s+b)\ln\left(1+\frac{s}{b}\right)-s\right)}. \tag{5.1}$$

Here, s and b are the total yields of the expected signal and background events, respectively. The Eq. 5.1 reduces to $s/\sqrt{b}$ in the $s \ll b$ limit.

Events selected for analysis are required to pass standard ATLAS data-quality requirements described in Ref. [201]. Events must contain at least one reconstructed primary vertex with at least two associated tracks, each having p_{T} greater than 500 MeV, to reduce non-collision backgrounds originating from beam-halo events and cosmic rays. Among all vertices in the event, the one with the highest sum of squared p_{T} of the associated tracks is identified as the primary vertex. Events that contain jets must also satisfy the quality criteria described in Ref. [202].

Events were collected using two-lepton triggers that select pairs of electrons [111], muons [112] or electron–muon combinations [111] without online isolation applied. The p_{T} thresholds of the unprescaled two-lepton triggers were raised during Run 2 because of the increasing luminosity of the colliding beams but were never higher than 24 GeV (24 GeV) for the (sub-)leading electron and 22 GeV (14 GeV) for the (sub-)leading muon. Low p_{T} thresholds are essential to ensure looser trigger requirements than the identification and isolation requirements of electrons and muons, which could otherwise lead to trigger bias. A summary of the unprescaled triggers used in the analysis is presented in Table 5.1.

Table 5.1: A summary of unprescaled two-lepton triggers used in the analysis, specific for each data-taking year, is shown. The lepton p_{T} threshold in GeV is encoded in the trigger name as the number after the "e" and "mu" characters for electrons and muons, respectively.

	2015	2016	2017 and 2018
ee	HLT_2e12_lhloose_L12EM10VH	HLT_2e17_lhvloose_nod0	HLT_2e17_lhvloose_nod0 or HLT_2e24_lhvloose_nod0
$e\mu$	HLT_e17_lhloose_mu14	HLT_e17_lhloose_nod0_mu14	
$\mu\mu$	HLT_mu18_mu8noL1	HLT_mu22_mu8noL1	

The baseline event selection requires at least two light leptons to be identified as Tight, as described in Section 4.2. Events with at least one b-tagged jet are vetoed in all regions to suppress background events arising from top-quark decays. In regions with more than two leptons, the so-called Z-veto condition is required, i.e. events containing same-flavour lepton pairs having invariant masses within 20 GeV of the Z-boson mass, $71.2\,\mathrm{GeV} < m(\ell,\ell) < 111.2\,\mathrm{GeV}$, are rejected in order to suppress events featuring a Z boson in the final state. The Z-veto is not applied in four-lepton control and validation regions to increase the number of simulated diboson events.

The analysis is sensitive to final states with three different lepton multiplicities. Therefore, regions are optimised to search for one same-charge lepton pair in the case of regions requiring two or three leptons, while four-lepton events must feature two same-charge pairs with zero total sum of charges. Two control regions are defined to constrain major Drell–Yan (DYCR) and diboson (DBCR2L) backgrounds in the two-lepton channel, while a single control region suffices for each of the three- (DBCR3L) or four-lepton (DBCR4L) channels. Similarly, one SR (VR) per lepton multiplicity is constructed - SR2L, SR3L, and SR4L (VR2L, VR3L, and VR4L). The $m(\ell^{\pm}\ell'^{\pm})_{\mathrm{lead}}$ is the principal variable to distinguish control, validation, and signal regions. Due to low available statistics in three- and four-lepton channels, only two-lepton ones are further split into all possible flavour arrangements, with different selections applied for each flavour combination.

5.3 Object Definitions

Physics object definitions are chosen based on different studies to obtain the highest analysis sensitivity by compromising between reaching high reconstruction efficiencies and removing

too much of the expected signal. Two types of lepton definitions, LOOSE and TIGHT, are needed for the data-driven method implemented in the analysis. Leptons selected in the TIGHT category are estimated using Monte Carlo samples and predominantly consist of prompt leptons originating from prompt leptonic τ decays or decays of Z, W, and H bosons. LOOSE leptons are mostly non-prompt and misidentified leptons used for reducible background estimation, presented in Section 6. Lepton definitions described in the following three paragraphs correspond to the TIGHT category, and the corresponding selection is referred to as *baseline event selection*. Tables 5.2 and 5.3 summarise the selection criteria for electrons and muons, respectively.

Electron candidates are reconstructed using an electromagnetic calorimeter and ID information to match an isolated calorimeter energy deposit to a charged-particle track. They are required to stay within the fiducial volume of the inner detector, $|\eta| < 2.47$, and have transverse momenta $p_{\mathrm{T}} > 40\,\mathrm{GeV}$. Moreover, electrons must pass at least the `Tight` identification level, introduced in Section 4.2, which relies on track and calorimeter energy cluster information. Electron candidates within the transition region ($1.37 < |\eta| < 1.52$), i.e. between the barrel and endcap electromagnetic calorimeters, are not considered in the analysis because their reconstruction quality is degraded. The track associated with the electron candidate must have a transverse impact parameter d_0 that, evaluated at the point of closest approach of the track to the beam axis in the transverse plane, satisfies $|d_0|/\sigma(d_0) < 5$, where $\sigma(d_0)$ is the uncertainty on d_0. In addition, the longitudinal distance z_0 from the primary vertex to the point where d_0 is measured must satisfy $|z_0 \sin(\theta)| < 0.5\,\mathrm{mm}$, where θ is the polar angle of the track. Electron candidates must also fulfil the `Loose` isolation requirement, which uses calorimeter-based and track-based isolation criteria that reach an efficiency of about 99%. Electron candidates are discarded if their angular distance from a jet lies between $0.2 < \Delta R < 0.4$. If $\Delta R(e, j) < 0.2$, a jet is rejected.

A dedicated machine-learning algorithm (BDT) is applied to reject electrons with incorrectly identified charges [179]. A selection requirement on the BDT output is chosen to achieve a rejection factor between 7 and 10 for electrons having a wrong charge assignment while selecting properly measured electrons with an efficiency of 97%.

Table 5.2: Object definitions requirements for TIGHT (left) and LOOSE (right) electrons. Note that LOOSE electrons can either satisfy `Loose` identification, fail `Loose` isolation requirements, or both.

Requirement	**Signal electrons (TIGHT)**	**Background electrons (LOOSE)**
Identification	`Tight`	`Loose` or
Isolation	`Loose`	fail `Loose` selection
p_{T} cut	$p_{\mathrm{T}} > 40\,\mathrm{GeV}$	$p_{\mathrm{T}} > 40\,\mathrm{GeV}$
η cut	$\lvert\eta\rvert < 2.47$ and veto $1.37 < \lvert\eta\rvert < 1.52$	$\lvert\eta\rvert < 2.47$ and veto $1.37 < \lvert\eta\rvert < 1.52$
$\lvert d_0\rvert/\sigma_{d_0}$ cut	$\lvert d_0\rvert/\sigma_{d_0} < 5.0$	$\lvert d_0\rvert/\sigma_{d_0} < 5.0$
$\lvert z_0 \sin(\theta)\rvert$ cut	$\lvert z_0 \sin(\theta)\rvert < 0.5\,\mathrm{mm}$	$\lvert z_0 \sin(\theta)\rvert < 0.5\,\mathrm{mm}$
Bad cluster veto	yes	yes

Muon candidates are reconstructed by matching tracks from the muon spectrometer and inner detector. The candidates must have $p_{\mathrm{T}} > 40\,\mathrm{GeV}$, $|\eta| < 2.5$, and satisfy the impact parameter requirements $|d_0|/\sigma(d_0) < 3$ and $|z_0 \sin(\theta)| < 0.5\,\mathrm{mm}$. If a muon candidate has a p_{T} higher

than 300 GeV, it must fulfil a special High-p_T muon quality requirement. Otherwise, the Medium quality requirement is used. The muon candidates must also meet the track-based FixedCutTightTrackOnly isolation requirement. If a muon and a jet featuring more than three tracks lie $\Delta R < 0.4$ apart and the muon's transverse momentum is less than half of the jet's p_T, the muon is discarded. Furthermore, a muon candidate that deposits a sufficiently large fraction of its energy in the calorimeter is rejected if it also shares a reconstructed ID track with an electron.

Table 5.3: Object definitions requirements for TIGHT (left) and LOOSE (right) muons. The only difference is in the muon isolation requirement.

Requirement	Signal muons (TIGHT)	Background muons (LOOSE)
Quality	High-p_T if $p_T > 300$ GeV else Medium	High-p_T if $p_T > 300$ GeV else Medium
Isolation	FixedCutTightTrackOnly	fail FixedCutTightTrackOnly
p_T cut	$p_T > 40$ GeV	$p_T > 40$ GeV
η cut	$\lvert\eta\rvert < 2.5$	$\lvert\eta\rvert < 2.5$
$\lvert d_0\rvert/\sigma_{d_0}$ cut	$\lvert d_0\rvert/\sigma_{d_0} < 3.0$	$\lvert d_0\rvert/\sigma_{d_0} < 3.0$
$\lvert z_0 \sin(\theta)\rvert$ cut	$\lvert z_0 \sin(\theta)\rvert < 0.5$ mm	$\lvert z_0 \sin(\theta)\rvert < 0.5$ mm
Bad muon veto	yes	yes

Jets are reconstructed using an anti-k_t algorithm with a radius parameter $R = 0.4$, as described in Section 4.4. A Medium JVT working point with an average efficiency of 92% is used for jets with $p_T < 60$ GeV and $|\eta| < 2.4$ to help reject additional jets produced by pile-up.

Jets considered in this analysis must have $p_T > 20$ GeV and $|\eta| < 2.5$. Jets within $\Delta R = 0.2$ of an electron are removed. Furthermore, jets within $\Delta R = 0.2$ of a muon and having fewer than three tracks or having $p_T^{\mu}/p_T^{\text{jet}} > 0.5$ are also discarded. Events containing b-jets are vetoed to reduce the fake background. They are identified with a DL1r b-tagging algorithm using a working point that provides a b-tagging efficiency of 77%. The working point provides rejection factors of roughly 250 and 6 for light-flavour jets and c-jets, respectively, with slight p_T and η dependence.

5.4 Cut-Based Analysis Strategy and Selection

The signal regions, independently of the lepton multiplicity and flavour combination, require invariant masses of the same-charge leading lepton pair to be above 300 GeV. Additional requirements, regardless of the flavour, are imposed on same-charge lepton pairs to maximise the sensitivity. These exploit both the boosted decay topology of the $H^{\pm\pm}$ resonance and the high energy of the decay products. The same-charge lepton angular separation in the two-lepton signal region (SR2L) is required to be $\Delta R(\ell^{\pm}, \ell'^{\pm}) < 3.5$. Furthermore, the vector sum of the two leading leptons' transverse momenta, $p_T(\ell^{\pm}\ell'^{\pm})_{\text{lead}}$, must exceed 300 GeV in both two-lepton and three-lepton (SR3L) signal regions. In the four-lepton signal region (SR4L), the signal significance is increased by requiring the average invariant mass of the two same-charge lepton pairs to satisfy $\overline{m}_{\text{SC}} = (m_{\ell^+\ell'^+} + m_{\ell^-\ell'^-})/2 > 300$ GeV.

The efficiency for signal events to pass the signal region selections depends on the signal mass and the flavour combination of the leptons in the final states. For the benchmark $H^{\pm\pm}$ masses, the efficiencies range between 10% and 20% in the two-lepton signal regions, while the typical efficiencies in the three- and four-lepton ones vary from 30% to 40%. Generally, the efficiencies increase with the $H^{\pm\pm}$ mass. In the two-lepton regions, the efficiencies are highest for the $e\mu$, lower for the ee and lowest for the $\mu\mu$ channels, which is an effect of the two-lepton triggers used in the search.

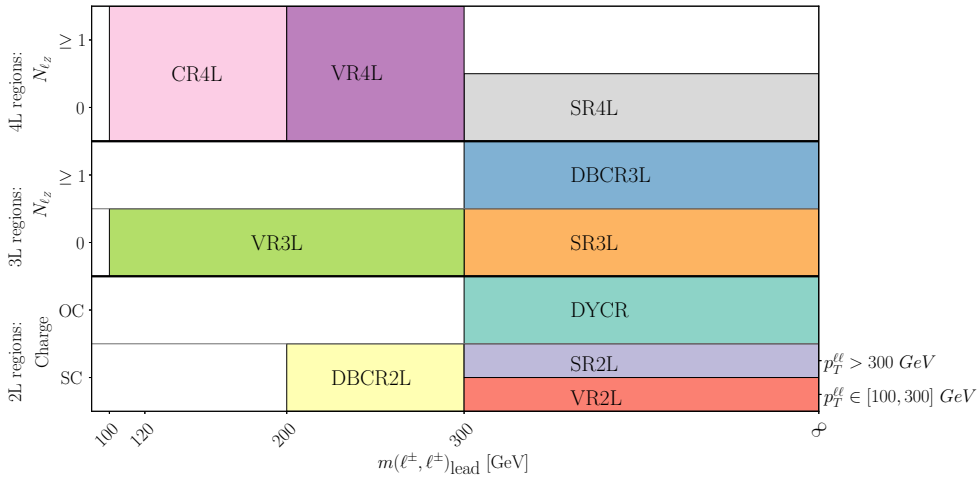

Figure 5.2: A schematic representation of cut-based SR2L, SR3L, SR4L and relative control and validation regions to show their orthogonality. The SC and OC stand for the same and opposite charge, respectively, and the N_{ℓ_Z} stands for the number of lepton candidates originating from a Z boson.

The following control and validation regions either span a lower $m(\ell^\pm\ell'^\pm)_{\text{lead}}$ interval or require other orthogonal selections if the same $m(\ell^\pm\ell'^\pm)_{\text{lead}}$ window as in the signal regions is used.

Firstly, the two-lepton diboson control region (DBCR2L) is defined to constrain the dominant diboson contribution in the same-charge two-lepton final states and spans a $m(\ell^\pm\ell'^\pm)_{\text{lead}} \in [200,\ 300)$ GeV range. A significant Drell–Yan event yield was observed in the ee channel, so additional selections on $E_{\text{T}}^{\text{miss}}$ and the pseudorapidity of the same-charge lepton pair, $|\eta(\ell^\pm, \ell'^\pm)|$, are required to suppress the Drell–Yan background specifically. The Drell–Yan background is further constrained by the opposite-charge Drell–Yan control region (DYCR), where precisely two electrons with opposite charges are required. Since it is designed to target only opposite-charge electron pairs, the invariant mass of the opposite-charge electron pair is required to be $m(e^\pm, e^\mp)_{\text{lead}} > 300$ GeV and is also used as the fit variable. Then, the three-lepton diboson control region (DBCR3L) is used to constrain the diboson background yield independently of the flavour combination. Since the $m(\ell^\pm\ell'^\pm)_{\text{lead}}$ requirement is the same as in the corresponding three-lepton signal region, at least one Z-boson candidate is required to achieve orthogonality. Finally, the four-lepton control region (CR4L) is used to constrain the yield of the dominant diboson background in four-lepton regions, where $m(\ell^\pm\ell'^\pm)_{\text{lead}}$ is restricted to be between 100 GeV and 200 GeV. The signal contamination in all control regions is negligible.

The two-lepton validation region (VR2L) is used to validate the data-driven fake-lepton back-

ground estimation and to assess the diboson modelling in the two-lepton channel. The $m(\ell^{\pm}\ell'^{\pm})_{\text{lead}}$ selection is the same as in the SR2L, thus requiring an inverted $p_{\text{T}}(\ell^{\pm}\ell'^{\pm})_{\text{lead}}$ cut relative to the corresponding signal region. Similarly to the DBCR2L, additional requirements on $E_{\text{T}}^{\text{miss}}$ and $|\eta(\ell^{\pm}, \ell'^{\pm})|$ are imposed only in the ee channel to reject the Drell–Yan contribution. The three-lepton validation region (VR3L) is used to validate the diboson and fake-lepton backgrounds with three reconstructed leptons in the final states. The $m(\ell^{\pm}\ell'^{\pm})_{\text{lead}}$ value is required to be within the interval of $[100,\ 300)$ GeV. Additionally, a Z-veto condition is applied. The four-lepton validation region (VR4L) is used to validate the diboson modelling in the four-lepton region and is defined by the $200\,\text{GeV} < m(\ell^{\pm}\ell'^{\pm})_{\text{lead}} < 300\,\text{GeV}$ requirement. The signal yield does not exceed a few per cent of the background yield in any validation region.

The selection criteria for each region defined in the cut-based analysis are summarised in Table 5.4 and schematically presented in Figure 5.2.

Table 5.4: Summary of regions defined in the cut-based analysis approach. The table is split into four horizontal blocks: the upper block indicates the final states, the second block lists the lepton multiplicities, the third block indicates the mass range of the corresponding final state, and the lower block indicates the event selection criteria for the region. The application of a selection requirement is labelled by a checkmark (✓) or by *inverted* when it is inverted. The three- and four-lepton regions include all light-lepton flavour combinations. No selection is applied when a dash is present in the corresponding cell. A requirement on the average invariant mass of the two same-charge lepton pairs, $\overline{m}_{\text{SC}} \equiv (m_{\ell^+\ell'^+} + m_{\ell^-\ell'^-})/2$, is defined to increase the signal significance in the four-lepton signal region. Additionally, b-jet veto is applied in all regions.

	Control regions				**Signal regions**			**Validation regions**		
	DYCR	DBCR2L	DBCR3L	CR4L	SR2L	SR3L	SR4L	VR2L	VR3L	VR4L
Channel	e^+e^-	$e^{\pm}e^{\pm}$ $e^{\pm}\mu^{\pm}$ $\mu^{\pm}\mu^{\pm}$	$\ell^{\pm}\ell^{\pm}\ell^{\mp}$	$\ell^+\ell^+\ell^-\ell^-$	$e^{\pm}e^{\pm}$ $e^{\pm}\mu^{\pm}$ $\mu^{\pm}\mu^{\pm}$	$\ell^{\pm}\ell^{\pm}\ell^{\mp}$	$\ell^+\ell^+\ell^-\ell^-$	$e^{\pm}e^{\pm}$ $e^{\pm}\mu^{\pm}$ $\mu^{\pm}\mu^{\pm}$	$\ell^{\pm}\ell^{\pm}\ell^{\mp}$	$\ell^+\ell^+\ell^-\ell^-$
Number of leptons	2	2	3	4	2	3	4	2	3	4
$m(\ell^{\pm}, \ell'^{\mp})_{\text{lead}}$ [GeV]	≥ 300	-	-	-	-	-	-	-	-	-
$m(\ell^{\pm}\ell'^{\pm})_{\text{lead}}$ [GeV]	-	$[200,\ 300)$	≥ 300	$[100,\ 200)$	≥ 300	≥ 300	≥ 300	≥ 300	$[100,\ 300)$	$[200,\ 300)$
$p_{\text{T}}(\ell^{\pm}\ell'^{\pm})_{\text{lead}}$ [GeV]	-	-	-	-	≥ 300	≥ 300	-	$[200,\ 300)$	-	-
$\Delta R(\ell^{\pm}\ell'^{\pm})_{\text{lead}}$	-	-	-	-	< 3.5	-	-	< 3.5	-	-
$\overline{m}_{\text{SC}}$ [GeV]	-	-	-	-	-	-	≥ 300	-	-	-
$E_{\text{T}}^{\text{miss}}$ [GeV]	-	> 30 -	-	-	-	-	-	> 30 -	-	-
$\lvert\eta(\ell, \ell')\rvert$	-	< 3.0 -	-	-	-	-	-	< 3.0 -	-	-
Z-boson veto	-	-	inverted	-	-	✓	✓	-	✓	-

The region definitions are optimised considering the so-called $N-1$ studies to increase the signal significance defined in Eq. 5.1. The $N-1$ plots are a series of distributions where one of all applied cuts in a region is consecutively switched off, and the impact of that specific cut on the variable under inspection is studied. The $N-1$ distributions representing the most significant cuts in two-, three- and four-lepton signal regions of the cut-based analysis are shown in Figures 5.3–5.5.

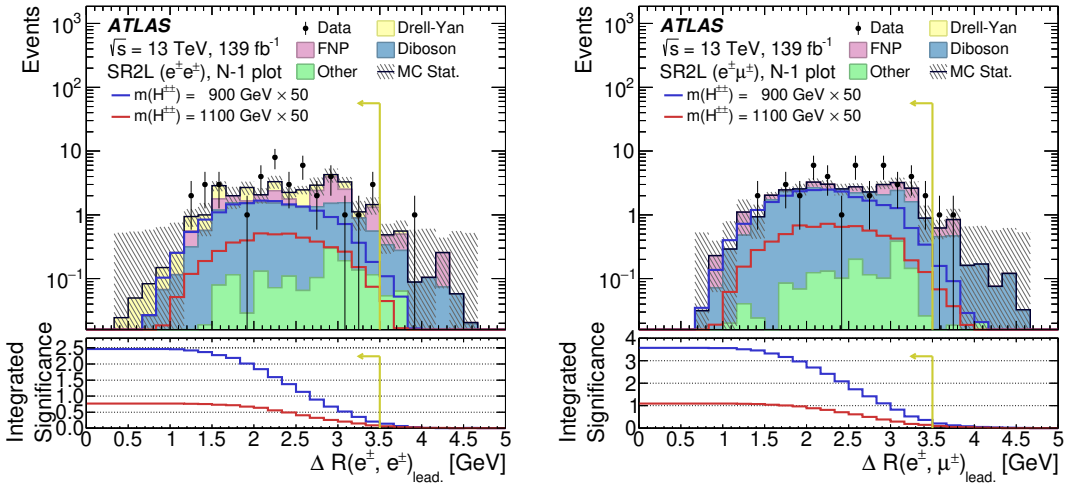

(a)

(b)

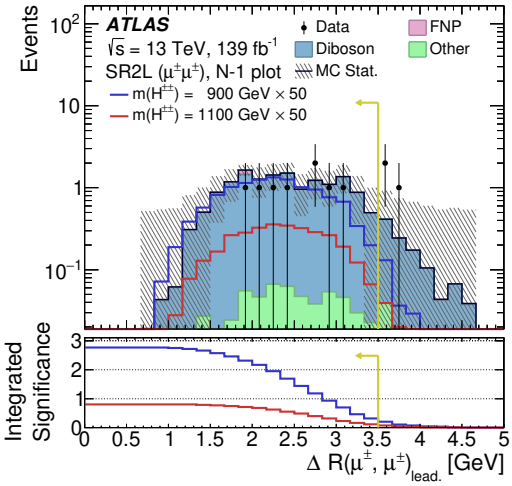

(c)

Figure 5.3: Distributions of $\Delta R(\ell^{\pm}\ell'^{\pm})_{\text{lead}}$ in the two-lepton signal regions (SR2L) of the cut-based analysis, namely (a) the electron–electron two-lepton signal region, (b) the electron–muon two-lepton signal region, and (c) the muon–muon two-lepton signal region, before the $\Delta R(\ell^{\pm}\ell'^{\pm})_{\text{lead}} < 3.5$ cut. The yellow arrows indicate the cut and the selected $\Delta R(\ell^{\pm}\ell'^{\pm})_{\text{lead}}$ interval. The integrated significance represents the cumulative bin significance as defined in Eq. 5.1. The hatched band indicates the statistical uncertainties.

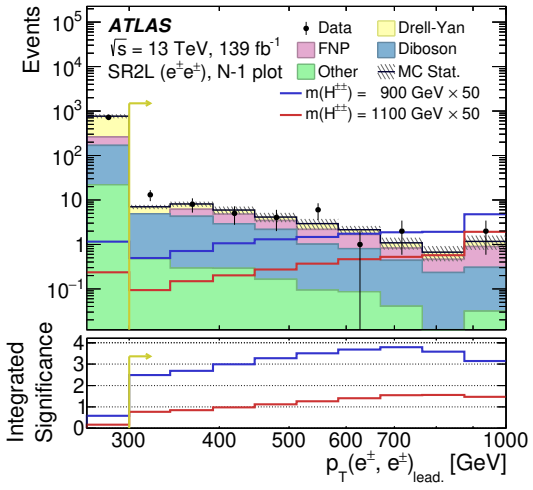

(a)

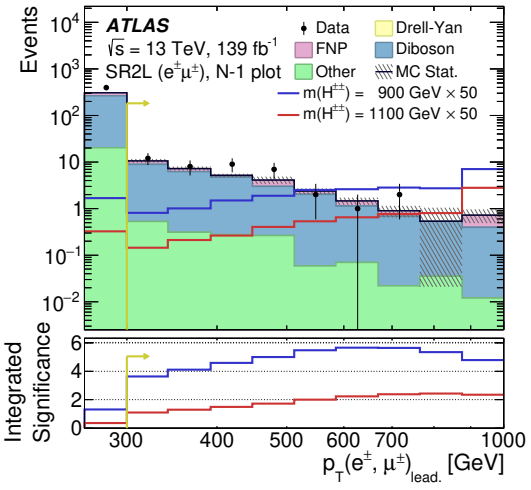

(b)

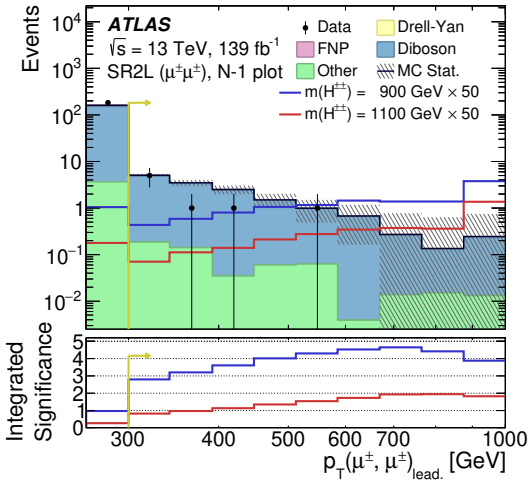

(c)

Figure 5.4: Distributions of $p_{\mathrm{T}}(\ell^{\pm}\ell'^{\pm})_{\mathrm{lead}}$ in the two-lepton signal regions (SR2L) of the cut-based analysis, namely (a) the electron–electron two-lepton signal region, (b) the electron–muon two-lepton signal region, and (c) the muon–muon two-lepton signal region, before the $p_{\mathrm{T}}(\ell^{\pm}\ell'^{\pm})_{\mathrm{lead}} > 300$ GeV cut. The yellow arrows indicate the cut and the selected $p_{\mathrm{T}}(\ell^{\pm}\ell'^{\pm})_{\mathrm{lead}}$ interval. The integrated significance represents the cumulative bin significance as defined in Eq. 5.1. The hatched band indicates the statistical uncertainties.

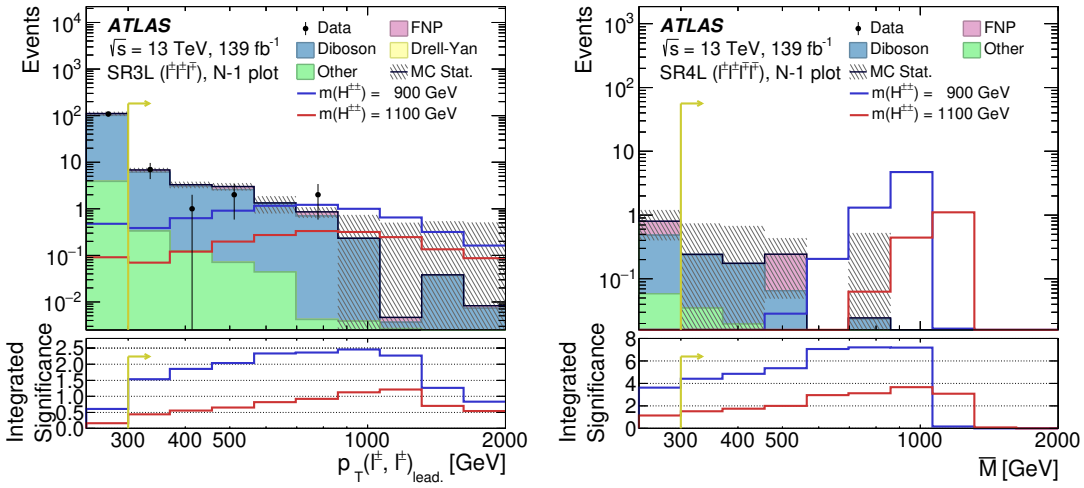

(a) (b)

Figure 5.5: Distributions of (a) $p_{\mathrm{T}}(\ell^{\pm}\ell'^{\pm})_{\mathrm{lead}}$ in three- and (b) $\overline{m}_{\mathrm{SC}}$ in four-lepton signal regions of the cut-based analysis before the $p_{\mathrm{T}}(\ell^{\pm}\ell'^{\pm})_{\mathrm{lead}} > 300\,\mathrm{GeV}$ and $\overline{m}_{\mathrm{SC}} > 300\,\mathrm{GeV}$ cuts, respectively. The yellow arrows indicate the cut and the selected $p_{\mathrm{T}}(\ell^{\pm}\ell'^{\pm})_{\mathrm{lead}}$ and $\overline{m}_{\mathrm{SC}}$ intervals. The integrated significance represents the cumulative bin significance as defined in Eq. 5.1. The hatched band indicates the statistical uncertainties.

CHAPTER 6

Background Estimation

Background estimation techniques are described in this Chapter. Different lepton multiplicities and flavour channels in the presented analysis have different background compositions and thus require multiple various treatments. Firstly, the charge misidentification probability estimation is presented in Section 6.1 then the fake lepton background measurements are outlined in Section 6.2.

Backgrounds are categorised into irreducible and reducible types, depending on their source. The former category is derived from MC simulation and the latter with data-driven methods.

Irreducible background sources are SM processes producing the same prompt final-state lepton pairs as the signal, with the dominant contributions in this analysis coming from diboson production. These prompt SM backgrounds are estimated using the simulated samples listed in Section 3.3. The final diboson and Drell–Yan MC sample normalisations are not taken as obtained from MC simulation but are left floating in the simultaneous likelihood fit to the data in dedicated control regions, as described in Chapter 7.

Events containing leptons whose charges were incorrectly assigned are sources of reducible background. An example of this type of background is the Drell–Yan background, where the contribution is normalised in the DYCR, then reweighted for the charge misidentification probability and finally used to predict yields in the same-charge selections. Electrons are the only significant source of charge misidentification. Muons are much heavier and do not lose energy to bremsstrahlung as rapidly as electrons. Additionally, their tracks are measured both in ID and MS, which provides a larger lever arm for the curvature measurement and, consequently, charge reconstruction. Since the modelling of charge misidentification does not match very well between data and MC simulation, scale factors are derived using data-driven techniques, presented in Section 6.1.

Processes where reconstructed leptons originate from mis-reconstructed objects such as jets, from light- or heavy-quark decays or, in the electron case, from photon conversions also enter the reducible background category. These types of events thus contain at least one fake or non-prompt lepton and are not estimated from MC simulation due to the large intrinsic uncertainties in the hadronisation and jet simulation. Therefore, a data-driven approach presented in Section 6.2 is needed to evaluate their contribution from $W+$ jets, $t\bar{t}$ and multi-jet events.

Events from the MC background samples are only considered if reconstructed leptons are matched to their prompt generator-level counterparts to avoid overlap between the irreducible backgrounds estimated using MC simulation and the data-driven reducible ones.

6.1 Electron Charge Misidentification

Electrons passing the detector material are subjected to bremsstrahlung which is a dominant source of charge misidentification and leads to *trident events* and *stiff tracks*. The photon, emitted when an electron loses its energy, can either convert to an electron–positron pair due to the interactions with the detector material (trident events, $e^{\pm} \longrightarrow e^{\pm}\gamma^{*} \longrightarrow e^{\pm}e^{+}e^{-}$) or pass through the inner detector without leaving any tracks (stiff tracks). The calorimeter energy cluster, corresponding to the initial electron, can be matched to the positron track or assigned to the pair-produced electron in the first case. An example of a trident event is depicted in Figure 6.1. On the other hand, stiff tracks arise when the photon does not convert into an electron–positron

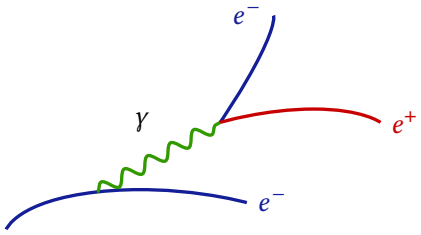

Figure 6.1: A sketch of a trident event, where an initial electron loses energy via bremsstrahlung. The emitted photon converts into an electron–positron pair.

pair, so the electron usually leaves very few hits inside the ID, making curvature determination challenging. Fortunately, the energy of an electron is correctly reconstructed in this case as the photon similarly deposits its energy as would the electron inside the EM calorimeter. Since electron charges are determined from track curvatures, they are likely to be incorrectly resolved for highly energetic and very forward electrons as their tracks inside ID are almost straight.

A detailed detector description and accurate modelling of the particle–detector interactions are needed to provide sufficiently precise simulations of charge misidentification. However, such GEANT4 simulations still deviate from data, so data-driven measurements are performed. The mis-modelling is corrected by introducing p_{T} and η dependent scale factors obtained from a likelihood fit on a specific $Z \longrightarrow ee$ data sample [179]. Scale factors are then applied to the simulated background events to improve the agreement between data and simulation. Electron pairs from the Z boson peak are grouped into opposite-charge (OC) and same-charge (SC) categories, while electrons originating from other processes are estimated with simulations and subtracted from the observed data. The OC and SC yields, N_{OC}^{ij} and N_{SC}^{ij}, respectively, are split into central and sideband regions and are subsequently used as input to the fit. The probability of observing N_{SC}^{ij} same-charge pairs follows a Poissonian distribution

$$f(N_{\mathrm{SC}}^{ij};\lambda) = \frac{\lambda^{N_{\mathrm{SC}}^{ij}} e^{-\lambda}}{N_{\mathrm{SC}}^{ij}!}, \tag{6.1}$$

where N_{SC}^{ij} is the measured number of SC pairs, $\lambda = N^{ij}\left(p_i\left(1-p_j\right) + p_j\left(1-p_j\right)\right)$ is the expected number of SC pairs in the ij-th bin, and i and j are the two electrons from the pair. The p_i

and p_j are the charge misidentification probabilities. The log-likelihood is defined as

$$-\log L(\boldsymbol{p}\,|\boldsymbol{N}_{\mathrm{SC}}, \boldsymbol{N}) = \sum_{ij} \log\left[N^{ij}\left(p_i\left(1-p_j\right)+p_j\left(1-p_i\right)\right)\right] N_{\mathrm{SC}}^{ij} - N^{ij}\left[p_i\left(1-p_j\right)+p_j\left(1-p_i\right)\right]. \tag{6.2}$$

The scale factors (SF) are defined as

- correctly reconstructed charge: $\mathrm{SF} = \frac{1-p(p_{\mathrm{T}},\,\eta;\,\mathrm{data})}{1-p(p_{\mathrm{T}},\,\eta;\,\mathrm{MC})}$,
- wrongly reconstructed charge: $\mathrm{SF} = \frac{p(p_{\mathrm{T}},\,\eta;\,\mathrm{data})}{p(p_{\mathrm{T}},\,\eta;\,\mathrm{MC})}$.

The SC and OC Z boson peaks are presented in Figure 6.2. The Z boson peak for SC pairs is slightly broader and shifted towards lower values ($\sim$ 2 GeV), mainly due to bremsstrahlung energy losses.

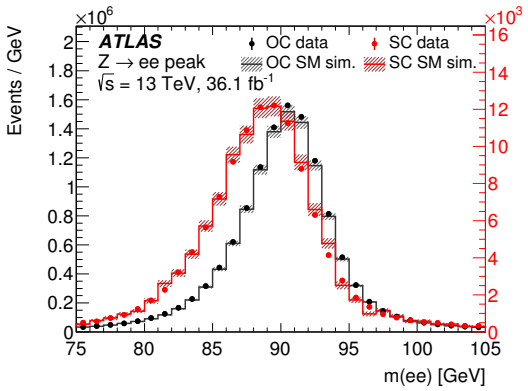

Figure 6.2: The two-electron SC (red) and OC (black) invariant mass distributions for data (filled markers) and MC simulation (solid line), which includes a correction for charge misidentification, are shown. Statistical uncertainties are indicated by a hatched band. Taken from Ref. [77].

6.2 Fake and Non-Prompt Lepton Estimation

An event with a final state which would ideally not pass the selection criteria of a specific signal region, can sometimes still be accepted due to particles from secondary decays being incorrectly reconstructed as they would originate from the IP (*non-prompt leptons*) or physics objects such as hadronic jets being falsely reconstructed as leptons (*fake leptons*). Collectively, such events are referred to as the *fake/non-prompt* (FNP) background.

Non-prompt leptons arise from semileptonic decays of hadrons containing $c-$ or b-quarks, e.g. a b-hadron, which is produced in the IP decays into light quarks in a secondary vertex. Electrons and muons from secondary decay closely mimic leptons originating directly from the IP. They are true leptons but do not originate from the primary vertex. Hence, their name is non-prompt leptons.

An additional background component is represented by fake electrons, which are mainly hadronic jets being incorrectly reconstructed as leptons. A charged component of a jet can cause a similar detector response in the ID and EM calorimeter as would the charged, prompt electron. When some ID tracking information is lost, a jet can be identified as an electron.

Backgrounds are usually estimated using MC simulation, as described in Chapter 3. However, a data-driven technique is implemented to describe incorrect identification in the FNP events due to difficulties in precisely assessing these contributions. Moreover, substantial statistics of simulated events would be needed as the probabilities for FNP events is low. FNP background is estimated with the so-called *fake factor* method [203].

The fake factor method is derived from the matrix method, which relies on loosening specific identification criteria applied in the baseline selection to estimate the probability that a looser object passes the baseline selection. Sideband regions enriched with fake leptons are constructed, and the number of fake leptons is extrapolated to the signal regions by multiplying events that contain fake leptons with the so-called *fake factors*, F_ℓ. The fake factor is a weight that represents the probability for an FNP lepton to be identified as a prompt.

As discussed in Section 5.3, two categories are needed for the fake factor method:

- the TIGHT (T) category is used as baseline selection in the analysis, and
- the LOOSE (L) category is a superset of the baseline selection but is made orthogonal by requiring events to fail TIGHT criteria.

Definitions of LOOSE and TIGHT electrons and muons are given in Tables 5.2 and 5.3, respectively, while a sketch of LOOSE and TIGHT regions is shown in Figure 6.3. Fake lepton composition was scrutinised to optimise definitions of the fake estimation regions, with the studies presented in Appendix A.

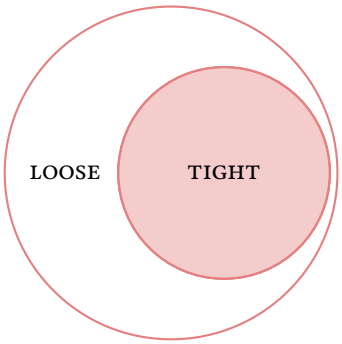

Figure 6.3: The LOOSE and the TIGHT regions in the fake factor method are shown schematically. The LOOSE is a superset of the TIGHT region but is made orthogonal by requiring that events fail TIGHT criteria.

Fake factors are measured in a control region that needs to be orthogonal to the CRs, VRs and SRs used in the primary analysis. These control samples are defined in Sections 6.2.1 and

6.2.2 for electrons and muons, respectively. The fake rate, representing the misidentification probability, is defined as

$$f = \frac{N_{\text{TIGHT}}}{N_{\text{TIGHT}} + N_{\text{LOOSE}}}, \tag{6.3}$$

where N_{LOOSE} and N_{TIGHT} are the numbers of non-prompt leptons satisfying the LOOSE and TIGHT identification conditions previously imposed. The fake factor is defined as

$$F_\ell = \frac{f}{1-f} = \frac{N_{\text{TIGHT}}}{N_{\text{LOOSE}}}, \tag{6.4}$$

and is usually measured as a function of some kinematic variable. In this analysis, F_ℓ depends on p_{T}, $E_{\text{T}}^{\text{miss}}$ and η and is applied to LOOSE leptons. The fake factor needs to be evaluated for each LOOSE lepton separately, so multiple fake factors that need to be appropriately combined are generally applied to each event. Furthermore, the prompt contribution estimated with MC simulation must be subtracted from the data to avoid double counting. The final fake background yield in the signal region can be written as

$$N_{\text{fake}} = \left[\sum_{\text{events}}^{N_{\text{LOOSE}}} (-1)^{n-1} \prod_{i}^{n} F_{\ell i}\right]_{\text{data}} - \left[\sum_{\text{events}}^{N_{\text{LOOSE}}} (-1)^{n-1} \prod_{i}^{n} F_{\ell i}\right]_{\text{promptMC}} \tag{6.5}$$

where the sum is performed over all events that contain at least one LOOSE lepton. The fake factor is applied to the event according to the kinematical properties of such lepton with index i. In the case of two-lepton events, Eq. 6.5 simplifies to

$$N_{\text{fake}} \overset{\text{if } l=2}{=} \left[\sum_{TL} F_2 + \sum_{LT} F_1 - \sum_{LL} F_1 F_2\right]_{\text{data}} - \left[\sum_{TL} F_2 + \sum_{LT} F_1 - \sum_{LL} F_1 F_2\right]_{\text{promptMC}}. \tag{6.6}$$

6.2.1 Electron Fake Factor Measurements

Defining fake-enriched estimation regions, which are also kinematically close to the signal region, is crucial for accurate fake factor measurements in data. Since prompt lepton contribution can not be completely suppressed, a subtraction of the estimated prompt lepton contamination is done by using the MC prediction. Electron fake factors are measured in the fake-enriched electron + jets control region. The measurement assumes that the probability of reconstructing fake leptons does not depend on the number of leptons in the event, so even if the primary analysis targets two-, three- and four-lepton regions, the one-electron fake estimation region is reasonable.

Events must contain precisely one reconstructed electron that satisfies either the TIGHT selection criteria or a relaxed LOOSE selection, contain at least one jet without muons or b-jets, and pass prescaled support single-lepton triggers without isolation criteria to be selected into the fake-enriched region. A second control region is defined analogously with an additional requirement to contain at least two jets to check the stability of the method, which should be independent of the number of jets in the event. Furthermore, the difference between the two regions can be used as a source of systematic uncertainty.

Since there are too many events with at least one low-p_{T} electron to all be reconstructed, triggers are not fired on each such event, but a prescale is used. A prescale is a number defining a fraction of kept events out of all that would pass the trigger requirements. It increases with decreasing trigger p_{T} threshold as more and more events contain low-p_{T} electrons passing the trigger requirements. Each electron in the event is assigned to the corresponding trigger depending on its p_{T}. If a trigger with a lower prescale and higher p_{T} threshold is available, it is used instead. If the trigger fires and an electron is matched to it, an electron is included in the region. The nominal single-electron triggers have tighter requirements on electron identification, as do the dilepton triggers used in the primary analysis, see Section 5.2, which could artificially bias the sample, enhancing isolated electrons compared to non-isolated ones. Therefore, prescaled single electron triggers, summarised in Table 6.1, are used in the electron fake factor estimation.

Table 6.1: Prescaled single electron triggers used in the fake factor estimation. The prescales are averaged over the entire period when the specific trigger was used.

Trigger	Average prescale	Periods
HLT_e26_lhvloose_nod0_L1EM20VH	111.2	2015–2016
HLT_e28_lhvloose_nod0_L1EM20VH	367.6	2017
HLT_e28_lhvloose_nod0_L1EM22VH	384.5	2018
HLT_e60_lhvloose_nod0	32.93	2015–2018
HLT_e70_lhvloose_nod0	64.13	2018
HLT_e80_lhvloose_nod0	40.43	2018
HLT_e100_lhvloose_nod0	19.45	2018
HLT_e120_lhvloose_nod0	12.15	2016, 2018
HLT_e140_lhvloose_nod0	2.637	2017–2018
HLT_e160_lhvloose_nod0	1.601	2017–2018
HLT_e200_etcut	/	2015
HLT_e300_etcut	/	2016–2018

The p_{T} and η distributions of LOOSE and TIGHT electrons in the fake-enriched region with at least one jet are presented in Figure 6.4. The filled histograms, representing prompt electrons from W+jets, Drell–Yan, $t\bar{t}$, diboson, single top, rare top, and multiboson processes, are subtracted from data before any fake factor computation is performed. One can see that the MC subtraction is lower in the LOOSE region by comparing Figures 6.4(a) and 6.4(b). The discontinuity at $\sim$ 300 GeV in Figure 6.4(a) is attributed to the different ID requirements on triggers, as the HLT_e300_etcut does not have any ID requirements, and its efficiency is almost 100%.

The electron fake factor is parameterised as a function of p_{T} in four η and two $E_{\mathrm{T}}^{\mathrm{miss}}$ intervals. The p_{T} has a variable binning, driven by the uncertainty in a specific bin which means that the bins are combined so that a statistical uncertainty stays above a specific value. The last p_{T} bin contains overflow, and the fake factors are not extrapolated to higher p_{T} values. Pseudorapidity, η, is divided into four slices, $0 < |\eta| < 0.7$, $0.7 < |\eta| < 1.37$, $1.52 < |\eta| < 2.01$, and $2.01 < |\eta| < 2.47$, excluding the crack region.

The dominant contributions to the systematic uncertainties in the electron fake factor estimation

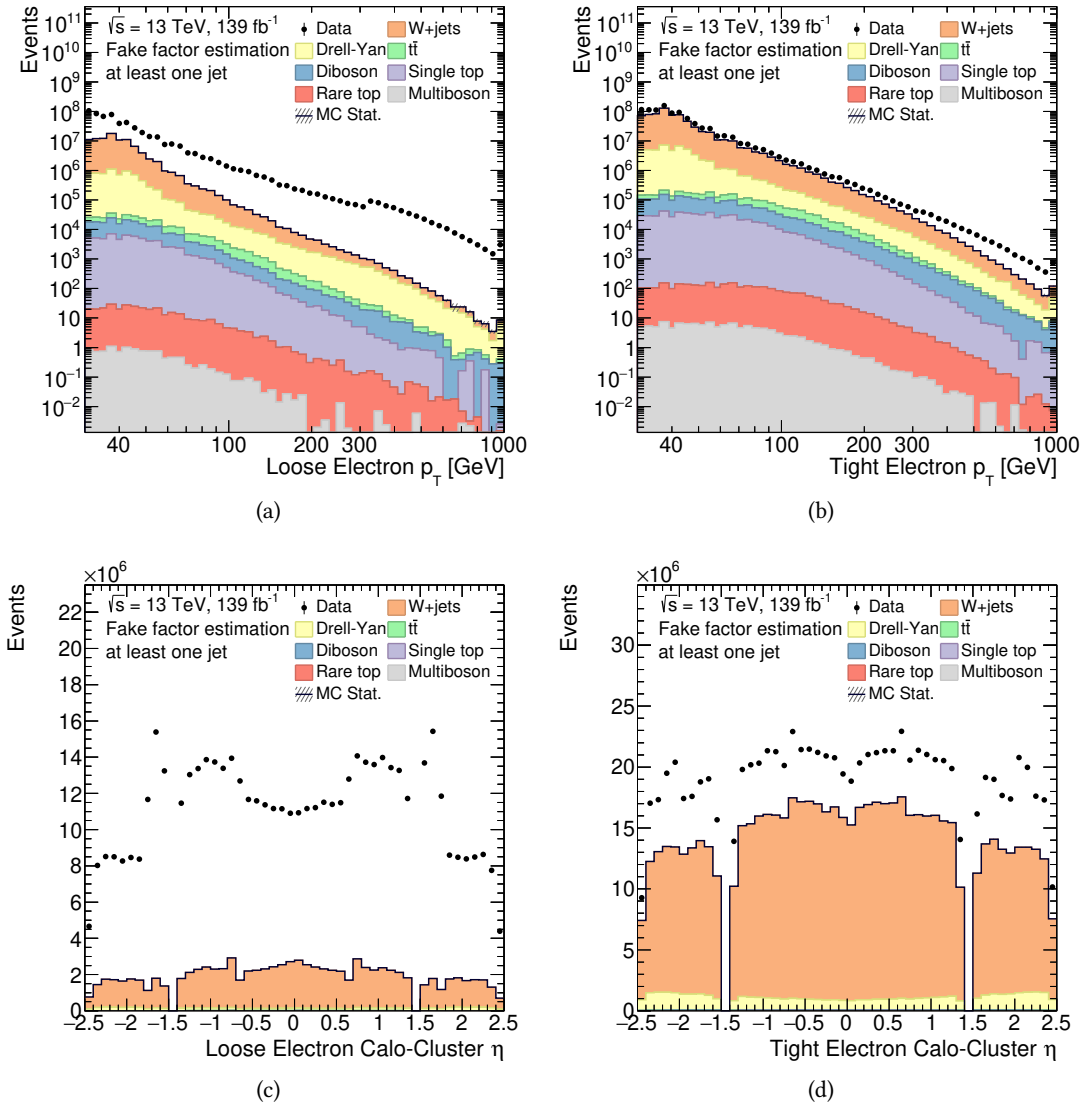

Figure 6.4: The p_{T} and η distributions of LOOSE and TIGHT electrons in the fake-enriched region with at least one jet in the event. The p_{T} distribution of (a) LOOSE and (b) TIGHT electrons. The η distribution of (c) LOOSE and (d) TIGHT electrons. All the distributions show data (black dots) events and the prompt MC component (filled histograms), subtracted from data to ensure a region dominated by fake electrons.

stem from the MC modelling of the subtracted leptons, differences in the composition of fake electrons between the fake-enriched and signal regions, and the normalisation of MC samples in the fake-enriched region. All these sources were studied by varying the nominal fake-enriched region requirements, as presented in Table 6.2.

The electron fake factors are measured for each variation separately, as shown in Figure 6.5. Systematic uncertainties of all variations are added together with statistical uncertainty in quadrature to obtain the total systematic uncertainty, with the highest contribution coming from MC scaling. The measurement is relatively stable overall up to very high electron p_{T}, but the maximum uncertainty can get very high, up to 100%.

Table 6.2: A summary of variations performed to estimate systematic uncertainties in electron fake factor measurements.

Variation	**Purpose**
Flipped requirement on the number of jets	fake composition
Removing $E_{\mathrm{T}}^{\mathrm{miss}}$ requirement	fake composition
MC scaled up by 10%	MC modelling, cross-section and luminosity
MC scaled down by 10%	MC modelling, cross-section and luminosity

A direct closure test in the electron fake-enriched region is carried out to assess the measured electron fake factors. The same event selection and object definitions (see Section 5.3) are used as in the nominal event selection and are compared to the combined prediction of Monte Carlo and the fake factor method.

Prompt MC processes considered in the closure tests are the same as for the fake factor derivation, while the remaining events are well represented by the estimated fake factor contribution, as shown in Figure 6.6. Only the systematic uncertainty related to the fake factor is considered. Overall the agreement is adequate even for high-p_{T} electrons.

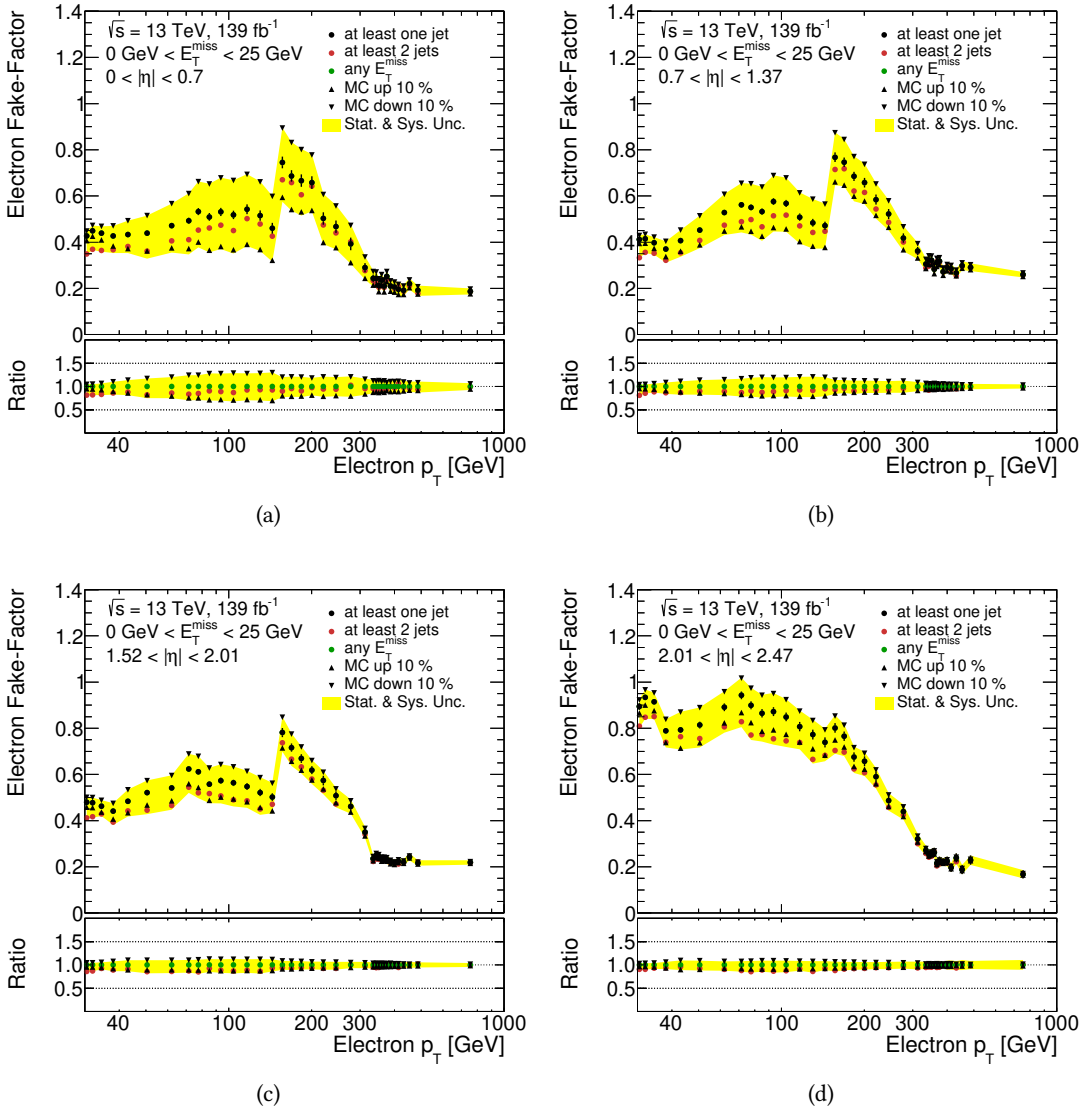

Figure 6.5: The measured electron fake factors are presented in four η bins for each systematic variation, summarised in Table 6.2. At least one jet and $E_{\mathrm{T}}^{\mathrm{miss}} < 25\,\mathrm{GeV}$ is required. The discontinuity at 150 GeV roots in the trigger bias.

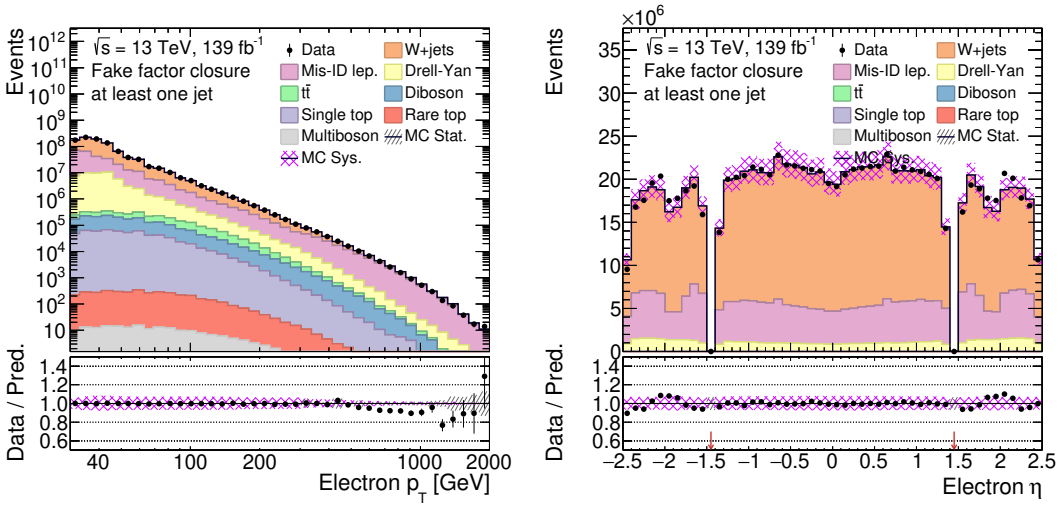

(a) (b)

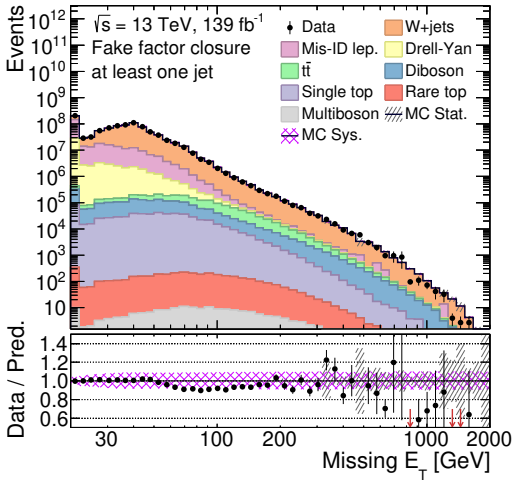

(c)

Figure 6.6: The electron fake factor closure in a region requiring at least one jet in the event. (a) electron p_{T} distribution, (b) electron η distribution, (c) and $E_{\mathrm{T}}^{\mathrm{miss}}$ distribution. The magenta band shows the systematic uncertainty associated with the fake factor measurement.

6.2.2 Muon Fake Factor Measurements

The dominant source of muon fakes is the in-flight decay of heavy flavour hadrons within jets. Muon fake factors are measured using a data-driven way of measuring efficiencies, the *tag-and-probe* technique. A *tag* object that passes a series of tight selection criteria, e.g. identification and isolation, and a *probe* object passing a looser selection is chosen. The efficiency is then the ratio between tagged and tagged + probe objects.

Dijet events are targeted with precisely one jet in the event, the *tag*, and one reconstructed muon, the *probe*. The benefits of dijet events are twofold: they provide high statistics, which is much needed for measuring fake factors, and allow addressing systematic uncertainties using the properties of the recoiling jet. Prescaled non-isolated single-muon triggers listed in Table 6.3 are needed to select muon events.

Table 6.3: Prescaled single muon triggers used in the fake factor estimation. The prescales are averaged over the entire period when the specific trigger was used.

Trigger	Average prescale	Periods
HLT_mu24	49.36	2015–2018
HLT_mu50	/	2015–2018

The tag and the probe in the event need to be back-to-back in the transverse plane, i.e. $\Delta\phi(\mu, \text{jet}) > 2.7$, and have transverse momenta $p_{\text{T}}^{\text{jet}} > 35\,\text{GeV}$ and $p_{\text{T}}^{\mu} > 30\,\text{GeV}$ to enrich the sideband region. Additionally, the b-jet veto is applied to suppress fakes from heavy flavour decays, and $W \to \mu\nu$ events are rejected by requiring $E_{\text{T}}^{\text{miss}} < 40\,\text{GeV}$. The p_{T} and η distributions of LOOSE and TIGHT muons in the fake-enriched region with at least one jet are presented in Figure 6.7. The filled histograms, representing prompt muons from W+ jets, Drell–Yan, $t\bar{t}$, diboson, single top, rare top, and multiboson processes, are subtracted from data before any fake factor computation is performed.

The systematic uncertainties in the muon fake factor measurement are assessed by modifying the nominal selection of dijet events:

- The effect of additional W+ jets contamination, i.e. the fraction of prompt muons, is estimated by varying the requirement on the $E_{\text{T}}^{\text{miss}}$ by 10 GeV upward and downward for both LOOSE and TIGHT muons simultaneously.
- The topology of the event is different when rising the $p_{\text{T}}^{\text{jet}}$ threshold up to 40 GeV. This way, the collimation of the fake muon is altered, and a further handle on how the isolation of the fake muon impacts the fake factor measurement is obtained.
- The back-to-back requirement on the jet and the reconstructed muon, $\Delta\phi(\mu, \text{jet})$, which affects the fake muon isolation, is varied up and down by 0.1.

The muon fake factors are measured for each variation separately in five η slices, as shown in Figure 6.8. Systematic uncertainties of all variations are added together with statistical

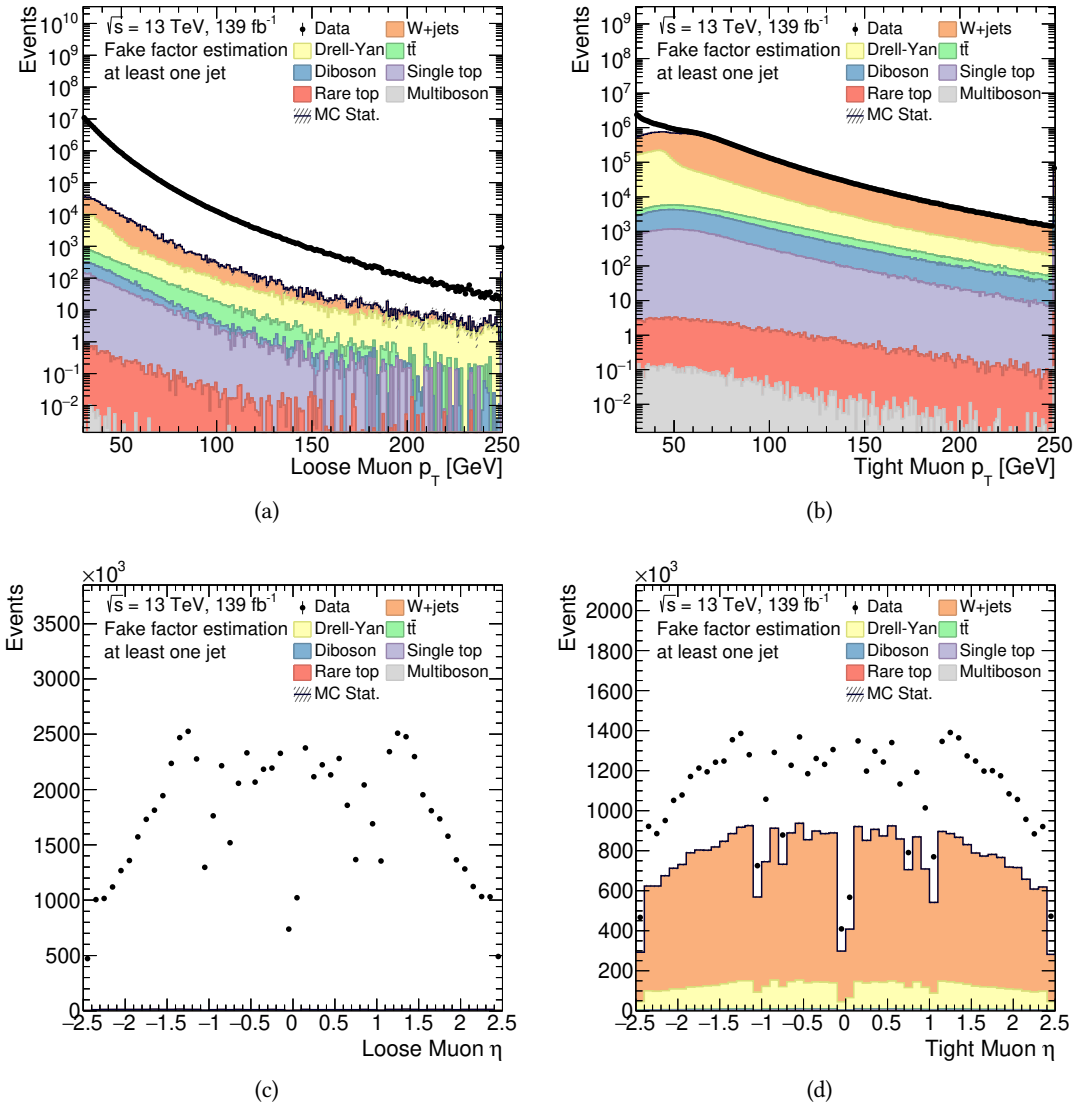

Figure 6.7: The p_T and η distributions of LOOSE and TIGHT muons in the fake-enriched region with at least one jet in the event. The p_T distribution of (a) LOOSE and (b) TIGHT muons. The η distribution of (c) LOOSE and (d) TIGHT muons. All the distributions show data (black dots) events and the prompt MC component (filled histograms), subtracted from data to ensure a region dominated by fake muons.

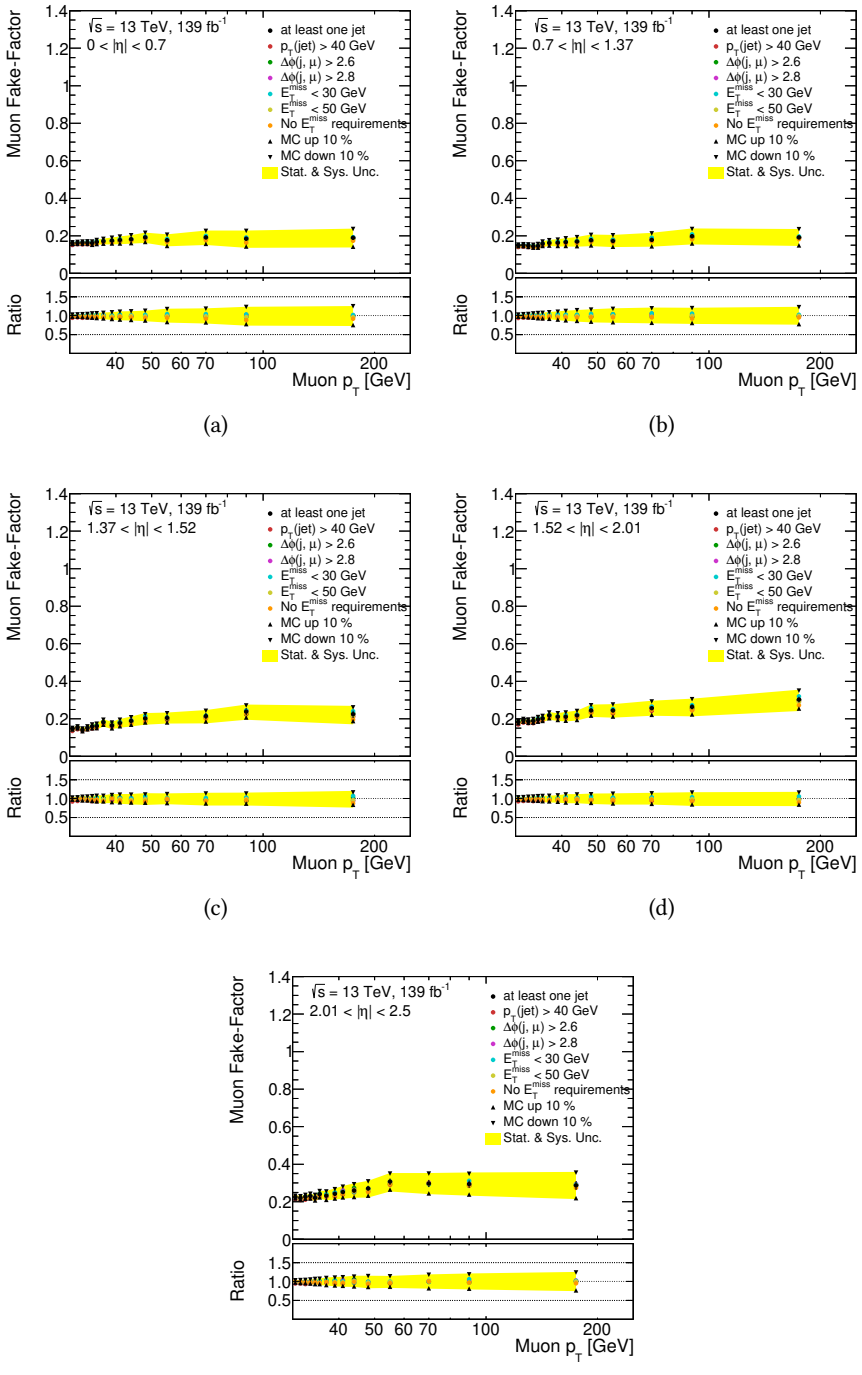

Figure 6.8: The measured muon fake factors are presented in five η bins for each systematic variation described in the text.

uncertainty in quadrature to obtain the total systematic uncertainty. An uncertainty between $\sim 10\%$ and $\sim 50\%$ is achieved across p_{T} intervals.

A closure test in the muon fake-enriched region is performed to validate the muon fake factors. The event selection in the closure test is similar to the fake-factor derivation, but this time omitting the jet angular requirements.

Prompt MC processes considered in the closure tests are the same as for the fake factor derivation. The remaining events are well represented by the estimated fake factor contribution, as shown in Figure 6.9. Only the systematic uncertainty related to the fake factor is considered.

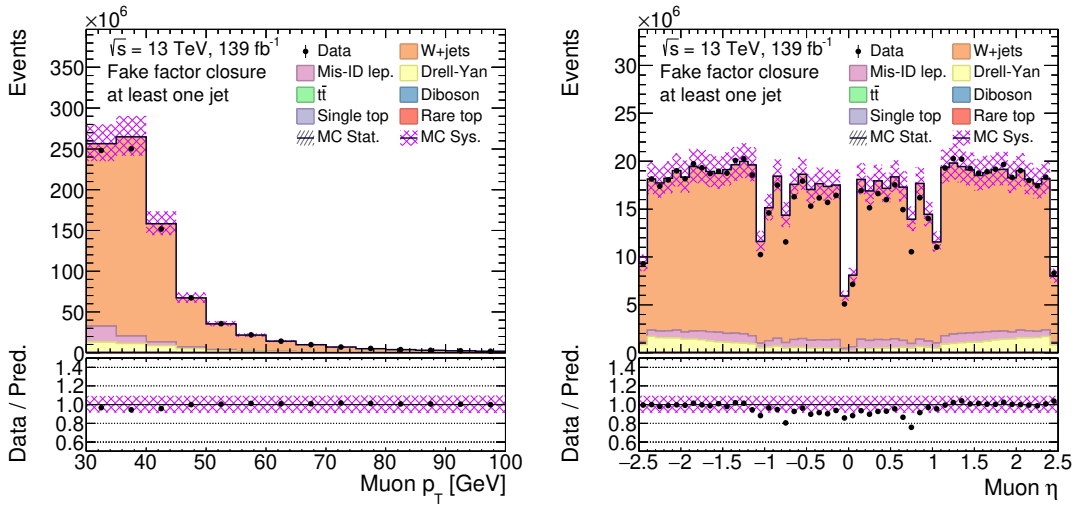

(a) (b)

Figure 6.9: The muon fake factor closure in a region requiring at least one jet in the event. (a) muon p_{T} distribution and (b) muon η distribution. The magenta band shows the systematic uncertainty associated with the fake factor measurement.

6.3 Systematic Uncertainties

Several sources of experimental and theoretical systematic uncertainties affecting the background and signal predictions are accounted for in the analysis to compensate for the detector and simulation limitations. Each systematic uncertainty is assessed by varying the corresponding nuisance parameter (NP) by one standard deviation, σ, and reweighing all the events accordingly. This results in two shifted distributions of each variable of interest representing the fluctuation ($\pm 1\sigma$) around the nominal distribution. The maximal variation is symmetrised if both $\pm 1\sigma$ variations appear on one side of the nominal distribution. Some systematic uncertainties can not be treated this way and require a specific case-dependent approach. All considered sources of systematic uncertainty affect the total event yield, and all, except the luminosity and cross-section uncertainties, also affect the shape of kinematical distributions. Only shape

systematics are considered for the signal samples and diboson and Drell–Yan backgrounds, as their normalisation is determined from the fit.

6.3.1 Theoretical Uncertainties

Monte Carlo generators used for modelling signal and background processes, or for calculating the cross-sections to normalise the MC samples, rely on various assumptions. Examples of these assumptions are the choice of renormalisation and factorisation scales, μ_R and μ_F, the choice of PDFs, ME+PS matching algorithm, parton shower, hadronisation model, and the experimental input parameters, e.g. α_s or m_t. These assumptions induce modelling uncertainties that need to be quantified, which is done either by varying the internal parameters of the nominal simulation or by comparing the nominal simulation result to one obtained with an alternative generator setup.

The partonic cross-section from Eq. 1.65 can be expanded in powers of the strong coupling constant, α_s, as

$$\hat{\sigma}^{(n)} = \alpha_s \hat{\sigma}^{(0)} + \alpha_s^2 \hat{\sigma}^{(1)} + \ldots + \alpha_s^n \hat{\sigma}^{(n-1)} + O\left(\alpha_s^{n+1}\right). \tag{6.7}$$

From Eqs. 1.65 and 6.7, three leading sources of uncertainty in perturbative QCD calculations can be extracted:

Missing higher orders: These uncertainties provide an estimate for the last, $O\left(\alpha_s^{n+1}\right)$, term in Eq. 6.7. The usual way to estimate them is to perform scale variations by varying the μ_R and μ_F up and down by a factor of two, e.g. the Sherpa samples come with seven-point pairwise scale variations, as shown in Table 6.4.

PDF uncertainties: Several sources of uncertainty influence the PDF determination, mainly experimental uncertainties entering the datasets used in the PDF fits and the uncertainty on the functional form used in the PDF fits. Other theory uncertainties, e.g. flavour scheme and nuclear effects, are not considered, but some of these effects are probed when comparing different PDF sets. PDF uncertainties are calculated using the LHAPDF interface [86].

The strong coupling constant uncertainties: The α_s is determined experimentally from the combination of different datasets, and its value is quoted at the scale of the Z boson mass. There are two sources of uncertainty, namely the experimental errors when determining the α_s and the fact that cross-section calculation is truncated at a fixed order in perturbation theory. The cross-sections of the processes used in the PDF fit depend on the α_s value. Therefore, there is a low correlation between the α_s and PDF uncertainties. The two uncertainties are combined in squares,

$$\delta^{\alpha_s+\mathrm{PDF}}\sigma = \sqrt{\left(\delta^{\alpha_s}\sigma\right)^2 + \left(\delta^{\mathrm{PDF}}\sigma\right)^2}. \tag{6.8}$$

Scale variation uncertainties, PDF uncertainties, and α_s uncertainties are estimated for signal samples and two backgrounds, $t\bar{t}$ and diboson. For $t\bar{t}$, ISR and FSR variations are additionally considered. Theoretical uncertainties for specific samples are described in detail in Section 3.3.

The majority of the MC samples are interfaced with showering and hadronisation generators, which convert the inclusive partonic cross-sections into exclusive hadron-level ones. This step introduces further uncertainties like matching and merging uncertainty or PS and hadronisation uncertainty. The former is associated with the double-counting removal arising from the combination of final states with different multiplicities, while the latter is related to algorithmic differences in the PS and the hadronisation modelling.

Table 6.4: The seven-point renormalisation and factorisation scale variations. The nominal choice is marked with ✓, variations labelled with ✻ are taken as uncertainties, while the ones denoted by ✘ are usually not used to avoid large logarithms in the calculation induced by the large scale differences.

μ_F \ μ_R	0.5	1	2
0.5	✻	✻	✘
1	✻	✓	✻
2	✘	✻	✻

6.3.2 Experimental Uncertainties

It is necessary to consider experimental systematic uncertainties due to the differences between the simulated events and reconstructed data. They are determined from dedicated performance measurements and applied to signal and background MC predictions but not to the data. Experimental systematic uncertainties can be divided into two main categories. Calibration uncertainties are related to the energy and momentum scale measurements, while efficiency uncertainties address the reconstructed objects' reconstruction, identification and selection efficiencies. The experimental systematic uncertainties are:

Luminosity uncertainty is set to 0.83% on the full Run 2 ATLAS pp data sample. The evaluation is documented in Ref. [137] and is covered by one NP.

Pile-up reweighing uncertainty is associated with the pile-up reweighting procedure adopted to match distributions of the average number of interactions per bunch-crossing between simulation and observed data. One NP is assigned.

Electron uncertainties are described by scale factors in different p_{T} and η bins because of the different detector geometries in the different regions and to adapt the rejection rates against the background, which is highest for low p_{T}. The *simplified* scheme is adopted, which in total includes 67 correlated and 108 uncorrelated variations of the identification, isolation, reconstruction, trigger, and charge misidentification scale factors across different p_{T} and η bins. Additional sources of systematic uncertainties are the electron energy scale and resolution, described by three NPs. All electron-related uncertainties, except charge misidentification uncertainties, are found to have a negligible impact on the final result.

Muon uncertainties include uncertainties in momentum resolution and scale (5 NPs). Reconstruction, isolation, and trigger efficiency uncertainties with the additional track-to-vertex

association are split into a statistical and a systematic component and are described by 9 NPs combined.

Jet uncertainties include JER, JES, JVT and flavour tagging uncertainties. The JES uncertainties arise from several primary sources: the standard calibration, which has 14 NPs, the flavour dependence by the jet composition, the pile-up uncertainty due to the number of primary vertices and μ values, the punch-through uncertainty depending on the number of muon segments behind the jet, and the MC non-closure, which affects samples where kinematic observables of the calibrated jet are not restored to that of the corresponding truth jet. JER systematic has 9 NPs that cover the case in which the resolution is higher in MC than in data and vice versa. One NP is used to vary the JVT algorithm efficiency, and 6 NPs are related to the flavour-tagging procedure.

$E_{\mathrm{T}}^{\mathrm{miss}}$ uncertainties are affected by the uncertainties related to electrons, muons and jets. Additional uncertainties on the scale and resolution of the soft term, which is split into a component parallel and one perpendicular to $E_{\mathrm{T}}^{\mathrm{miss}}$, are considered. Three independent NPs are introduced: one for the uncertainty on the resolution of the measurement of the longitudinal component, one for the transverse component and one for the scale measurement.

Fake factor uncertainty is assessed by altering the nominal fake factor, as discussed in Sections 6.2.1 and 6.2.2. The normalisation of the subtracted prompt lepton contribution in the fake-enriched regions is varied within its uncertainties to address the uncertainties related to the luminosity, cross-section, and corrections applied to MC predictions. The FNP systematic uncertainties are correlated across all different regions and bins, while the statistical uncertainties in each bin are uncorrelated. One NP per light-lepton flavour is assigned.

All theoretical and experimental systematics considered in this analysis are reported in Table 6.5 with the number of corresponding nuisance parameters.

Table 6.5: A summary of systematic uncertainties used in the analysis with the number of corresponding nuisance parameters is shown. Where two NP numbers are listed, the first corresponds to the correlated, and the second to the uncorrelated uncertainties.

Category	**Type**	**Nuisance parameters**
Luminosity		1
Pile-up reweighting		1
Theoretical uncertainties	Diboson modelling	3
	$t\bar{t}$ modelling	7
	Signal modelling	4
Data-driven background	Electron fake factors	1
	Muon fake factors	1
Electron calibration	Resolution	1
	Momentum scale	2
Electron efficiencies	ID	16 + 18
	Reconstruction	7 + 18
	Isolation	11 + 18
	Trigger	22 + 36
	Charge misidentification	11 + 18
Muon calibration	Smearing of the ID and MS track	2
	Momentum scale	3
Muon efficiencies	Reconstruction	3
	Isolation	2
	Track-to-vertex association	2
	Trigger	2
Jet calibration	Jet energy scale: calibration	14
	Jet energy scale: flavour dependence	3
	Jet energy scale: pile-up dependence	4
	Jet energy scale: calo punch-through	2
	Jet energy scale: MC non-closure	2
	Jet energy resolution	9
Jet efficiencies	JVT	1
	Flavour tagging	6
$E_{\mathrm{T}}^{\mathrm{miss}}$ uncertainties		3
Total		254

CHAPTER 7

Statistical Analysis

A detailed description of the statistical procedures implemented in the analysis to extract the final results is given in this chapter. The likelihood function and the statistical procedures used to test the fit results are described. In addition, this chapter illustrates the tools used to scrutinise and validate the fit results.

7.1 Statistical Treatment

A binned maximum-likelihood fit is performed to measure the signal yield. The expected signal yield is fitted in the SRs, while the background yield predictions from the MC simulation are simultaneously fitted in the CRs. The fit performance is finally evaluated in VRs when the fitted parameters are applied. A maximum-likelihood fit is implemented in the HistFitter [204] statistical analysis package, that is based on Root [205] and RooFit [206] frameworks.

7.1.1 The Likelihood Function

The likelihood is defined as the product over all bins of the Poisson probability to observe N_i events in a particular bin i:

$$L_{\text{phys}}(\text{data} \,|\, \mu) = L_{\text{phys}}(\mu) = \prod_{i \in \text{bins}} \text{Pois}(N_i \,|\, \mu S_i + B_i) = \prod_{i \in \text{bins}} \frac{(\mu S_i + B_i)^{N_i}}{N_i!} e^{-(\mu S_i + B_i)}, \tag{7.1}$$

where S_i and B_i are the expected signal and background yields, respectively. The likelihood is introduced with one or more parameters of interest (POI), denoted as μ. The cross-section of the process and the $H^{\pm\pm}$ particle mass are POIs in this analysis.

The systematic uncertainties are included in the likelihood via a set of nuisance parameters, denoted as $\boldsymbol{\theta} = (\boldsymbol{\alpha}, \boldsymbol{\gamma}, \boldsymbol{\tau})$, that modify the expected signal and background yields, i.e. $\{S_i, B_i\} \rightarrow \{S_i(\boldsymbol{\theta}), B_i(\boldsymbol{\theta})\}$. The NPs can be classified into three categories:

- Free-floating nuisance parameters $\boldsymbol{\tau}$ are the unconstrained parameters controlling the normalisation of the backgrounds and are free to float in the fit.
- Nuisance parameters $\boldsymbol{\gamma}$ represent the statistical uncertainties originating from the limited size of simulated background samples. Such NPs are applied to the total yield of all the backgrounds in each analysis bin.
- Nuisance parameters $\boldsymbol{\alpha}$ represent the modelling and the experimental uncertainties that affect both signal and background events. Their central value and uncertainty are determined beforehand in data or auxiliary calibration measurements.

The constraints from calibration measurements can be fully encoded in an auxiliary likelihood function $L_{\text{aux}}(\boldsymbol{\alpha})$, often approximated by a Gaussian function

$$L_{\text{aux}}(\boldsymbol{\alpha}) = \prod_{\alpha \in \boldsymbol{\alpha}} \text{Gauss}(\boldsymbol{\alpha} \mid \theta, \sigma_\theta), \tag{7.2}$$

where σ_θ is the uncertainty on θ. Furthermore, the NPs are usually shifted and rescaled to have zero mean and unit variance so the L_{aux} can be rewritten as

$$L_{\text{aux}}(\alpha) = \text{Gauss}(\alpha \mid 0, 1) = \frac{1}{\sqrt{2\pi}} e^{-\alpha^2/2}, \tag{7.3}$$

where $\alpha = (\theta - \hat{\theta})/\hat{\sigma}_\theta$, $\hat{\theta}$ and $\hat{\sigma}_\theta$ are determined from the maximum-likelihood fit. The $\alpha_i = 0$ defines the nominal prediction, while $\alpha_i = \pm 1$ are the two modified *up/down templates* for the $\pm 1\sigma$ variations.

The uncertainties on the background predictions due to the limited number of simulated events are accounted for in the likelihood function considering Poisson terms

$$L_{\text{stat}}(\boldsymbol{\gamma}) = \prod_{i \in \text{bins}} \frac{(\gamma_i B_i)^{B_i} e^{-\gamma_i B_i}}{\Gamma(B_i)}, \tag{7.4}$$

where Γ is the Gamma function. In a lightweight version of the Barlow–Beeston method [207], only one NP, γ_i, is defined for each bin i and is associated with the total MC estimate and the total statistical uncertainty in that bin. The final *profile likelihood* function can finally be defined as a product of three likelihoods

$$L(\mu, \boldsymbol{\alpha}, \boldsymbol{\gamma}, \boldsymbol{\tau}) = L_{\text{phys}}(\mu, \boldsymbol{\alpha}, \boldsymbol{\gamma}, \boldsymbol{\tau}) \cdot L_{\text{aux}}(\boldsymbol{\alpha}) \cdot L_{\text{stat}}(\boldsymbol{\gamma}). \tag{7.5}$$

A binned likelihood fit is performed to determine the POIs and their uncertainties. The measured signal strengths and the NPs are obtained as the values of the parameters that maximise the likelihood function $L(\mu, \boldsymbol{\theta})$ or, equivalently, minimise $-\ln L(\mu, \boldsymbol{\theta})$, where $\boldsymbol{\theta}$ represents the previously introduced NPs, $\boldsymbol{\theta} = (\boldsymbol{\alpha}, \boldsymbol{\gamma}, \boldsymbol{\tau})$.

7.1.2 Hypothesis Test

The likelihood is also used to test the hypothesised value of μ. A profile likelihood ratio, $\lambda(\mu)$, is defined as

$$\lambda(\mu) = \frac{L(\mu, \hat{\hat{\boldsymbol{\theta}}}(\mu))}{L(\hat{\mu}, \hat{\boldsymbol{\theta}})}. \tag{7.6}$$

Here, $\hat{\mu}$ and $\hat{\boldsymbol{\theta}}$ are the parameters that maximise the overall likelihood, and $\hat{\hat{\boldsymbol{\theta}}}$ are the NP values that maximise the likelihood for a particular value of μ. The *test statistics* is then defined as $q_\mu = -2 \ln \lambda(\mu)$, for which the lower values indicate better compatibility between the data and the hypothesised value of μ. The test statistic is used to calculate a *p-value* that quantifies the agreement

$$p_\mu = \int_{q_\mu^{\text{obs}}}^{\infty} f(q_\mu \mid \mu)\, \mathrm{d}q_\mu, \tag{7.7}$$

where q_μ^{obs} is the value of test statistics observed in data, and $f(q_\mu \mid \mu)$ is the probability density function of the test statistic q_μ under the signal strength assumption, μ. The distribution of the test statistic for different μ hypotheses is required to perform a hypothesis test, which can be obtained using Monte Carlo pseudo-experiments or asymptotic formulae [200]. The p-value can be expressed in units of Gaussian standard deviations $Z = \Phi^{-1}(1-p)$, where Φ^{-1} is the inverse Gaussian CDF. The rejection of the background-only hypothesis with a significance of at least $Z = 5$ (corresponding to $p_0 = 2.87 \times 10^{-7}$) is considered a discovery.

A test statistic used in the $H^{\pm\pm}$ analysis is the one for the positive signal discovery in which the background-only hypothesis with $\mu = 0$ is tested. If the data are compatible with the background-only hypothesis, the nominator and the denominator of the test statistic, $q_0 = -2\ln\lambda(\mu = 0)$, are similar. Then, q_0 is close to 0, and p_0 value is 0.5. In this case, upper limits on the signal production cross-section are derived at a 95% confidence level using the CL_S method [208], for which both the signal plus background, p_{s+b}, and background-only, p_b, p-values need to be calculated. For a given set of signal masses or branching ratios, the signal hypothesis is tested for several values of μ. The final confidence level CL_S is computed as the ratio

$$\text{CL}_\text{S} \equiv \frac{p_{s+b}}{1-p_b}, \tag{7.8}$$

which allows to exclude a hypothesis at 95% CL if below 5%.

7.1.3 Nuisance Parameters

The impact of all the experimental and modelling uncertainties is quantified using histograms that correspond to $\pm1\sigma$ variation of each NP, as discussed in Section 6.3. An example of a nice behaving systematics is presented in Figure 7.1(a). However, some systematics can be one-sided, e.g. jet resolution uncertainty. Such systematic uncertainties must be symmetrised across the nominal histogram to obtain the variation also in the other direction. Furthermore, some systematics might switch their up-and-down variations from bin to bin, as shown in Figure 7.1(b). In such cases, an envelope of $\pm1\sigma$ variation is chosen, and up/down templates are redefined.

When switching to the simplified electron correlation model, a lot of new NPs were introduced, making calculations quite unstable. However, only some of them had a sizeable impact on the fit templates. A *pruning* procedure was applied to reduce the number of NPs and thus obtain a more solid and simple fit model. The procedure removed systematics uncertainties that had a negligible impact on the final result. Normalisation and shape uncertainties were dropped if the variation of the corresponding template was below 1% in all the bins.

The pull plot of a nuisance parameter θ, with the expectation θ_0, is defined as

$$\text{pull}(\theta) = \frac{\hat{\theta} - \theta_0}{\sigma_\theta}, \tag{7.9}$$

where $\hat{\theta}$ is the NP value obtained from the maximum-likelihood fit [209]. The pull represents the distance from the expected value in terms of σ_θ, that arose during maximum-likelihood estimation. A desirable scenario is when the average pull is zero, and its

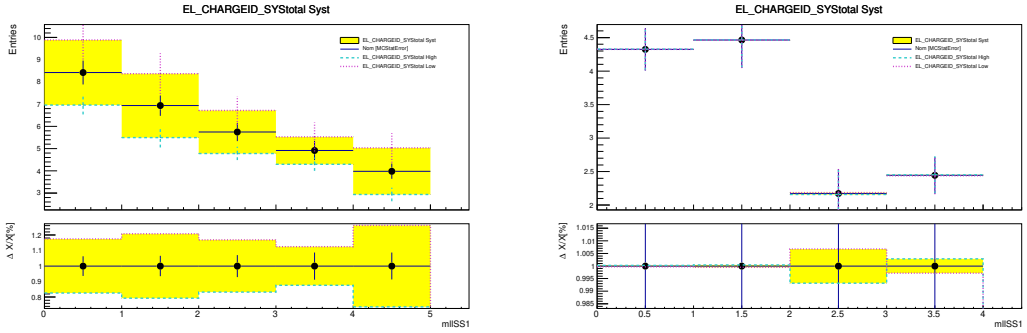

(a) (b)

Figure 7.1: An example of an electron charge ID systematics in the cut-based analysis, showing the up and down templates for the (a) 'Other' background in the DBCR2L's *ee* channel and (b) diboson background in the SR3L, where the up and down templates are switched between third and fourth bin.

standard deviation is close to 1. If this is not the case, further investigation is needed. The expected value and assumed standard deviation of an NP are determined based on auxiliary measurements or Monte Carlo studies.

The correlation matrix is another convenient tool to assess the goodness of fit. The correlation between θ_i and θ_j NPs or even POIs is given by the covariance matrix of the estimators of all the parameters, $V_{ij} = \mathrm{cov}[\hat{\theta}_i, \hat{\theta}_j]$, which is defined as

$$\mathrm{cov}[\hat{\theta}_i, \hat{\theta}_j] = \left[-\frac{\partial^2 \ln L(\theta)}{\partial\theta_i \partial\theta_j} \right]^{-1} \tag{7.10}$$

at $\hat{\mu}$ and $\hat{\theta}$ in the large sample limit [200]. The correlation coefficients can take values between -1 and 1, with 0 meaning no correlation, which is the desired value.

The ranking plot presents information on how much the POI varies when changing the NP value and is used to sort the NPs by the largest *impact*. The impact of a nuisance parameter θ on the fitted POI is defined as [209]:

$$\mathrm{impact} = \Delta\mu^{\pm} = \hat{\hat{\mu}}_{\theta_0 \pm \sigma_\theta} - \hat{\mu}, \tag{7.11}$$

where $\hat{\hat{\mu}}_{\theta_0 \pm \sigma_\theta}$ is the maximum-likelihood estimator of μ when all parameters are allowed to vary, except θ, which is set to its $\pm 1\sigma$ values, $\theta_0 \pm \sigma_\theta$. An NP with low impact can be discarded in the pruning procedure.

CHAPTER 8

Results of the Doubly Charged Higgs Analysis

This chapter presents results obtained with the $H^{\pm\pm}$ analysis using the full Run 2 dataset considering only lepton final states. It describes the results obtained by implementing the cut-based analysis.

8.1 Results of the Cut-Based Analysis

The final normalisations of Drell–Yan and diboson MC samples are not taken from MC calculations but are derived in the simultaneous likelihood fit to data in dedicated Drell–Yan and diboson CRs, as described in Section 5.4. Free-floating parameters are introduced to fit the yields in the control regions. These free parameters are then used to normalise relevant backgrounds in the signal and validation regions. Fitting the yields of the dominant backgrounds reduces the systematic uncertainty in the predicted yield from SM sources. After a background-only likelihood fit, the normalisation factors are compatible with their SM predictions within the uncertainties and are listed in Table 8.1. The diboson yield is described by three free parameters, one each for the two-, three- and four-lepton multiplicity channels, while one parameter is defined to scale the Drell–Yan contribution.

Table 8.1: Drell–Yan and diboson normalisation scale factors with their corresponding uncertainties are listed for the cut-based analysis.

MC process	**Normalisation factor**
Drell–Yan	1.13 ± 0.04
diboson 2ℓ	1.10 ± 0.06
diboson 3ℓ	0.92 ± 0.05
diboson 4ℓ	1.08 ± 0.11

Post-fit binned $m(\ell^{\pm}\ell'^{\pm})_{\text{lead}}$ distributions in the control regions are shown in Figures 8.1 and 8.2. The derived normalisation is assessed in the VRs. Good agreement between data and prediction is observed, as seen in Figures 8.3 and 8.4. Additional selected distributions are shown in Appendix B.

Systematic uncertainties and corresponding NPs can be assessed after the fit using techniques described in Section 7.1. The nominal value and the uncertainties of relevant NPs should desirably not move significantly from their predicted values. The pull plots, showing the uncertainties that are constrained using data from CRs and remain in the fit after pruning, are presented in Figures 8.5 and 8.6 for background-only and full likelihood fit, respectively. The accuracy of fit performance is tested using MC prediction with injected signal events in the SRs. There is no significant deviation from the prediction.

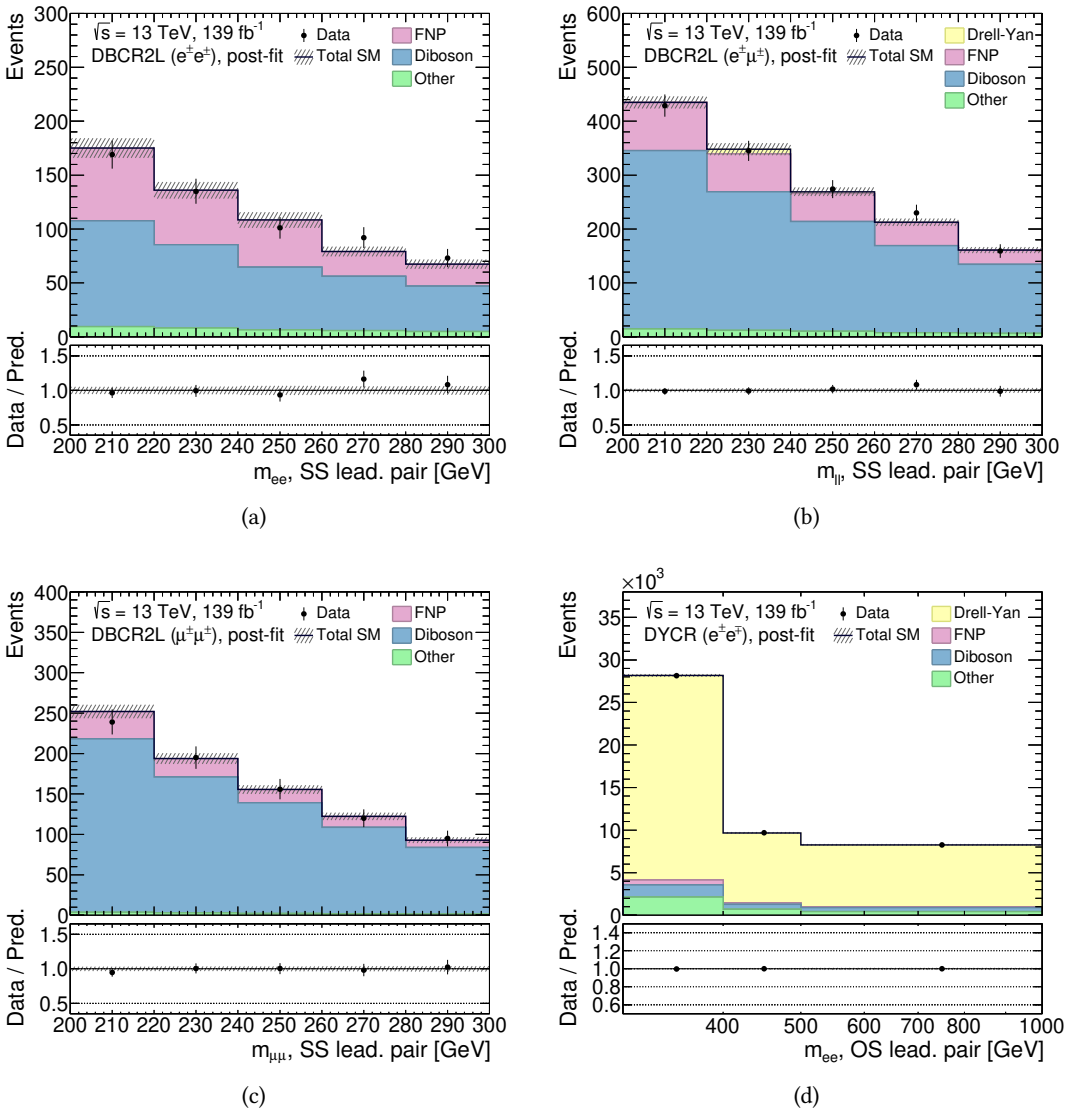

Figure 8.1: The two-lepton invariant mass, $m(\ell^{\pm}\ell'^{\pm})_{\text{lead}}$, distributions for data and SM background predictions in cut-based control regions: (a) the electron–electron, (b) the electron–muon, (c) the muon–muon diboson control regions, and (d) DYCR. Backgrounds from top-quark and multiboson processes are merged, forming the 'Other' category. The hatched bands include all systematic uncertainties after a background-only fit to data (post-fit), with the correlations between various sources considered. The last bin also includes any overflow entries. The error bars show statistical uncertainties. The lower panels show the ratio of the observed data to the estimated SM background.

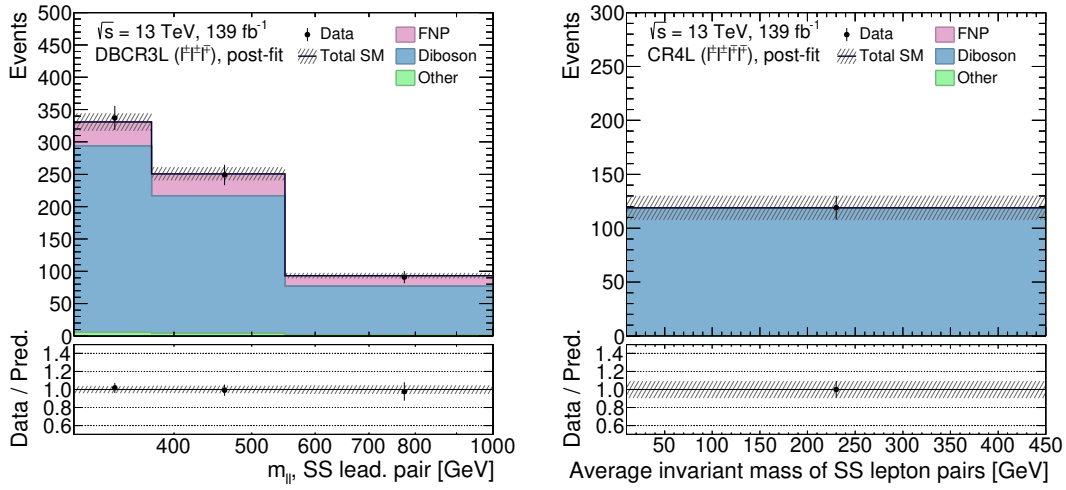

(a) (b)

Figure 8.2: (a) The two-lepton invariant mass, $m(\ell^{\pm}\ell'^{\pm})_{\text{lead}}$, distributions for data and SM background predictions in cut-based CR3L and (b) event yield in the cut-based CR4L. Backgrounds from top-quark and multiboson processes are merged, forming the 'Other' category. The hatched bands include all systematic uncertainties after a background-only fit to data (post-fit), with the correlations between various sources considered. The last bin also includes any overflow entries. The error bars show statistical uncertainties. The lower panels show the ratio of the observed data to the estimated SM background.

The impact of statistical and systematic uncertainties on signal strength, μ_{sig}, can be studied using ranking plots. One NP at a time is fixed to its $\pm 1\sigma$ variations, while others are free to float. The real data is used for all regions except SRs in the fit. An injected MC signal is used in the SRs instead. The dominant uncertainties are presented in Figure 8.7, with the per-bin γ parameters included. The dominant uncertainty is statistical, reaching almost 35%, while the leading systematic uncertainties are multiple electron identification efficiency NPs and some γ factors, but they all remain below 5%.

Finally, the correlations between individual NPs are studied using the correlation matrix, presented in Figure 8.8. Only NPs having at least the absolute value of the correlation of magnitude 0.2 or higher with another NP are shown in the matrix. The correlation matrix looks more or less diagonal with several sub-blocks of correlated nuisance parameters.

The total relative background systematic uncertainty after the background-only fit and its breakdown into components is presented in Figure 8.9. Theoretical and experimental uncertainties remain below 10% in each analysis region, while the MC statistic can grow up to 35% but is reduced in the final fit combination except for SR4L, which suffers from very low statistics.

After ensuring that the fit is stable and that uncertainties are accurately modelled, the observed data can be used to fit the expected background in signal regions, which allows for the possibility of new physics with the parameter of interest, μ_{sig}, to be considered. The compatibility of the

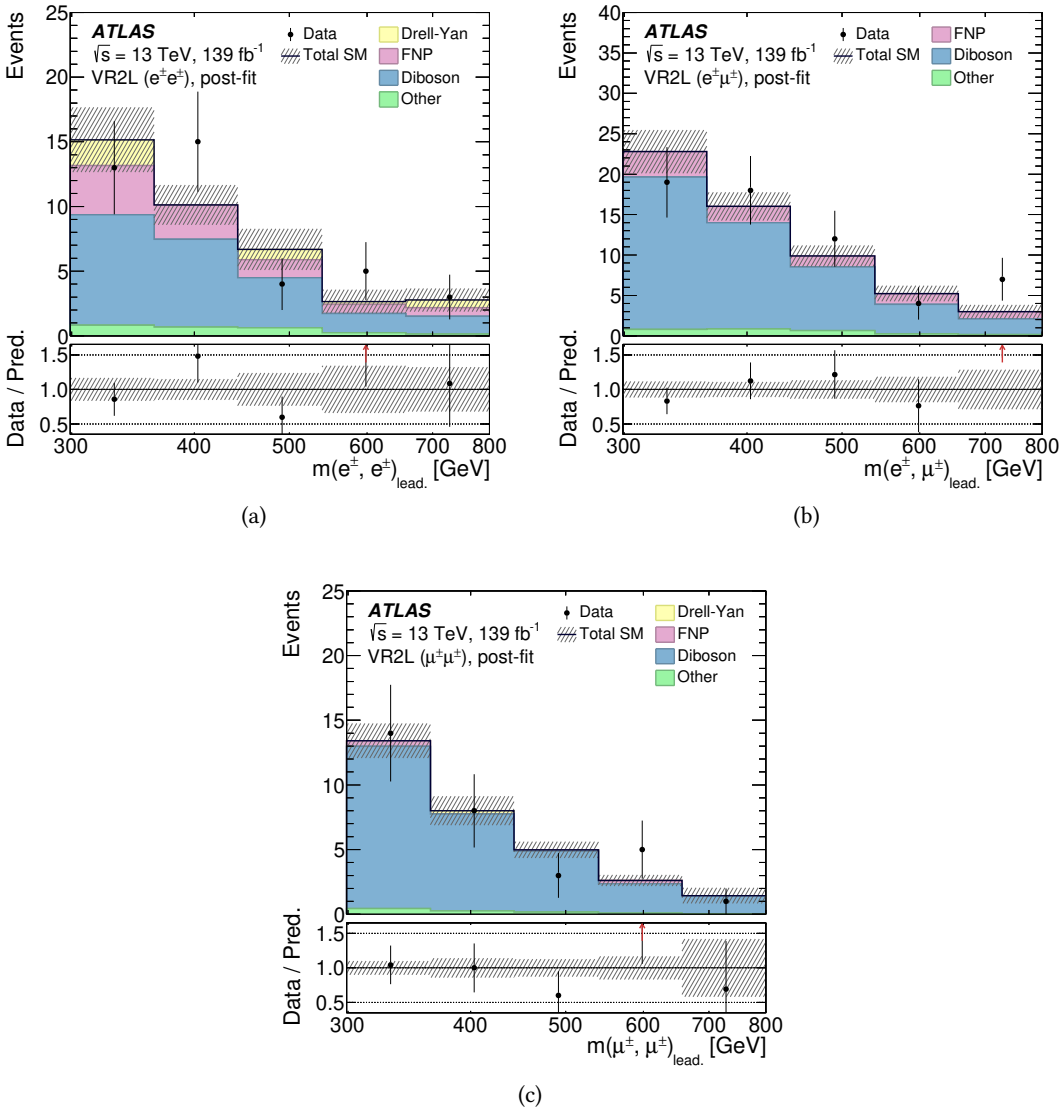

Figure 8.3: The two-lepton invariant mass, $m(\ell^{\pm}\ell'^{\pm})_{\text{lead}}$, distributions for data and SM background predictions in cut-based validation regions: (a) the electron–electron, (b) the electron–muon, and (c) the muon–muon two-lepton validation regions. Backgrounds from top-quark and multiboson processes are merged, forming the 'Other' category. The hatched bands include all systematic uncertainties after a background-only fit to data (post-fit), with the correlations between various sources considered. The last bin also includes any overflow entries. The error bars show statistical uncertainties. The lower panels show the ratio of the observed data to the estimated SM background. The red arrows indicate points that are outside the vertical range of the figure.

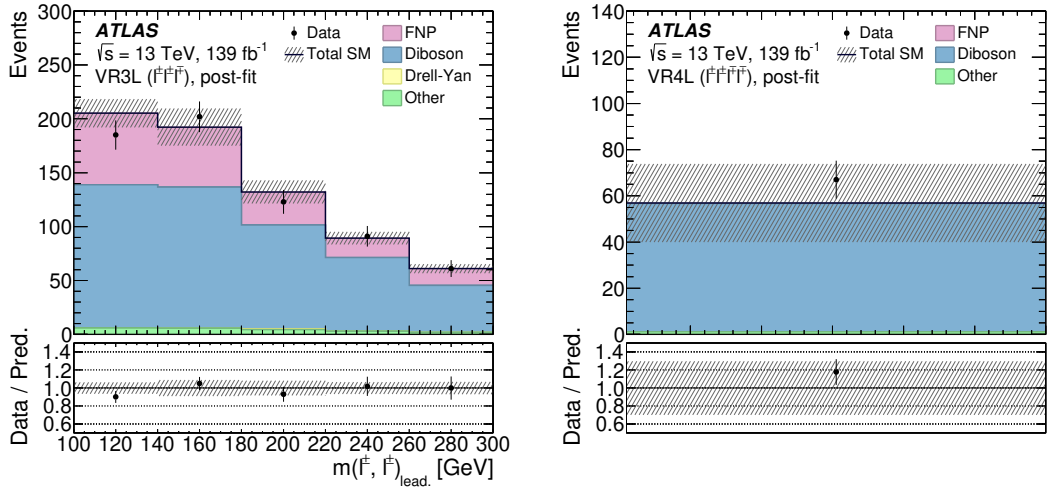

(a) (b)

Figure 8.4: (a) The two-lepton invariant mass, $m(\ell^{\pm}\ell'^{\pm})_{\text{lead}}$, distributions for data and SM background predictions in cut-based VR3L and (b) event yield in the cut-based VR4L. Backgrounds from top-quark and multiboson processes are merged, forming the 'Other' category. The hatched bands include all systematic uncertainties after a background-only fit to data (post-fit), with the correlations between various sources considered. The last bin also includes any overflow entries. The error bars show statistical uncertainties. The lower panels show the ratio of the observed data to the estimated SM background.

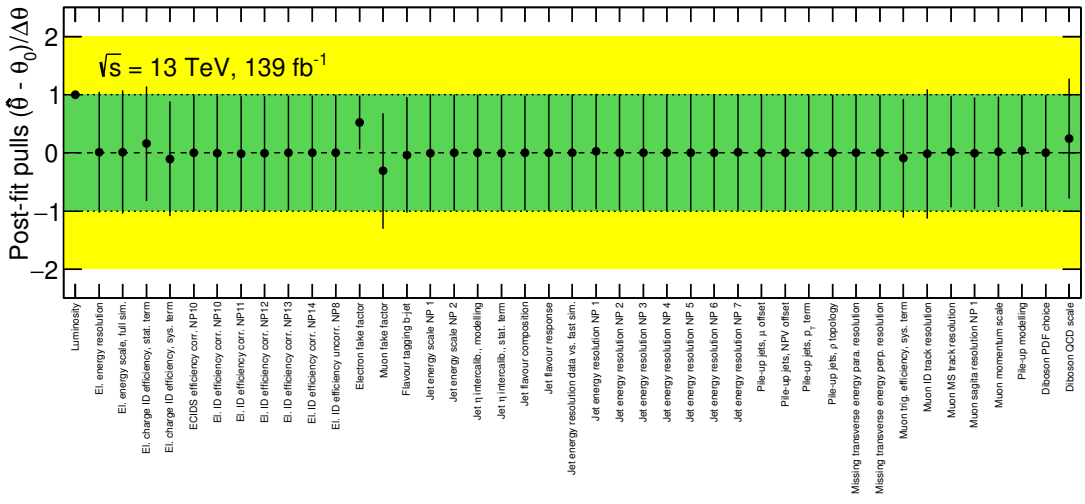

Figure 8.5: Post-fit nuisance parameters of the cut-based background-only fit expressed in units of standard deviation.

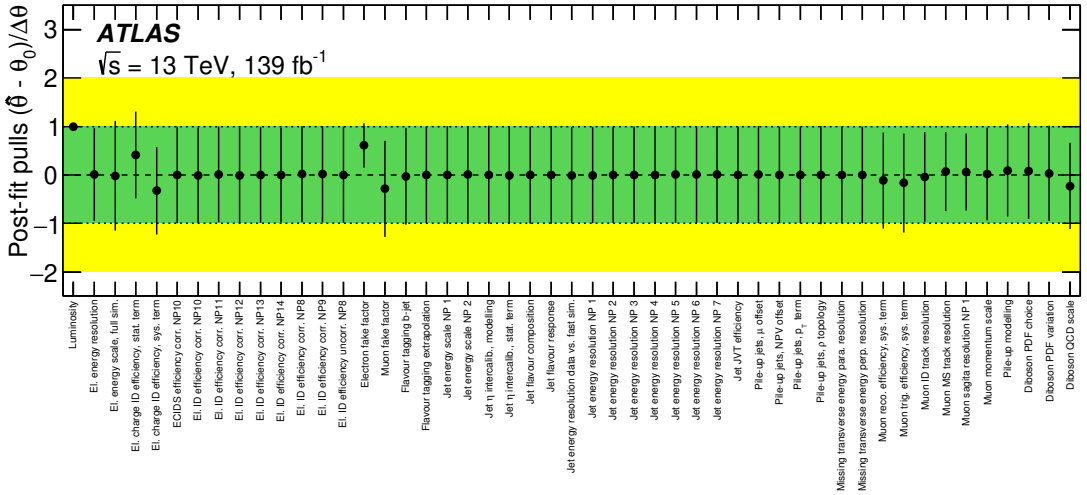

Figure 8.6: Post-fit nuisance parameters of the cut-based exclusion fit with real data in all regions, expressed in units of standard deviation.

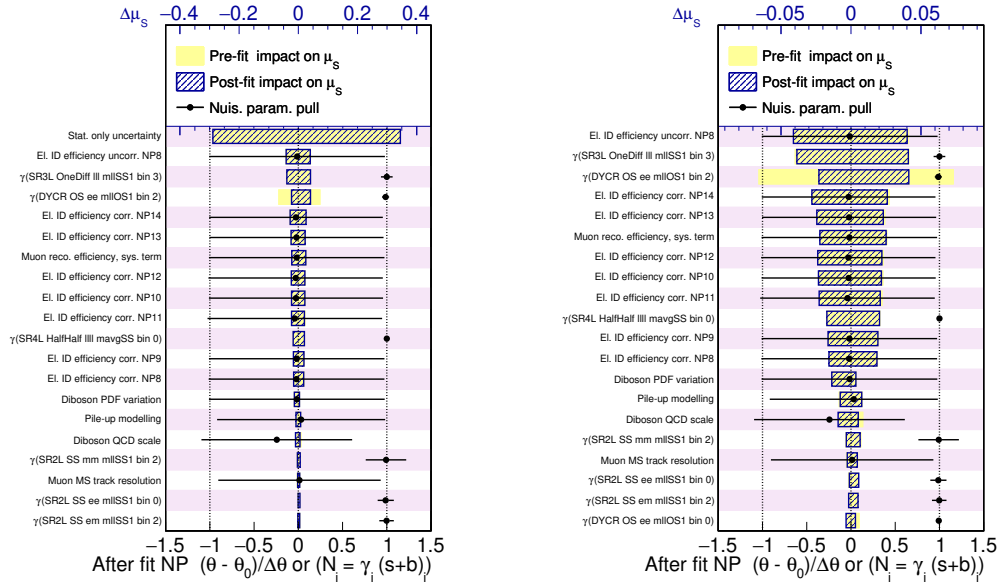

(a) (b)

Figure 8.7: Impact of systematic uncertainties on μ_{sig} in cut-based analysis, constructed by fixing one nuisance parameter at the time to its $\pm 1\sigma$ variations and minimising others. After the fit, the impact on μ_{sig} is inspected with respect to the nominal fit, where all parameters are free. The per-bin γ parameters affecting the fit are also visible. (a) The impact of systematic sources and MC statistical uncertainty, and (b) only the impact of systematic sources.

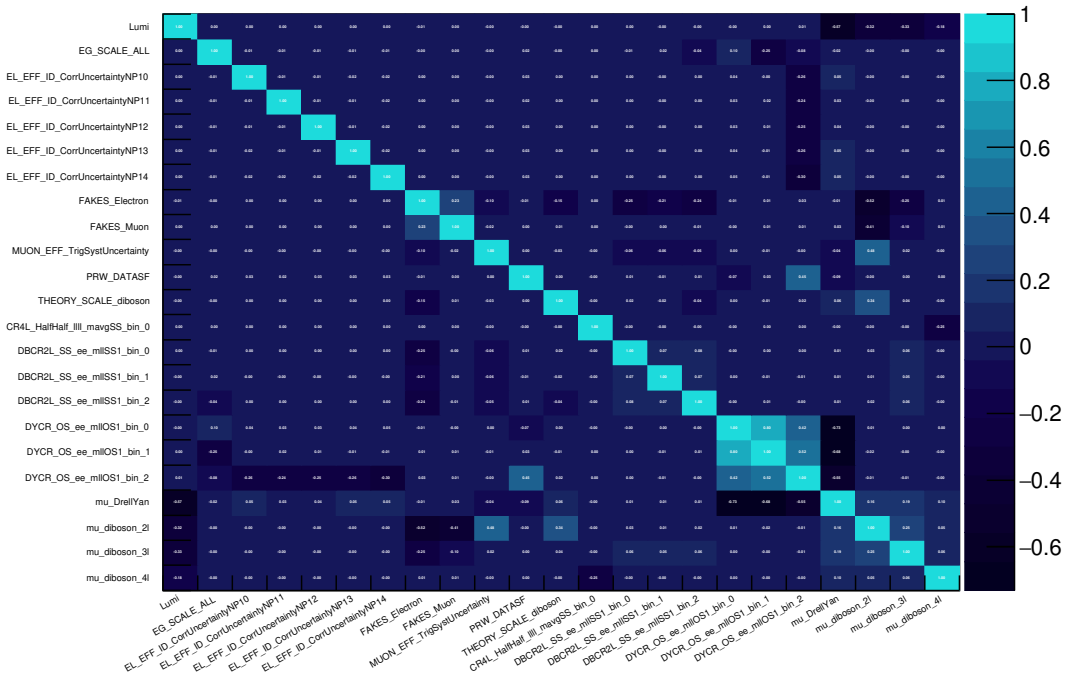

Figure 8.8: A reduced correlation matrix of nuisance parameters used in the fit in the cut-based analysis. Only correlations higher than 20% are shown.

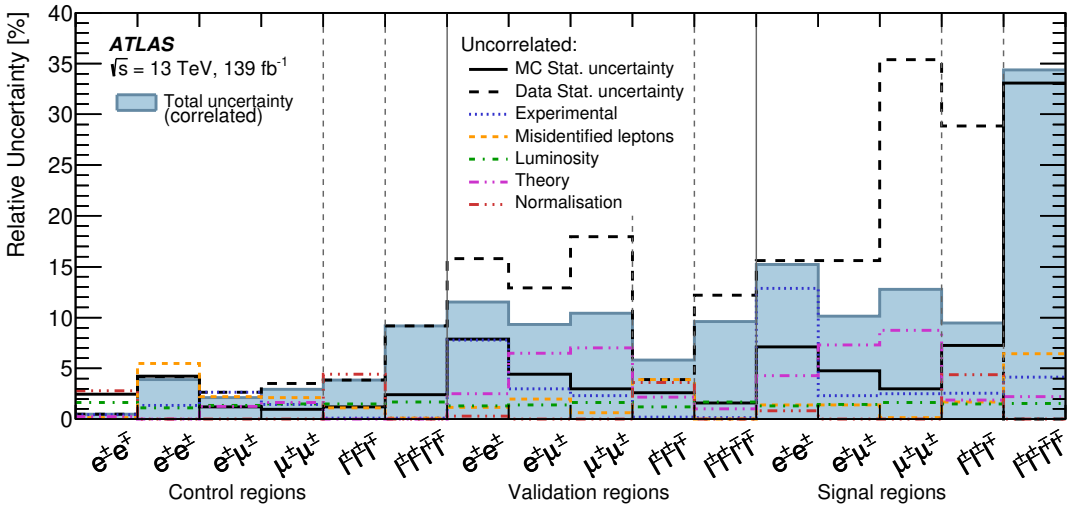

Figure 8.9: Relative contributions of different sources of statistical and systematic uncertainty in the total background yield estimation after the background-only fit in the cut-based analysis. Systematic uncertainties are calculated in an uncorrelated way by shifting in turn only one nuisance parameter from the post-fit value by one standard deviation, keeping all the other parameters at their post-fit values, and comparing the resulting event yield with the nominal yield. Validation regions do not constrain the normalisation factors or nuisance parameters. Individual uncertainties can be treated as correlated across the regions. Some backgrounds are constrained by the CR data and have strong anti-correlations as a result. The total background uncertainty is indicated by 'Total uncertainty'.

data with the expected background is evaluated in the SRs after the fit, and generally, good agreement is observed, yielding a p_0-value of 0.5 for the background-only hypothesis.

The signal regions were designed to fully exploit the pair production of the $H^{\pm\pm}$ boson and its boosted topology by applying selections that target same-charge high-p_{T} leptons. The observed and expected yields in all control, validation, and signal regions used in the analysis are presented in Figure 8.10 and summarised in Tables 8.2–8.4. Here, 'pre-fit' denotes the nominal simulated MC yields, and 'post-fit' denotes the simulated yields scaled with the normalisation factors obtained from the likelihood fit to the two-, three- and four-lepton control and signal regions. Generally, good agreement within statistical and systematic uncertainties between data and SM predictions is observed in various regions, demonstrating the validity of the background estimation procedure.

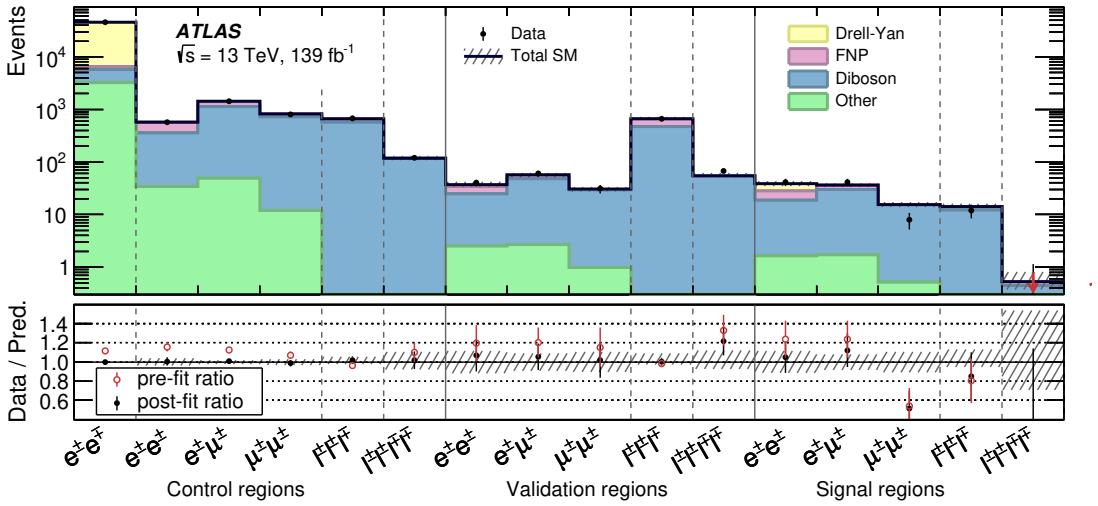

Figure 8.10: The numbers of observed and expected events in the control, validation, and signal regions for all channels in the cut-based analysis, split by lepton flavour and electric charge combination. The symbol ℓ only stands for light leptons ($\ell, \ell' = e,\ \mu$). The background expectation is the result of the background-only fit described in the text. The hatched bands include all post-fit systematic uncertainties with the correlations between various sources considered. The error bars show statistical uncertainties. FNP refers to the fake/non-prompt lepton background. Backgrounds from top-quark and multiboson processes are merged, forming the 'Other' category. The lower panel shows the ratio of the observed data to the estimated SM background.

The SR2L $m(\ell^{\pm}\ell'^{\pm})_{\mathrm{lead}}$ distributions for each lepton flavour channel are presented in Figure 8.11, and those of the three- and four-lepton signal regions are shown in Figure 8.12. No data event passed the SR4L selection, which is still within the expected yield. No significant excess is observed in any of the signal regions. Correlations between various sources of uncertainty are evaluated and used to estimate the total uncertainty in the SM background prediction. Some uncertainties, particularly those connected with the normalisation of the background contributions and the FNP background, are anti-correlated.

Figure 8.13 shows the upper limit on the cross-section as a function of the $H^{\pm\pm}$ boson mass, where decays into each leptonic final state are equally probable. Since the yields are low in some

Table 8.2: The number of predicted background events in cut-based control regions after the background-only fit, compared with the number of events observed in data. Uncertainties correspond to the uncertainties in the predicted event yields and their total is smaller than the sum of the components in quadrature due to correlations between these components. Due to rounding, the totals can differ from the sums of components. FNP refers to the fake/non-prompt lepton background. Backgrounds from top-quark and multiboson processes are merged, forming the 'Other' category. Background processes with a negligible yield are marked with a dash (–).

	DYCR e^+e^-	**DBCR2L** $e^\pm e^\pm$	**DBCR2L** $e^\pm\mu^\pm$	**DBCR2L** $\mu^\pm\mu^\pm$	**DBCR3L** $\ell^\pm\ell^\pm\ell^\mp$	**CR4L** $\ell^\pm\ell^\pm\ell^\mp\ell^\mp$
Observed events	46 116	570	1437	805	677	119
Total background	46 120 ± 220	571 ± 24	1400 ± 40	798 ± 28	675 ± 26	119 ± 11
Diboson	3200 ± 600	410 ± 70	1170 ± 70	686 ± 33	595 ± 31	116 ± 11
FNP lepton	660 ± 150	130 ± 70	220 ± 60	100 ± 17	69 ± 15	0.5 ± 0.4
Drell–Yan	39 100 ± 600	–	11.7 ± 2.0	–	–	–
Other	3230 ± 220	32 ± 7	45 ± 9	11.9 ± 0.9	10.9 ± 0.6	1.76 ± 0.13

Table 8.3: The number of predicted background events in cut-based validation regions after the background-only fit, compared with the number of events observed in data. Uncertainties correspond to the uncertainties in the predicted event yields and their total is smaller than the sum of the components in quadrature due to correlations between these components. Due to rounding, the totals can differ from the sums of components. FNP refers to the fake/non-prompt lepton background. Backgrounds from top-quark and multiboson processes are merged, forming the 'Other' category. Background processes with a negligible yield are marked with a dash (–).

	VR2L $e^\pm e^\pm$	**VR2L** $e^\pm\mu^\pm$	**VR2L** $\mu^\pm\mu^\pm$	**VR3L** $\ell^\pm\ell^\pm\ell^\mp$	**VR4L** $\ell^\pm\ell^\pm\ell^\mp\ell^\mp$
Observed events	40	60	31	662	67
Total background	37 ± 4	57 ± 5	30.5 ± 3.2	680 ± 40	56 ± 5
Diboson	22.0 ± 2.5	45 ± 5	28.4 ± 3.2	472 ± 30	55 ± 5
FNP lepton	9.2 ± 0.8	8.7 ± 1.3	0.79 ± 0.20	186 ± 29	–
Drell–Yan	3.6 ± 2.3	–	0.251 ± 0.028	0.92 ± 0.29	–
Other	2.5 ± 0.6	2.7 ± 0.5	0.98 ± 0.09	21.0 ± 1.5	1.30 ± 0.09

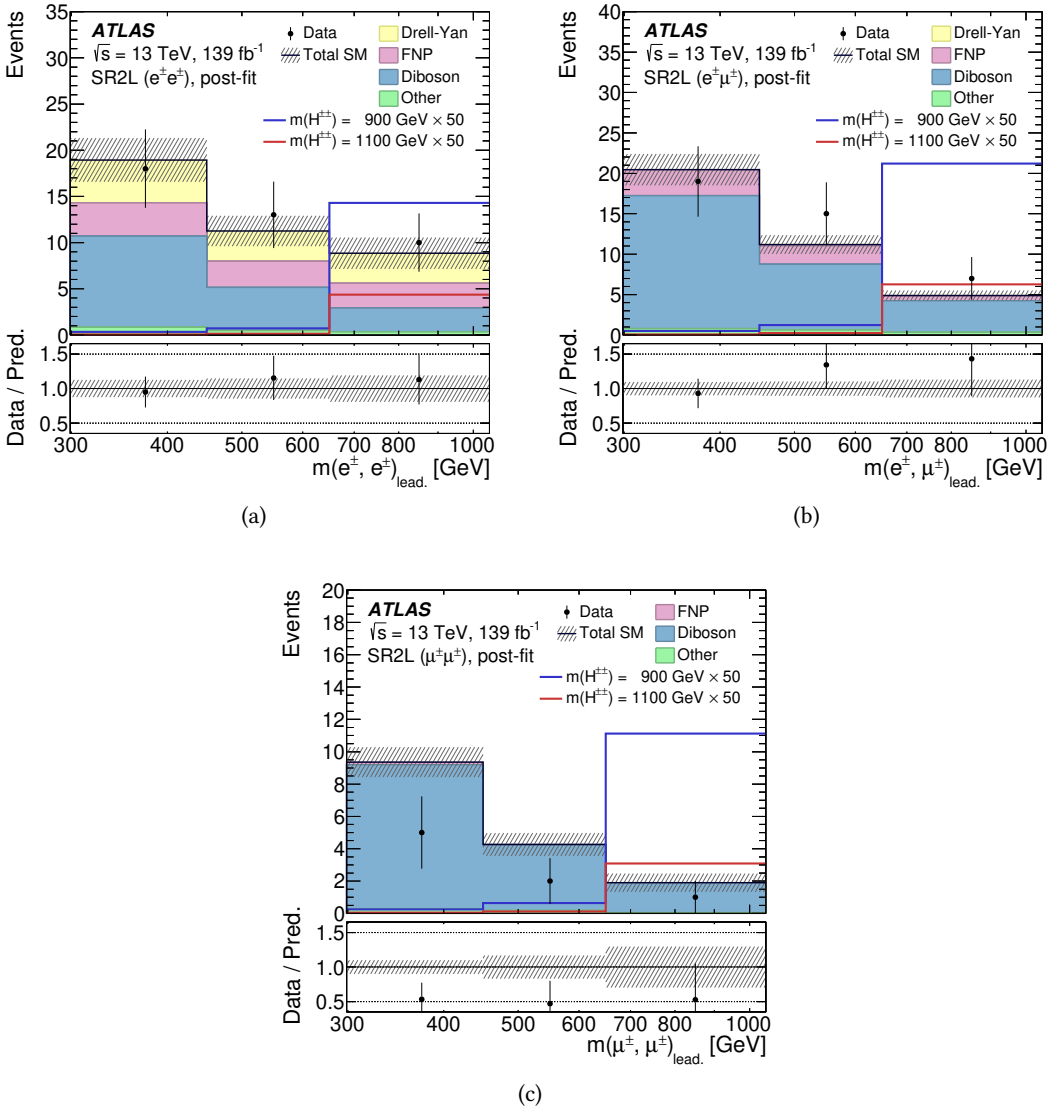

Figure 8.11: The two-lepton invariant mass, $m(\ell^{\pm}\ell'^{\pm})_{\text{lead}}$, distributions in cut-based signal regions, namely (a) the electron–electron two-lepton signal region (SR2L), (b) the electron–muon two-lepton signal region (SR2L) and (c) the muon–muon two-lepton signal region (SR2L). The background expectation is the result of the background-only fit described in the text. The hatched bands include all systematic uncertainties post-fit with the correlations between various sources considered. The solid coloured lines correspond to signal samples, normalised using the theory cross-section, with the $H^{\pm\pm}$ mass marked in the legend. The ×50 in the legend indicates the scaling of the signal yield to make it clearly visible in the plots. The error bars show statistical uncertainties. Backgrounds from top-quark and multiboson processes are merged, forming the 'Other' category. The last bin also includes any overflow entries. The lower panels show the ratio of the observed data to the estimated SM background. The binning presented in the figures is used in the fit.

Table 8.4: The number of predicted background events in cut-based signal regions after the background-only fit, compared with the number of events observed in data. Uncertainties correspond to the uncertainties in the predicted event yields and their total is smaller than the sum of the components in quadrature due to correlations between these components. Due to rounding, the totals can differ from the sums of components. FNP refers to the fake/non-prompt lepton background. Backgrounds from top-quark and multiboson processes are merged, forming the 'Other' category. Background processes with a negligible yield are marked with a dash (–).

	SR2L $e^{\pm}e^{\pm}$	**SR2L** $e^{\pm}\mu^{\pm}$	**SR2L** $\mu^{\pm}\mu^{\pm}$	**SR3L** $\ell^{\pm}\ell^{\pm}\ell^{\mp}$	**SR4L** $\ell^{\pm}\ell^{\pm}\ell^{\mp}\ell^{\mp}$
Observed events	41	41	8	12	0
Total background	40 ± 5	37.1 ± 3.1	14.8 ± 1.6	14.6 ± 1.3	0.62 ± 0.23
Diboson	21 ± 4	30.5 ± 3.3	14.2 ± 1.6	12.7 ± 1.2	0.44 ± 0.17
FNP lepton	7.8 ± 1.1	4.8 ± 1.1	0.158 ± 0.034	1.2 ± 0.5	0.11 ± 0.05
Drell–Yan	9.7 ± 3.5	0.15 ± 0.07	–	–	–
Other	1.56 ± 0.29	1.63 ± 0.25	0.52 ± 0.05	0.58 ± 0.06	0.067 ± 0.025

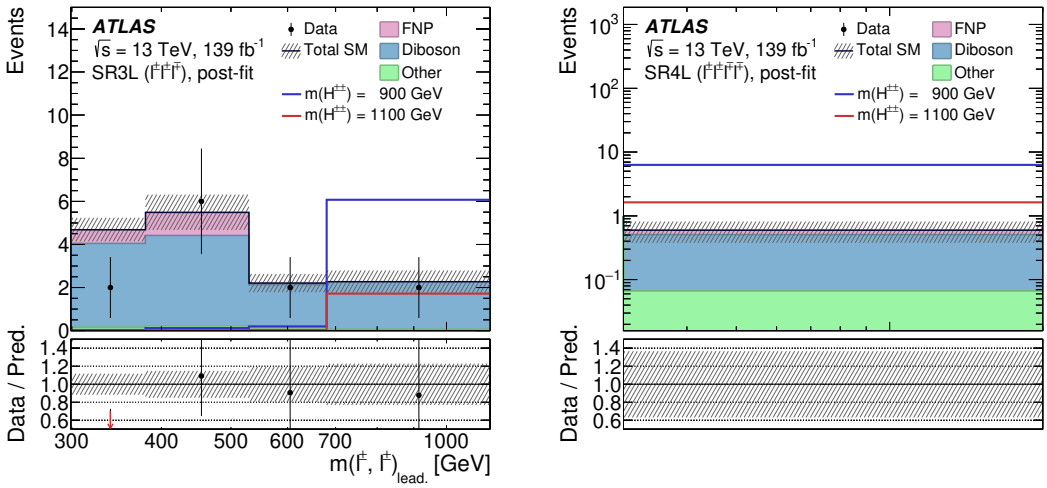

(a) (b)

Figure 8.12: (a) The two-lepton invariant mass, $m(\ell^{\pm}\ell'^{\pm})_{\text{lead}}$, distributions for data and SM background predictions in cut-based SR3L and (b) event yield in the cut-based SR4L, where no events are observed. The background expectation is the result of the background-only fit described in the text. The hatched bands include all systematic uncertainties post-fit with the correlations between various sources considered. The solid coloured lines correspond to signal samples, normalised using the theory cross-section, with the $H^{\pm\pm}$ mass marked in the legend. The error bars show statistical uncertainties. Backgrounds from top-quark and multiboson processes are merged, forming the 'Other' category. The lower panels show the ratio of the observed data to the estimated SM background. The binning presented in the figures is used in the fit. (a) The red arrow indicates a point that is outside the vertical range of the figure. The last bin also includes any overflow entries.

regions, the asymptotic approximation [200] cannot be used reliably, so 10^5 pseudo-experiments were run instead to obtain the final limits. The sensitivity of individual lepton multiplicity channels alongside older results is estimated using the asymptotic formulae and presented in Figure 8.14. Furthermore, a comparison between the limits obtained with asymptotic formulae and pseudo-experiments is presented in Figure 8.15.

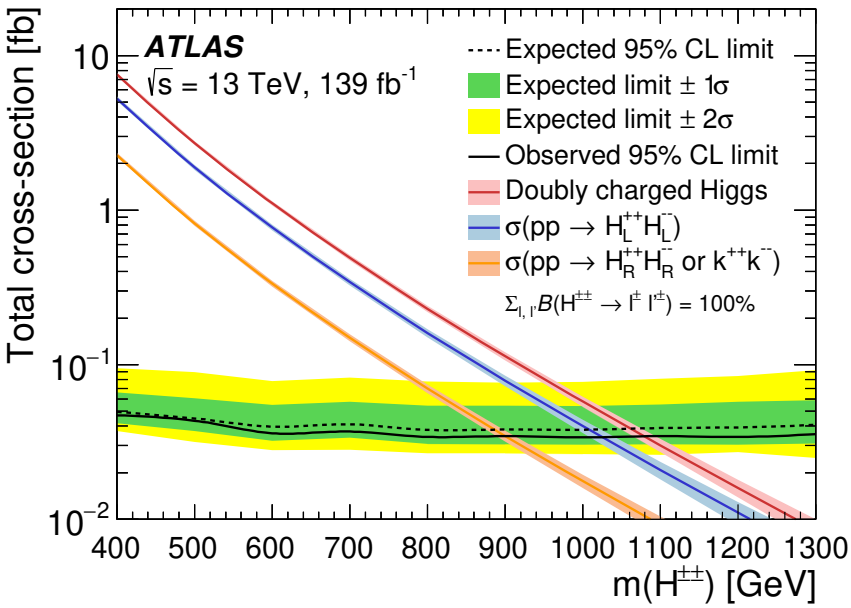

Figure 8.13: Observed (solid line) and expected (dashed line) 95% CL upper limits on the $H^{\pm\pm}$ pair production cross-section as a function of $m_{H^{\pm\pm}}$ in a cut-based analysis resulting from the combination of all analysis channels, assuming $\sum_{\ell\ell'} \mathcal{B}(H^{\pm\pm} \to \ell^{\pm}\ell'^{\pm}) = 100\%$, where $\ell, \ell' = e, \mu, \tau$. The surrounding green and yellow bands correspond to the ±1 and ±2 standard deviation ($\pm 1\sigma$ and $\pm 2\sigma$) uncertainty around the combined expected limit, respectively, as estimated using the frequentist approach, where toy experiments based on both the background-only and signal+background hypotheses are generated for this purpose. The theoretical signal cross-section predictions, given by the NLO calculation [65, 69], are shown as blue, orange and red lines for the left-handed $H_L^{\pm\pm}$, right-handed $H_R^{\pm\pm}$ (which is the same as the Zee–Babu $k^{\pm\pm}$), and a sum of the two LRSM chiralities, respectively, with the corresponding uncertainty bands.

The observed lower limits on the $H^{\pm\pm}$ mass within LRSMs (the Zee–Babu model) vary from 520 GeV to 1050 GeV (410 GeV to 880 GeV), depending on the lepton multiplicity channel, with $\sum_{\ell\ell'} \mathcal{B}(H^{\pm\pm} \to \ell^{\pm}\ell'^{\pm}) = 100\%$. The observed lower limit on the mass reaches 1080 GeV and 900 GeV when combining all three channels for LRSMs and the Zee–Babu model, respectively. The expected exclusion limit is 1065^{+30}_{-50} GeV for LRSMs and 880^{+30}_{-40} GeV for the Zee–Babu model, where the uncertainties of the limit are extracted from the $\pm 1\sigma$ band. The limit obtained from the four-lepton final state is the strongest and drives the combined result.

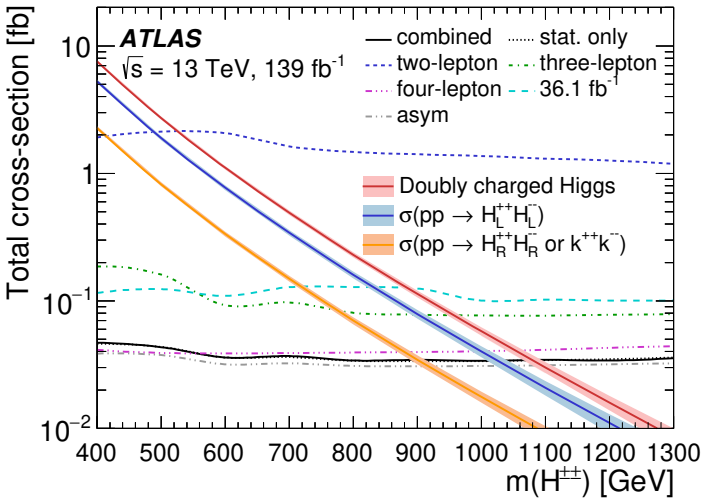

Figure 8.14: Breakdown of the observed 95% CL upper limits on the $H^{\pm\pm}$ pair production cross-section as a function of $m_{H^{\pm\pm}}$ in the cut-based analysis assuming $\sum_{\ell\ell'} \mathcal{B}(H^{\pm\pm} \to \ell^{\pm}\ell'^{\pm}) = 100\%$, where $\ell, \ell' = e, \mu, \tau$. The dashed blue, green, and purple lines indicate the observed limit using the two-, three- and four-lepton exclusive final states, respectively. The limit obtained from the four-lepton final state is the strongest and drives the combined result. The black lines show the combined observed limit obtained using the frequentist approach for a fit with only statistical uncertainties (dotted) and a fit with statistical and systematic uncertainties (solid). The grey line shows the limit using the asymptotic approximation [200], and the cyan dashed line shows the combined observed limit obtained analysing the first 36.1 fb^{-1} of Run 2 [77]. The theoretical signal cross-section predictions, given by the NLO calculation [65, 69], are shown as blue, orange and red lines for the left-handed $H_L^{\pm\pm}$, right-handed $H_R^{\pm\pm}$ (which is the same as the Zee–Babu $k^{\pm\pm}$), and a sum of the two LRSM chiralities, respectively, with the corresponding uncertainty bands.

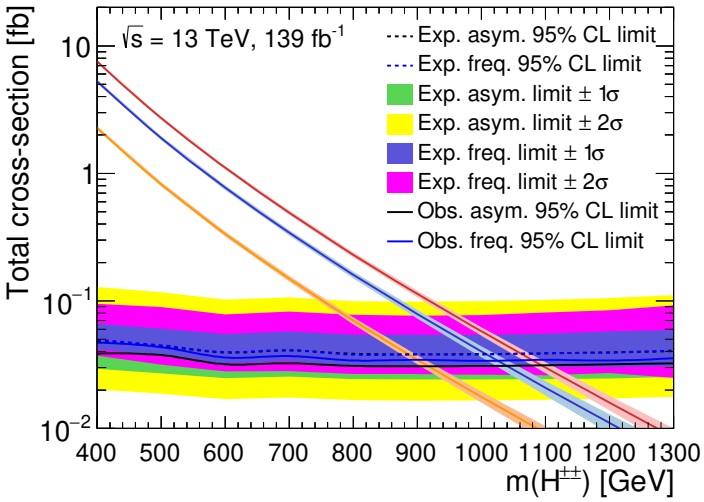

Figure 8.15: A comparison between observed 95% CL exclusion limits obtained with asymptotic formulae or pseudo-experiments in the cut-based analysis. Pseudo-experiments are overlaid over central values shown in blue, with uncertainty bands in shades of blue and pink.

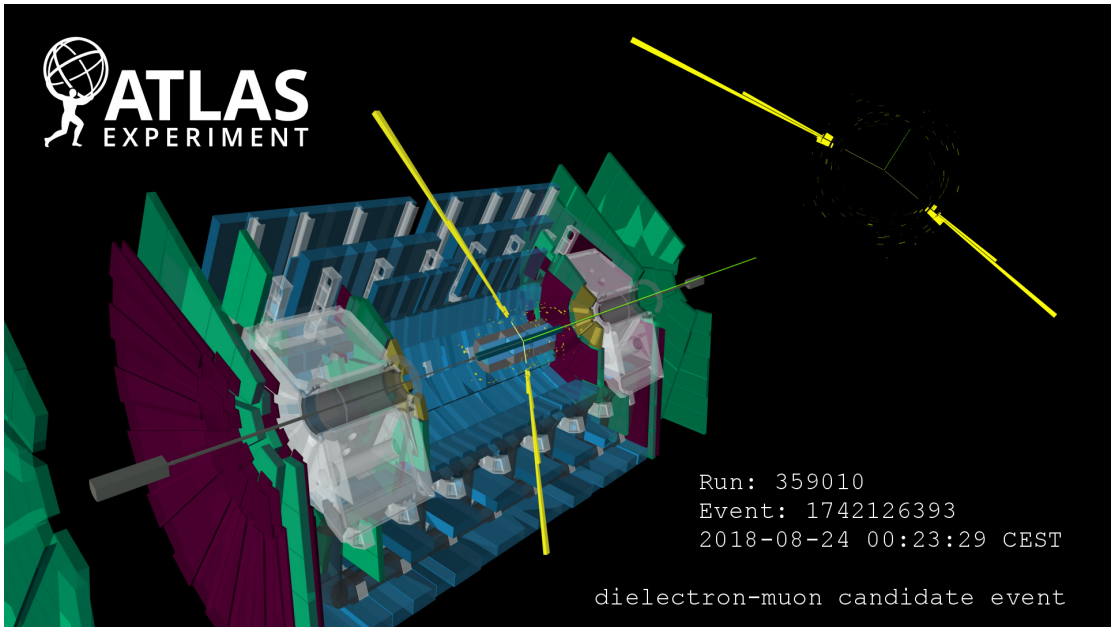

Figure 8.16: Display of a candidate $pp \to H^{++}H^{--}$ event from proton–proton collisions recorded by ATLAS with LHC stable beams at a collision energy of 13 TeV. The candidate event is reconstructed in the two-electron, one muon final state $e^+e^-\mu^-$. The display on the right-hand side shows the $r-\varphi$ view, while the central display shows a 3-dimensional view. The path of the muon is indicated by the green line and the paths of the electrons are indicated by yellow lines. The energy deposits in the electromagnetic calorimeter are shown with yellow boxes. The display only shows leptons passing the analysis minimal p_{T} requirement $p_{\mathrm{T}} > 40$ GeV. The back-to-back electrons have transverse momenta of 517 GeV (e^+) and 306 GeV (e^-), while the muon is very close to the beamline and thus has a lower $p_{\mathrm{T}} = 82$ GeV. The invariant mass of the three-lepton system is 1257 GeV and the invariant mass of the same-charge electron–muon pair is 600 GeV.

CHAPTER 9

Multivariate Analysis

This chapter presents the studies of the upgraded $H^{\pm\pm}$ analysis using the multivariate approach on the same Run 2 dataset. The analysis strategy is presented first, followed by the preliminary results.

9.1 Analysis Strategy and Selection

As machine learning (ML) techniques are used increasingly in high-energy physics and generally provide better results, it is natural to implement basic ML models to improve the results of the cut-based analysis with better discrimination between signal and background events. Two different algorithms are tested: a gradient boosting on decision trees (BDT) implemented in *CatBoost* [210], and a deep neural network (NN) provided by an ML library *PyTorch* [211]. The goal is to compare their performance on preselected data and MC events and finally proceed with the better one. Therefore, the same input structure is used in both cases.

Firstly, very loose preselections of events disregarding lepton flavour or charge are defined, requiring precisely two, three, or four leptons, for each lepton multiplicity separately. A b-jet veto is applied to reject the SM backgrounds involving heavy flavour jets. Additionally, a lower constraint on the invariant mass of the two-lepton system, $m(\ell\ell)$, is introduced at 100 GeV to suppress leptons originating from the Drell–Yan $Z \to ee$ process, whose charges might potentially be misidentified.

The MC events are categorised as signal or background events using binary classification, which is a supervised learning algorithm, meaning that the simulated events are labelled according to their type. When the algorithm's training on labelled MC samples is finished, the algorithm can be applied to observed data. All signal mass points are trained at the same time. However, since the topologies of two-, three- and four-lepton final states are different, a specific ML model is trained for each lepton multiplicity. All MC samples are randomly split into training, validation and test sets in the 50% : 25% : 25% ratio, but using the *stratified sampling*, each preserving the same fraction of different background and signal events. Each model is firstly trained using approximately 50 low- and high-level physics variables as input *features*, but the number is then reduced by examining the physics impact on the selection and considering the feature importance method provided by the BDT algorithm. The final list of features used in two-, three- and four-lepton ML models is presented in Figure 9.1. The subscripts in ℓ represent the leading (1), sub-leading (2) or third leading (3) lepton in p_{T}. The m_{T} stands for the transverse mass and H_{T} for the scalar sum of transverse momenta, with "lep" denoting only their leptonic part. The $\overline{m}_{\mathrm{SC}}$ and $\overline{m}_{\mathrm{OC}}$ are the average invariant masses of two same- and opposite-charge lepton pairs, respectively.

The three most discriminating variables are $N_{b\text{-jets}}$, $m(\ell^{\pm}\ell'^{\pm})_{\text{lead}}$, and $\Delta R(\ell^{\pm}\ell'^{\pm})_{\text{lead}}$ in the two-lepton case, $m(\ell^{\pm}\ell'^{\pm})_{\text{lead}}$, $\Delta R(\ell_2\ell'_3)$, and $H_{\text{T}}^{\text{lep}} + E_{\text{T}}^{\text{miss}}$ in the three-lepton case, and $m(\ell^{\pm}\ell'^{\pm})_{\text{sublead}}$, $m(\ell^{\pm}\ell'^{\pm})_{\text{lead}}$, and $\overline{m}_{\text{OC}}$ in the four-lepton case.

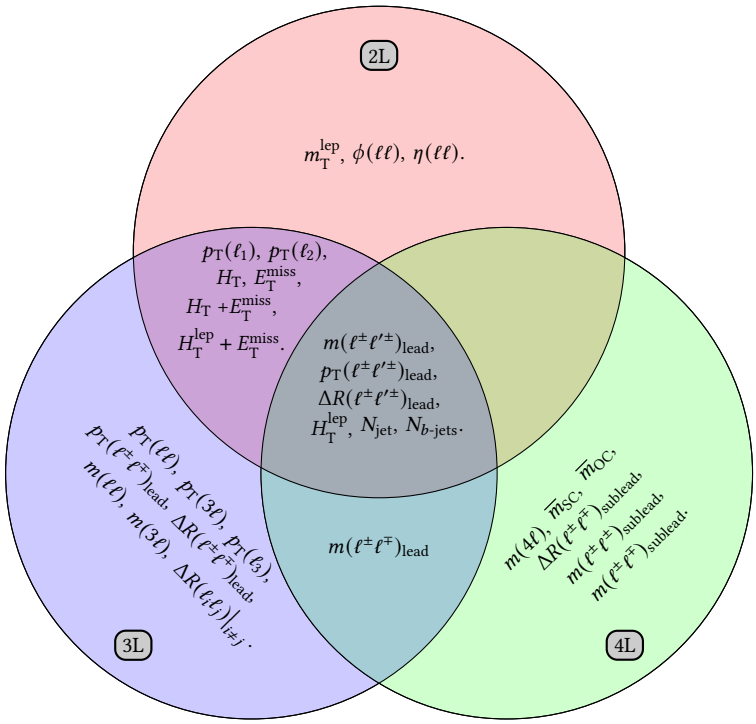

Figure 9.1: List of features used in the three machine learning models, one for each lepton multiplicity. The features were selected based on the CatBoost feature importance algorithm, finally yielding 15, 23, and 13 features for two-, three- and four-lepton channels, respectively.

The BDT model was learning over 5000 iterations for each lepton multiplicity with no additional requirements on input hyperparameters but was early stopped when reaching and maintaining the best validation score for five consecutive iterations to prevent overfitting. On the other hand, the NN models consisted of three hidden layers, each having 256 neurons that were activated by the ReLU activation function. The last output layers used the sigmoid function to map the predictions into a $[0, 1]$ interval so the output can be interpreted as signal probability or likelihood. The output of a classifier is referred to as the *MVA score*. However, after the region optimisation, it was found that the ML performs so well, separating background and signal to values very close to 0 and 1, that it was challenging to construct sensible region cuts and definitions. It was decided to use the raw NN output, known as *logit MVA score*, instead. Logits are interpreted to be the unnormalised (before taking the sigmoid function) predictions. The models were trained in batches of 128 events for 50 epochs. Nonetheless, due to early stopping, the training stopped at 10, 22, and 35 epochs for two-, three- and four-lepton ML models, respectively. In addition, correct signal mass values were added as input features to the model for signal samples, while a randomly sampled value, chosen from the studied mass range, was assigned to other samples, including data. This procedure is known as a *parametrised neural network* [212], giving the model the ability to interpolate between the mass points and

replace sets of classifiers trained at individual values. Furthermore, it simplifies the training process and improves performance at intermediate values.

A representative comparison of the two algorithms' performance is presented in Figure 9.2, where the ROC curve shows the true positive rate against the false positive rate. Although both give good results, the NNs outperform the BDTs for each lepton multiplicity, regularly reaching AUC[1] scores above 0.99. The difference in performance is also evident from the distribution of event classification scores, presented in Figure 9.2(a), with the NN showing superior discriminative power. Consequently, the results from neural networks are used to define selection criteria for multivariate (MVA) analysis regions.

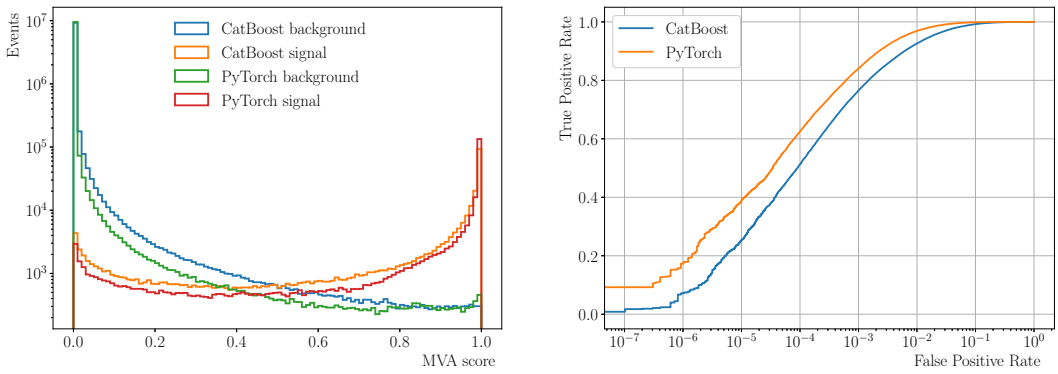

(a) (b)

Figure 9.2: Performance comparison of two distinct machine learning models, showing (a) event classification score distribution for three-lepton events and (b) ROC curve for two-lepton events. The event distribution is not weighted by cross-section or any other efficiency corrections. Therefore, each entry represents one simulated event. Note the logarithmic x-axis in (b).

The regions for the ML approach are constructed using the knowledge obtained from the cut-based analysis. Due to the low-statistics limitations, the cuts are loosened as much as possible. A compromise between signal significance and the number of selected events still needs to be made. The MVA score distributions of inclusive (at the state of preselection) two-, three- and four-lepton channels are presented in Figure 9.3, with the weights and efficiency corrections applied. The main discriminating variable, and the one, also used in the fit described in Section 9.2, is the logit MVA output score, which encodes the probability of an event being a signal event. The logit MVA distributions for the same setup are presented in Figure 9.4.

A logit MVA score above 0 is required to pass the SR2L and SR4L selection criteria and achieve good signal significance. The topology of three-lepton events allows the NN to extract signal from the background more efficiently, so the lower bound on the logit MVA score is increased to 3 in SR3L. The rest of the MVA range is used for validation regions, while the CRs are defined using other variables, e.g. $m(\ell^{\pm}\ell'^{\pm})_{\text{lead}}$, $p_{\text{T}}(\ell^{\pm}\ell'^{\pm})_{\text{lead}}$ and $\overline{m}_{\text{SC}}$ cuts, similarly as in the cut-based

[1] The AUC stands for the area under the ROC curve and is a metric widely used to evaluate the performance of a binary classification model.

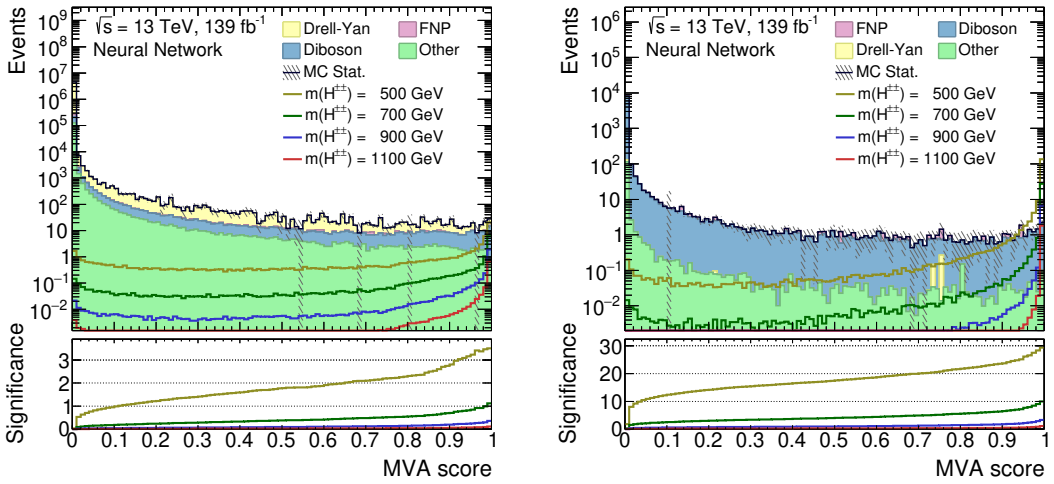

(a) (b)

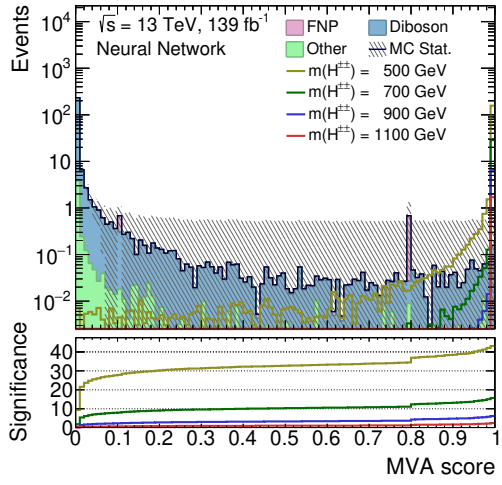

(c)

Figure 9.3: The MVA score distribution in flavour-inclusive regions. The (a) two-lepton, (b) three-lepton, and (c) four-lepton regions, are presented. No preselection cuts other than b-jet veto and lepton multiplicity are applied to the MC samples. The integrated significance represents the cumulative bin significance as defined in Eq. 5.1. The hatched band indicates the statistical uncertainties.

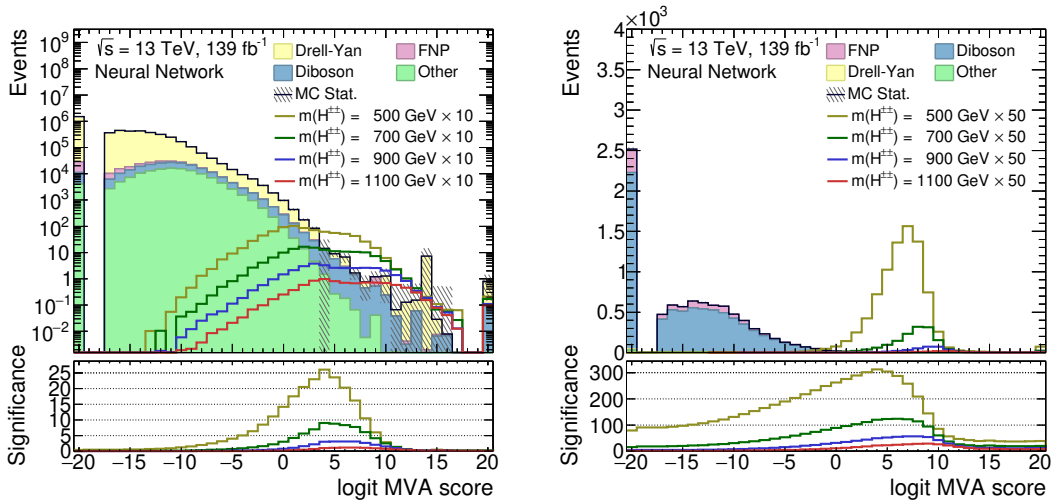

(a) (b)

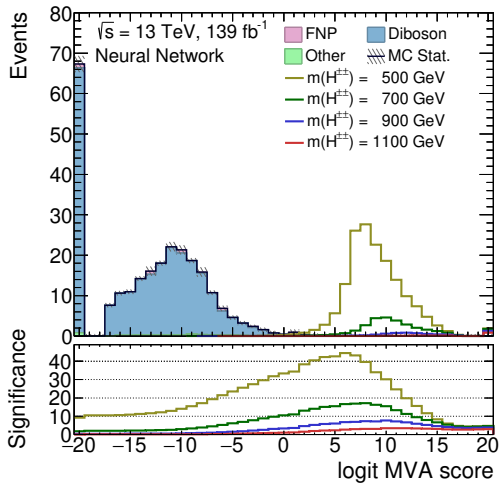

(c)

Figure 9.4: The logit MVA score distribution in flavour-inclusive regions. The (a) two-lepton, (b) three-lepton, and (c) four-lepton regions, are presented. No preselection cuts other than b-jet veto and lepton multiplicity are applied to the MC samples. The integrated significance represents the cumulative bin significance as defined in Eq. 5.1. The hatched band indicates the statistical uncertainties.

analysis. These cuts additionally suppress the Drell–Yan background, as seen from the N-1 distributions in Figures 9.5 and 9.6. A Z-boson veto is applied in SR3L and VR3L regions to increase signal significance. Contrary, the DBCR3L is defined by requiring at least one Z boson lepton pair candidate. The Drell–Yan events in the VR2L region (especially ee channel) are found to bring large uncertainties, so additional cut $|\eta(\ell, \ell')| < 3.0$ is implemented.

The dominant background contribution in the signal regions comes from diboson events with a low 'Other' contribution, which is composed of top-quark and multiboson events.

The logit MVA score variable is divided into three bins, used in the likelihood fit for all CRs and VRs, where the first and last bins contain any under- or overflow values. Due to the low number of events passing the SR requirements, only the total event yield is fitted there.

The selection criteria for each region defined in the multivariate analysis are summarised in Table 9.1. The N-1 distributions for inclusive two-, three- and four-lepton channels are presented in Figures 9.5 and 9.6.

Table 9.1: Summary of regions defined in the machine-learning analysis approach. The table is split into two horizontal blocks: the upper block indicates the final states, and the second indicates the event selection criteria for the region. The application of a selection requirement is labelled by a checkmark (✓) or by *inverted* when it is inverted. The three- and four-lepton regions include all light-lepton flavour combinations. No selection is applied when a dash is present in the corresponding cell. Additionally, a b-jet veto is applied in all regions.

	Control regions				**Signal regions**			**Validation regions**		
	DYCR	DBCR2L	DBCR3L	CR4L	SR2L	SR3L	SR4L	VR2L	VR3L	VR4L
Channel	e^+e^-	$e^\pm e^\pm$ $e^\pm\mu^\pm$ $\mu^\pm\mu^\pm$	$\ell^\pm\ell^\pm\ell^\mp$	$\ell^+\ell^+\ell^-\ell^-$	$e^\pm e^\pm$ $e^\pm\mu^\pm$ $\mu^\pm\mu^\pm$	$\ell^\pm\ell^\pm\ell^\mp$	$\ell^+\ell^+\ell^-\ell^-$	$e^\pm e^\pm$ $e^\pm\mu^\pm$ $\mu^\pm\mu^\pm$	$\ell^\pm\ell^\pm\ell^\mp$	$\ell^+\ell^+\ell^-\ell^-$
logit MVA score	-	-	-	-	≥ 0	≥ 3	≥ 0	< 0	< 3	< 0
$m(\ell^\pm\ell'^\pm)_{\text{lead}}$ [GeV]*	≥ 300	[200, 300)	-	-	≥ 300	-	-	≥ 300	-	-
$p_{\text{T}}(\ell^\pm\ell'^\pm)_{\text{lead}}$ [GeV]	-	-	-	-	≥ 300	-	-	-	-	-
$\overline{m}_{\text{SC}}$ [GeV]	-	-	-	< 200	-	-	≥ 200	-	-	≥ 200
$\lvert\eta(\ell, \ell')\rvert$	-	-	-	-	-	-	-	< 3.0	-	-
Z-boson veto	-	-	inverted	-	-	✓	-	-	✓	-

*Note that the cut on the invariant mass of the leading **opposite-charge** lepton pair is applied in DYCR region.

9.2 Results of the Multivariate Analysis

The analysis strategy for the multivariate approach closely follows the cut-based one. The final normalisations of Drell–Yan and diboson MC samples are derived in the simultaneous likelihood fit to data in dedicated Drell–Yan and diboson CRs, as described in Section 9.1. Free-floating parameters are introduced to fit the yields in the control regions and are used to normalise relevant backgrounds in the signal and validation regions. After a background-only likelihood fit, the normalisation factors are close to their SM predictions, with the Drell–Yan contribution corrected for about 17%, and are listed in Table 9.2. The diboson yield is described by three free parameters, one each for the two-, three- and four-lepton multiplicity channels, while one parameter is defined to scale the Drell–Yan contribution.

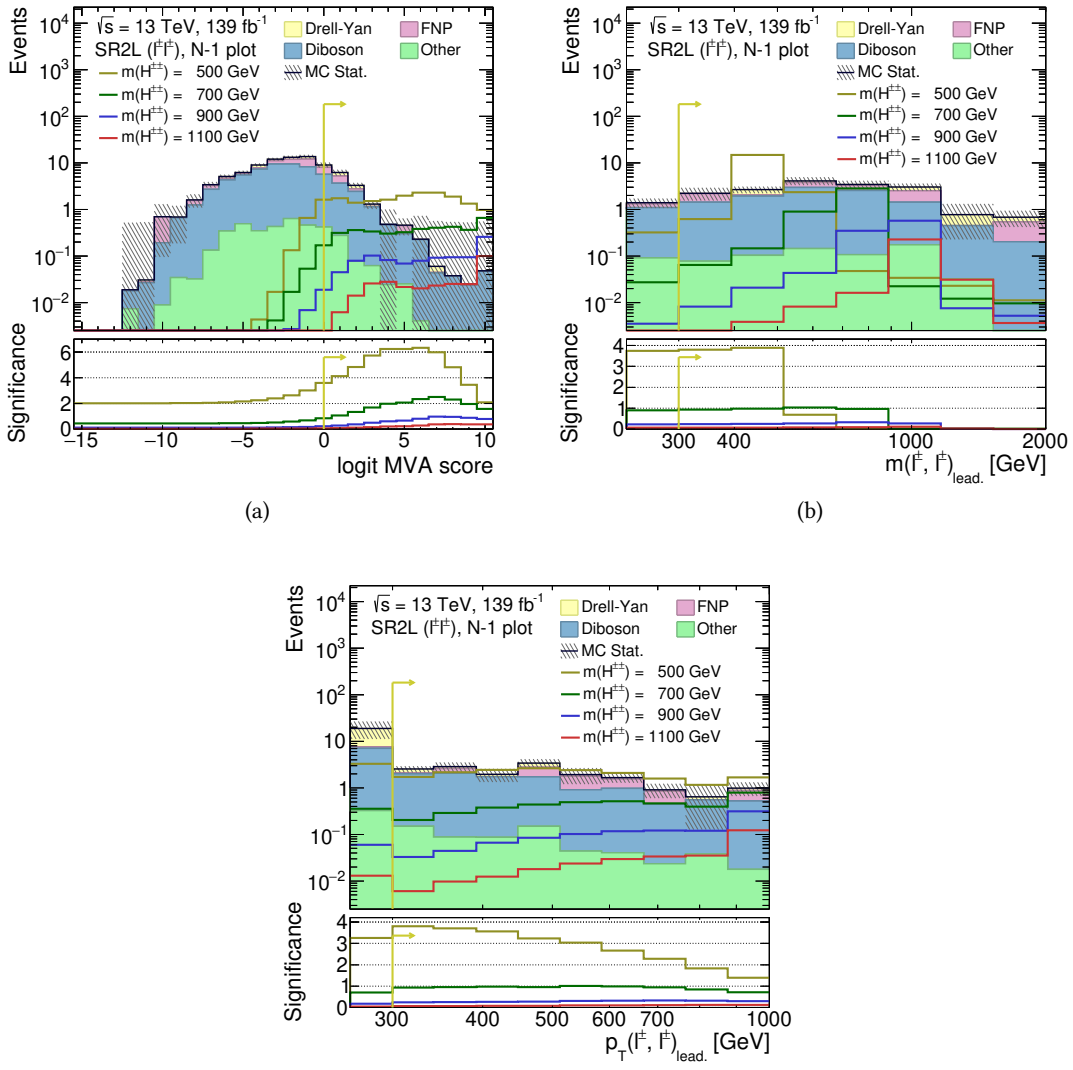

(a) (b)

(c)

Figure 9.5: The N-1 distributions in the inclusive SR2L region of the MVA analysis. The (a) logit MVA score, (b) $m(\ell^{\pm}\ell'^{\pm})_{\text{lead}}$, and (c) $p_{\text{T}}(\ell^{\pm}\ell'^{\pm})_{\text{lead}}$ are presented. The significance represents the cumulative bin significance as defined in Eq. 5.1. The hatched band indicates the statistical uncertainties.

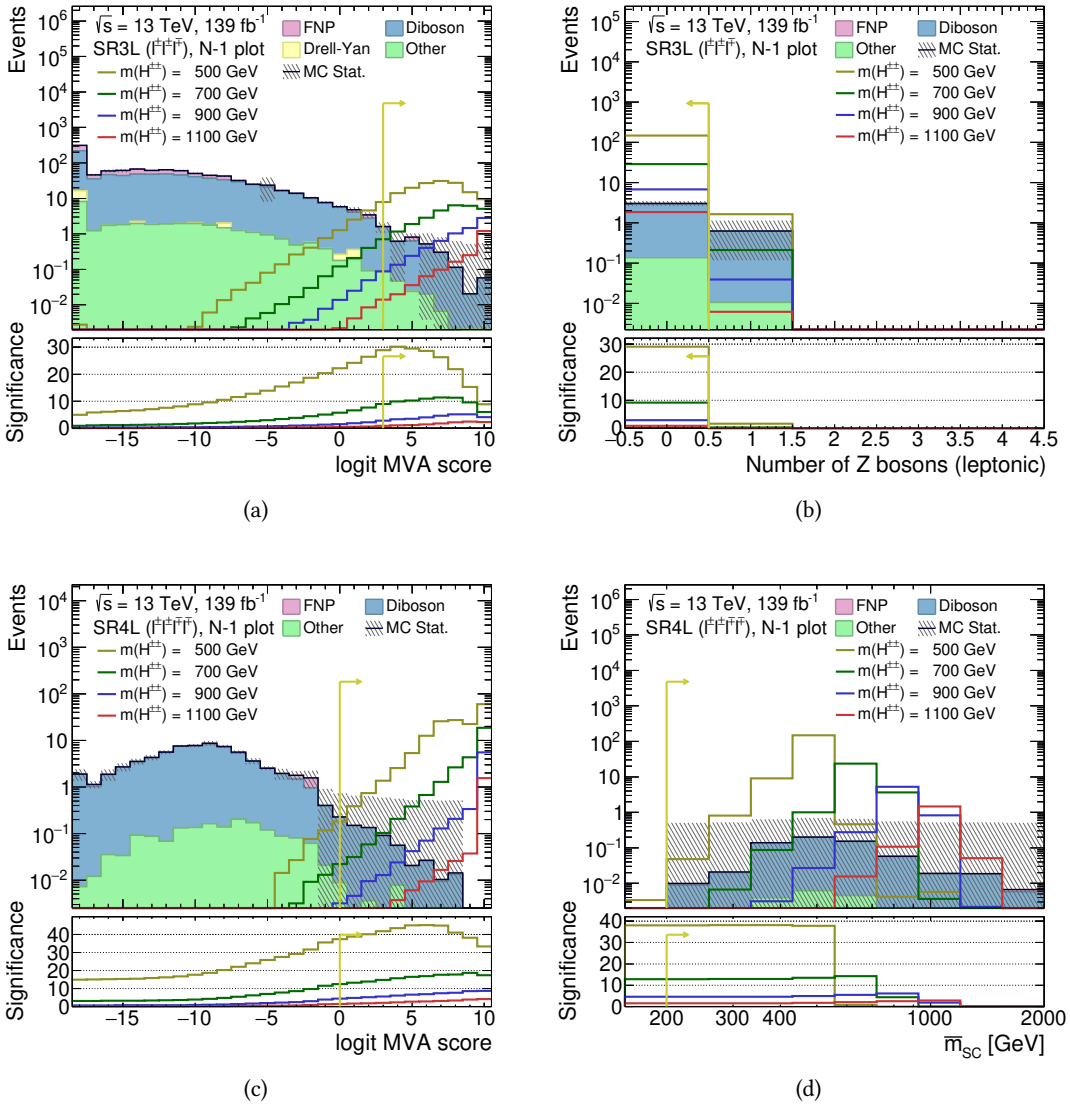

Figure 9.6: The N-1 distributions in the inclusive SR3L (upper plots) and SR4L (lower plots) regions of the MVA analysis. The (a) logit MVA score in SR3L, (b) number of lepton candidates originating from Z boson in SR3L, (c) logit MVA score in SR4L, and (d) $\overline{m}_{\mathrm{SC}}$ in SR4L are presented. The significance represents the cumulative bin significance as defined in Eq. 5.1. The hatched band indicates the statistical uncertainties.

Table 9.2: Drell–Yan and diboson normalisation scale factors with their corresponding uncertainties are listed for the multivariate analysis.

MC process	Normalisation factor
Drell–Yan	1.17 ± 0.03
diboson 2ℓ	1.08 ± 0.08
diboson 3ℓ	0.90 ± 0.03
diboson 4ℓ	1.07 ± 0.08

Post-fit binned logit MVA output distributions in the control regions are shown in Figures 9.7 and 9.8. The derived normalisation is assessed in the VRs. Good agreement between data and prediction is observed, as seen in Figures 9.9 and 9.10. Additional selected distributions are shown in Appendix C.

The pull plots, showing the uncertainties that are constrained using data from CRs and have a larger than 5% effect on either the pull average or its standard deviation are presented in Figures 9.11 and 9.12 for background-only and full likelihood fit, respectively. The full likelihood fit in the multivariate approach exhibits more scattered pulls than the one in the cut-based analysis, which may be the reason that the fit was also much harder to control. Note that the following results are preliminary and that the fit procedure is not refined as it is not always stable.

The impact of statistical and systematic uncertainties on signal strength, μ_{sig}, can be studied using ranking plots. The real data is used for all regions except SRs in the fit. An injected MC signal is used in the SRs instead. The dominant uncertainties are presented in Figure 9.13, with the per-bin γ parameters included. The dominant uncertainty is statistical, similarly as in the cut-based approach reaching almost 35%, while the leading systematic uncertainties are multiple muon NPs, followed by SR4L γ factor and later different electron reconstruction efficiencies. The systematic uncertainties are higher than in the cut-based analysis.

Finally, the correlations between individual NPs are studied using the correlation matrix, presented in Figure 9.14. Only NPs having at least the absolute value of the correlation of magnitude 0.2 or higher with another NP are shown in the matrix.

The total relative background systematic uncertainty after the background-only fit and its breakdown into components is presented in Figure 9.15. Uncertainties are much larger than in the cut-based analysis and are not entirely under control in these preliminary results. The inspection of systematic uncertainties showed that there is a lot of bin migration, especially in the Drell–Yan background, since the logit MVA output is a very sensitive variable, whose values can vary a lot with just small NP variations. The Drell–Yan contribution has a 100% uncertainty in the VR2L *ee* channel.

The observed and expected yields in all control, validation, and signal regions used in the analysis are presented in Figure 9.16 and summarised in Tables 9.3–9.5. Here, 'pre-fit' denotes the nominal simulated MC yields, and 'post-fit' denotes the simulated yields scaled with the

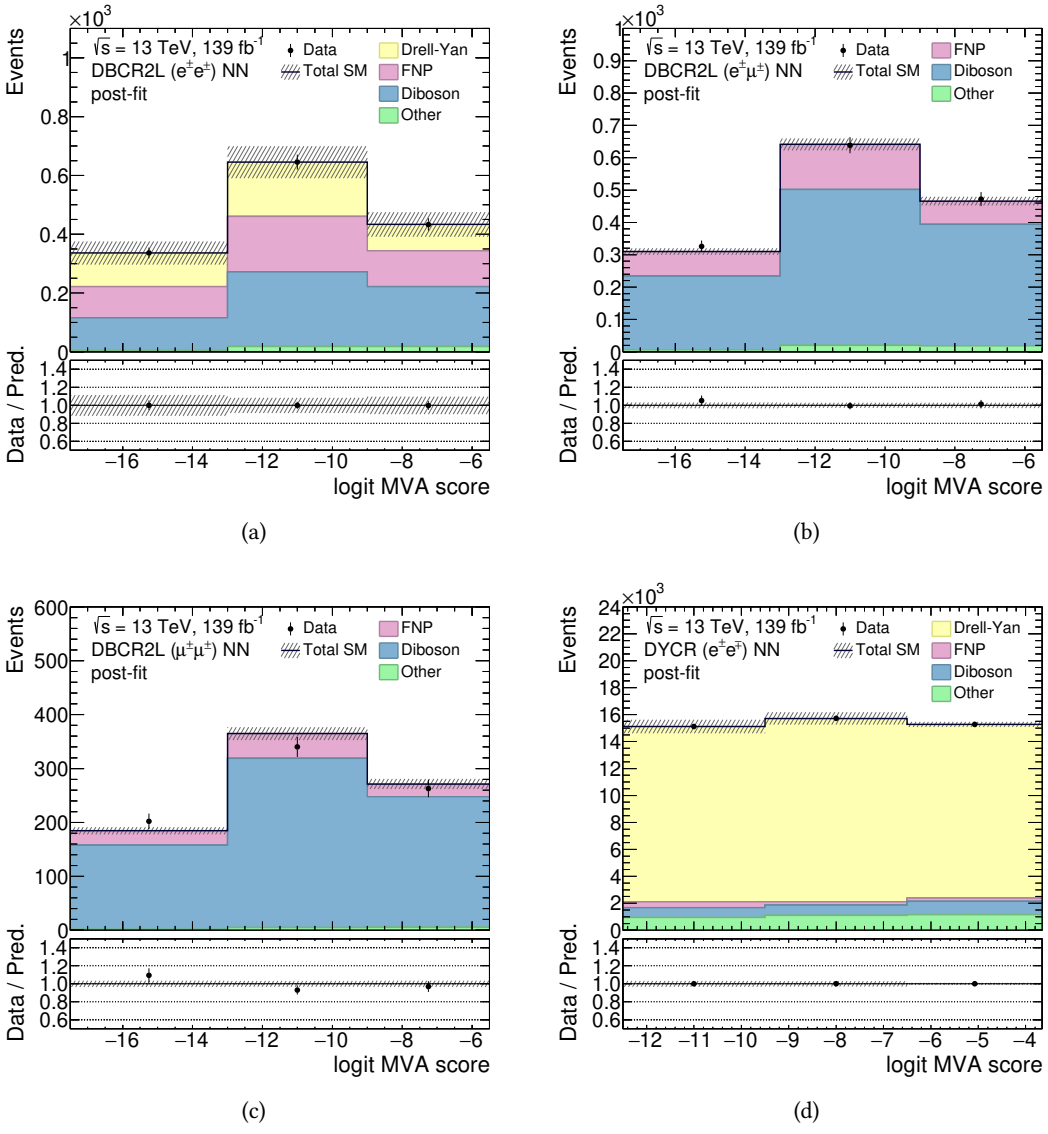

Figure 9.7: The logit MVA output distributions for data and SM background predictions in multivariate control regions: (a) the electron–electron, (b) the electron–muon, (c) the muon–muon diboson control regions, and (d) DYCR. Backgrounds from top-quark and multiboson processes are merged, forming the 'Other' category. The hatched bands include all systematic uncertainties after a background-only fit to data (post-fit), with the correlations between various sources considered. The last bin also includes any overflow entries. The error bars show statistical uncertainties. The lower panels show the ratio of the observed data to the estimated SM background.

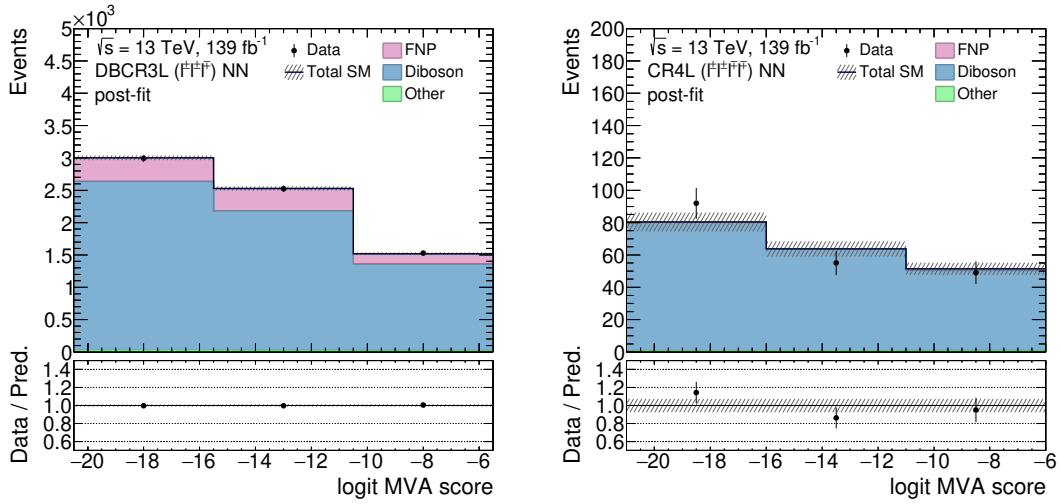

(a) (b)

Figure 9.8: The logit MVA output distributions in multivariate control regions: (a) DBCR3L and (b) CR4L. Backgrounds from top-quark and multiboson processes are merged, forming the 'Other' category. The hatched bands include all systematic uncertainties after a background-only fit to data (post-fit), with the correlations between various sources considered. The last bin also includes any overflow entries. The error bars show statistical uncertainties. The lower panels show the ratio of the observed data to the estimated SM background.

normalisation factors obtained from the likelihood fit to the two-, three- and four-lepton control and signal regions.

The total event yields for each lepton flavour in the SR2L are presented in Figure 9.17, and those of the three- and four-lepton signal regions are shown in Figure 9.18. Similarly to the cut-based approach, no data event passed the SR4L selection. No significant excess is observed in any of the signal regions.

Figure 9.19 shows the upper limit on the cross-section as a function of the $H^{\pm\pm}$ boson mass, where decays into each leptonic final state are equally probable. In the multivariate case, the limit is calculated using only the asymptotic formulae. The sensitivity of individual lepton multiplicity channels is presented in Figure 9.20. The preliminary results stay within the $\sim 10\%$ of the cut-based results with no significant improvement. Note that the fit procedure is not refined and that the signal mass points around the expected limit are excluded from the fit due to convergence difficulties. The limit is then interpolated there.

The observed lower limits on the $H^{\pm\pm}$ mass within LRSMs (the Zee–Babu model) vary from 570 GeV to 1050 GeV (430 GeV to 890 GeV), depending on the lepton multiplicity channel. The observed lower limit on the mass reaches 1050 GeV and 890 GeV when combining all three channels for LRSMs and the Zee–Babu model, respectively. The expected exclusion limit is 1010^{+80}_{-70} GeV for LRSMs and 810^{+20}_{-30} GeV for the Zee–Babu model, where the uncertainties of the limit are extracted from the $\pm 1\sigma$ band. The limit obtained from the four-lepton final state is the strongest and drives the combined result, similar to the cut-based analysis.

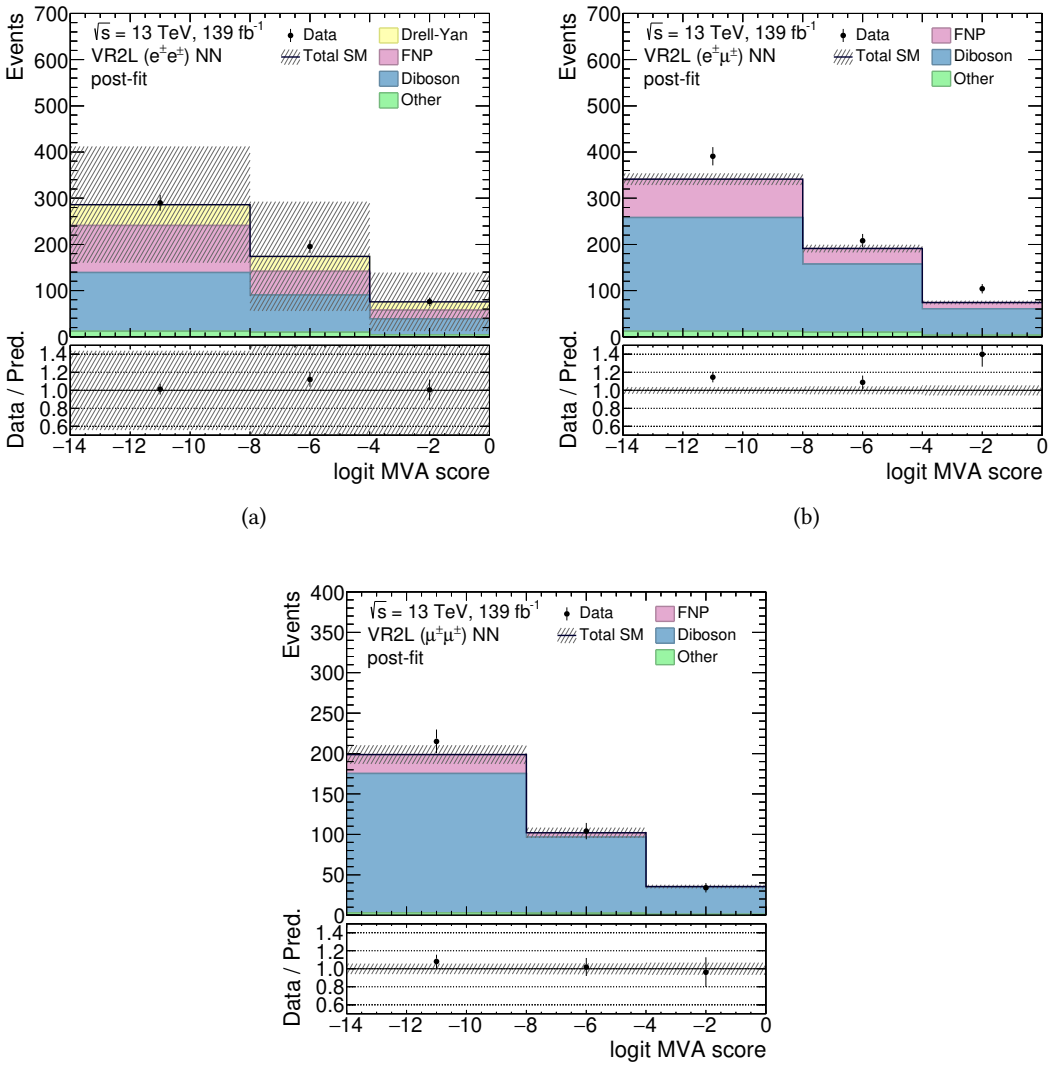

Figure 9.9: The logit MVA output distributions in two-lepton multivariate validation regions: (a) the electron–electron, (b) the electron–muon, and (c) the muon–muon two-lepton validation regions. Backgrounds from top-quark and multiboson processes are merged, forming the 'Other' category. The hatched bands include all systematic uncertainties after a background-only fit to data (post-fit), with the correlations between various sources considered. The last bin also includes any overflow entries. The error bars show statistical uncertainties. The lower panels show the ratio of the observed data to the estimated SM background.

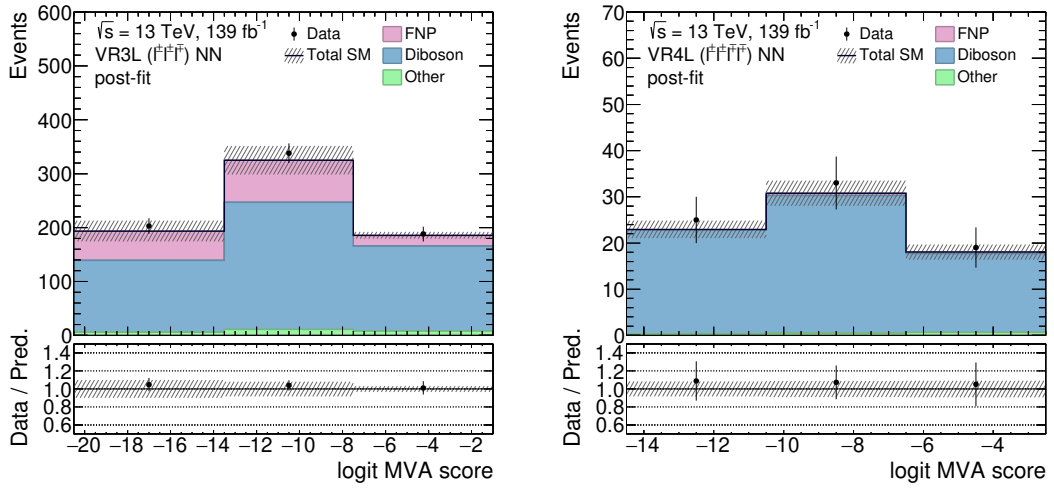

(a) (b)

Figure 9.10: The logit MVA output distributions in multivariate validation regions: (a) VR3L and (b) VR4L. Backgrounds from top-quark and multiboson processes are merged, forming the 'Other' category. The hatched bands include all systematic uncertainties after a background-only fit to data (post-fit), with the correlations between various sources considered. The last bin also includes any overflow entries. The error bars show statistical uncertainties. The lower panels show the ratio of the observed data to the estimated SM background.

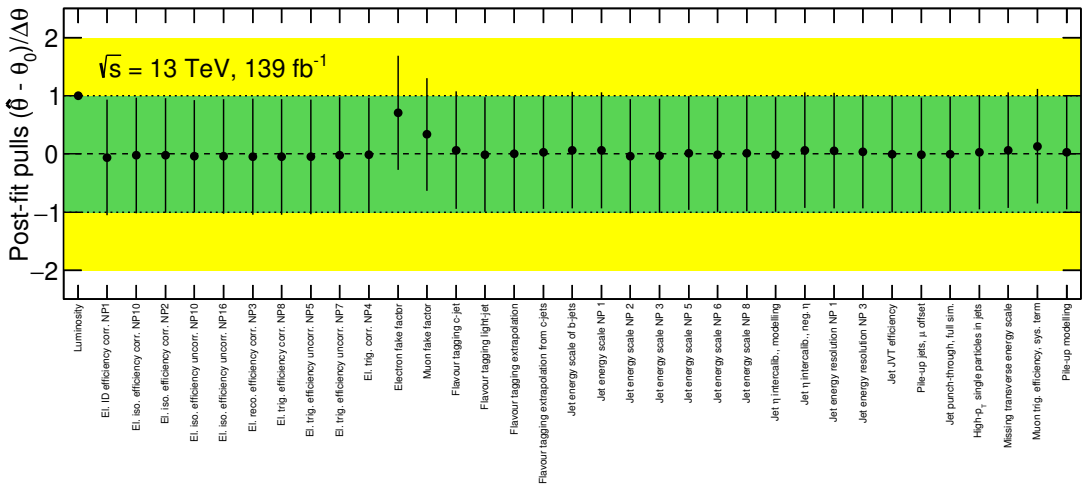

Figure 9.11: Post-fit nuisance parameters of the multivariate background-only fit expressed in units of standard deviation. Only NPs that have a larger than 5% effect are shown.

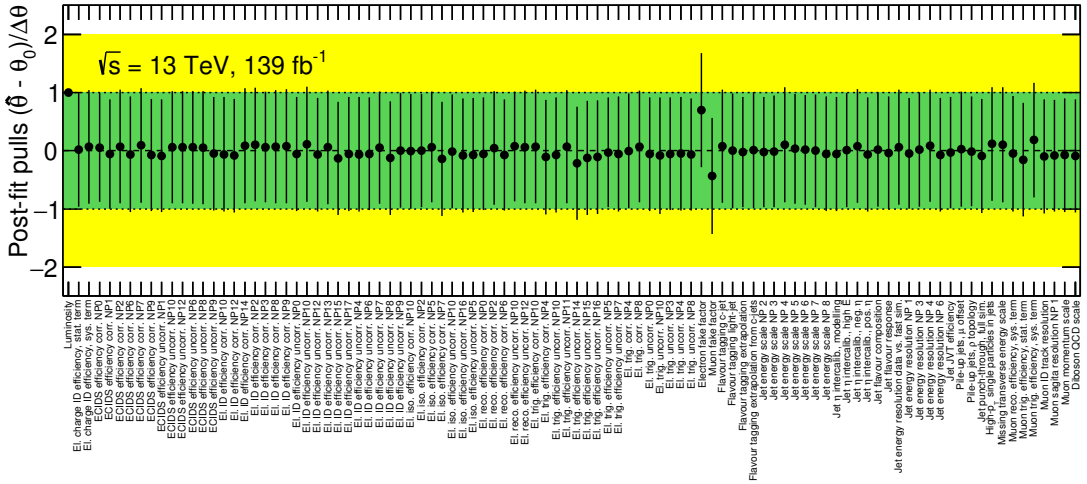

Figure 9.12: Post-fit nuisance parameters of the multivariate exclusion fit with real data in all regions, expressed in units of standard deviation. Only NPs that have a larger than 5% effect are shown.

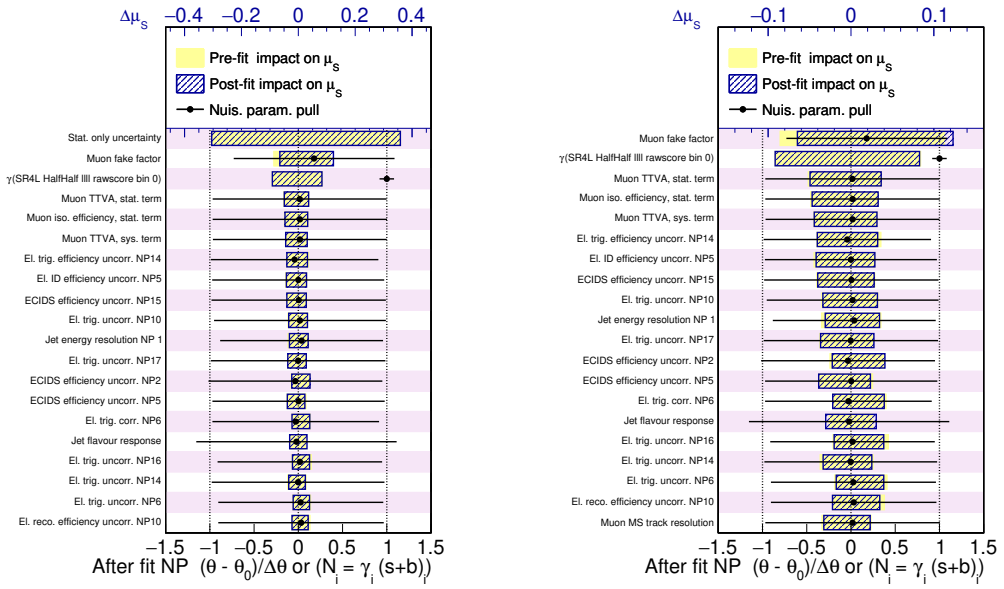

(a) (b)

Figure 9.13: Impact of systematic uncertainties on μ_{sig} in multivariate analysis, constructed by fixing one nuisance parameter at the time to its $\pm 1\sigma$ variations and minimising others. After the fit, the impact on μ_{sig} is inspected with respect to the nominal fit, where all parameters are free. The per-bin γ parameters affecting the fit are also visible. (a) The impact of systematic sources and MC statistical uncertainty, and (b) only the impact of systematic sources.

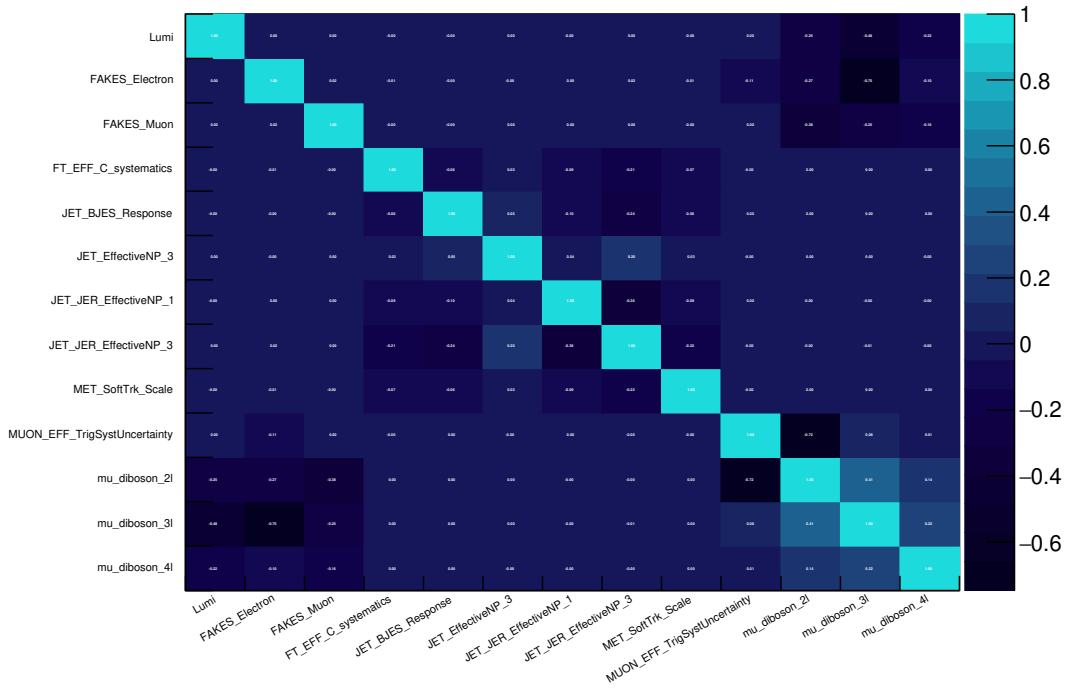

Figure 9.14: A reduced correlation matrix of nuisance parameters used in the fit in the multivariate analysis. Only correlations higher than 20% are shown.

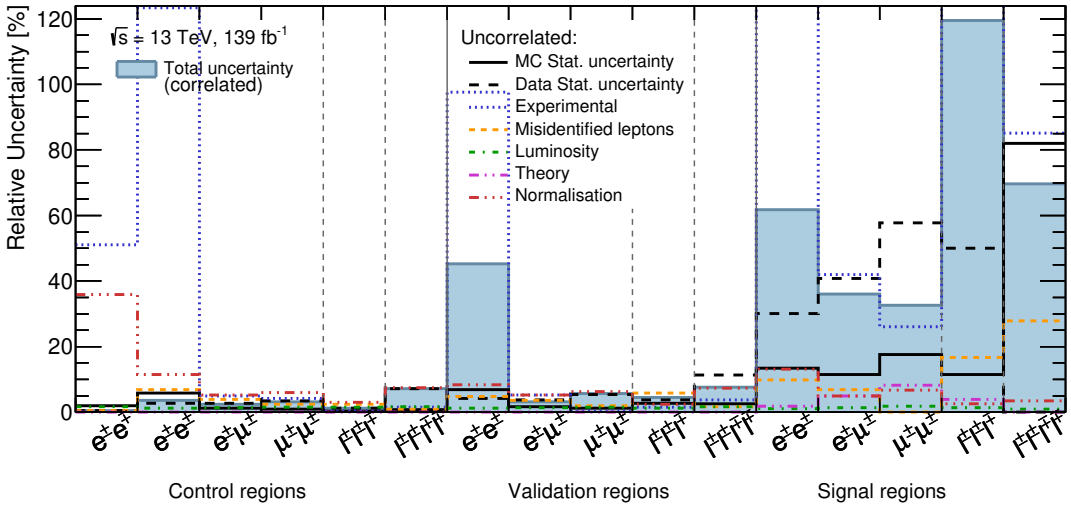

Figure 9.15: Relative contributions of different sources of statistical and systematic uncertainty in the total background yield estimation after the background-only fit in the multivariate analysis. Systematic uncertainties are calculated in an uncorrelated way by shifting in turn only one nuisance parameter from the post-fit value by one standard deviation, keeping all the other parameters at their post-fit values, and comparing the resulting event yield with the nominal yield. Validation regions do not constrain the normalisation factors or nuisance parameters. Individual uncertainties can be treated as correlated across the regions. Some backgrounds are constrained by the CR data and have strong anti-correlations as a result. The total background uncertainty is indicated by 'Total uncertainty'.

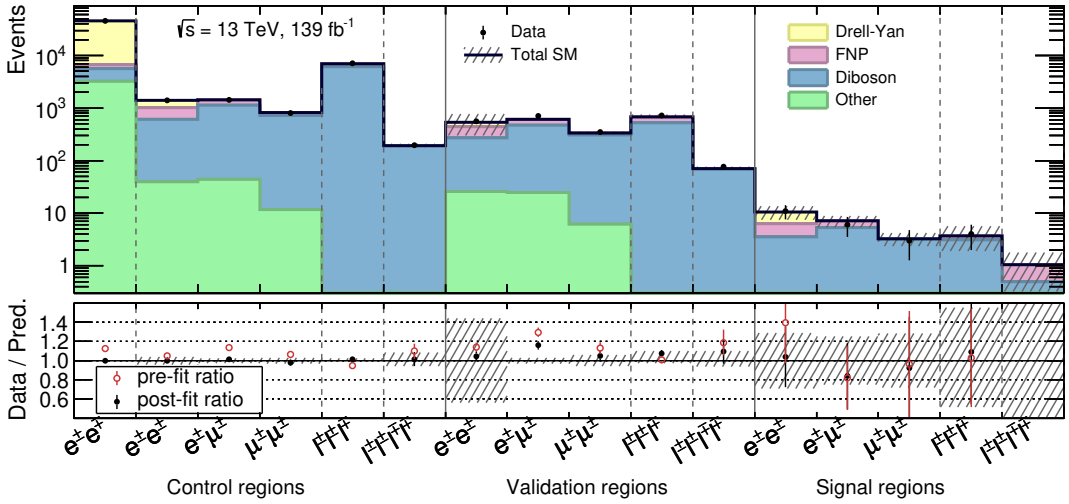

Figure 9.16: The numbers of observed and expected events in the control, validation, and signal regions for all channels in the multivariate analysis, split by lepton flavour and electric charge combination. The symbol ℓ only stands for light leptons ($\ell, \ell' = e,\ \mu$). The background expectation is the result of the background-only fit. The hatched bands include all post-fit systematic uncertainties with the correlations between various sources considered. The error bars show statistical uncertainties. FNP refers to the fake/non-prompt lepton background. Backgrounds from top-quark and multiboson processes are merged, forming the 'Other' category. The lower panel shows the ratio of the observed data to the estimated SM background.

Table 9.3: The number of predicted background events in multivariate control regions after the background-only fit, compared with the number of events observed in data. Uncertainties correspond to the uncertainties in the predicted event yields and their total is smaller than the sum of the components in quadrature due to correlations between these components. Due to rounding, the totals can differ from the sums of components. FNP refers to the fake/non-prompt lepton background. Backgrounds from top-quark and multiboson processes are merged, forming the 'Other' category. Background processes with a negligible yield are marked with a dash (–).

	DYCR e^+e^-	**DBCR2L** $e^\pm e^\pm$	**DBCR2L** $e^\pm\mu^\pm$	**DBCR2L** $\mu^\pm\mu^\pm$	**DBCR3L** $\ell^\pm\ell^\pm\ell^\mp$	**CR4L** $\ell^\pm\ell^\pm\ell^\mp\ell^\mp$
Observed events	46 116	1414	1437	805	7046	196
Total background	46 120 ± 240	1410 ± 60	1417 ± 35	821 ± 26	7050 ± 80	196 ± 14
Diboson	2460 ± 170	570 ± 50	1090 ± 50	713 ± 32	6080 ± 190	192 ± 14
FNP lepton	930 ± 200	420 ± 100	290 ± 60	96 ± 20	870 ± 180	1.4 ± 1.4
Drell–Yan	39 500 ± 400	390 ± 120	–	–	–	–
Other	3210 ± 260	40 ± 14	44 ± 14	11.6 ± 2.0	92 ± 11	2.6 ± 1.3

Table 9.4: The number of predicted background events in multivariate validation regions after the background-only fit, compared with the number of events observed in data. Uncertainties correspond to the uncertainties in the predicted event yields and their total is smaller than the sum of the components in quadrature due to correlations between these components. Due to rounding, the totals can differ from the sums of components. FNP refers to the fake/non-prompt lepton background. Backgrounds from top-quark and multiboson processes are merged, forming the 'Other' category. Background processes with a negligible yield are marked with a dash (–).

	VR2L $e^{\pm}e^{\pm}$	**VR2L** $e^{\pm}\mu^{\pm}$	**VR2L** $\mu^{\pm}\mu^{\pm}$	**VR3L** $\ell^{\pm}\ell^{\pm}\ell^{\mp}$	**VR4L** $\ell^{\pm}\ell^{\pm}\ell^{\mp}\ell^{\mp}$
Observed events	561	703	353	729	77
Total background	540 ± 240	606 ± 19	336 ± 19	700 ± 40	72 ± 6
Diboson	242 ± 24	451 ± 23	301 ± 21	526 ± 25	69 ± 6
FNP lepton	171 ± 29	131 ± 23	29 ± 7	150 ± 60	0.9 ± 0.9
Drell–Yan	100 ± 100	–	–	–	–
Other	26 ± 11	25 ± 10	6.1 ± 1.2	25 ± 11	1.4 ± 1.4

Table 9.5: The number of predicted background events in multivariate signal regions after the background-only fit, compared with the number of events observed in data. Uncertainties correspond to the uncertainties in the predicted event yields and their total is smaller than the sum of the components in quadrature due to correlations between these components. Due to rounding, the totals can differ from the sums of components. FNP refers to the fake/non-prompt lepton background. Backgrounds from top-quark and multiboson processes are merged, forming the 'Other' category. Background processes with a negligible yield are marked with a dash (–).

	SR2L $e^{\pm}e^{\pm}$	**SR2L** $e^{\pm}\mu^{\pm}$	**SR2L** $\mu^{\pm}\mu^{\pm}$	**SR3L** $\ell^{\pm}\ell^{\pm}\ell^{\mp}$	**SR4L** $\ell^{\pm}\ell^{\pm}\ell^{\mp}\ell^{\mp}$
Observed events	11	6	3	4	0
Total background	11 ± 3	7.1 ± 1.8	3.25 ± 0.92	3.8 ± 1.9	1.1 ± 0.7
Diboson	3.3 ± 1.9	5.0 ± 1.7	3.16 ± 0.91	3.1 ± 1.9	0.5 ± 0.4
FNP lepton	2.7 ± 0.99	1.9 ± 0.6	–	0.5 ± 0.5	0.6 ± 0.5
Drell–Yan	4 ± 4	–	–	–	–
Other	0.26 ± 0.26	0.23 ± 0.23	0.09 ± 0.09	0.14 ± 0.14	–

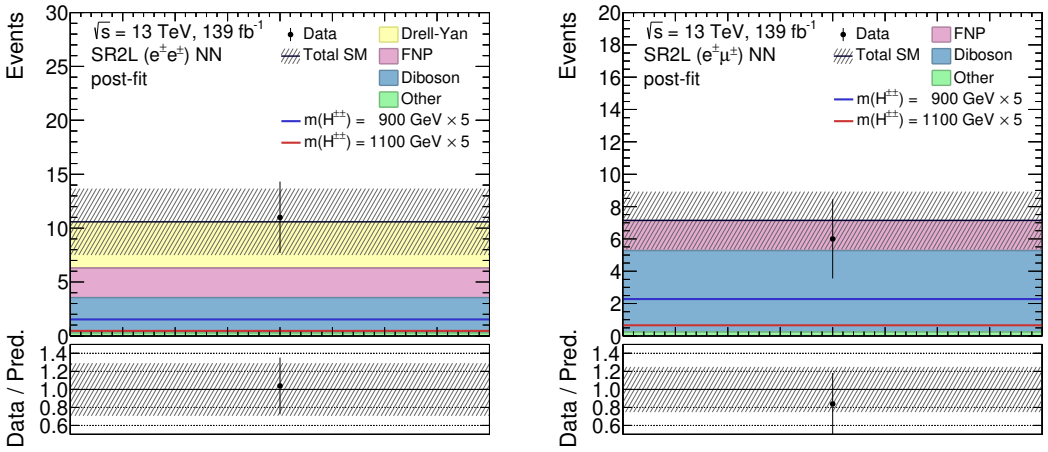

(a) (b)

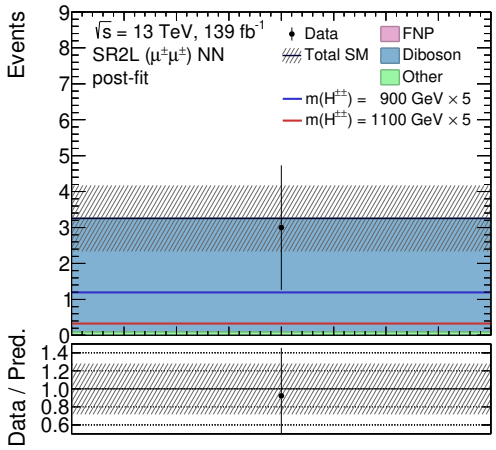

(c)

Figure 9.17: The total event yields for data and SM background predictions in multivariate signal regions, namely (a) the *ee* channel, (b) the $e\mu$ channel and (c) the $\mu\mu$ channel. The background expectation is the result of the background-only fit. The hatched bands include all systematic uncertainties post-fit with the correlations between various sources considered. The solid coloured lines correspond to signal samples, normalised using the theory cross-section, with the $H^{\pm\pm}$ mass marked in the legend. The ×5 in the legend indicates the scaling of the signal yield. The error bars show statistical uncertainties. Backgrounds from top-quark and multiboson processes are merged, forming the 'Other' category. The lower panels show the ratio of the observed data to the estimated SM background. The binning presented in the figures is used in the fit.

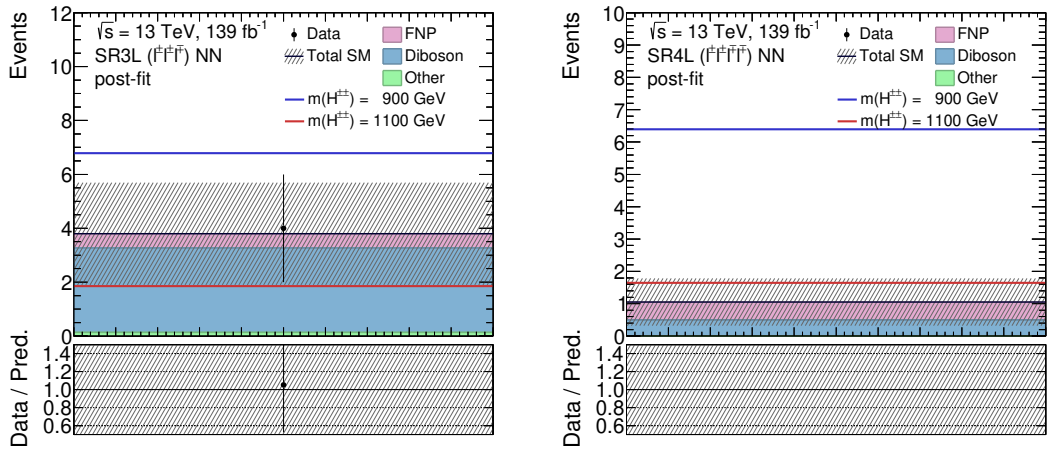

(a) (b)

Figure 9.18: The total event yields in multivariate signal regions: (a) SR3L and (b) SR4L, where no events are observed. The background expectation is the result of the background-only fit. Note the logarithmic y scale. The hatched bands include all systematic uncertainties post-fit with the correlations between various sources considered. The solid coloured lines correspond to signal samples, normalised using the theory cross-section, with the $H^{\pm\pm}$ mass marked in the legend. The error bars show statistical uncertainties. Backgrounds from top-quark and multiboson processes are merged, forming the 'Other' category. The lower panels show the ratio of the observed data to the estimated SM background. The binning presented in the figures is used in the fit.

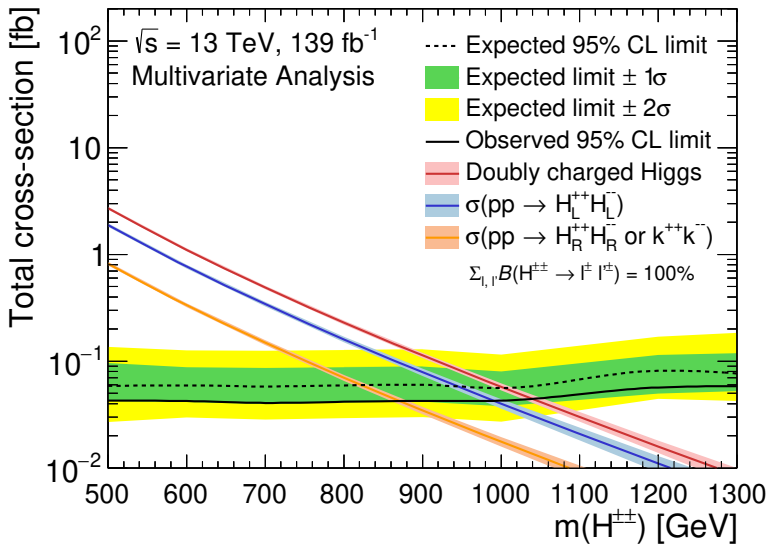

Figure 9.19: Observed (solid line) and expected (dashed line) 95% CL upper limits on the $H^{\pm\pm}$ pair production cross-section as a function of $m_{H^{\pm\pm}}$ in a multivariate analysis. The theoretical signal cross-section predictions, given by the NLO calculation [65, 69], are shown as blue, orange and red lines for the left-handed $H_L^{\pm\pm}$, right-handed $H_R^{\pm\pm}$ (which is the same as the Zee–Babu $k^{\pm\pm}$), and a sum of the two LRSM chiralities, respectively, with the corresponding uncertainty bands. Mass points $m_{H^{\pm\pm}} = 1$ TeV and 1.1 TeV are interpolated.

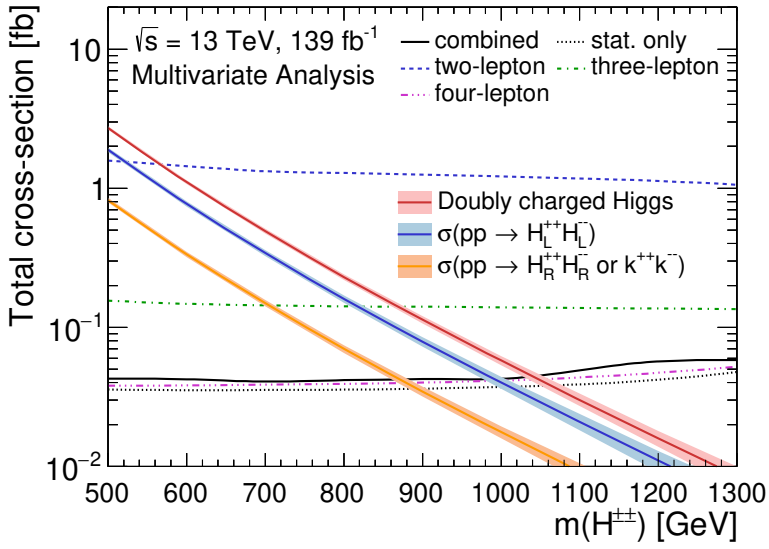

Figure 9.20: Breakdown of the observed 95% CL upper limits on the $H^{\pm\pm}$ pair production cross-section as a function of $m_{H^{\pm\pm}}$ in the multivariate analysis. The limit obtained from the four-lepton final state is the strongest and drives the combined result. The black lines show the combined observed limit obtained using the asymptotic formulae for a fit with only statistical uncertainties (dotted) and a fit with statistical and systematic uncertainties (solid). Mass points $m_{H^{\pm\pm}} = 1$ TeV and 1.1 TeV are interpolated.

CHAPTER 10

Conclusions and Summary

A search for the doubly charged Higgs boson, $H^{\pm\pm}$, was investigated in this work by studying pp collisions produced by the LHC at $\sqrt{s} = 13\,\text{TeV}$ and recorded by the ATLAS experiment during Run 2, which lasted between 2015 and 2018.

Doubly charged Higgs bosons appear in multiple SM extensions, and the thesis focuses on $H^{\pm\pm}$ particles in LRSM, which incorporates the type-II seesaw mechanism. Since it was found that right-handed chirality, $H_R^{\pm\pm}$, is the same as $k^{\pm\pm}$ from the Zee–Babu model, the results can also be interpreted for this model. If $H^{\pm\pm}$ was found, it could reveal the mechanism for generating small neutrino masses and open a window into new physics. Furthermore, it would provide direct observation of lepton number and flavour violation. The $H^{\pm\pm}$ pair production occurring through the Drell–Yan process was considered, yielding final states with prompt and highly energetic leptons with the same charge. The $H^{\pm\pm}$ analysis targets final states with two, three and four light leptons (electrons and muons), including leptonic τ decays. These are the golden channels to search for the mass resonance, which would signify the production of $H^{\pm\pm}$ particles at the LHC because the expected SM background is low, and leptons can be efficiently measured.

Compared to the previous iteration of the analysis [77], which was performed using the first part of the LHC Run 2 data set, the work presented in this thesis was performed with an integrated luminosity of $139\,\text{fb}^{-1}$. The $H^{\pm\pm}$ analysis shown in this thesis was published in Eur. Phys. J C 83 (2023) 605.

Dominant irreducible background contributions are simulated with Monte Carlo generators. Free normalisation parameters are introduced for the Drell–Yan and diboson background contributions to fit their yields, allowing them to constrain both the modelling and the detector-related systematic uncertainties affecting the SM background predictions. A data-driven technique based on statistically-independent control regions to correct the SM prediction of reducible background processes is applied.

Multiple regions enriched with signal candidates are defined based on the expected signal significance in two analysis approaches: a common cut-based and a multivariate analysis strategy. All the analysis regions are considered in a statistical likelihood fit to check their compatibility with the Standard Model hypotheses. As expected, the fit procedure showed a low contribution of systematics to the total uncertainty, which is dominated by the statistical uncertainty.

No significant excess above the Standard Model prediction was found. Lower limits are set on the mass of doubly charged Higgs bosons in the context of the left-right symmetric type-II seesaw and Zee–Babu models. These vary between 520 GeV and 1050 GeV for LRSMs and between 410 GeV and 880 GeV for the Zee–Babu model, depending on the lepton multiplicity channel, assuming that $\sum_{\ell\ell'} \mathcal{B}(H^{\pm\pm} \to \ell^{\pm}\ell'^{\pm}) = 100\%$ and that decays to each of the ee, $e\mu$, $\mu\mu$, $e\tau$, $\mu\tau$, $\tau\tau$ final states are equally probable. The observed combined lower limit on the $H^{\pm\pm}$ mass is

1080 GeV within LRSMs and 900 GeV within the Zee–Babu model. These limits are consistent with the expected limits of 1065^{+30}_{-50} GeV and 880^{+30}_{-40} GeV for LRSM and Zee–Babu doubly charged Higgs bosons, respectively. The lower limits on the LRSM $H^{\pm\pm}$ masses are 300 GeV higher than those from the previous ATLAS result. Moreover, this search provides the first direct test of the Zee–Babu model at the LHC. The preliminary results from the multivariate approach do not improve the obtained limits, but the analysis can be further optimised.

The LHC Run 3, which started in 2022, will provide an integrated luminosity of about 300 fb^{-1} leading to better precision in the presented results. In High-luminosity LHC [213] Run 4, planned for 2029, the collider will reach centre-of-mass energy $\sqrt{s} = 14$ TeV, with an integrated luminosity of about 3000 fb^{-1} [214], opening the possibility to explore uncovered phase-space regions and allowing to improve the current exclusion limits and their uncertainties.

The analysis sensitivity can be further increased with the implementation of hadronic tau decays to the final states, which needs an additional background estimation to separate such processes from genuine hadronic jets.

The presented work uses a simple binary classification neural network to demonstrate the possibility of improvements and, while preliminary, shows that there would be a modest increase from it, indicating that the current cut-based analysis is well executed. More advanced machine-learning algorithms are available nowadays, which would better discriminate between background and signal events, producing more stringent limits on $H^{\pm\pm}$ particles. Machine learning can not only be used for selection but also simulation, reconstruction and other background estimation techniques.

Furthermore, with better analysis methods, tools and constant improvements in reconstruction performance and event selection, as well as all experimental developments including the new tracking system in ATLAS, new physics phenomena may still be observed in final states with same-charge leptons.

APPENDIX

APPENDIX A

Fake Lepton Composition

It is convenient to study fake lepton composition to optimise the fake factor estimation sideband regions and to make them compatible with the analysis regions. The source of fake leptons in MC simulation is reviewed in this appendix. The leptons are categorised according to the classification used by the ATLAS Isolation and Fake Forum [215] into

- prompt isolated electrons and muons,
- prompt isolated electrons with misidentified charge,
- prompt photon conversions,
- non-prompt muon decay,
- non-prompt τ-lepton decay,
- b-hadron decay,
- c-hadron decay,
- light hadron decay, and
- known unclassified fake lepton.

The fake electron and muon compositions in the fake estimation regions are presented in Figures A.1 and A.2, respectively, while signal regions are shown in Figures A.3–A.7 for cut-based and neural network analysis approaches.

A predominant contribution to electron fakes is expected to originate from light hadron and b-hadron decays within jets. On the other hand, muon fakes arise from heavy-flavour jets, i.e. from c-jets or b-jets. As can be seen in Figures A.1 and A.2, dijet events constitute the primary source of fake leptons in the estimation regions, with a minor contribution from $W+$ jets and $t\bar{t}$ events.

Generally, the composition in the fake estimation region agrees well with the distributions in cut-based and neural network signal regions. Since the selection does not differ much between the two analysis approaches, the compositions are also expected to be similar. Indeed, there are minor differences due to the stricter MC event weight cuts in the machine learning strategy, which can be seen as a deficit of $t\bar{t}$, diboson, and mutiboson events compared to the cut-based approach in some of the plots. Most of the electron fake yield in the ee and $e\mu$ channels of the SR2L region comes from $W+$ jets events, while muon fakes in $e\mu$ and $\mu\mu$ channels are categorised as known unclassified particles originating from multiboson processes. Two fake leptons occur very rarely ($< 3\%$) in the ee and $e\mu$ channels, while in the $\mu\mu$ channel, two fake leptons are found in $\sim 25\%$ of events containing at least one fake lepton.

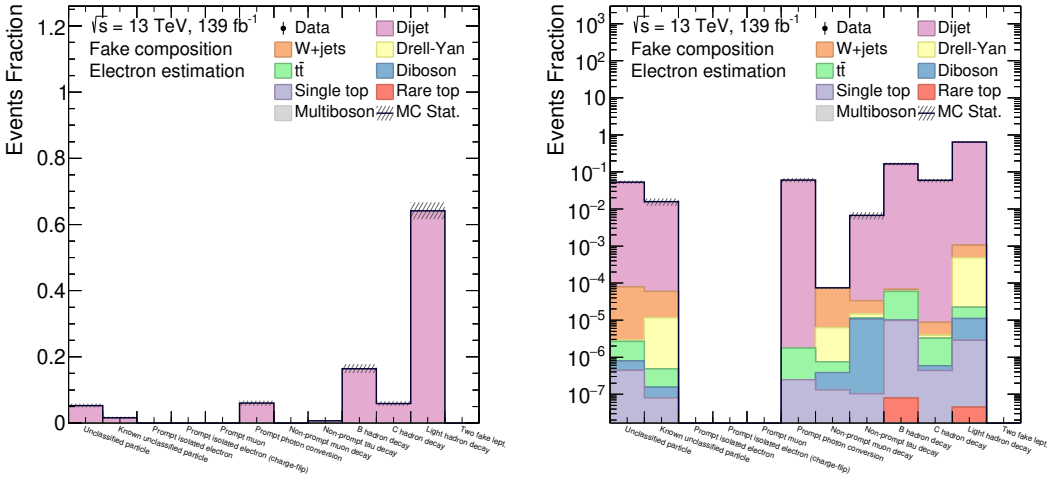

(a) (b)

Figure A.1: Fake composition in the electron fake estimation region in (a) linear and (b) logarithmic scale.

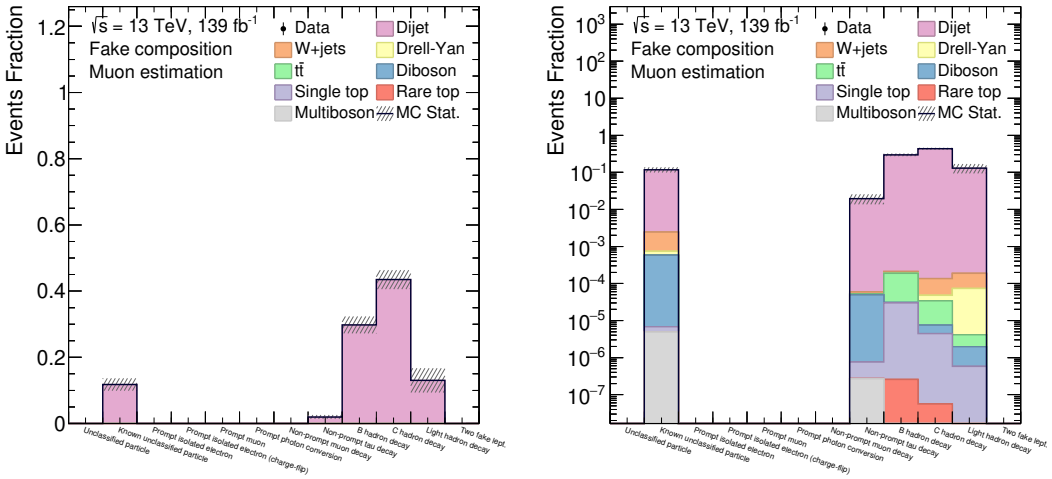

(a) (b)

Figure A.2: Fake composition in the muon fake estimation region in (a) linear and (b) logarithmic scale.

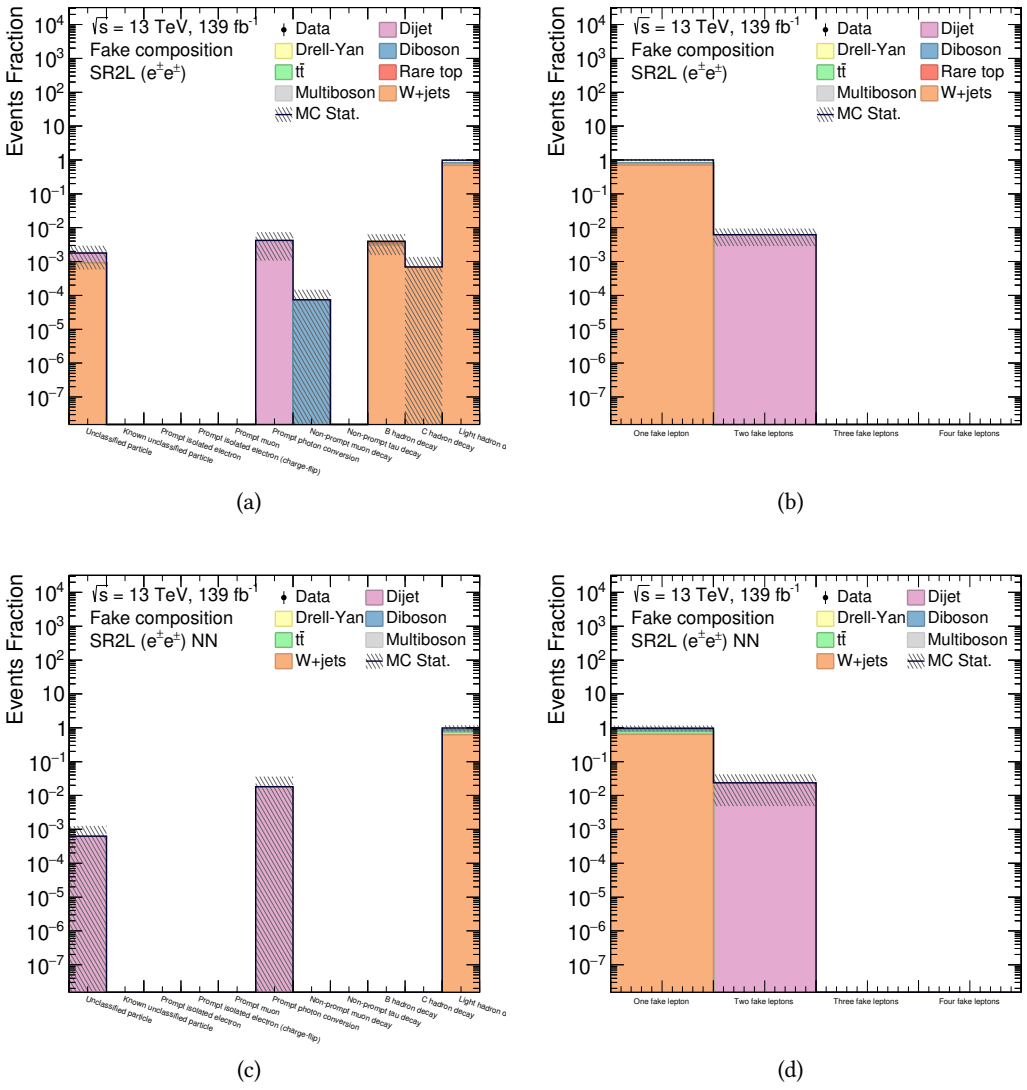

Figure A.3: (a) and (c) Fake lepton compositions. (b) and (d) Fake electron yields in the electron–electron channel of the cut-based (upper plots) and neural network (lower plots) two-lepton signal regions, SR2L *ee*.

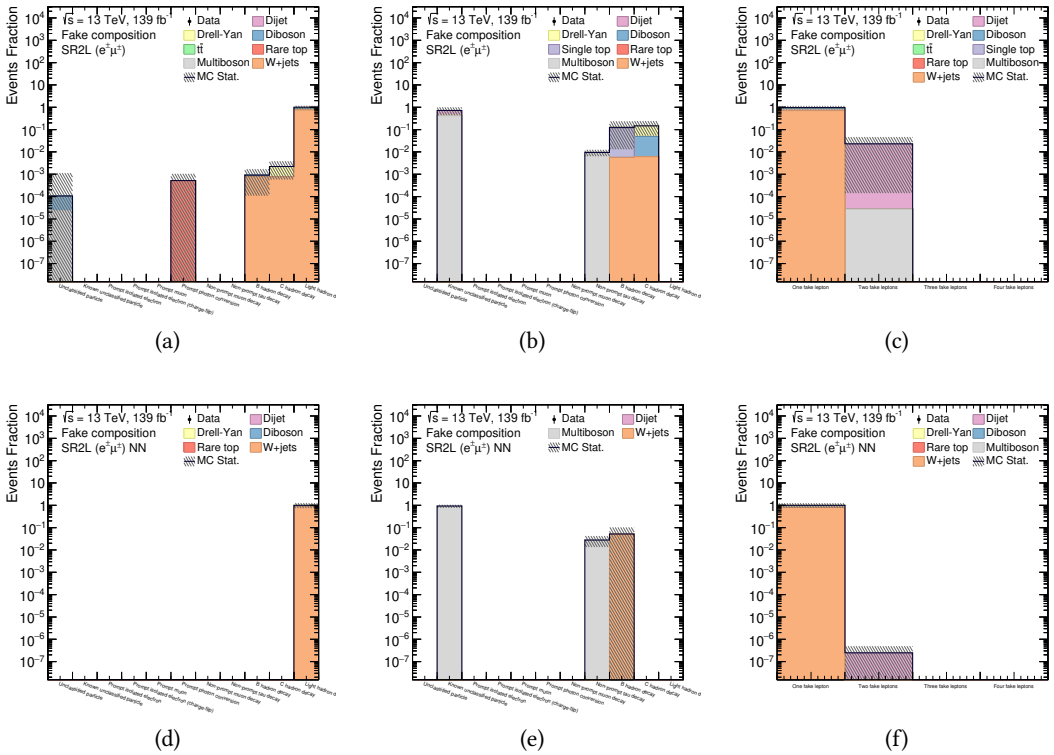

Figure A.4: Fake (a), (d) electron and (b), (e) muon compositions. (c) and (f) Fake lepton yields in the electron–muon channel of the cut-based (upper plots) and neural network (lower plots) two-lepton signal regions, SR2L $e\mu$.

The electron (muon) fakes originate primarily from Drell–Yan (multiboson) processes in the three-lepton signal region, SR3L, and are predominantly classified as coming from light-hadron decays (known unclassified particles). The majority of the considered three-lepton events ($\sim$ 78%) contain one fake lepton, with only $\sim$ 7% of events having three fake leptons.

In the four-lepton signal regions, SR4L and SR4L_NN, fake electrons approximately equally originate from diboson and multiboson events. Fakes from the multiboson process are being unclassified, and diboson events featuring light-hadron decays in the cut-based analysis approach, while electron fakes from both processes originate from light-hadron decays in the neural network approach. Unclassified particles and minor contributions of non-prompt τ-lepton decays represent muon fakes that predominantly originate from multiboson processes. Almost 40% of fake lepton events contain three (one) fake leptons in the SR4L (SR4L_NN).

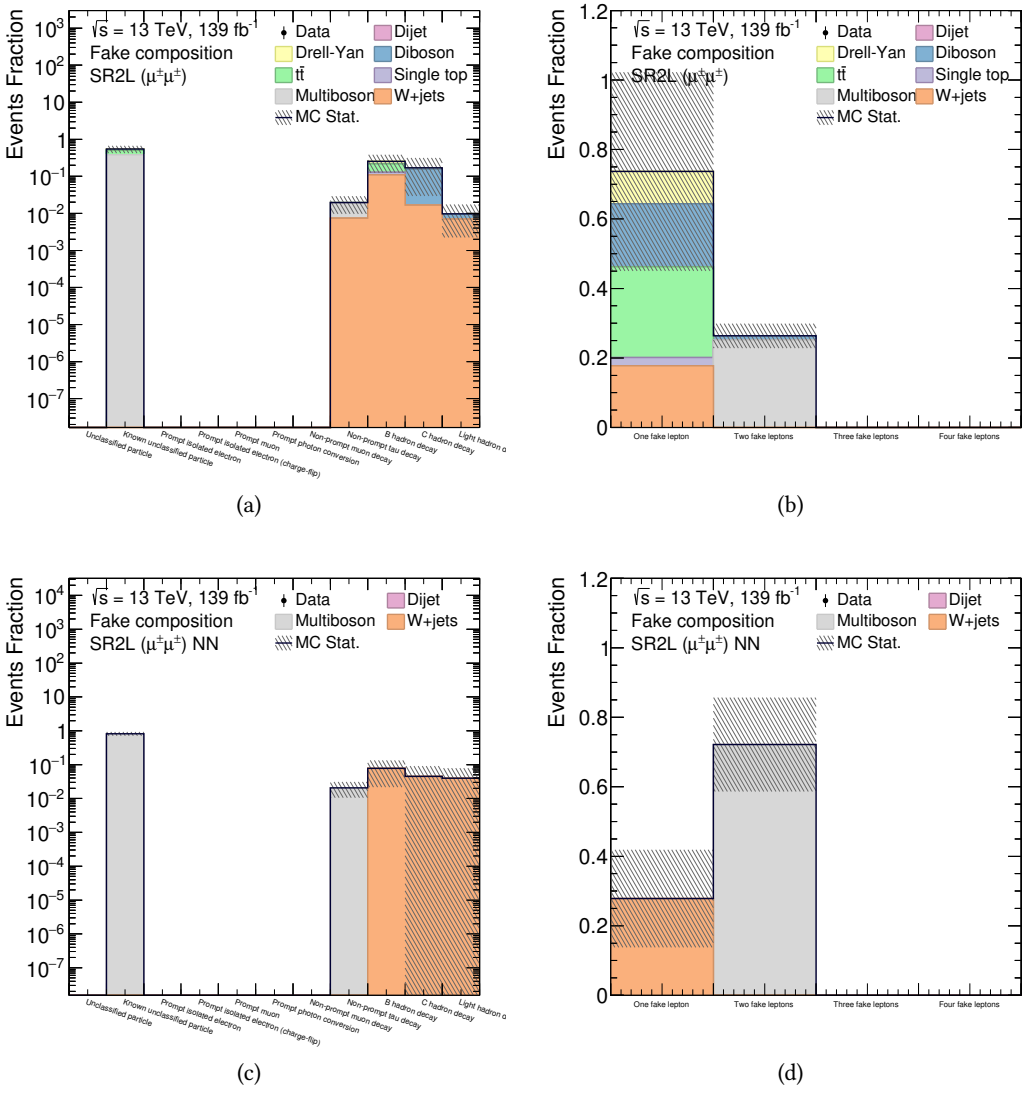

Figure A.5: (a) and (c) Fake lepton compositions. (b) and (d) Fake muon yields in the muon–muon channel of the cut-based (upper plots) and neural network (lower plots) two-lepton signal regions, SR2L $\mu\mu$.

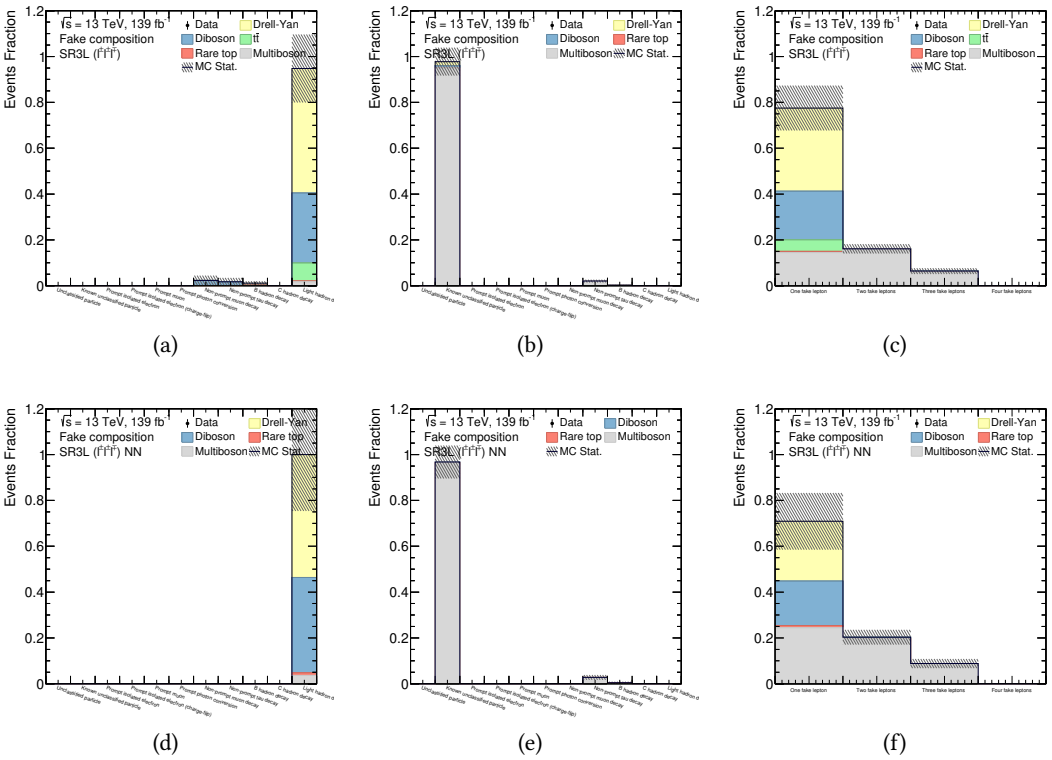

Figure A.6: Fake (a), (d) electron and (b), (e) muon compositions. (c) and (f) Fake lepton yields in the inclusive $\ell^{\pm}\ell^{\pm}\ell^{\mp}$ channel of the cut-based (upper plots) and neural network (lower plots) three-lepton signal regions, SR3L $\ell^{\pm}\ell^{\pm}\ell^{\mp}$.

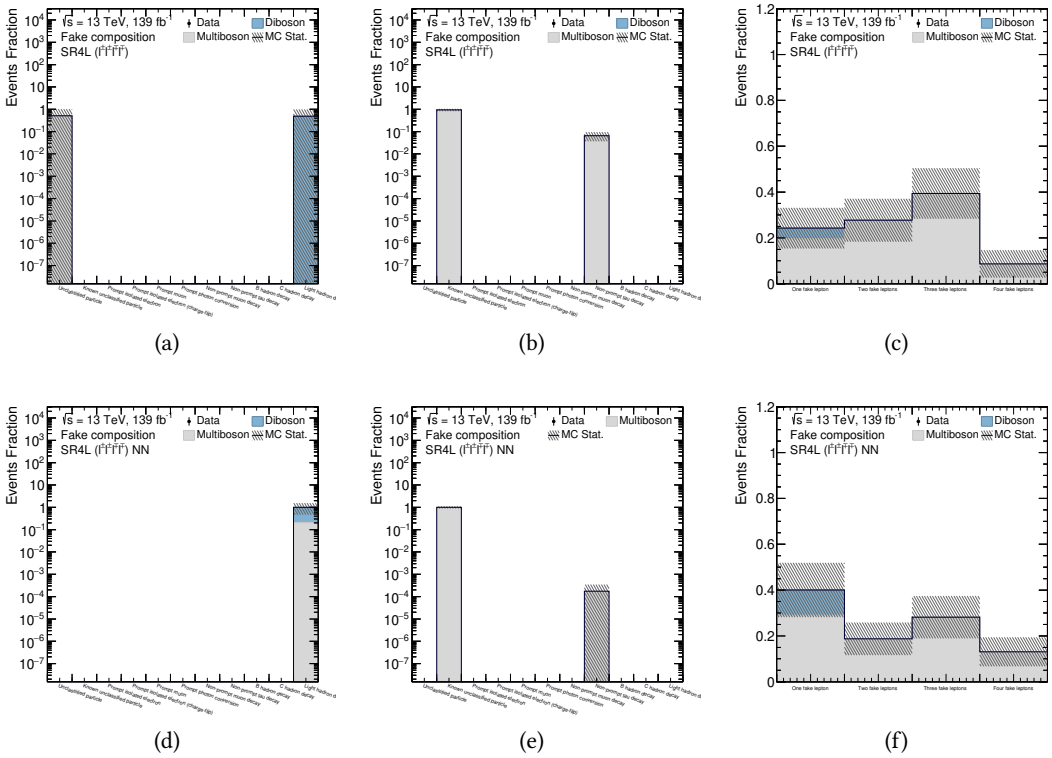

Figure A.7: Fake (a), (d) electron and (b), (e) muon compositions. (c) and (f) Fake lepton yields in the inclusive $\ell^{\pm}\ell^{\pm}\ell^{\mp}\ell^{\mp}$ channel of the cut-based (upper plots) and neural network (lower plots) three-lepton signal regions, SR4L $\ell^{\pm}\ell^{\pm}\ell^{\mp}\ell^{\mp}$.

APPENDIX B

Selected Distributions of the Cut-Based Analysis Regions

Selected kinematic distributions are showcased, demonstrating the consistency between expected and observed events across all cut-based analysis regions.

Two sets of plots are presented for each two-lepton region. First, transverse momenta of leading (left) and sub-leading (right) leptons are presented. Then, transverse momenta, $p_{\mathrm{T}}(\ell^{\pm}\ell'^{\pm})_{\mathrm{lead}}$, (left) and angular separation, $\Delta R(\ell^{\pm}\ell'^{\pm})_{\mathrm{lead}}$, (right) distributions of the leading lepton pair for each channel are shown. The ee channel is presented in the first, the $e\mu$ channel in the middle and the $\mu\mu$ channel in the last row.

Six distributions also used during region optimisation are given for three- and four-lepton regions, i.e. $p_{\mathrm{T}}(\ell_1)$, $p_{\mathrm{T}}(\ell_2)$, $p_{\mathrm{T}}(\ell^{\pm}\ell'^{\pm})_{\mathrm{lead}}$, $\Delta R(\ell^{\pm}\ell'^{\pm})_{\mathrm{lead}}$, $E_{\mathrm{T}}^{\mathrm{miss}}$, and N_{jet}. The N_{jet} distribution is replaced by $\overline{m}_{\mathrm{SC}}$ in four-lepton regions.

The contents of this chapter are as follows:

- **DYCR:** Drell–Yan control region in Figure B.1,
- **DBCR2L:** Two-lepton diboson control region in Figures B.2 and B.3,
- **DBCR3L:** Three-lepton diboson control region in Figure B.4,
- **CR4L:** Four-lepton control region in Figure B.5,
- **VR2L:** Two-lepton validation region in Figures B.6 and B.7,
- **VR3L:** Three-lepton validation region in Figure B.8,
- **VR4L:** Four-lepton validation region in Figure B.9,
- **SR2L:** Two-lepton signal region in Figures B.10 and B.11,
- **SR3L:** Three-lepton signal region in Figure B.12, and
- **SR4L:** Four-lepton signal region in Figure B.13.

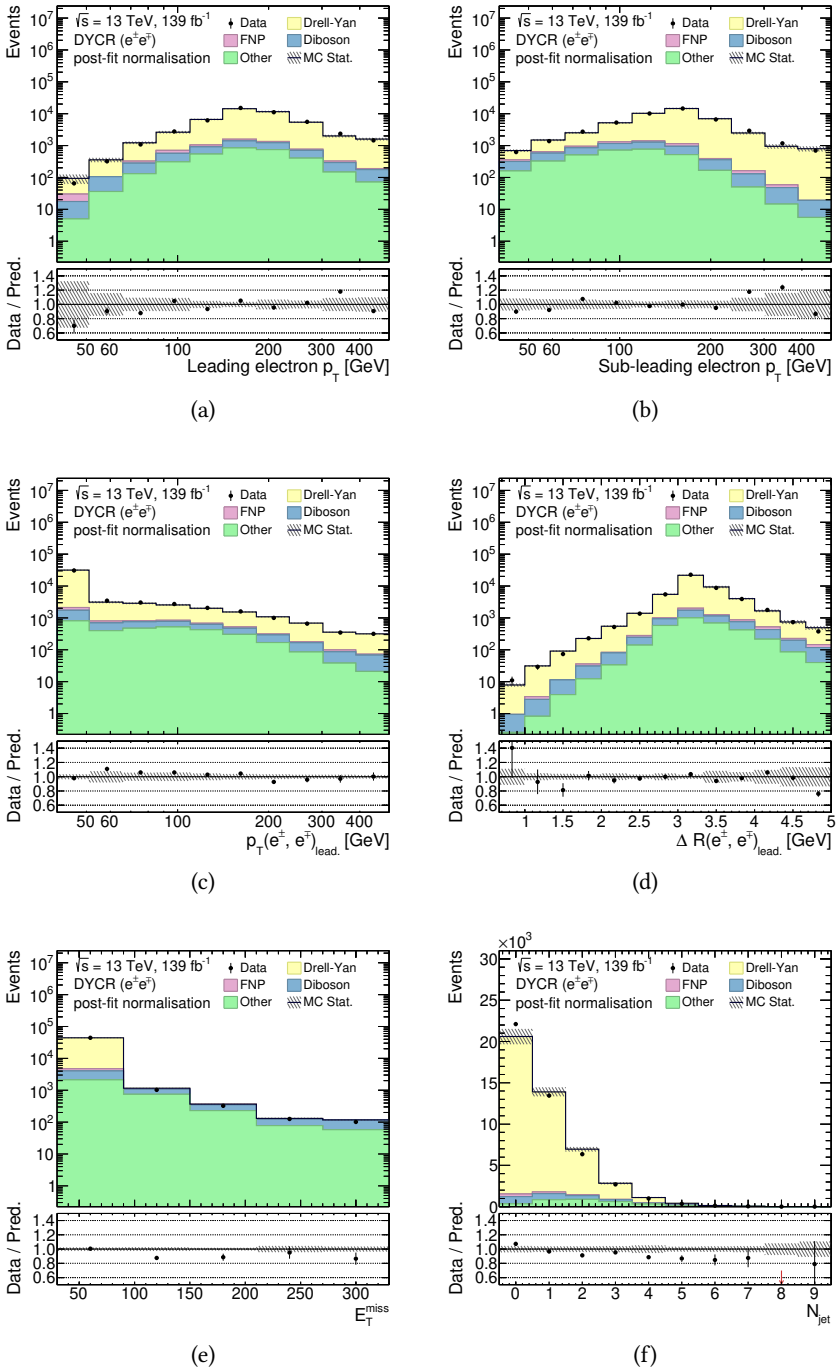

Figure B.1: Different kinematical distributions in the **DYCR**, the two-lepton cut-based Drell–Yan control region. (a) $p_{\mathrm{T}}(\ell_1)$, (b) $p_{\mathrm{T}}(\ell_2)$, (c) $p_{\mathrm{T}}(e^{\pm}e^{\mp})_{\mathrm{lead}}$, (d) $\Delta R(e^{\pm}e^{\mp})_{\mathrm{lead}}$, (e) $E_{\mathrm{T}}^{\mathrm{miss}}$, and (f) N_{jet}. Post-fit normalisation scales are applied. Uncertainties are statistical only.

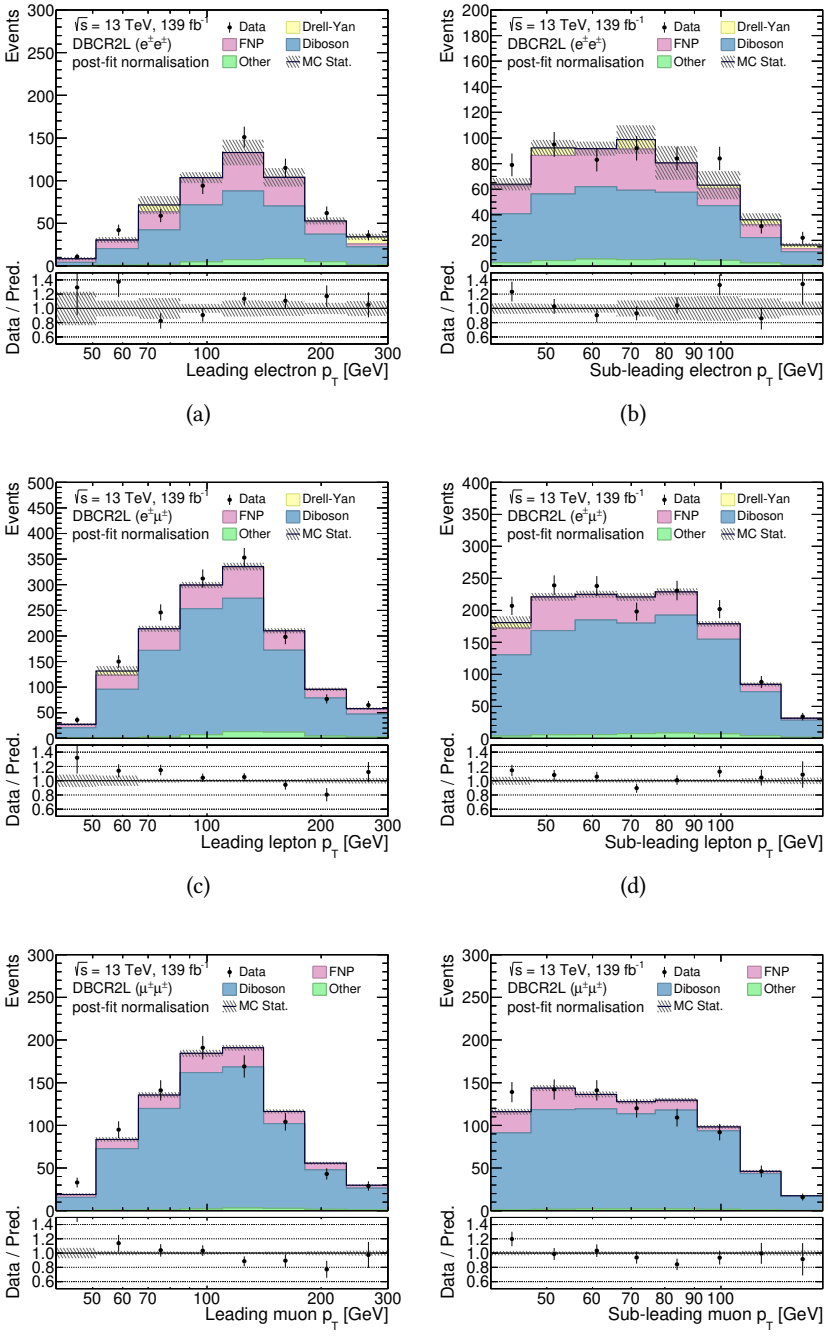

Figure B.2: Leading and sub-leading lepton momentum distributions in the **DBCR2L**, the two-lepton cut-based diboson control region, for all flavour combinations. Post-fit normalisation scales are applied. Uncertainties are statistical only.

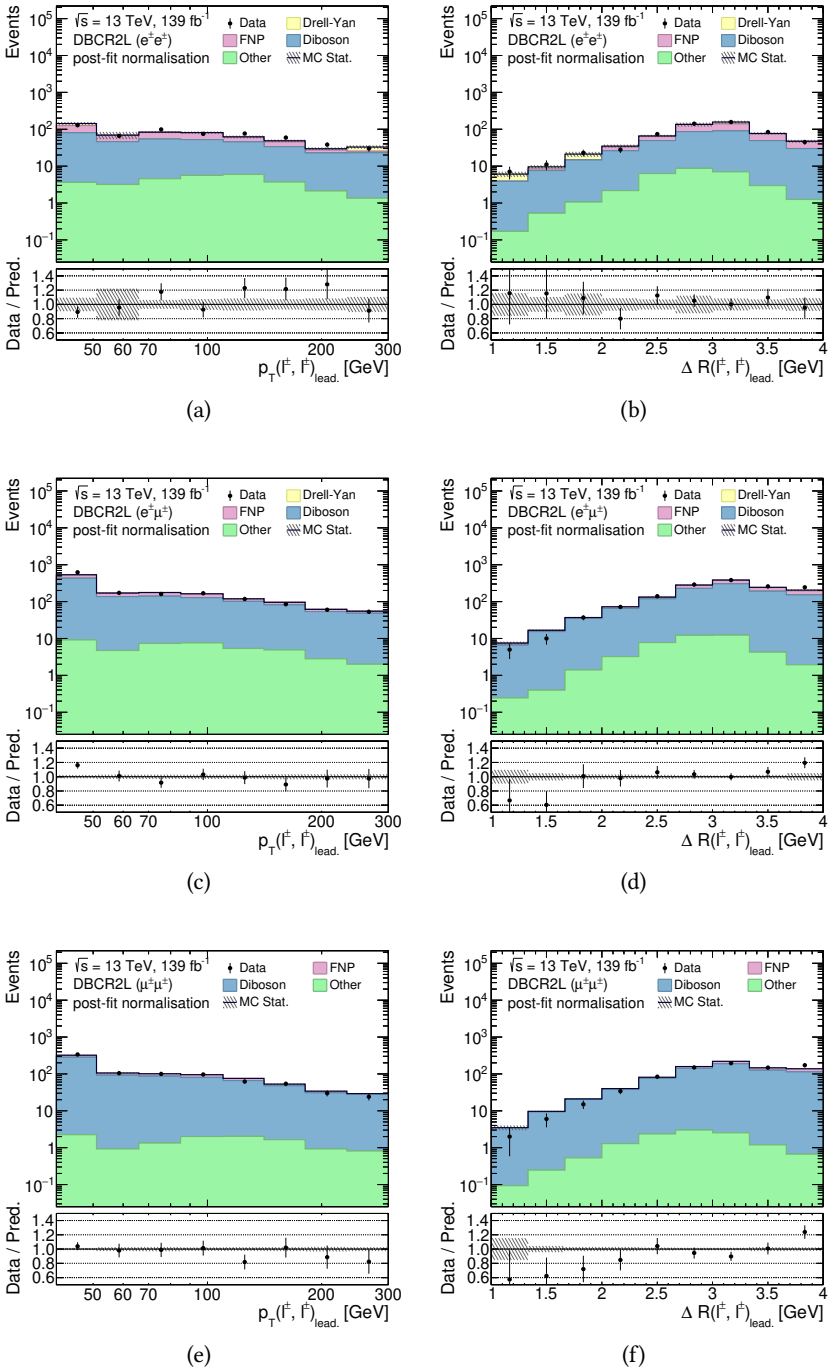

Figure B.3: Transverse momenta, $p_{\mathrm{T}}(\ell^{\pm}\ell'^{\pm})_{\mathrm{lead}}$, (left) and angular separation, $\Delta R(\ell^{\pm}\ell'^{\pm})_{\mathrm{lead}}$, (right) distributions of the leading lepton pair in the **DBCR2L**, the two-lepton cut-based diboson control region for all flavour combinations. Post-fit normalisation scales are applied. Uncertainties are statistical only.

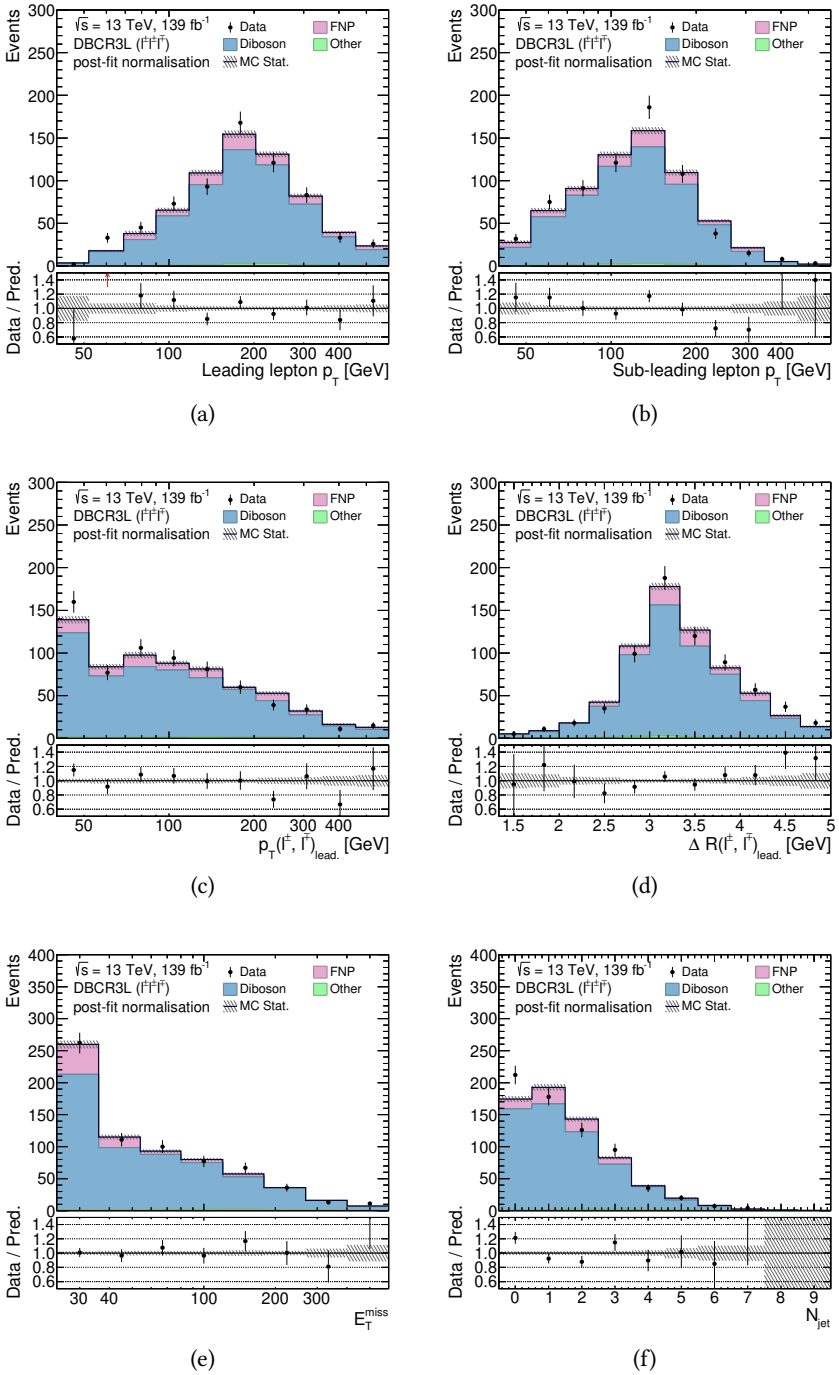

Figure B.4: Different kinematical distributions in the **DBCR3L**, the three-lepton cut-based diboson control region. (a) $p_{\mathrm{T}}(\ell_1)$, (b) $p_{\mathrm{T}}(\ell_2)$, (c) $p_{\mathrm{T}}(\ell^{\pm}\ell'^{\pm})_{\mathrm{lead}}$, (d) $\Delta R(\ell^{\pm}\ell'^{\pm})_{\mathrm{lead}}$, (e) $E_{\mathrm{T}}^{\mathrm{miss}}$, and (f) N_{jet}. Post-fit normalisation scales are applied. Uncertainties are statistical only.

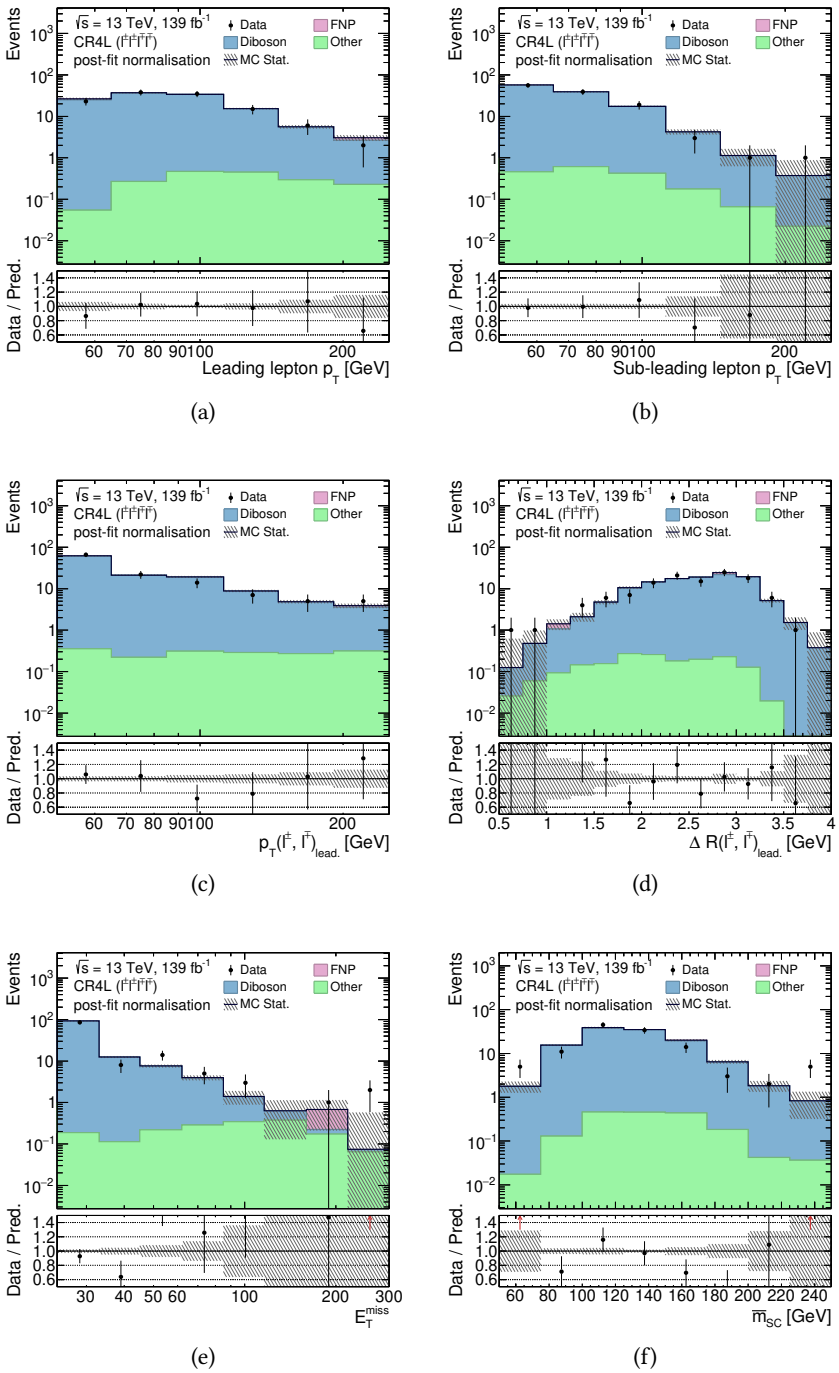

Figure B.5: Different kinematical distributions in the **CR4L**, the four-lepton cut-based control region. (a) $p_{\mathrm{T}}(\ell_1)$, (b) $p_{\mathrm{T}}(\ell_2)$, (c) $p_{\mathrm{T}}(\ell^{\pm}\ell'^{\pm})_{\mathrm{lead}}$, (d) $\Delta R(\ell^{\pm}\ell'^{\pm})_{\mathrm{lead}}$, (e) $E_{\mathrm{T}}^{\mathrm{miss}}$, and (f) $\overline{m}_{\mathrm{SC}}$. Post-fit normalisation scales are applied. Uncertainties are statistical only.

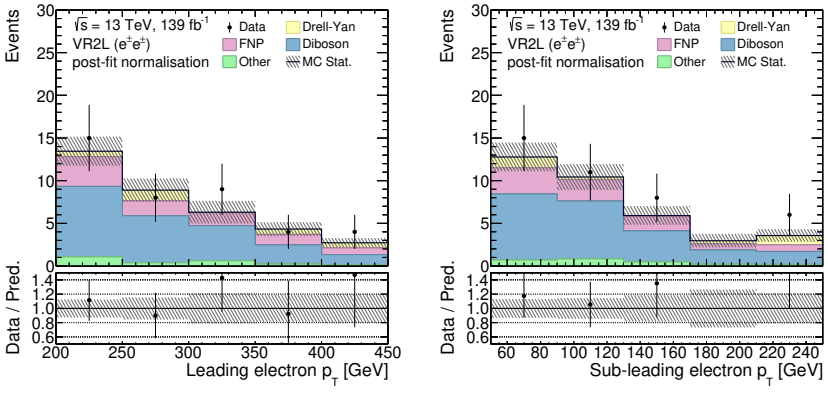

(a)

(b)

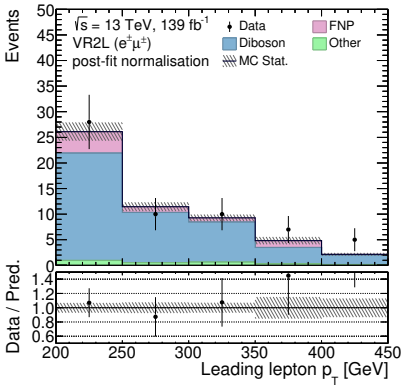

(c)

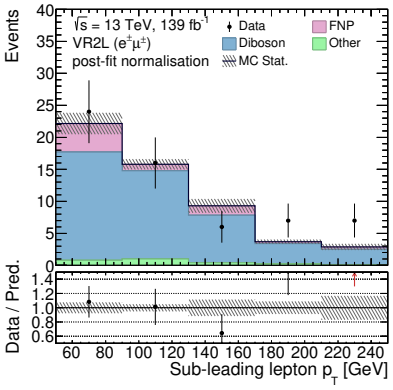

(d)

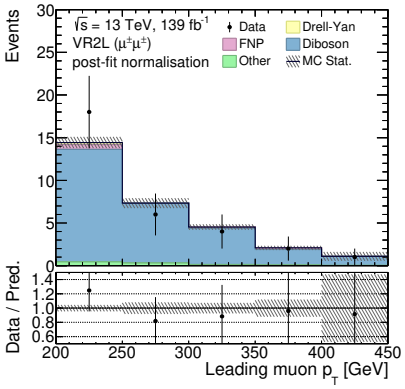

(e)

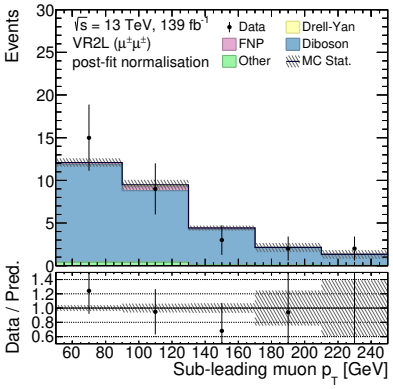

(f)

Figure B.6: Leading and sub-leading lepton momentum distributions in the **VR2L**, the two-lepton cut-based validation region, for all flavour combinations. Post-fit normalisation scales are applied. Uncertainties are statistical only.

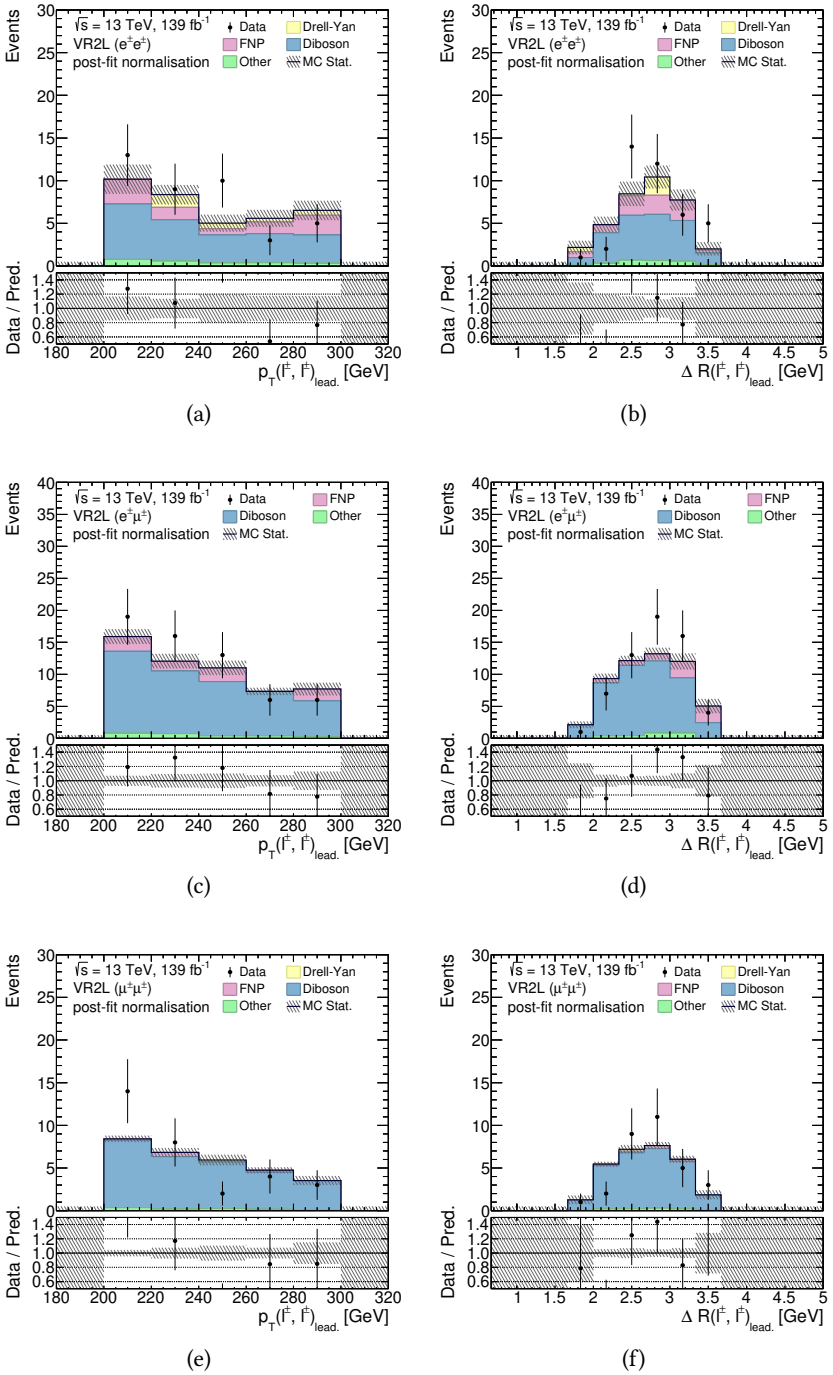

Figure B.7: Transverse momenta, $p_{\mathrm{T}}(\ell^{\pm}\ell'^{\pm})_{\mathrm{lead}}$, (left) and angular separation, $\Delta R(\ell^{\pm}\ell'^{\pm})_{\mathrm{lead}}$, (right) distributions of the leading lepton pair in the **VR2L**, the two-lepton cut-based validation region, for all flavour combinations. Post-fit normalisation scales are applied. Uncertainties are statistical only.

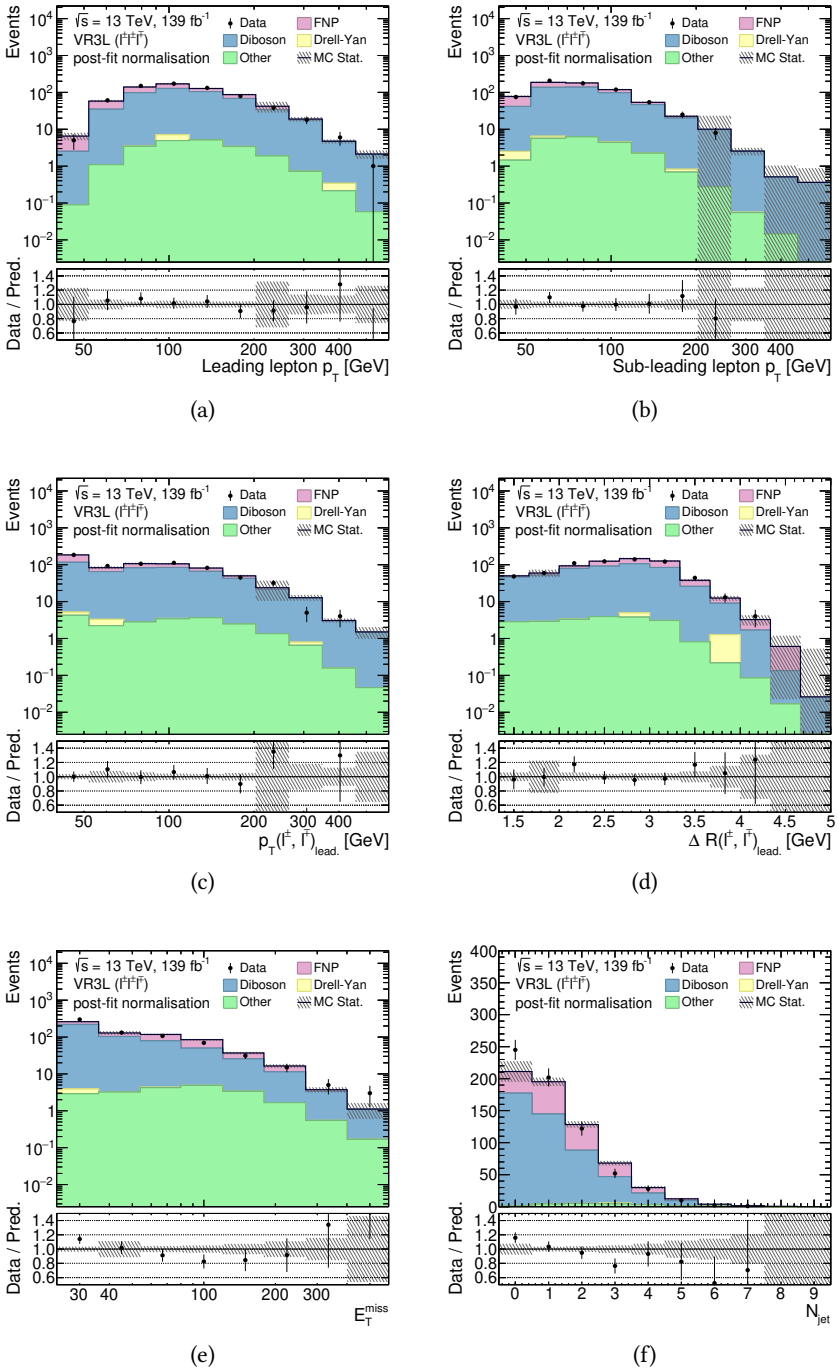

Figure B.8: Different kinematical distributions in the **VR3L**, the three-lepton cut-based validation region. (a) $p_{\mathrm{T}}(\ell_1)$, (b) $p_{\mathrm{T}}(\ell_2)$, (c) $p_{\mathrm{T}}(\ell^{\pm}\ell'^{\pm})_{\mathrm{lead}}$, (d) $\Delta R(\ell^{\pm}\ell'^{\pm})_{\mathrm{lead}}$, (e) $E_{\mathrm{T}}^{\mathrm{miss}}$, and (f) N_{jet}. Post-fit normalisation scales are applied. Uncertainties are statistical only.

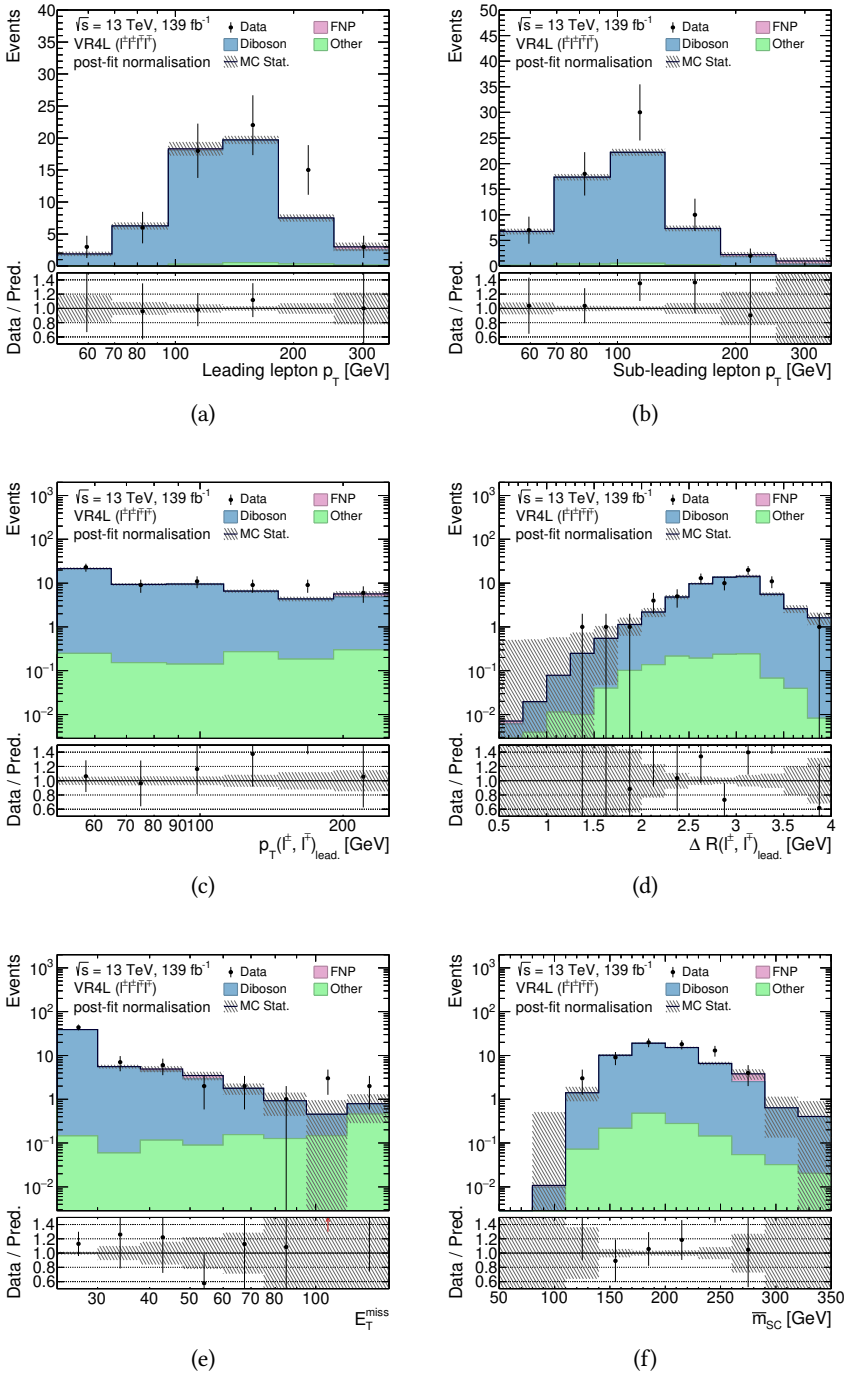

Figure B.9: Different kinematical distributions in the **VR4L**, the four-lepton cut-based validation region. (a) $p_{\mathrm{T}}(\ell_1)$, (b) $p_{\mathrm{T}}(\ell_2)$, (c) $p_{\mathrm{T}}(\ell^{\pm}\ell'^{\pm})_{\mathrm{lead}}$, (d) $\Delta R(\ell^{\pm}\ell'^{\pm})_{\mathrm{lead}}$, (e) $E_{\mathrm{T}}^{\mathrm{miss}}$, and (f) $\overline{m}_{\mathrm{SC}}$. Post-fit normalisation scales are applied. Uncertainties are statistical only.

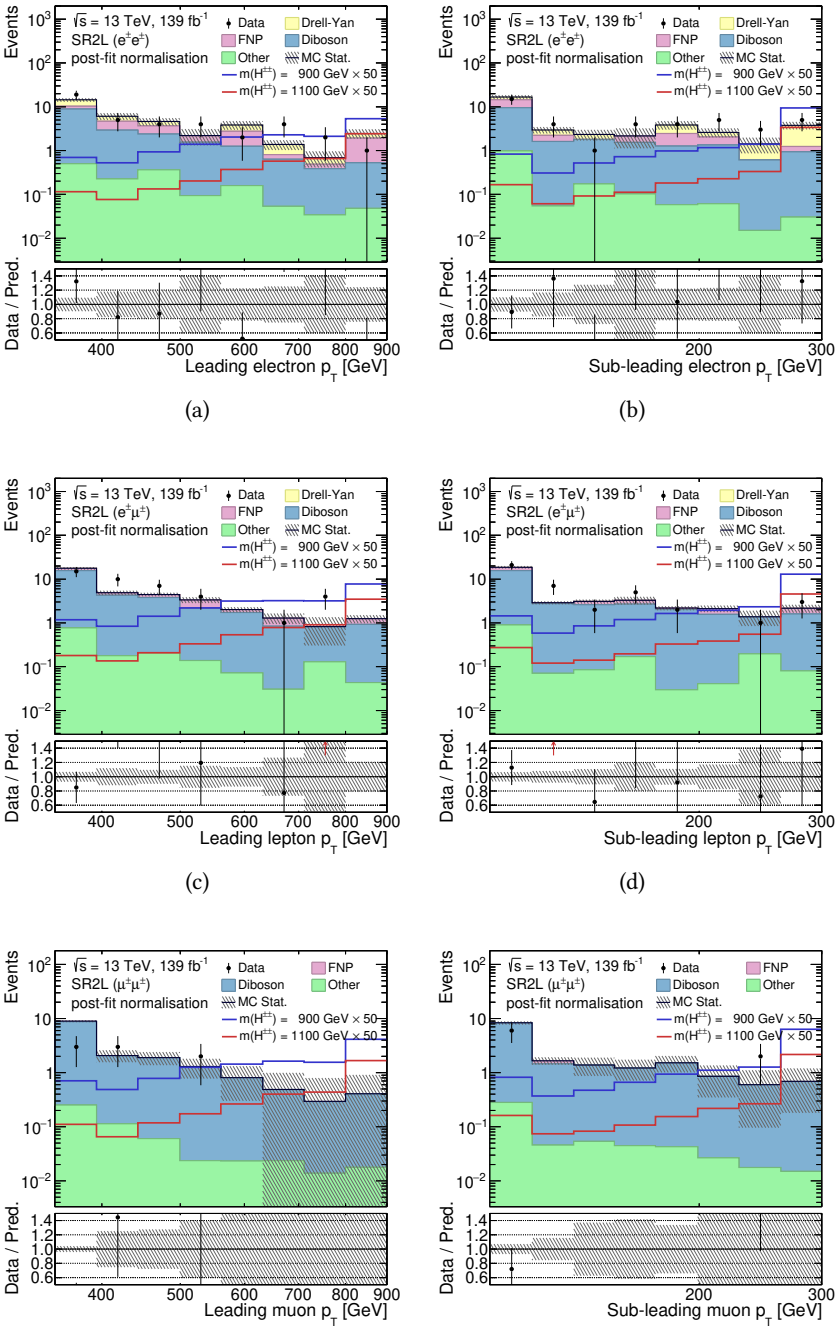

Figure B.10: Leading and sub-leading lepton momentum distributions in the **SR2L**, the two-lepton cut-based signal region for all flavour combinations. Post-fit normalisation scales are applied. Uncertainties are statistical only.

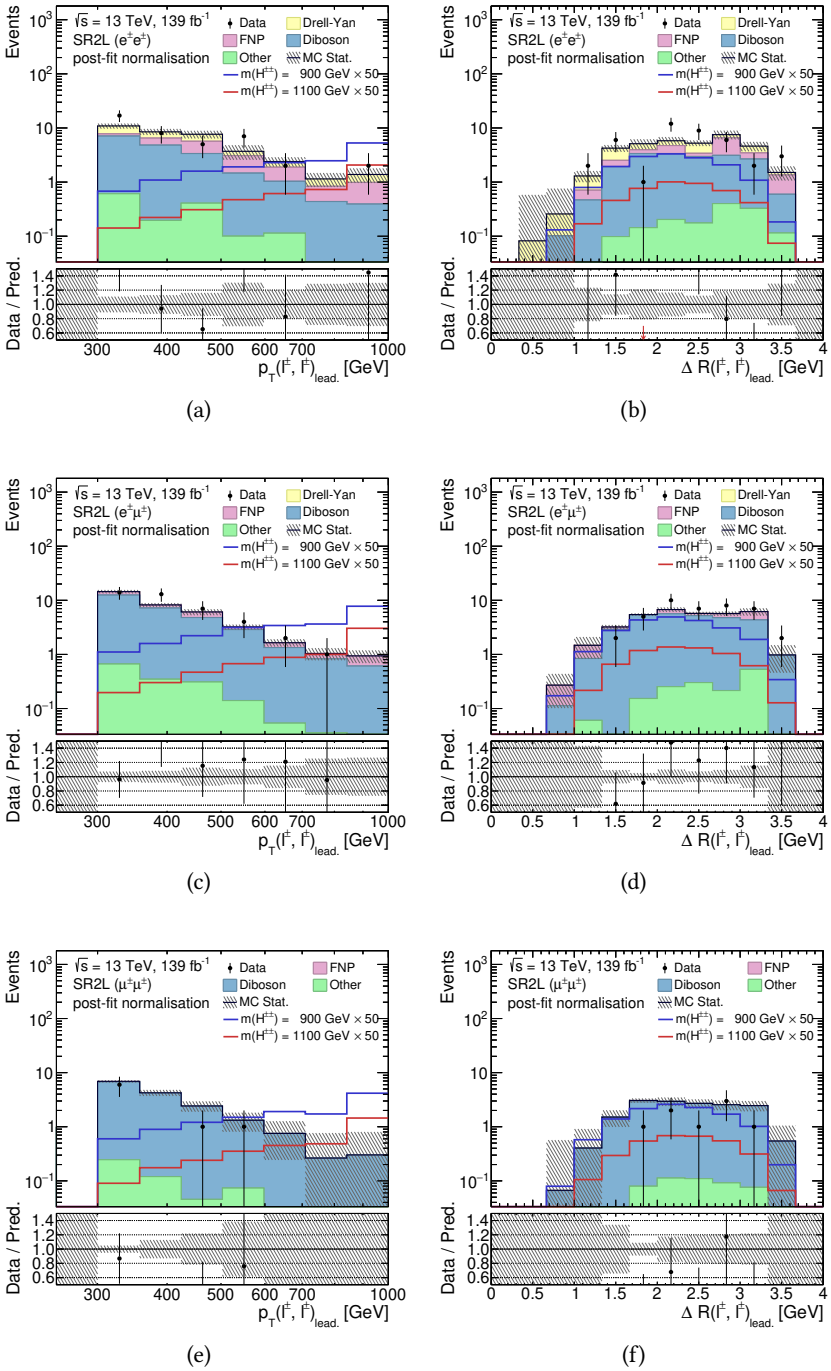

Figure B.11: Transverse momenta, $p_{\mathrm{T}}(\ell^{\pm}\ell'^{\pm})_{\mathrm{lead}}$, (left) and angular separation, $\Delta R(\ell^{\pm}\ell'^{\pm})_{\mathrm{lead}}$, (right) distributions of the leading lepton pair in the **SR2L**, the two-lepton cut-based signal region for all flavour combinations. Post-fit normalisation scales are applied. Uncertainties are statistical only.

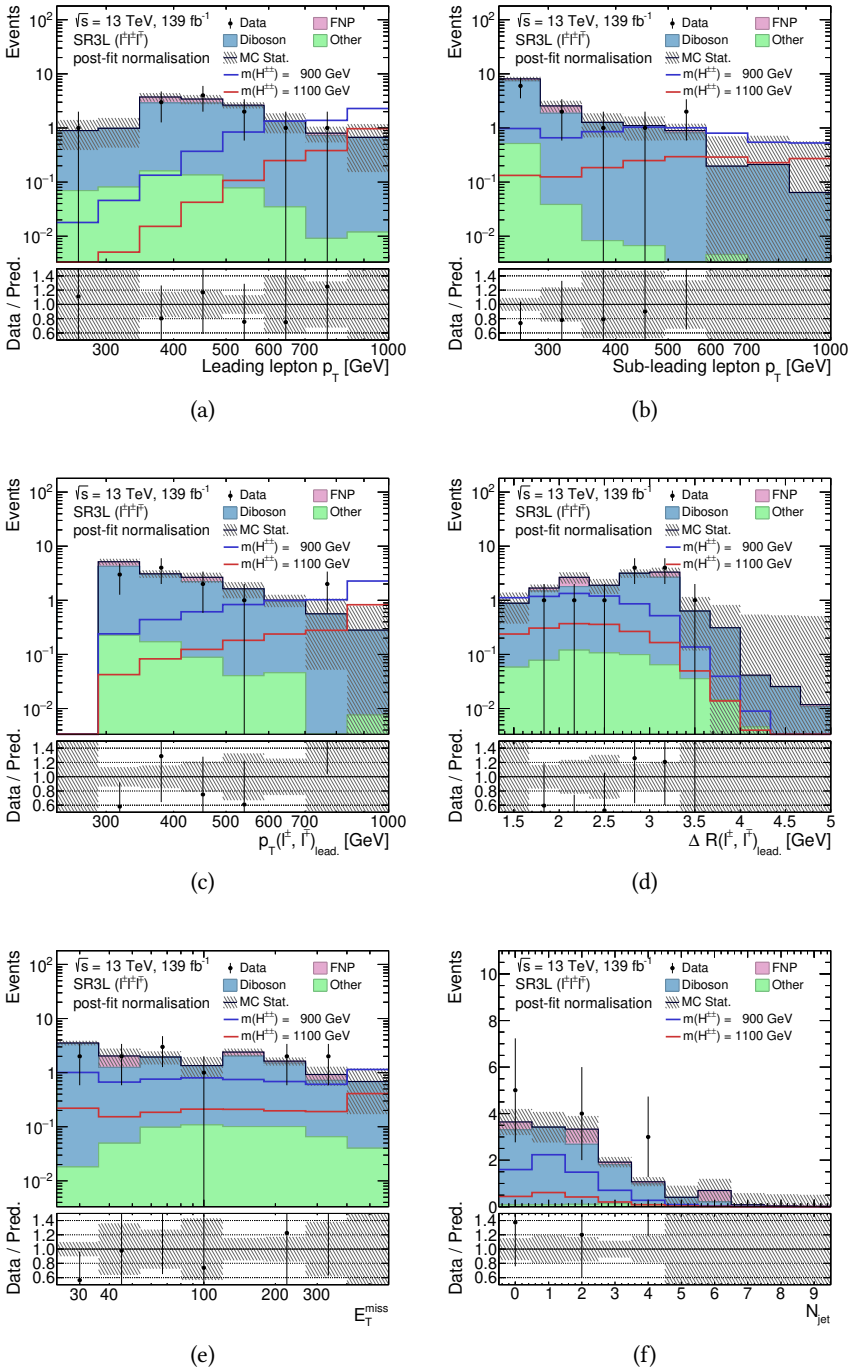

Figure B.12: Different kinematical distributions in the **SR3L**, the three-lepton cut-based signal region. (a) $p_{\mathrm{T}}(\ell_1)$, (b) $p_{\mathrm{T}}(\ell_2)$, (c) $p_{\mathrm{T}}(\ell^{\pm}\ell'^{\pm})_{\mathrm{lead}}$, (d) $\Delta R(\ell^{\pm}\ell'^{\pm})_{\mathrm{lead}}$, (e) $E_{\mathrm{T}}^{\mathrm{miss}}$, and (f) N_{jet}. Post-fit normalisation scales are applied. Uncertainties are statistical only.

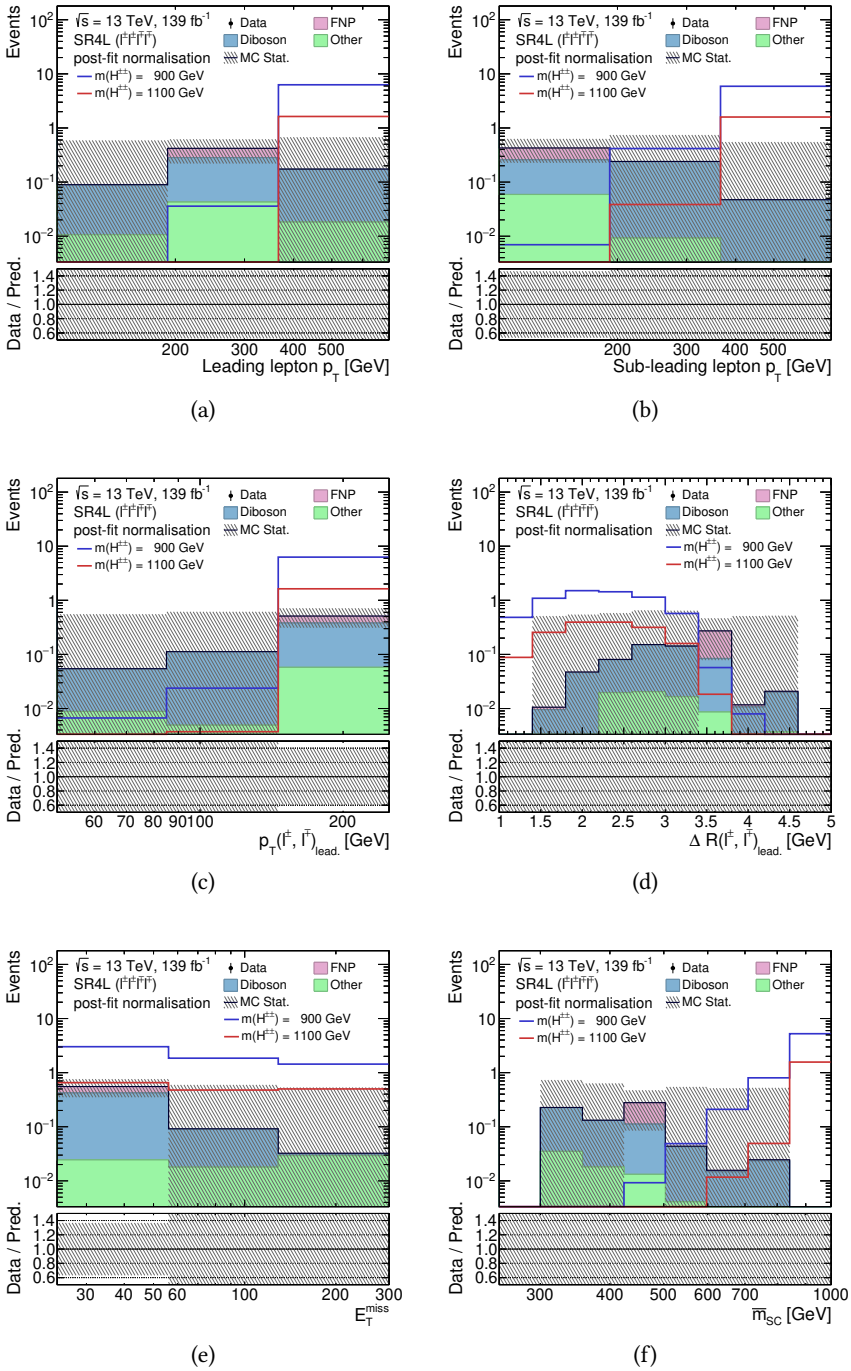

Figure B.13: Different kinematical distributions in the **SR4L**, the four-lepton cut-based signal region. (a) $p_{\mathrm{T}}(\ell_1)$, (b) $p_{\mathrm{T}}(\ell_2)$, (c) $p_{\mathrm{T}}(\ell^{\pm}\ell'^{\pm})_{\mathrm{lead}}$, (d) $\Delta R(\ell^{\pm}\ell'^{\pm})_{\mathrm{lead}}$, (e) $E_{\mathrm{T}}^{\mathrm{miss}}$, and (f) $\overline{m}_{\mathrm{SC}}$. Post-fit normalisation scales are applied. Uncertainties are statistical only.

APPENDIX C

Selected Distributions of the Multivariate Analysis Regions

Selected kinematic distributions are showcased, demonstrating the consistency between expected and observed events across all multivariate analysis regions.

Two sets of plots are presented for each two-lepton region. First, transverse momenta of leading (left) and sub-leading (right) leptons are presented. Then, transverse momenta, $p_{\mathrm{T}}(\ell^{\pm}\ell'^{\pm})_{\mathrm{lead}}$, (left) and angular separation, $\Delta R(\ell^{\pm}\ell'^{\pm})_{\mathrm{lead}}$, (right) distributions of the leading lepton pair for each channel are shown. The *ee* channel is presented in the first, the $e\mu$ channel in the middle and the $\mu\mu$ channel in the last row.

Six distributions also used during region optimisation are given for three- and four-lepton regions, i.e. $p_{\mathrm{T}}(\ell_1)$, $p_{\mathrm{T}}(\ell_2)$, $p_{\mathrm{T}}(\ell^{\pm}\ell'^{\pm})_{\mathrm{lead}}$, $\Delta R(\ell^{\pm}\ell'^{\pm})_{\mathrm{lead}}$, $E_{\mathrm{T}}^{\mathrm{miss}}$, and N_{jet}. The N_{jet} distribution is replaced by $\overline{m}_{\mathrm{SC}}$ in four-lepton regions.

The contents of this chapter are as follows:

- **DYCR:** Drell–Yan control region in Figure C.1,
- **DBCR2L:** Two-lepton diboson control region in Figures C.2 and C.3,
- **DBCR3L:** Three-lepton diboson control region in Figure C.4,
- **CR4L:** Four-lepton control region in Figure C.5,
- **VR2L:** Two-lepton validation region in Figures C.6 and C.7,
- **VR3L:** Three-lepton validation region in Figure C.8,
- **VR4L:** Four-lepton validation region in Figure C.9,
- **SR2L:** Two-lepton signal region in Figures C.10 and C.11,
- **SR3L:** Three-lepton signal region in Figure C.12, and
- **SR4L:** Four-lepton signal region in Figure C.13.

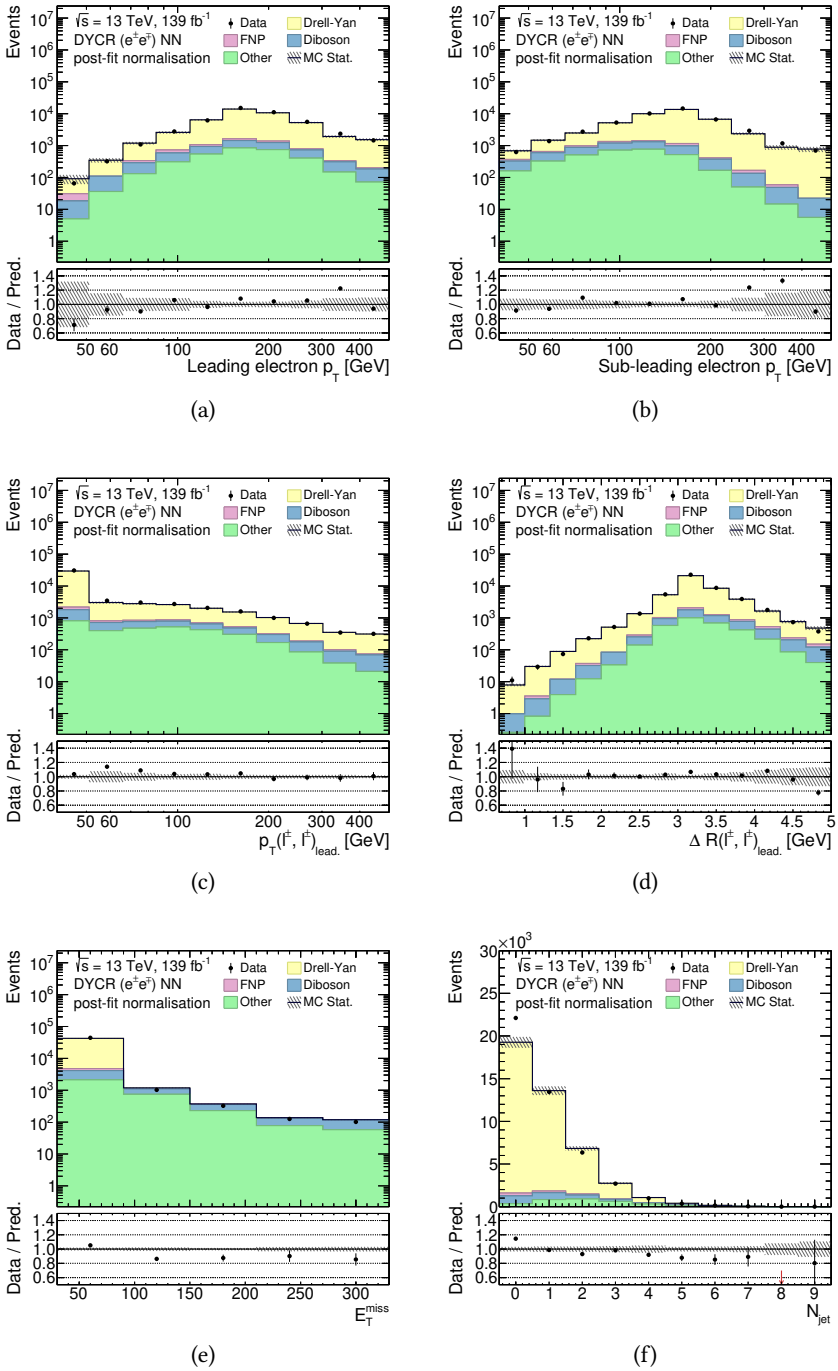

Figure C.1: Different kinematical distributions in the **DYCR**, the two-lepton multivariate Drell–Yan control region. (a) $p_{\mathrm{T}}(\ell_1)$, (b) $p_{\mathrm{T}}(\ell_2)$, (c) $p_{\mathrm{T}}(e^{\pm}e^{\mp})_{\mathrm{lead}}$, (d) $\Delta R(e^{\pm}e^{\mp})_{\mathrm{lead}}$, (e) $E_{\mathrm{T}}^{\mathrm{miss}}$, and (f) N_{jet}. Post-fit normalisation scales are applied. Uncertainties are statistical only.

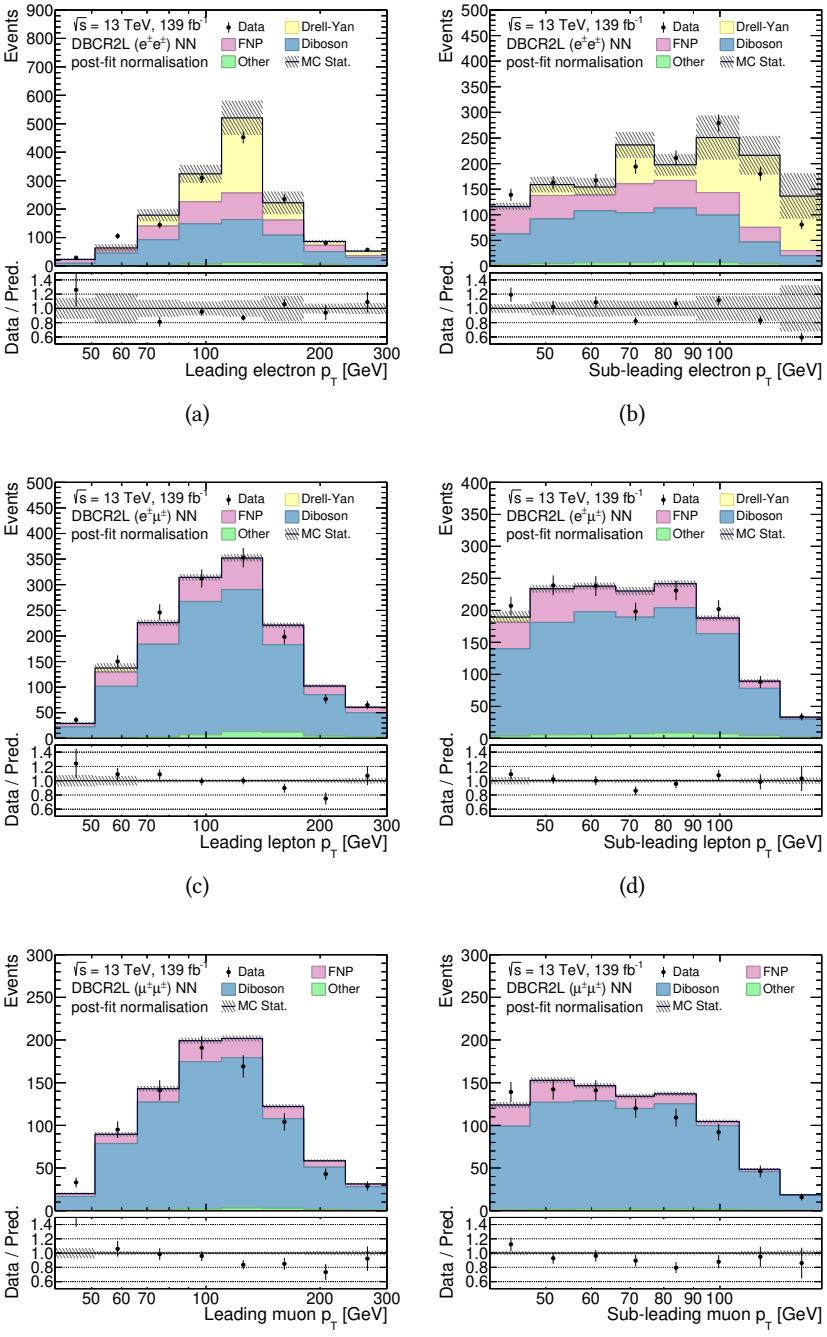

Figure C.2: Leading and sub-leading lepton momentum distributions in the **DBCR2L**, the two-lepton multivariate diboson control region, for all flavour combinations. Post-fit normalisation scales are applied. Uncertainties are statistical only.

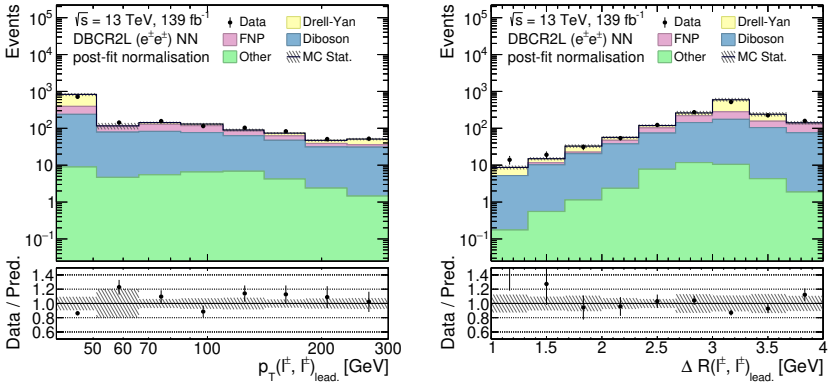

(a)

(b)

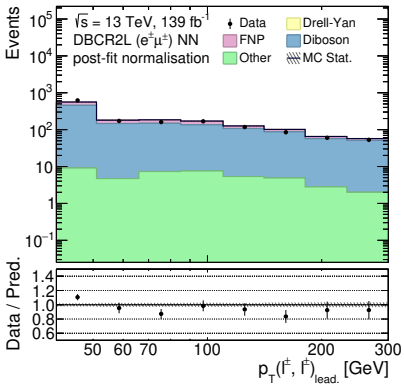

(c)

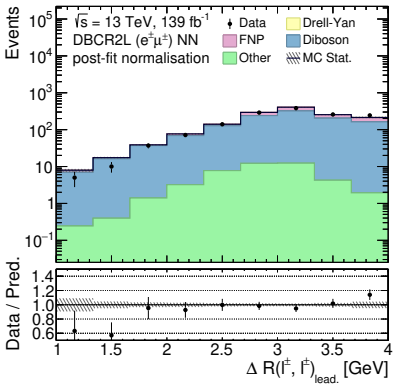

(d)

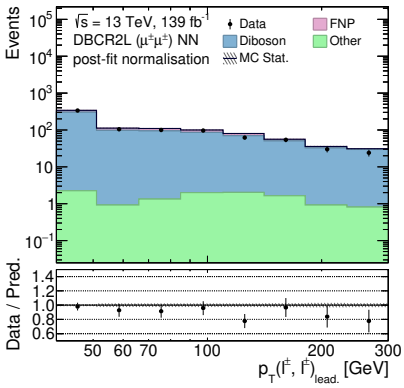

(e)

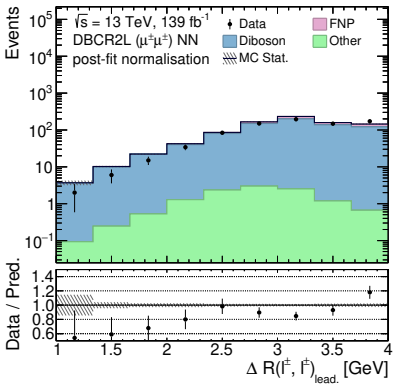

(f)

Figure C.3: Transverse momenta, $p_{\mathrm{T}}(\ell^{\pm}\ell'^{\pm})_{\mathrm{lead}}$, (left) and angular separation, $\Delta R(\ell^{\pm}\ell'^{\pm})_{\mathrm{lead}}$, (right) distributions of the leading lepton pair in the **DBCR2L**, the two-lepton multivariate diboson control region for all flavour combinations. Post-fit normalisation scales are applied. Uncertainties are statistical only.

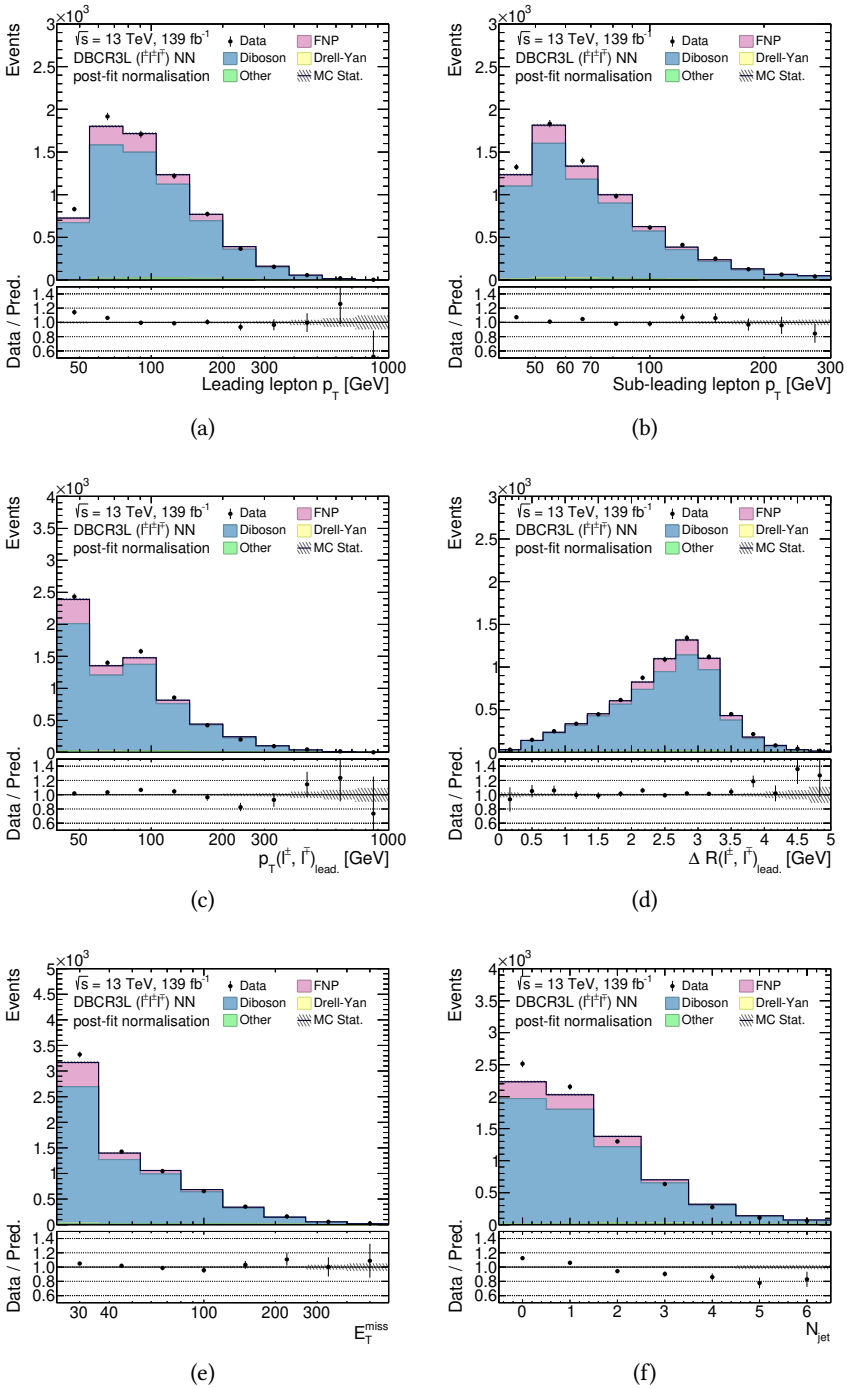

Figure C.4: Different kinematical distributions in the **DBCR3L**, the three-lepton multivariate diboson control region. (a) $p_{\mathrm{T}}(\ell_1)$, (b) $p_{\mathrm{T}}(\ell_2)$, (c) $p_{\mathrm{T}}(\ell^{\pm}\ell'^{\pm})_{\mathrm{lead}}$, (d) $\Delta R(\ell^{\pm}\ell'^{\pm})_{\mathrm{lead}}$, (e) $E_{\mathrm{T}}^{\mathrm{miss}}$, and (f) N_{jet}. Post-fit normalisation scales are applied. Uncertainties are statistical only.

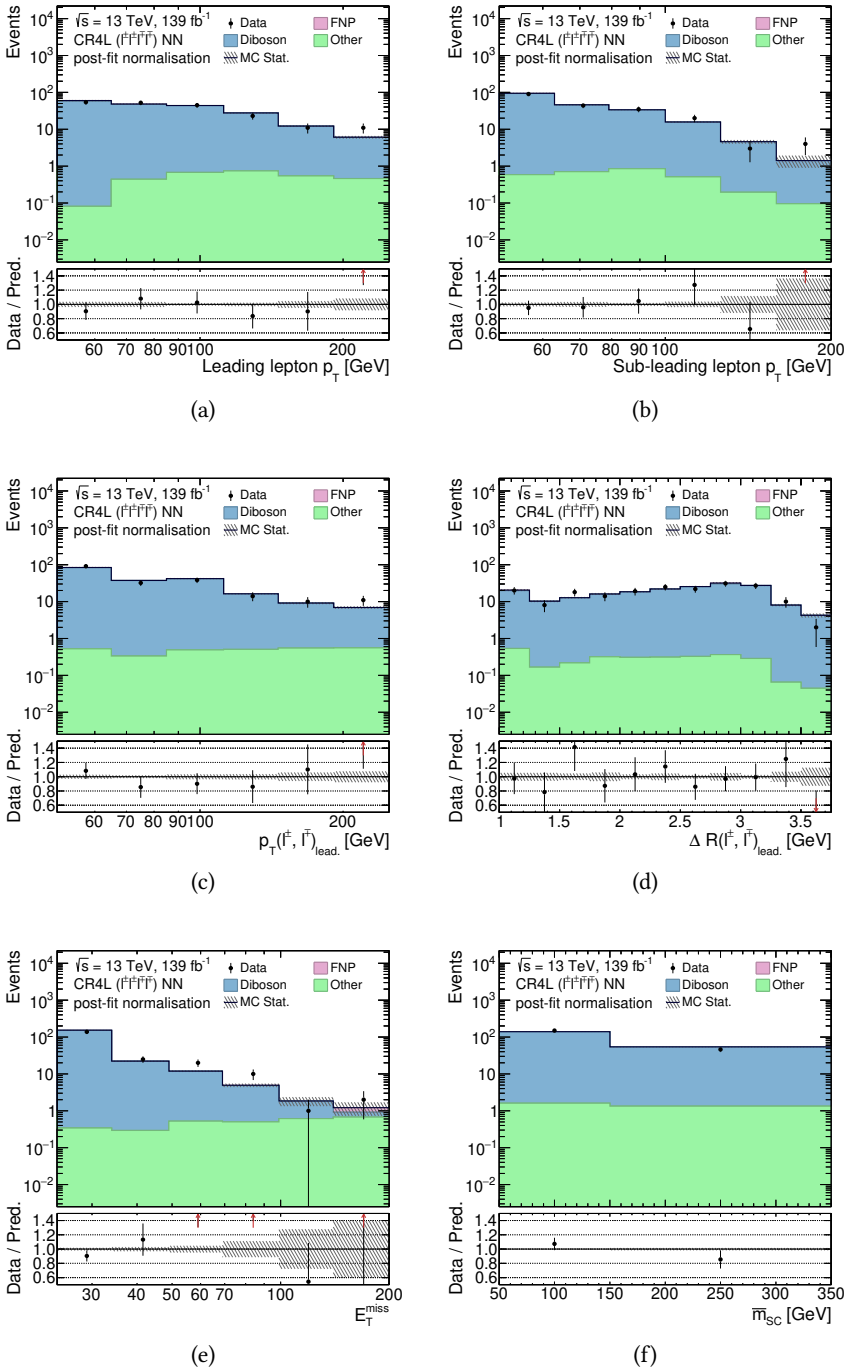

Figure C.5: Different kinematical distributions in the **CR4L**, the four-lepton multivariate control region. (a) $p_{\mathrm{T}}(\ell_1)$, (b) $p_{\mathrm{T}}(\ell_2)$, (c) $p_{\mathrm{T}}(\ell^{\pm}\ell'^{\pm})_{\mathrm{lead}}$, (d) $\Delta R(\ell^{\pm}\ell'^{\pm})_{\mathrm{lead}}$, (e) $E_{\mathrm{T}}^{\mathrm{miss}}$, and (f) $\overline{m}_{\mathrm{SC}}$. Post-fit normalisation scales are applied. Uncertainties are statistical only.

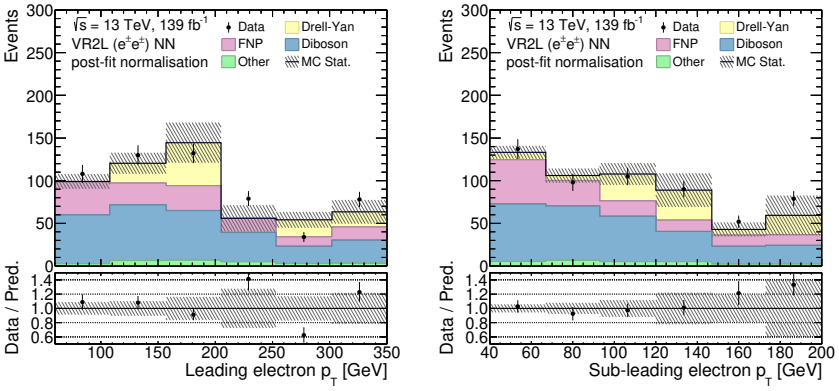

(a)

(b)

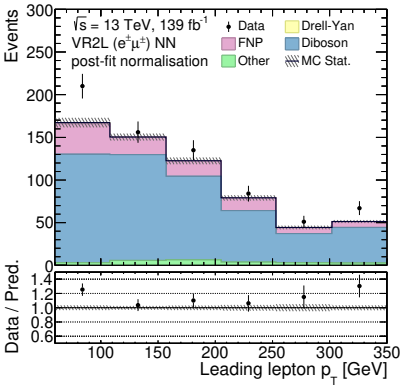

(c)

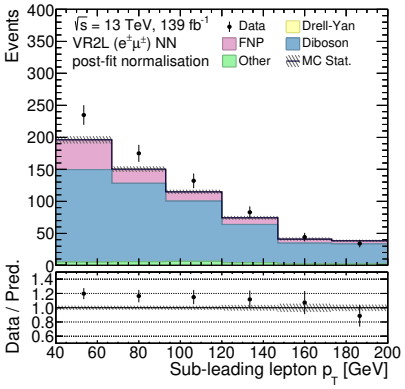

(d)

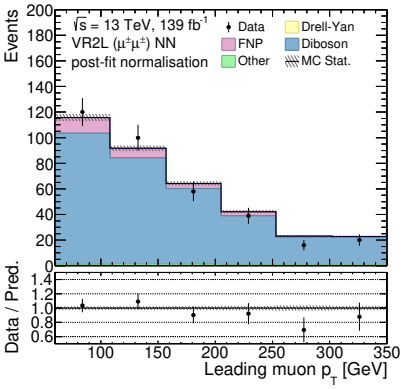

(e)

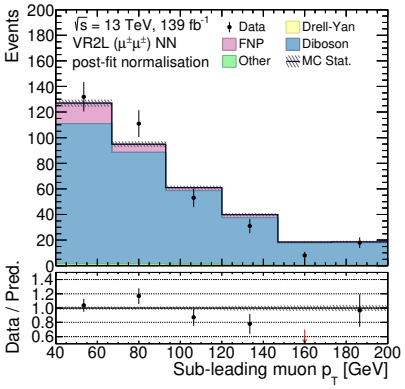

(f)

Figure C.6: Leading and sub-leading lepton momentum distributions in the **VR2L**, the two-lepton multivariate validation region, for all flavour combinations. Post-fit normalisation scales are applied. Uncertainties are statistical only.

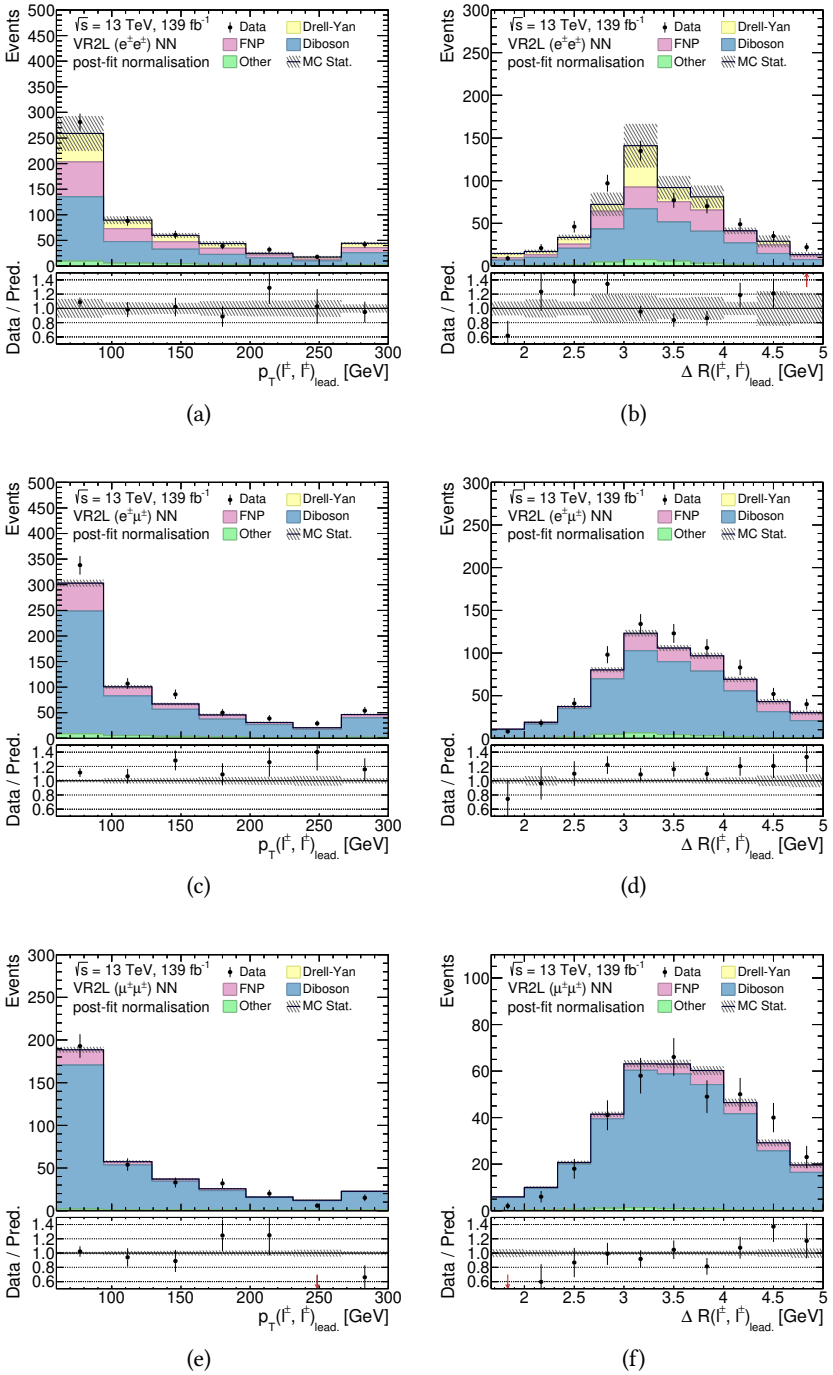

Figure C.7: Transverse momenta, $p_{\mathrm{T}}(\ell^{\pm}\ell'^{\pm})_{\mathrm{lead}}$, (left) and angular separation, $\Delta R(\ell^{\pm}\ell'^{\pm})_{\mathrm{lead}}$, (right) distributions of the leading lepton pair in the **VR2L**, the two-lepton multivariate validation region, for all flavour combinations. Post-fit normalisation scales are applied. Uncertainties are statistical only.

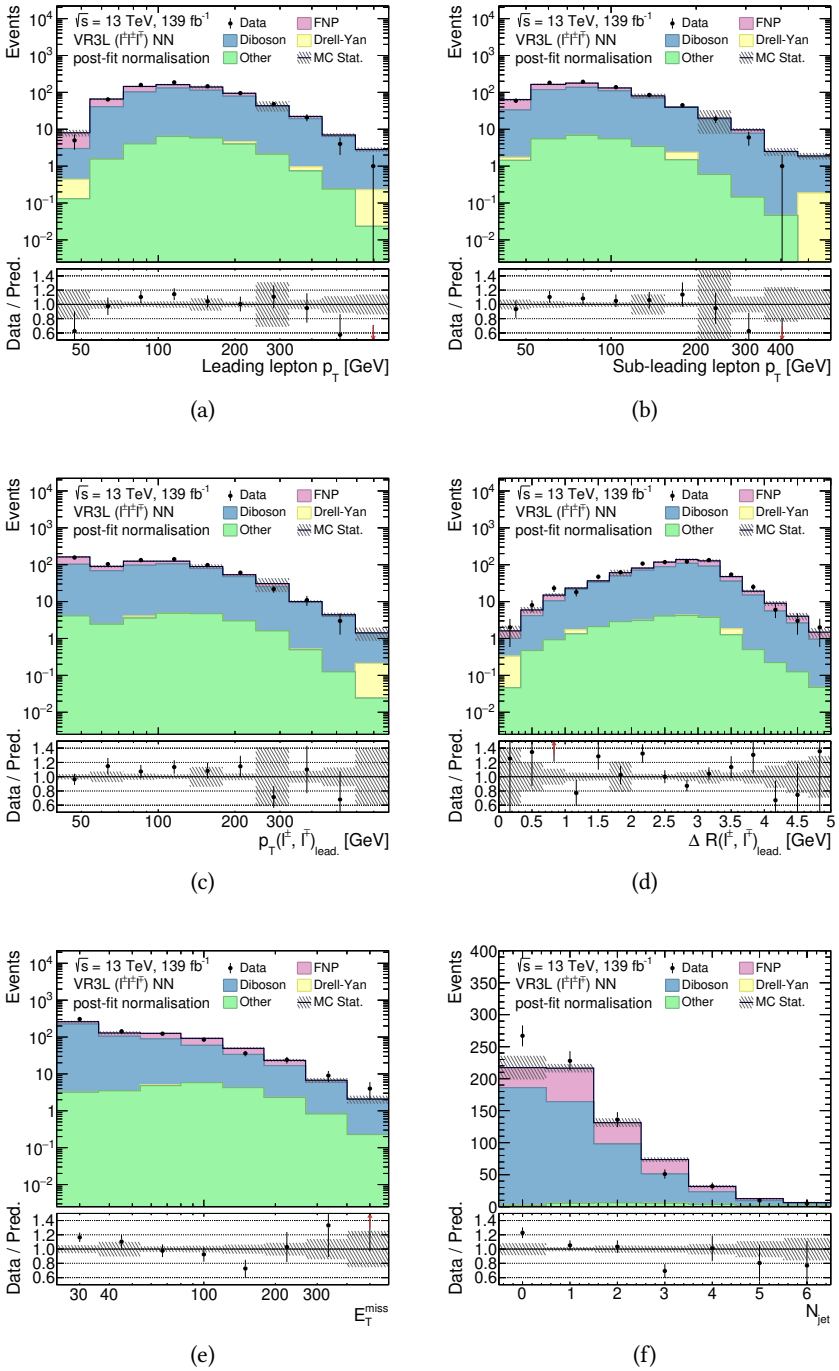

Figure C.8: Different kinematical distributions in the **VR3L**, the three-lepton multivariate validation region. (a) $p_{\mathrm{T}}(\ell_1)$, (b) $p_{\mathrm{T}}(\ell_2)$, (c) $p_{\mathrm{T}}(\ell^{\pm}\ell'^{\pm})_{\mathrm{lead}}$, (d) $\Delta R(\ell^{\pm}\ell'^{\pm})_{\mathrm{lead}}$, (e) $E_{\mathrm{T}}^{\mathrm{miss}}$, and (f) N_{jet}. Post-fit normalisation scales are applied. Uncertainties are statistical only.

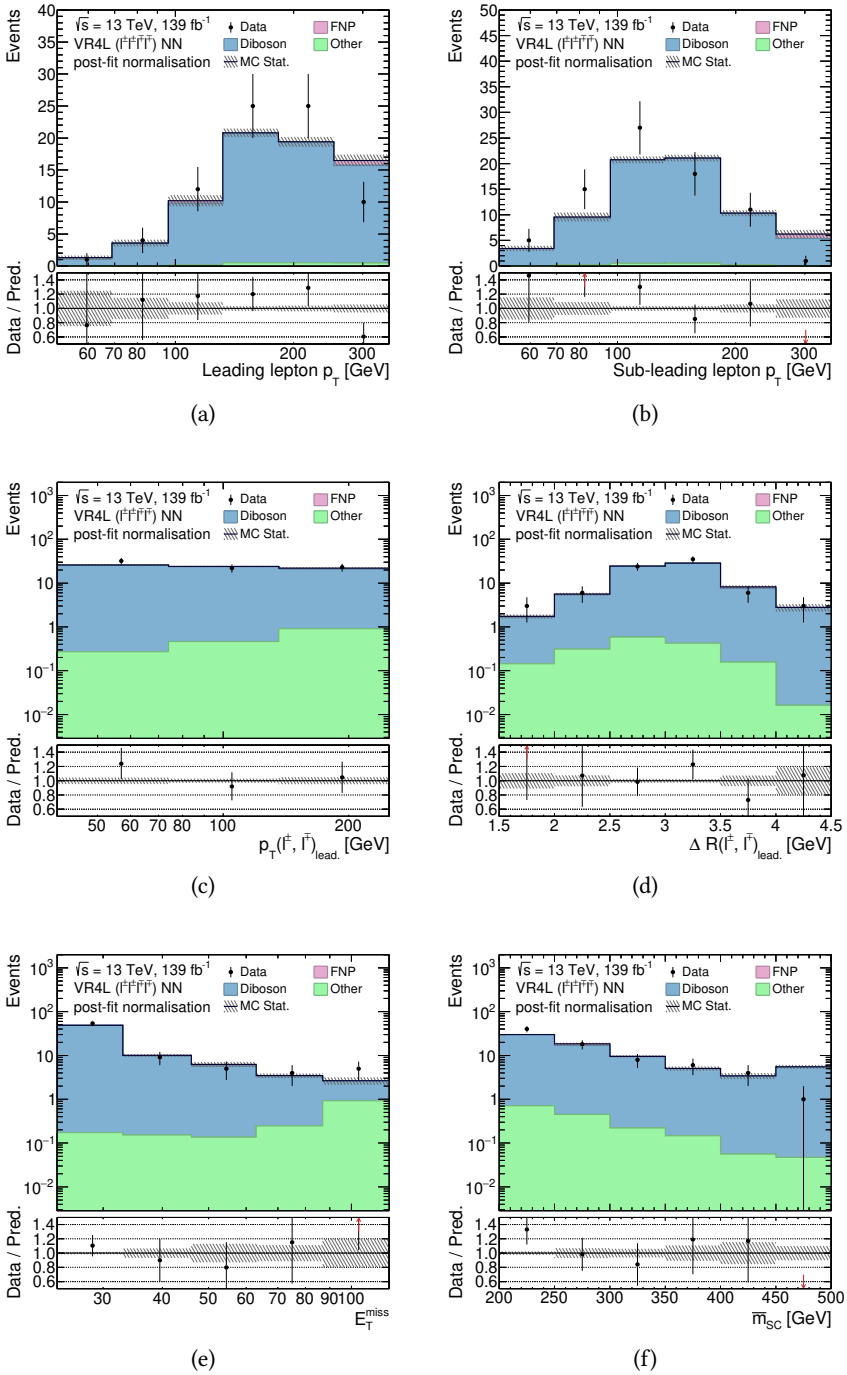

Figure C.9: Different kinematical distributions in the **VR4L**, the four-lepton multivariate validation region. (a) $p_{\mathrm{T}}(\ell_1)$, (b) $p_{\mathrm{T}}(\ell_2)$, (c) $p_{\mathrm{T}}(\ell^{\pm}\ell'^{\pm})_{\mathrm{lead}}$, (d) $\Delta R(\ell^{\pm}\ell'^{\pm})_{\mathrm{lead}}$, (e) $E_{\mathrm{T}}^{\mathrm{miss}}$, and (f) $\overline{m}_{\mathrm{SC}}$. Post-fit normalisation scales are applied. Uncertainties are statistical only.

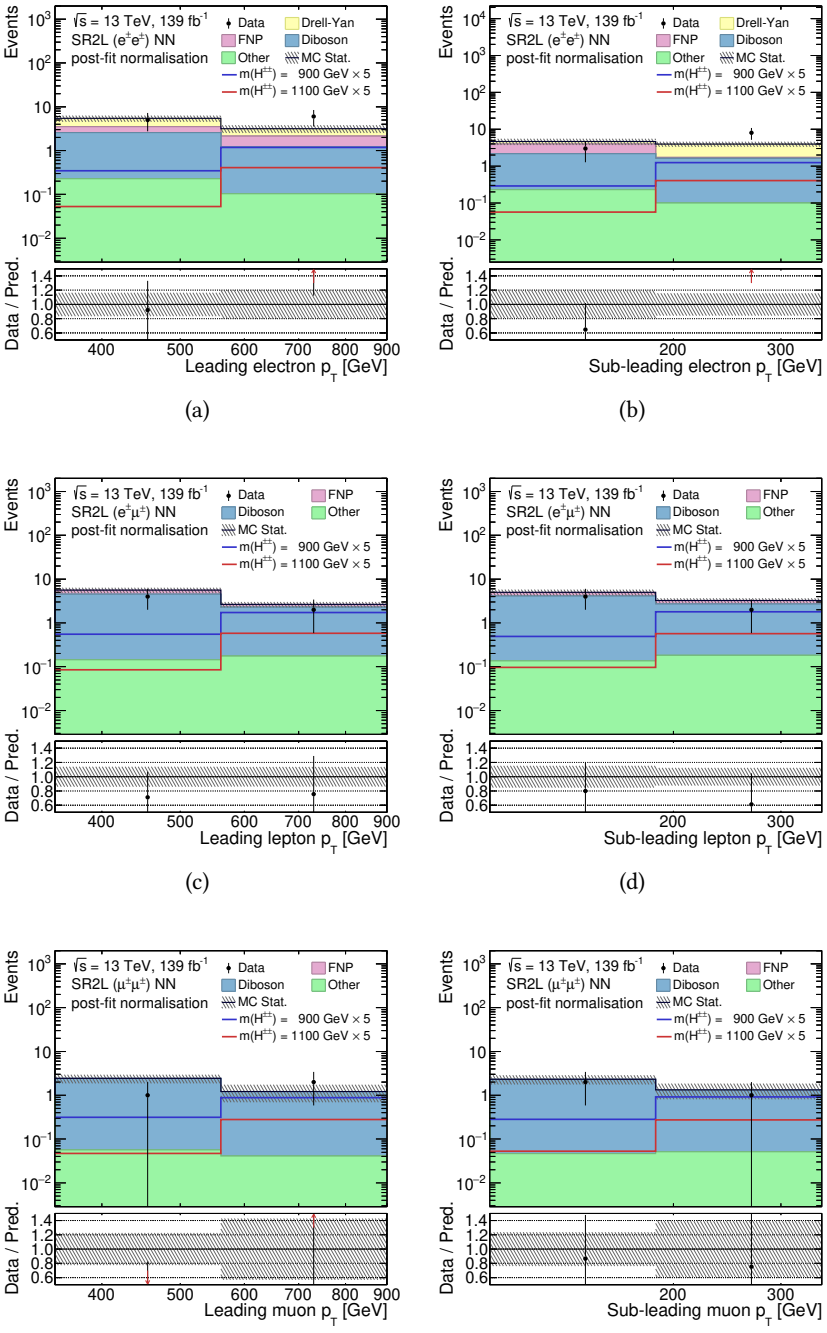

Figure C.10: Leading and sub-leading lepton momentum distributions in the **SR2L**, the two-lepton multivariate signal region for all flavour combinations. Post-fit normalisation scales are applied. Uncertainties are statistical only.

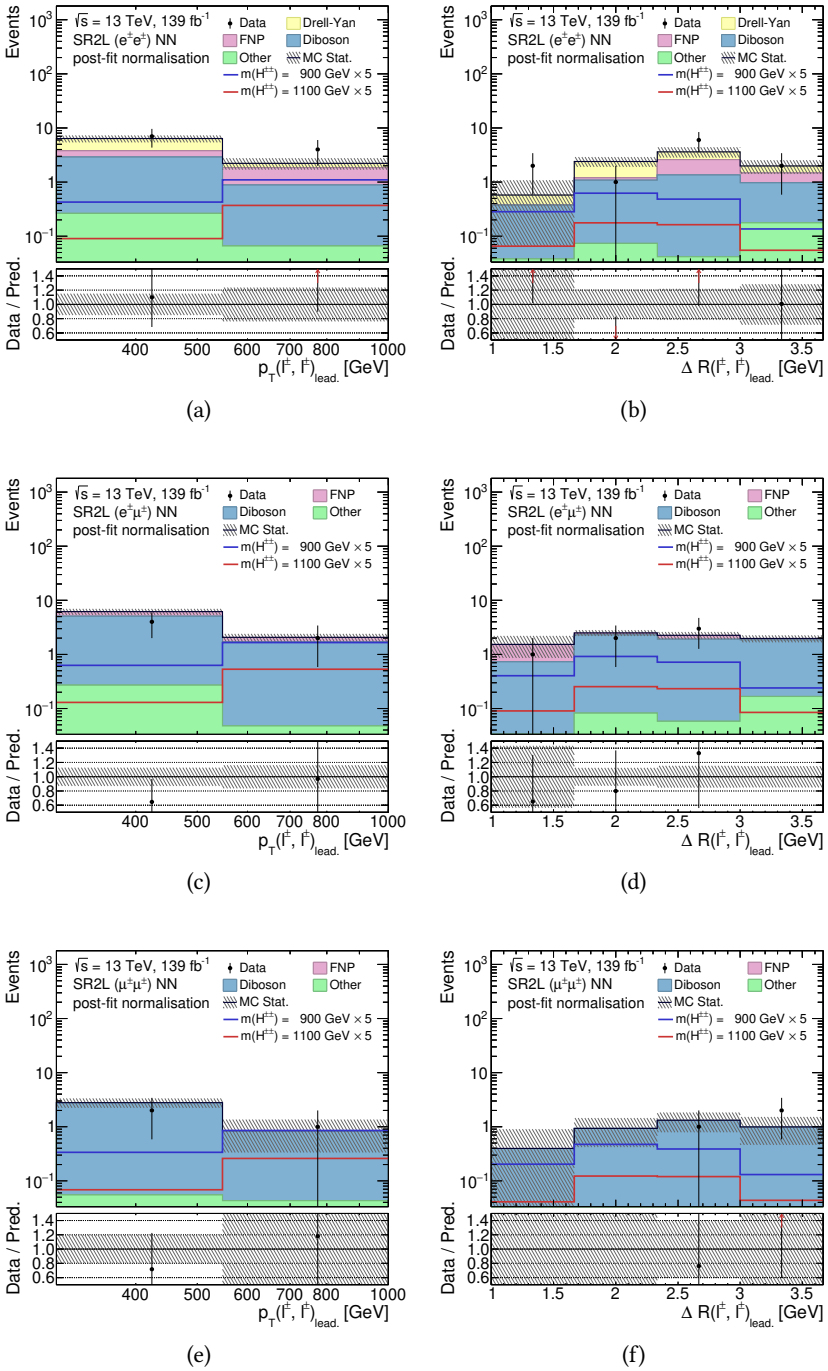

Figure C.11: Transverse momenta, $p_{\mathrm{T}}(\ell^{\pm}\ell'^{\pm})_{\mathrm{lead}}$, (left) and angular separation, $\Delta R(\ell^{\pm}\ell'^{\pm})_{\mathrm{lead}}$, (right) distributions of the leading lepton pair in the **SR2L**, the two-lepton multivariate signal region for all flavour combinations. Post-fit normalisation scales are applied. Uncertainties are statistical only.

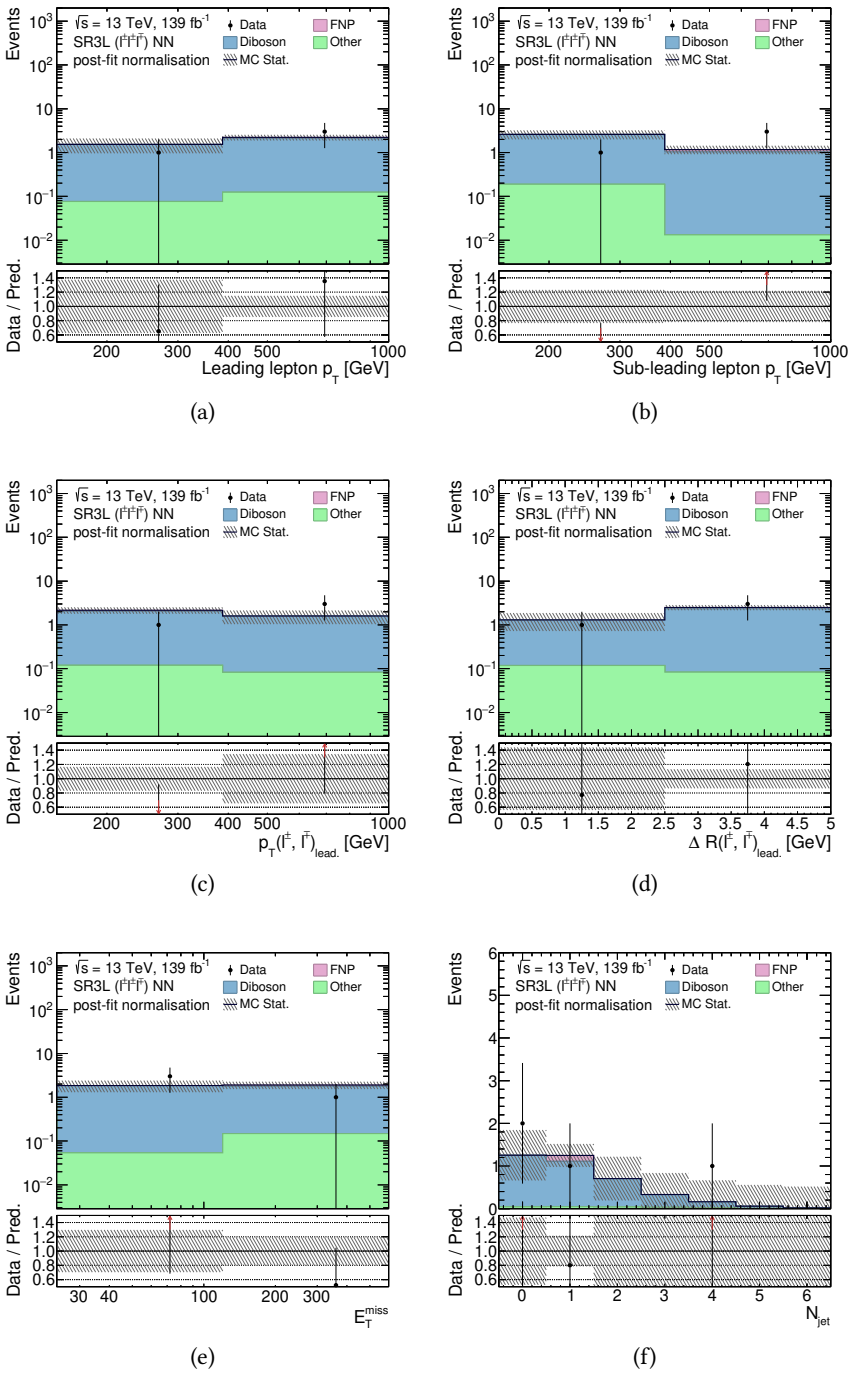

Figure C.12: Different kinematical distributions in the **SR3L**, the three-lepton multivariate signal region. (a) $p_{\mathrm{T}}(\ell_1)$, (b) $p_{\mathrm{T}}(\ell_2)$, (c) $p_{\mathrm{T}}(\ell^{\pm}\ell'^{\pm})_{\mathrm{lead}}$, (d) $\Delta R(\ell^{\pm}\ell'^{\pm})_{\mathrm{lead}}$, (e) $E_{\mathrm{T}}^{\mathrm{miss}}$, and (f) N_{jet}. Post-fit normalisation scales are applied. Uncertainties are statistical only.

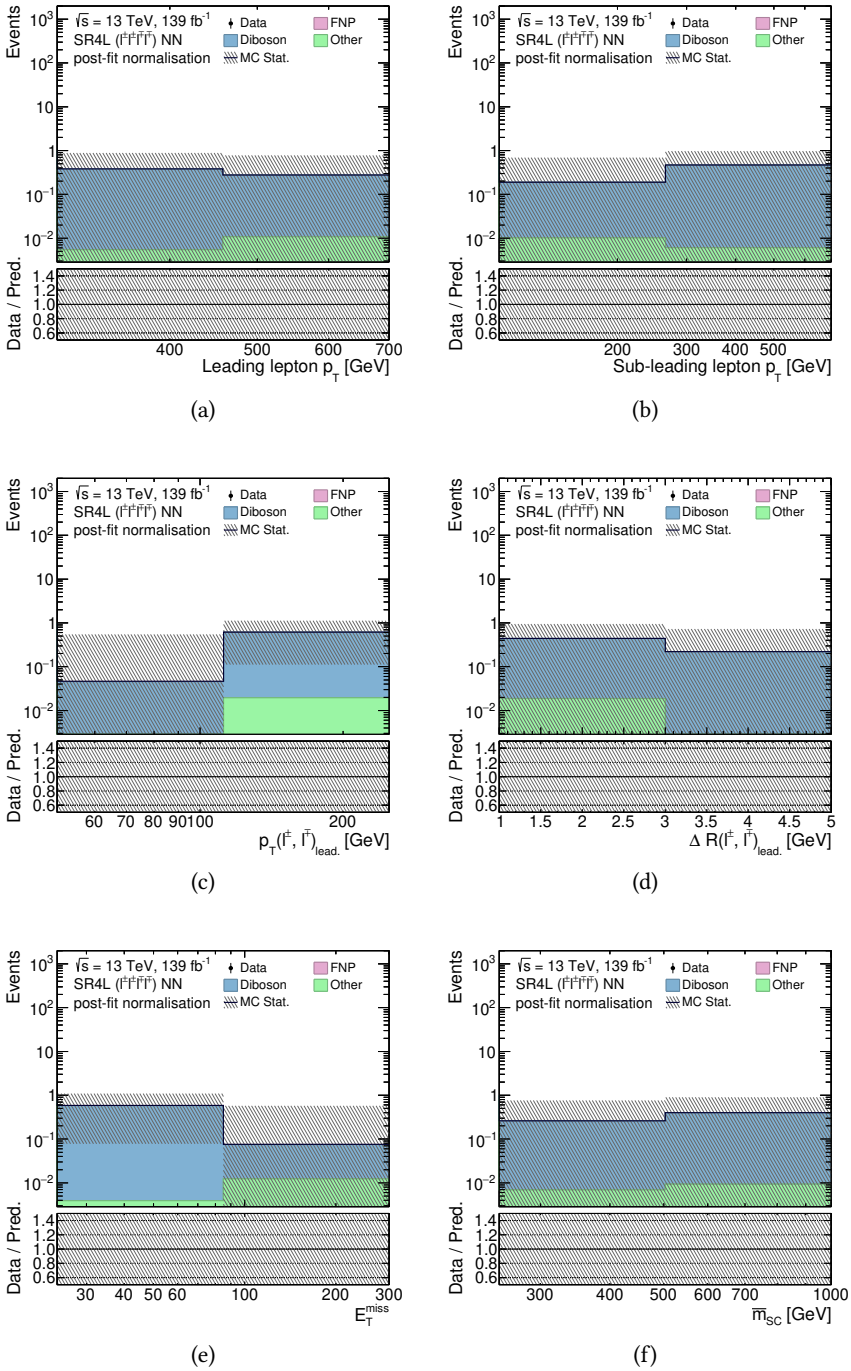

Figure C.13: Different kinematical distributions in the **SR4L**, the four-lepton multivariate signal region. (a) $p_{\mathrm{T}}(\ell_1)$, (b) $p_{\mathrm{T}}(\ell_2)$, (c) $p_{\mathrm{T}}(\ell^{\pm}\ell'^{\pm})_{\mathrm{lead}}$, (d) $\Delta R(\ell^{\pm}\ell'^{\pm})_{\mathrm{lead}}$, (e) $E_{\mathrm{T}}^{\mathrm{miss}}$, and (f) $\overline{m}_{\mathrm{SC}}$. Post-fit normalisation scales are applied. Uncertainties are statistical only.

Bibliography

[1] S. L. Glashow, *The renormalizability of vector meson interactions*, Nucl. Phys. **10** (1959) 107 (cit. on pp. 3, 4, 6, 9, 203).

[2] S. L. Glashow, *The Future of Elementary Particle Physics*, NATO Sci. Ser. B **61** (1980) 687 (cit. on pp. 3, 18, 204).

[3] S. Weinberg, *A Model of Leptons*, Phys. Rev. Lett. **19** (1967) 1264 (cit. on pp. 3, 4, 6, 9, 203).

[4] A. Salam, *Weak and Electromagnetic Interactions*, Conf. Proc. C **680519** (1968) 367 (cit. on pp. 3, 4, 6, 9, 203).

[5] D. Griffiths, *Introduction to elementary particles*, 2008, ISBN: 978-3-527-40601-2 (cit. on pp. 3, 6, 203).

[6] M. Thomson, *Modern particle physics*, New York: Cambridge University Press, 2013, ISBN: 978-1-107-03426-6 (cit. on pp. 3, 203).

[7] M. Gell-Mann, *A Schematic Model of Baryons and Mesons*, Phys. Lett. **8** (1964) 214 (cit. on pp. 4, 203).

[8] G. Zweig, 'An SU(3) model for strong interaction symmetry and its breaking. Version 2', *DEVELOPMENTS IN THE QUARK THEORY OF HADRONS. VOL. 1. 1964 - 1978*, ed. by D. B. Lichtenberg and S. P. Rosen, 1964 22 (cit. on pp. 4, 203).

[9] D. J. Gross and F. Wilczek, *Ultraviolet Behavior of Nonabelian Gauge Theories*, Phys. Rev. Lett. **30** (1973) 1343, ed. by J. C. Taylor (cit. on pp. 4, 203).

[10] H. D. Politzer, *Reliable Perturbative Results for Strong Interactions?*, Phys. Rev. Lett. **30** (1973) 1346, ed. by J. C. Taylor (cit. on pp. 4, 203).

[11] J. C. Maxwell, *A dynamical theory of the electromagnetic field*, Phil. Trans. Roy. Soc. Lond. **155** (1865) 459 (cit. on p. 4).

[12] S. Tomonaga, *On a relativistically invariant formulation of the quantum theory of wave fields*, Prog. Theor. Phys. **1** (1946) 27 (cit. on pp. 4, 203).

[13] R. P. Feynman, *Mathematical formulation of the quantum theory of electromagnetic interaction*, Phys. Rev. **80** (1950) 440, ed. by L. M. Brown (cit. on pp. 4, 203).

[14] J. S. Schwinger, *Quantum electrodynamics. I A covariant formulation*, Phys. Rev. **74** (1948) 1439, ed. by K. A. Milton (cit. on pp. 4, 203).

[15] E. Fermi, *An attempt of a theory of beta radiation. 1.*, Z. Phys. **88** (1934) 161 (cit. on pp. 4, 8, 203).

[16] G. 't Hooft, *Renormalization of Massless Yang-Mills Fields*, Nucl. Phys. B **33** (1971) 173 (cit. on pp. 4, 203).

[17] I. Newton, *Philosophiæ Naturalis Principia Mathematica*, England, 1687 (cit. on p. 4).

[18] A. Einstein, *The Field Equations of Gravitation*,
Sitzungsber. Preuss. Akad. Wiss. Berlin (Math. Phys.) **1915** (1915) 844 (cit. on p. 4).

[19] ATLAS Collaboration, *Improved W boson Mass Measurement using $\sqrt{s} = 7$ TeV Proton–Proton Collisions with the ATLAS Detector*, ATLAS-CONF-2023-004, 2023,
URL: https://cds.cern.ch/record/2853290 (cit. on p. 5).

[20] S. Schael et al., *Precision electroweak measurements on the Z resonance*,
Phys. Rept. **427** (2006) 257, arXiv: hep-ex/0509008 (cit. on p. 5).

[21] ATLAS Collaboration, *Observation of a new particle in the search for the Standard Model Higgs boson with the ATLAS detector at the LHC*, Phys. Lett. B **716** (2012) 1,
arXiv: 1207.7214 [hep-ex] (cit. on pp. 5, 15, 203).

[22] CMS Collaboration,
Observation of a new boson at a mass of 125 GeV with the CMS experiment at the LHC,
Phys. Lett. B **716** (2012) 30, arXiv: 1207.7235 [hep-ex] (cit. on pp. 5, 15, 203).

[23] ATLAS Collaboration,
Measurement of the Higgs boson mass in the $H \to ZZ^* \to 4\ell$ decay channel using 139 fb^{-1} of $\sqrt{s} = 13$ TeV pp collisions recorded by the ATLAS detector at the LHC,
Phys. Lett. B **843** (2022) 137880, arXiv: 2207.00320 [hep-ex] (cit. on p. 5).

[24] B. R. Holstein, *Graviton physics*, American Journal of Physics **74** (2006) 1002,
ISSN: 0002-9505, eprint: https://pubs.aip.org/aapt/ajp/article-pdf/74/11/1002/13128457/1002_1_online.pdf,
URL: https://doi.org/10.1119/1.2338547 (cit. on p. 5).

[25] E. Noether, *Invariant Variation Problems*, Gott. Nachr. **1918** (1918) 235,
arXiv: physics/0503066 (cit. on p. 6).

[26] M. Gell-Mann, *The interpretation of the new particles as displaced charge multiplets*,
Nuovo Cim. **4** (1956) 848 (cit. on p. 9).

[27] T. Nakano and K. Nishijima, *Charge Independence for V-particles*,
Prog. Theor. Phys. **10** (1953) 581 (cit. on p. 9).

[28] F. Englert and R. Brout, *Broken Symmetry and the Mass of Gauge Vector Mesons*,
Phys. Rev. Lett. **13** (1964) 321, ed. by J. C. Taylor (cit. on p. 10).

[29] P. W. Higgs, *Broken Symmetries and the Masses of Gauge Bosons*,
Phys. Rev. Lett. **13** (1964) 508, ed. by J. C. Taylor (cit. on p. 10).

[30] G. S. Guralnik, C. R. Hagen and T. W. B. Kibble,
Global Conservation Laws and Massless Particles,
Phys. Rev. Lett. **13** (1964) 585, ed. by J. C. Taylor (cit. on p. 10).

[31] H. Yukawa, *On the Interaction of Elementary Particles I*,
Proc. Phys. Math. Soc. Jap. **17** (1935) 48 (cit. on p. 11).

[32] R. L. Workman et al., *Review of Particle Physics*, PTEP **2022** (2022) 083C01
(cit. on pp. 12, 16, 17, 82, 209).

[33] N. Cabibbo, *Unitary Symmetry and Leptonic Decays*, Phys. Rev. Lett. **10** (1963) 531 (cit. on p. 13).

[34] M. Kobayashi and T. Maskawa, *CP Violation in the Renormalizable Theory of Weak Interaction*, Prog. Theor. Phys. **49** (1973) 652 (cit. on p. 13).

[35] F. J. Hasert et al., *Search for Elastic ν_μ Electron Scattering*, Phys. Lett. B **46** (1973) 121 (cit. on p. 15).

[36] G. Arnison et al., *Experimental Observation of Isolated Large Transverse Energy Electrons with Associated Missing Energy at $\sqrt{s} = 540$ GeV*, Phys. Lett. B **122** (1983) 103 (cit. on pp. 15, 31).

[37] M. Banner et al., *Observation of Single Isolated Electrons of High Transverse Momentum in Events with Missing Transverse Energy at the CERN anti-p p Collider*, Phys. Lett. B **122** (1983) 476 (cit. on pp. 15, 31).

[38] F. Abe et al., *Observation of top quark production in $\bar{p}p$ collisions*, Phys. Rev. Lett. **74** (1995) 2626, arXiv: hep-ex/9503002 (cit. on p. 15).

[39] S. Abachi et al., *Observation of the top quark*, Phys. Rev. Lett. **74** (1995) 2632, arXiv: hep-ex/9503003 (cit. on p. 15).

[40] K. Kodama et al., *Observation of tau neutrino interactions*, Phys. Lett. B **504** (2001) 218, arXiv: hep-ex/0012035 (cit. on p. 15).

[41] A. G. Riess et al., *Observational evidence from supernovae for an accelerating universe and a cosmological constant*, Astron. J. **116** (1998) 1009, arXiv: astro-ph/9805201 (cit. on p. 15).

[42] M. B. Gavela, P. Hernandez, J. Orloff and O. Pene, *Standard model CP violation and baryon asymmetry*, Mod. Phys. Lett. A **9** (1994) 795, arXiv: hep-ph/9312215 (cit. on p. 16).

[43] Y. Fukuda et al., *Evidence for oscillation of atmospheric neutrinos*, Phys. Rev. Lett. **81** (1998) 1562, arXiv: hep-ex/9807003 (cit. on p. 16).

[44] Q. R. Ahmad et al., *Measurement of the rate of $\nu_e + d \rightarrow p + p + e^-$ interactions produced by ^8B solar neutrinos at the Sudbury Neutrino Observatory*, Phys. Rev. Lett. **87** (2001) 071301, arXiv: nucl-ex/0106015 (cit. on p. 16).

[45] S. Abe et al., *Precision Measurement of Neutrino Oscillation Parameters with KamLAND*, Phys. Rev. Lett. **100** (2008) 221803, arXiv: 0801.4589 [hep-ex] (cit. on p. 16).

[46] Z. Maki, M. Nakagawa and S. Sakata, *Remarks on the unified model of elementary particles*, Prog. Theor. Phys. **28** (1962) 870 (cit. on p. 17).

[47] E. Majorana, *Teoria simmetrica dell'elettrone e del positrone*, Nuovo Cim. **14** (1937) 171 (cit. on pp. 17, 205).

[48] R. N. Mohapatra and G. Senjanovic, *Neutrino Mass and Spontaneous Parity Nonconservation*, Phys. Rev. Lett. **44** (1980) 912 (cit. on pp. 18, 204).

[49] J. Schechter and J. W. F. Valle, *Neutrino Masses in SU(2) x U(1) Theories*, Phys. Rev. D **22** (1980) 2227 (cit. on pp. 18, 22, 204, 205).

[50] T. P. Cheng and L.-F. Li, *Neutrino Masses, Mixings and Oscillations in SU(2) x U(1) Models of Electroweak Interactions*, Phys. Rev. D **22** (1980) 2860 (cit. on pp. 18, 22, 205).

[51] W. Konetschny and W. Kummer, *Nonconservation of Total Lepton Number with Scalar Bosons*, Phys. Lett. B **70** (1977) 433 (cit. on pp. 18, 22, 205).

[52] R. N. Mohapatra and G. Senjanovic, *Neutrino Masses and Mixings in Gauge Models with Spontaneous Parity Violation*, Phys. Rev. D **23** (1981) 165 (cit. on pp. 18, 205).

[53] J. C. Pati and A. Salam, *Is Baryon Number Conserved?*, Phys. Rev. Lett. **31** (1973) 661 (cit. on pp. 18, 22, 205).

[54] J. C. Pati and A. Salam, *Unified Lepton-Hadron Symmetry and a Gauge Theory of the Basic Interactions*, Phys. Rev. D **8** (1973) 1240 (cit. on pp. 18, 22, 205).

[55] J. C. Pati and A. Salam, *Lepton Number as the Fourth Color*, Phys. Rev. D **10** (1974) 275, [Erratum: Phys.Rev.D 11, 703–703 (1975)] (cit. on pp. 18, 22, 205).

[56] R. N. Mohapatra and J. C. Pati, *A Natural Left-Right Symmetry*, Phys. Rev. D **11** (1975) 2558 (cit. on pp. 18, 22, 205).

[57] G. Senjanovic and R. N. Mohapatra, *Exact Left-Right Symmetry and Spontaneous Violation of Parity*, Phys. Rev. D **12** (1975) 1502 (cit. on pp. 18, 22, 205).

[58] R. N. Mohapatra and R. E. Marshak, *Local B-L Symmetry of Electroweak Interactions, Majorana Neutrinos and Neutron Oscillations*, Phys. Rev. Lett. **44** (1980) 1316, [Erratum: Phys.Rev.Lett. 44, 1643 (1980)] (cit. on pp. 18, 22, 205).

[59] G. Senjanovic, *Is left–right symmetry the key?*, Mod. Phys. Lett. A **32** (2017) 1730004, arXiv: 1610.04209 [hep-ph] (cit. on pp. 18, 22, 205).

[60] G. Senjanovic, *Spontaneous Breakdown of Parity in a Class of Gauge Theories*, Nucl. Phys. B **153** (1979) 334 (cit. on p. 19).

[61] M. Nemevsek, G. Senjanovic and V. Tello, *Connecting Dirac and Majorana Neutrino Mass Matrices in the Minimal Left-Right Symmetric Model*, Phys. Rev. Lett. **110** (2013) 151802, arXiv: 1211.2837 [hep-ph] (cit. on p. 21).

[62] A. Zee, *Charged scalar field and quantum number violations*, Phys. Lett. B **161** (1985) 141 (cit. on pp. 21, 22, 205).

[63] A. Zee, *Quantum numbers of Majorana neutrino masses*, Nucl. Phys. B **264** (1986) 99 (cit. on pp. 21, 22, 205).

[64] K. S. Babu, *Model of "calculable" Majorana neutrino masses*, Phys. Lett. B **203** (1988) 132 (cit. on pp. 21, 22, 205).

[65] R. Ruiz,
Doubly Charged Higgs Boson Production at Hadron Colliders II: A Zee-Babu Case Study,
(2022), arXiv: 2206.14833 [hep-ph] (cit. on pp. 21, 23, 56, 57, 124, 125, 146, 206, 212).

[66] J. Herrero-Garcia, M. Nebot, N. Rius and A. Santamaria,
The Zee–Babu model revisited in the light of new data, Nucl. Phys. B **885** (2014) 542,
arXiv: 1402.4491 [hep-ph] (cit. on p. 22).

[67] G. Corcella, C. Corianò, A. Costantini and P. H. Frampton,
Exploring scalar and vector bileptons at the LHC in a 331 model,
Phys. Lett. B **785** (2018) 73, arXiv: 1806.04536 [hep-ph] (cit. on p. 22).

[68] H. Georgi and M. Machacek, *Doubly Charged Higgs Bosons*,
Nucl. Phys. B **262** (1985) 463 (cit. on p. 22).

[69] B. Fuks, M. Nemevšek and R. Ruiz,
Doubly charged Higgs boson production at hadron colliders,
Phys. Rev. D **101** (2020) 075022, arXiv: 1912.08975 [hep-ph]
(cit. on pp. 22–24, 56, 57, 124, 125, 146, 206, 212).

[70] K. S. Babu and S. Jana,
Probing Doubly Charged Higgs Bosons at the LHC through Photon Initiated Processes,
Phys. Rev. D **95** (2017) 055020, arXiv: 1612.09224 [hep-ph] (cit. on p. 23).

[71] V. Rentala, W. Shepherd and S. Su,
A Simplified Model Approach to Same-sign Dilepton Resonances,
Phys. Rev. D **84** (2011) 035004, arXiv: 1105.1379 [hep-ph] (cit. on pp. 23, 206).

[72] B. Dutta, R. Eusebi, Y. Gao, T. Ghosh and T. Kamon, *Exploring the doubly charged Higgs boson of the left-right symmetric model using vector boson fusionlike events at the LHC*,
Phys. Rev. D **90** (2014) 055015, arXiv: 1404.0685 [hep-ph] (cit. on pp. 23, 206).

[73] V. Tello, M. Nemevsek, F. Nesti, G. Senjanovic and F. Vissani,
Left-Right Symmetry: from LHC to Neutrinoless Double Beta Decay,
Phys. Rev. Lett. **106** (2011) 151801, arXiv: 1011.3522 [hep-ph] (cit. on pp. 24, 206).

[74] M. Nemevšek, F. Nesti and J. C. Vasquez, *Majorana Higgses at colliders*,
JHEP **04** (2017) 114, arXiv: 1612.06840 [hep-ph] (cit. on pp. 24, 206).

[75] J. Alwall et al., *The automated computation of tree-level and next-to-leading order differential cross sections, and their matching to parton shower simulations*,
JHEP **07** (2014) 079, arXiv: 1405.0301 [hep-ph] (cit. on pp. 24, 52, 57, 59).

[76] R. Frederix et al., *The automation of next-to-leading order electroweak calculations*,
JHEP **07** (2018) 185, [Erratum: JHEP 11, 085 (2021)], arXiv: 1804.10017 [hep-ph]
(cit. on p. 24).

[77] ATLAS Collaboration, *Search for doubly charged Higgs boson production in multi-lepton final states with the ATLAS detector using proton–proton collisions at* $\sqrt{s} = 13$ *TeV*,
Eur. Phys. J. C **78** (2018) 199, arXiv: 1710.09748 [hep-ex]
(cit. on pp. 24, 93, 125, 147, 207).

[78] CMS Collaboration,
A search for a doubly-charged Higgs boson in pp collisions at $\sqrt{s} = 7$ TeV,
Eur. Phys. J. C **72** (2012) 2189, arXiv: 1207.2666 [hep-ex] (cit. on pp. 24, 207).

[79] ATLAS Collaboration, *Search for doubly and singly charged Higgs bosons decaying into vector bosons in multi-lepton final states with the ATLAS detector using proton–proton collisions at $\sqrt{s} = 13$ TeV*, JHEP **06** (2021) 146, arXiv: 2101.11961 [hep-ex]
(cit. on pp. 24, 206, 207).

[80] S. Höche, 'Introduction to parton-shower event generators',
Theoretical Advanced Study Institute in Elementary Particle Physics: Journeys Through the Precision Frontier: Amplitudes for Colliders, 2015 235, arXiv: 1411.4085 [hep-ph]
(cit. on p. 25).

[81] J. C. Collins, D. E. Soper and G. F. Sterman, *Factorization of Hard Processes in QCD*,
Adv. Ser. Direct. High Energy Phys. **5** (1989) 1, arXiv: hep-ph/0409313 (cit. on p. 25).

[82] Y. L. Dokshitzer, *Calculation of the Structure Functions for Deep Inelastic Scattering and e+ e- Annihilation by Perturbation Theory in Quantum Chromodynamics.*,
Sov. Phys. JETP **46** (1977) 641 (cit. on p. 26).

[83] V. N. Gribov and L. N. Lipatov, *Deep inelastic e p scattering in perturbation theory*,
Sov. J. Nucl. Phys. **15** (1972) 438 (cit. on p. 26).

[84] G. Altarelli and G. Parisi, *Asymptotic Freedom in Parton Language*,
Nucl. Phys. B **126** (1977) 298 (cit. on p. 26).

[85] R. D. Ball et al., *Parton distributions from high-precision collider data*,
Eur. Phys. J. C **77** (2017) 663, arXiv: 1706.00428 [hep-ph] (cit. on pp. 26, 27, 57).

[86] A. Buckley et al., *LHAPDF6: parton density access in the LHC precision era*,
Eur. Phys. J. C **75** (2015) 132, arXiv: 1412.7420 [hep-ph] (cit. on pp. 27, 105).

[87] L. Evans and P. Bryant, *LHC Machine*, JINST **3** (2008) S08001 (cit. on pp. 31, 34, 207).

[88] CERN, *The CERN accelerator complex*, 2019,
URL: http://cds.cern.ch/record/2684277 (visited on 05/04/2022) (cit. on p. 32).

[89] T. A. Collaboration, *The ALICE experiment at the CERN LHC*,
Journal of Instrumentation **3** (2008) S08002,
URL: https://doi.org/10.1088/1748-0221/3/08/s08002 (cit. on p. 33).

[90] ATLAS Collaboration, *The ATLAS Experiment at the CERN Large Hadron Collider*,
JINST **3** (2008) S08003 (cit. on pp. 33, 35, 36, 39–42, 45, 207).

[91] T. C. Collaboration, *The CMS experiment at the CERN LHC*,
Journal of Instrumentation **3** (2008) S08004,
URL: https://doi.org/10.1088/1748-0221/3/08/s08004 (cit. on p. 33).

[92] T. L. Collaboration, *The LHCb Detector at the LHC*,
Journal of Instrumentation **3** (2008) S08005,
URL: https://doi.org/10.1088/1748-0221/3/08/s08005 (cit. on p. 33).

[93] D. H. Perkins, *Introduction to High Energy Physics*, 4th ed.,
Cambridge University Press, 2000 (cit. on p. 34).

[94] A. Collaboration, *Luminosity Public Results for Run 2*, 2019, URL: https://twiki.cern.ch/twiki/bin/view/AtlasPublic/LuminosityPublicResultsRun2 (visited on 05/04/2022) (cit. on p. 35).

[95] A. Collaboration, *How ATLAS detects particles*, 2013, URL: https://cds.cern.ch/record/1505342 (visited on 07/04/2022) (cit. on p. 38).

[96] K. Potamianos, *The upgraded Pixel detector and the commissioning of the Inner Detector tracking of the ATLAS experiment for Run-2 at the Large Hadron Collider*, tech. rep., 15 pages, EPS-HEP 2015 Proceedings: CERN, 2016, arXiv: 1608.07850, URL: https://cds.cern.ch/record/2209070 (cit. on p. 39).

[97] ATLAS Collaboration, *ATLAS Pixel Detector: Technical Design Report*, ATLAS-TDR-11; CERN-LHCC-98-013, 1998, URL: https://cds.cern.ch/record/381263 (cit. on p. 38).

[98] ATLAS Collaboration, *ATLAS Insertable B-Layer: Technical Design Report*, ATLAS-TDR-19; CERN-LHCC-2010-013, 2010, URL: https://cds.cern.ch/record/1291633 (cit. on p. 39), Addendum: ATLAS-TDR-19-ADD-1; CERN-LHCC-2012-009, 2012, URL: https://cds.cern.ch/record/1451888.

[99] I. Connelly, *Performance and calibration of b-tagging with the ATLAS experiment at LHC Run-2*, tech. rep., CERN, 2016, URL: https://cds.cern.ch/record/2229557 (cit. on p. 39).

[100] ATLAS Collaboration, *ATLAS Inner Detector: Technical Design Report, Volume 2*, ATLAS-TDR-5, CERN-LHCC-97-017, 1997, URL: https://cds.cern.ch/record/331064 (cit. on p. 39).

[101] ATLAS Collaboration, *ATLAS Liquid Argon Calorimeter: Technical Design Report*, ATLAS-TDR-2; CERN-LHCC-96-041, 1996, URL: https://cds.cern.ch/record/331061 (cit. on pp. 40, 42).

[102] ATLAS Collaboration, *ATLAS Muon Spectrometer: Technical Design Report*, ATLAS-TDR-10; CERN-LHCC-97-022, CERN, 1997, URL: https://cds.cern.ch/record/331068 (cit. on pp. 42–44).

[103] ATLAS Collaboration, *ATLAS New Small Wheel: Technical Design Report*, ATLAS-TDR-020; CERN-LHCC-2013-006, 2013, URL: https://cds.cern.ch/record/1552862 (cit. on p. 44).

[104] ATLAS Collaboration, *ATLAS Magnet System: Magnet Project Technical Design Report, Volume 1*, ATLAS-TDR-6; CERN-LHCC-97-018, 1997, URL: https://cds.cern.ch/record/338080 (cit. on p. 45).

[105] ATLAS Collaboration, *ATLAS Barrel Toroid: Magnet Project Technical Design Report, Volume 2*, ATLAS-TDR-7; CERN-LHCC-97-019, 1997, URL: https://cds.cern.ch/record/331065 (cit. on p. 45).

[106] ATLAS Collaboration,
ATLAS End-Cap Toroids: Magnet Project Technical Design Report, Volume 3,
ATLAS-TDR-8; CERN-LHCC-97-020, CERN, 1997,
URL: https://cds.cern.ch/record/331066 (cit. on p. 45).

[107] ATLAS Collaboration,
ATLAS Central Solenoid: Magnet Project Technical Design Report, Volume 4,
ATLAS-TDR-9; CERN-LHCC-97-021, CERN, 1997,
URL: https://cds.cern.ch/record/331067 (cit. on p. 45).

[108] ATLAS Collaboration, *Operation of the ATLAS trigger system in Run 2*,
JINST **15** (2020) P10004, arXiv: 2007.12539 [hep-ex] (cit. on p. 46).

[109] ATLAS Collaboration, *Performance of the ATLAS trigger system in 2015*,
Eur. Phys. J. C **77** (2017) 317, arXiv: 1611.09661 [hep-ex] (cit. on pp. 46, 208).

[110] A. Collaboration, *Public DAQ plots*, 2019, URL:
https://twiki.cern.ch/twiki/bin/view/AtlasPublic/ApprovedPlotsDAQ
(visited on 12/04/2022) (cit. on p. 46).

[111] ATLAS Collaboration,
Performance of electron and photon triggers in ATLAS during LHC Run 2,
Eur. Phys. J. C **80** (2020) 47, arXiv: 1909.00761 [hep-ex] (cit. on pp. 48, 83).

[112] ATLAS Collaboration, *Performance of the ATLAS muon triggers in Run 2*,
JINST **15** (2020) P09015, arXiv: 2004.13447 [hep-ex] (cit. on pp. 48, 83).

[113] G. Avoni et al.,
The new LUCID-2 detector for luminosity measurement and monitoring in ATLAS,
JINST **13** (2018) P07017 (cit. on p. 49).

[114] ATLAS Collaboration, *The ATLAS Simulation Infrastructure*,
Eur. Phys. J. C **70** (2010) 823, arXiv: 1005.4568 [physics.ins-det]
(cit. on pp. 51, 52).

[115] ATLAS Collaboration, *ATLAS Computing: Technical Design Report*,
ATLAS-TDR-17; CERN-LHCC-2005-022, 2005,
URL: https://cds.cern.ch/record/837738 (cit. on p. 51).

[116] S. Agostinelli et al., *GEANT4 – a simulation toolkit*,
Nucl. Instrum. Meth. A **506** (2003) 250 (cit. on pp. 51, 209).

[117] A. Buckley et al., *General-purpose event generators for LHC physics*,
Phys. Rept. **504** (2011) 145, arXiv: 1101.2599 [hep-ph] (cit. on p. 51).

[118] E. Bothmann et al., *Event generation with Sherpa 2.2*, SciPost Phys. **7** (2019) 034,
arXiv: 1905.09127 [hep-ph] (cit. on pp. 52, 57, 58).

[119] S. Höche, F. Krauss, M. Schönherr and F. Siegert,
A critical appraisal of NLO+PS matching methods, JHEP **09** (2012) 049,
arXiv: 1111.1220 [hep-ph] (cit. on pp. 53, 58).

[120] S. Höche, F. Krauss, M. Schönherr and F. Siegert,
QCD matrix elements + parton showers. The NLO case, JHEP **04** (2013) 027,
arXiv: 1207.5030 [hep-ph] (cit. on pp. 53, 58).

[121] S. Catani, F. Krauss, B. R. Webber and R. Kuhn, *QCD Matrix Elements + Parton Showers*, JHEP **11** (2001) 063, arXiv: hep-ph/0109231 (cit. on pp. 53, 58).

[122] S. Höche, F. Krauss, S. Schumann and F. Siegert, *QCD matrix elements and truncated showers*, JHEP **05** (2009) 053, arXiv: 0903.1219 [hep-ph] (cit. on pp. 53, 58).

[123] B. Andersson, G. Gustafson, G. Ingelman and T. Sjöstrand, *Parton fragmentation and string dynamics*, Phys. Rept. **97** (1983) 31 (cit. on p. 53).

[124] B. R. Webber, *A QCD Model for Jet Fragmentation Including Soft Gluon Interference*, Nucl. Phys. B **238** (1984) 492 (cit. on p. 53).

[125] D. Amati and G. Veneziano, *Preconfinement as a Property of Perturbative QCD*, Phys. Lett. B **83** (1979) 87 (cit. on p. 53).

[126] ATLAS Collaboration, *Measurement of the underlying event in jet events from 7 TeV proton–proton collisions with the ATLAS detector*, Eur. Phys. J. C **74** (2014) 2965, arXiv: 1406.0392 [hep-ex] (cit. on p. 53).

[127] E. Barberio et al., *The Geant4-Based ATLAS Fast Electromagnetic Shower Simulation*, (2008) 802, ed. by M. Barone et al. (cit. on p. 54).

[128] E. Barberio et al., *Fast shower simulation in the ATLAS calorimeter*, J. Phys. Conf. Ser. **119** (2008) 032008, ed. by R. Sobie, R. Tafirout and J. Thomson (cit. on p. 54).

[129] W. Lukas, *Fast Simulation for ATLAS: Atlfast-II and ISF*, J. Phys. Conf. Ser. **396** (2012) 022031, ed. by M. Ernst, D. Düllmann, O. Rind and T. Wong (cit. on p. 54).

[130] K. Edmonds et al., *The fast ATLAS track simulation (FATRAS)*, (2008) (cit. on p. 54).

[131] ATLAS Collaboration, *The simulation principle and performance of the ATLAS fast calorimeter simulation FastCaloSim*, ATL-PHYS-PUB-2010-013, 2010, URL: https://cds.cern.ch/record/1300517 (cit. on p. 54).

[132] A. Salzburger, *The ATLAS Track Extrapolation Package*, (2007) (cit. on p. 55).

[133] ATLAS Collaboration, *AtlFast3: The Next Generation Of Fast Simulation in ATLAS*, Comput. Softw. Big Sci. **6** (2021) 7, arXiv: 2109.02551 [hep-ex] (cit. on p. 55).

[134] A. Hasib et al., *The new Fast Calorimeter Simulation in ATLAS*, tech. rep., CERN, 2018, URL: https://cds.cern.ch/record/2626157 (cit. on p. 55).

[135] ATLAS Collaboration, *Fast simulation of the ATLAS calorimeter system with Generative Adversarial Networks*, ATL-SOFT-PUB-2020-006, 2020, URL: https://cds.cern.ch/record/2746032 (cit. on p. 55).

[136] ATLAS Collaboration, *Luminosity determination in pp collisions at $\sqrt{s}$ = 13 TeV using the ATLAS detector at the LHC*, ATLAS-CONF-2019-021, 2019, URL: https://cds.cern.ch/record/2677054 (cit. on p. 55).

[137] ATLAS Collaboration, *Luminosity determination in pp collisions at $\sqrt{s}$ = 13 TeV using the ATLAS detector at the LHC*, (2022), arXiv: 2212.09379 [hep-ex] (cit. on pp. 56, 106).

[138] T. Sjöstrand et al., *An introduction to PYTHIA 8.2*, Comput. Phys. Commun. **191** (2015) 159, arXiv: 1410.3012 [hep-ph] (cit. on pp. 56–59).

[139] K. Huitu, J. Maalampi, A. Pietila and M. Raidal, *Doubly charged Higgs at LHC*, Nucl. Phys. B **487** (1997) 27, arXiv: hep-ph/9606311 (cit. on p. 56).

[140] A. Alloul, N. D. Christensen, C. Degrande, C. Duhr and B. Fuks, *FeynRules 2.0 - A complete toolbox for tree-level phenomenology*, Comput. Phys. Commun. **185** (2014) 2250, arXiv: 1310.1921 [hep-ph] (cit. on p. 56).

[141] ATLAS Collaboration, *ATLAS Pythia 8 tunes to 7 TeV data*, ATL-PHYS-PUB-2014-021, 2014, URL: https://cds.cern.ch/record/1966419 (cit. on pp. 56–59).

[142] NNPDF Collaboration, R. D. Ball et al., *Parton distributions with LHC data*, Nucl. Phys. B **867** (2013) 244, arXiv: 1207.1303 [hep-ph] (cit. on pp. 56–59).

[143] D. J. Lange, *The EvtGen particle decay simulation package*, Nucl. Instrum. Meth. A **462** (2001) 152 (cit. on pp. 56, 58, 59).

[144] J. Pumplin et al., *New Generation of Parton Distributions with Uncertainties from Global QCD Analysis*, JHEP **07** (2002) 012, arXiv: hep-ph/0201195 (cit. on p. 56).

[145] H.-L. Lai et al., *New parton distributions for collider physics*, Phys. Rev. D **82** (2010) 074024, arXiv: 1007.2241 [hep-ph] (cit. on pp. 56, 59).

[146] The NNPDF Collaboration, R. D. Ball et al., *Parton distributions for the LHC run II*, JHEP **04** (2015) 040, arXiv: 1410.8849 [hep-ph] (cit. on pp. 57–59).

[147] S. Frixione, G. Ridolfi and P. Nason, *A positive-weight next-to-leading-order Monte Carlo for heavy flavour hadroproduction*, JHEP **09** (2007) 126, arXiv: 0707.3088 [hep-ph] (cit. on pp. 57, 58).

[148] P. Nason, *A new method for combining NLO QCD with shower Monte Carlo algorithms*, JHEP **11** (2004) 040, arXiv: hep-ph/0409146 (cit. on pp. 57, 58).

[149] S. Frixione, P. Nason and C. Oleari, *Matching NLO QCD computations with parton shower simulations: the POWHEG method*, JHEP **11** (2007) 070, arXiv: 0709.2092 [hep-ph] (cit. on pp. 57, 58).

[150] S. Alioli, P. Nason, C. Oleari and E. Re, *A general framework for implementing NLO calculations in shower Monte Carlo programs: the POWHEG BOX*, JHEP **06** (2010) 043, arXiv: 1002.2581 [hep-ph] (cit. on pp. 57, 58).

[151] T. Gleisberg and S. Höche, *Comix, a new matrix element generator*, JHEP **12** (2008) 039, arXiv: 0808.3674 [hep-ph] (cit. on p. 58).

[152] F. Buccioni et al., *OpenLoops 2*, Eur. Phys. J. C **79** (2019) 866, arXiv: 1907.13071 [hep-ph] (cit. on p. 58).

[153] F. Cascioli, P. Maierhöfer and S. Pozzorini, *Scattering Amplitudes with Open Loops*, Phys. Rev. Lett. **108** (2012) 111601, arXiv: 1111.5206 [hep-ph] (cit. on p. 58).

[154] A. Denner, S. Dittmaier and L. Hofer,
COLLIER: A fortran-based complex one-loop library in extended regularizations,
Comput. Phys. Commun. **212** (2017) 220, arXiv: 1604.06792 [hep-ph] (cit. on p. 58).

[155] S. Schumann and F. Krauss,
A parton shower algorithm based on Catani–Seymour dipole factorisation,
JHEP **03** (2008) 038, arXiv: 0709.1027 [hep-ph] (cit. on p. 58).

[156] C. Anastasiou, L. Dixon, K. Melnikov and F. Petriello, *High-precision QCD at hadron colliders: Electroweak gauge boson rapidity distributions at next-to-next-to leading order*,
Phys. Rev. D **69** (2004) 094008, arXiv: hep-ph/0312266 (cit. on p. 58).

[157] E. Bothmann, M. Schönherr and S. Schumann,
Reweighting QCD matrix-element and parton-shower calculations,
Eur. Phys. J. C **76** (2016) 590, arXiv: 1606.08753 [hep-ph] (cit. on p. 58).

[158] J. Butterworth et al., *PDF4LHC recommendations for LHC Run II*,
J. Phys. G **43** (2016) 023001, arXiv: 1510.03865 [hep-ph] (cit. on pp. 58, 59).

[159] S. Dulat et al.,
New parton distribution functions from a global analysis of quantum chromodynamics,
Phys. Rev. D **93** (2016) 033006, arXiv: 1506.07443 [hep-ph] (cit. on p. 58).

[160] L. A. Harland-Lang, A. D. Martin, P. Motylinski and R. S. Thorne,
Parton distributions in the LHC era: MMHT 2014 PDFs, Eur. Phys. J. C **75** (2015) 204,
arXiv: 1412.3989 [hep-ph] (cit. on p. 58).

[161] ATLAS Collaboration, *Studies on top-quark Monte Carlo modelling for Top2016*,
ATL-PHYS-PUB-2016-020, 2016, URL: https://cds.cern.ch/record/2216168
(cit. on p. 58).

[162] S. Frixione, E. Laenen, P. Motylinski, C. White and B. R. Webber,
Single-top hadroproduction in association with a W boson, JHEP **07** (2008) 029,
arXiv: 0805.3067 [hep-ph] (cit. on p. 58).

[163] P. Artoisenet, R. Frederix, O. Mattelaer and R. Rietkerk,
Automatic spin-entangled decays of heavy resonances in Monte Carlo simulations,
JHEP **03** (2013) 015, arXiv: 1212.3460 [hep-ph] (cit. on p. 58).

[164] M. Czakon and A. Mitov,
Top++: A program for the calculation of the top-pair cross-section at hadron colliders,
Comput. Phys. Commun. **185** (2014) 2930, arXiv: 1112.5675 [hep-ph] (cit. on p. 59).

[165] A. D. Martin, W. J. Stirling, R. S. Thorne and G. Watt, *Parton distributions for the LHC*,
Eur. Phys. J. C **63** (2009) 189, arXiv: 0901.0002 [hep-ph] (cit. on p. 59).

[166] A. D. Martin, W. J. Stirling, R. S. Thorne and G. Watt, *Uncertainties on α_S in global PDF analyses and implications for predicted hadronic cross sections*,
Eur. Phys. J. C **64** (2009) 653, arXiv: 0905.3531 [hep-ph] (cit. on p. 59).

[167] J. Gao et al., *CT10 next-to-next-to-leading order global analysis of QCD*,
Phys. Rev. D **89** (2014) 033009, arXiv: 1302.6246 [hep-ph] (cit. on p. 59).

[168] T. Sjöstrand, S. Mrenna and P. Skands, *A brief introduction to PYTHIA 8.1*,
Comput. Phys. Commun. **178** (2008) 852, arXiv: 0710.3820 [hep-ph] (cit. on p. 59).

[169] ATLAS Collaboration, *The Pythia 8 A3 tune description of ATLAS minimum bias and inelastic measurements incorporating the Donnachie–Landshoff diffractive model*, ATL-PHYS-PUB-2016-017, 2016, URL: https://cds.cern.ch/record/2206965 (cit. on p. 59).

[170] ATLAS Collaboration, *Performance of the ATLAS track reconstruction algorithms in dense environments in LHC Run 2*, Eur. Phys. J. C **77** (2017) 673, arXiv: 1704.07983 [hep-ex] (cit. on pp. 61, 63).

[171] T. Cornelissen et al., *The new ATLAS track reconstruction (NEWT)*, J. Phys. Conf. Ser. **119** (2008) 032014, ed. by R. Sobie, R. Tafirout and J. Thomson (cit. on p. 61).

[172] R. Mankel, *A Concurrent track evolution algorithm for pattern recognition in the HERA-B main tracking system*, Nucl. Instrum. Meth. A **395** (1997) 169 (cit. on p. 62).

[173] R. Fruhwirth, *Application of Kalman filtering to track and vertex fitting*, Nucl. Instrum. Meth. A **262** (1987) 444 (cit. on p. 62).

[174] ATLAS Collaboration, *Alignment of the ATLAS Inner Detector in Run 2*, Eur. Phys. J. C **80** (2020) 1194, arXiv: 2007.07624 [hep-ex] (cit. on p. 62).

[175] ATLAS Collaboration, *Performance of the reconstruction of large impact parameter tracks in the inner detector of ATLAS*, (2023), arXiv: 2304.12867 [hep-ex] (cit. on p. 63).

[176] ATLAS Collaboration, *A neural network clustering algorithm for the ATLAS silicon pixel detector*, JINST **9** (2014) P09009, arXiv: 1406.7690 [hep-ex] (cit. on p. 63).

[177] ATLAS Collaboration, *Reconstruction of primary vertices at the ATLAS experiment in Run 1 proton–proton collisions at the LHC*, Eur. Phys. J. C **77** (2017) 332, arXiv: 1611.10235 [hep-ex] (cit. on p. 63).

[178] ATLAS Collaboration, *Electron reconstruction and identification in the ATLAS experiment using the 2015 and 2016 LHC proton–proton collision data at* $\sqrt{s} = 13$ *TeV*, Eur. Phys. J. C **79** (2019) 639, arXiv: 1902.04655 [hep-ex] (cit. on pp. 64–66, 68).

[179] ATLAS Collaboration, *Electron and photon performance measurements with the ATLAS detector using the 2015–2017 LHC proton–proton collision data*, JINST **14** (2019) P12006, arXiv: 1908.00005 [hep-ex] (cit. on pp. 64, 69, 84, 92).

[180] A. Collaboration, *Electron and photon efficiencies in LHC Run 2 with the ATLAS experiment*, (2023), arXiv: 2308.13362 [hep-ex] (cit. on pp. 64, 66–69).

[181] ATLAS Collaboration, *Topological cell clustering in the ATLAS calorimeters and its performance in LHC Run 1*, Eur. Phys. J. C **77** (2017) 490, arXiv: 1603.02934 [hep-ex] (cit. on p. 65).

[182] ATLAS Collaboration, *Improved electron reconstruction in ATLAS using the Gaussian Sum Filter-based model for bremsstrahlung*, ATLAS-CONF-2012-047, 2012, URL: https://cds.cern.ch/record/1449796 (cit. on p. 65).

[183] D. Scott,
Multivariate density estimation: Theory, practice, and visualization: Second edition, 2015
1, ISBN: 9780471697558 (cit. on p. 67).

[184] ATLAS Collaboration, *Muon reconstruction performance of the ATLAS detector in proton–proton collision data at* $\sqrt{s} = 13$ *TeV*, Eur. Phys. J. C **76** (2016) 292,
arXiv: 1603.05598 [hep-ex] (cit. on p. 70).

[185] ATLAS Collaboration, *Muon reconstruction and identification efficiency in ATLAS using the full Run 2 pp collision data set at* $\sqrt{s} = 13$ *TeV*, Eur. Phys. J. C **81** (2021) 578,
arXiv: 2012.00578 [hep-ex] (cit. on pp. 70, 72, 73).

[186] N. M. Koehler, *ATLAS Muon Reconstruction Performance in LHC Run 2*,
(2016) 621, ed. by V. T. Kim and D. E. Sosnov (cit. on p. 71).

[187] M. Cacciari, G. P. Salam and G. Soyez, *The anti-k_t jet clustering algorithm*,
JHEP **04** (2008) 063, arXiv: 0802.1189 [hep-ph] (cit. on p. 73).

[188] ATLAS Collaboration,
Jet reconstruction and performance using particle flow with the ATLAS Detector,
Eur. Phys. J. C **77** (2017) 466, arXiv: 1703.10485 [hep-ex] (cit. on p. 73).

[189] ATLAS Collaboration, *Charged-particle multiplicities in pp interactions measured with the ATLAS detector at the LHC*, New J. Phys. **13** (2011) 053033,
arXiv: 1012.5104 [hep-ex] (cit. on p. 74).

[190] M. Cacciari, G. P. Salam and G. Soyez, *FastJet user manual*,
Eur. Phys. J. C **72** (2012) 1896, arXiv: 1111.6097 [hep-ph] (cit. on p. 74).

[191] ATLAS Collaboration, *Jet energy scale measurements and their systematic uncertainties in proton–proton collisions at* $\sqrt{s} = 13$ *TeV with the ATLAS detector*,
Phys. Rev. D **96** (2017) 072002, arXiv: 1703.09665 [hep-ex] (cit. on p. 74).

[192] ATLAS Collaboration, *Jet energy scale and resolution measured in proton–proton collisions at* $\sqrt{s} = 13$ *TeV with the ATLAS detector*, Eur. Phys. J. C **81** (2020) 689,
arXiv: 2007.02645 [hep-ex] (cit. on p. 74).

[193] ATLAS Collaboration, *Forward Jet Vertex Tagging: A new technique for the identification and rejection of forward pileup jets*, ATL-PHYS-PUB-2015-034, 2015,
URL: https://cds.cern.ch/record/2042098 (cit. on p. 74).

[194] ATLAS Collaboration, *Performance of b-jet identification in the ATLAS experiment*,
JINST **11** (2016) P04008, arXiv: 1512.01094 [hep-ex] (cit. on p. 75).

[195] ATLAS Collaboration,
ATLAS flavour-tagging algorithms for the LHC Run 2 pp collision dataset,
Eur. Phys. J. C **83** (2022) 681, arXiv: 2211.16345 [physics.data-an] (cit. on p. 75).

[196] ATLAS Collaboration, *ATLAS b-jet identification performance and efficiency measurement with* $t\bar{t}$ *events in pp collisions at* $\sqrt{s} = 13$ *TeV*, Eur. Phys. J. C **79** (2019) 970,
arXiv: 1907.05120 [hep-ex] (cit. on p. 75).

[197] ATLAS Collaboration, *Performance of missing transverse momentum reconstruction with the ATLAS detector using proton–proton collisions at* $\sqrt{s} = 13$ *TeV*,
Eur. Phys. J. C **78** (2018) 903, arXiv: 1802.08168 [hep-ex] (cit. on pp. 76, 77).

[198] J. Catmore et al., *A new petabyte-scale data derivation framework for ATLAS*, J. Phys. Conf. Ser. **664** (2015) 072007 (cit. on p. 77).

[199] ATLAS Collaboration, *Search for doubly charged Higgs boson production in multi-lepton final states using 139 fb^{-1} of proton–proton collisions at $\sqrt{s}$ = 13 TeV with the ATLAS detector*, Eur. Phys. J. C **83** (2022) 605, arXiv: 2211.07505 [hep-ex] (cit. on pp. 82, 205).

[200] G. Cowan, K. Cranmer, E. Gross and O. Vitells, *Asymptotic formulae for likelihood-based tests of new physics*, Eur. Phys. J. C **71** (2011) 1554, arXiv: 1007.1727 [physics.data-an] (cit. on pp. 82, 111, 112, 124, 125, 209), Erratum: Eur. Phys. J. C **73** (2013) 2501.

[201] ATLAS Collaboration, *ATLAS data quality operations and performance for 2015–2018 data-taking*, JINST **15** (2020) P04003, arXiv: 1911.04632 [physics.ins-det] (cit. on pp. 82, 209).

[202] ATLAS Collaboration, *Selection of jets produced in 13 TeV proton–proton collisions with the ATLAS detector*, ATLAS-CONF-2015-029, 2015, URL: https://cds.cern.ch/record/2037702 (cit. on p. 82).

[203] ATLAS Collaboration, *Search for anomalous production of prompt same-sign lepton pairs and pair-produced doubly charged Higgs bosons with $\sqrt{s}$ = 8 TeV pp collisions using the ATLAS detector*, JHEP **03** (2015) 041, arXiv: 1412.0237 [hep-ex] (cit. on pp. 94, 210).

[204] M. Baak et al., *HistFitter software framework for statistical data analysis*, Eur. Phys. J. C **75** (2015) 153, arXiv: 1410.1280 [hep-ex] (cit. on p. 109).

[205] R. Brun and F. Rademakers, *ROOT – An object oriented data analysis framework*, Nucl. Instrum. Meth. A **389** (1997) 81, ISSN: 0168-9002 (cit. on p. 109).

[206] W. Verkerke and D. Kirkby, *The RooFit toolkit for data modeling*, 2003, arXiv: physics/0306116 [physics.data-an] (cit. on p. 109).

[207] R. J. Barlow and C. Beeston, *Fitting using finite Monte Carlo samples*, Comput. Phys. Commun. **77** (1993) 219 (cit. on p. 110).

[208] A. L. Read, *Presentation of search results: the CL_S technique*, J. Phys. G **28** (2002) 2693 (cit. on pp. 111, 212).

[209] *2017 European School of High-Energy Physics: Evora, Portugal 6 - 19 Sep 2017. The 2017 European School of High-Energy Physics*, CERN, Geneva: CERN, 2017, URL: http://cds.cern.ch/record/2255586 (cit. on pp. 111, 112).

[210] A. V. Dorogush, V. Ershov and A. Gulin, *CatBoost: gradient boosting with categorical features support*, 2018, arXiv: 1810.11363 [cs.LG] (cit. on pp. 127, 211).

[211] A. Paszke et al., *PyTorch: An Imperative Style, High-Performance Deep Learning Library*, 2019, arXiv: 1912.01703 [cs.LG] (cit. on pp. 127, 211).

[212] P. Baldi, K. Cranmer, T. Faucett, P. Sadowski and D. Whiteson, *Parameterized neural networks for high-energy physics*, Eur. Phys. J. C **76** (2016) 235, arXiv: 1601.07913 [hep-ex] (cit. on p. 128).

[213] G. Apollinari, O. Brüning, T. Nakamoto and L. Rossi, *High Luminosity Large Hadron Collider HL-LHC*, CERN Yellow Rep. (2015) 1, ed. by G. Apollinari, I. Béjar Alonso, O. Brüning, M. Lamont and L. Rossi, arXiv: 1705.08830 [physics.acc-ph] (cit. on p. 148).

[214] LHC Commissioning, *Longer term LHC schedule*, 2022, URL: https://lhc-commissioning.web.cern.ch/schedule/LHC-long-term.htm (visited on 09/08/2023) (cit. on p. 148).

[215] A. Collaboration, *ATLAS Isolation and Fake Forum*, 2022, URL: https://twiki.cern.ch/twiki/bin/view/AtlasProtected/IsolationFakeForum (visited on 20/07/2023) (cit. on p. 151).

[216] ATLAS Collaboration, *The ATLAS Collaboration Software and Firmware*, ATL-SOFT-PUB-2021-001, 2021, URL: https://cds.cern.ch/record/2767187 (cit. on p. 208).

Razširjeni povzetek v slovenskem jeziku

Standardni model [1, 3, 4, 7–10, 12–16] je uveljavljena kvantna teorija polja elementarnih delcev in njihovih interakcij z visoko napovedno močjo. Model je bil je obsežno preizkušen do visoke natančnosti z osupljivim ujemanjem med napovedmi in meritvami, zato ga pogosto označujejo kot enega najbolj impresivnih dosežkov znanosti. Razvit in preizkušen je bil po delih v drugi polovici 20. stoletja s prispevki številnih tako teoretičnih kot tudi eksperimentalnih fizikov. Matematično je zgrajen z uporabo $\mathrm{SU}(3)_C \times \mathrm{SU}(2)_L \times \mathrm{U}(1)_Y$ simetrijske grupe znotraj katere definiramo *akcijo*, S, ki mora zadoščati nekaterim pogojem, na primer, mora biti invariantna na Lorentzove in umeritvene transformacije, poleg tega pa mora biti renormalizabilna, da vrne omejene rezultate. Standardni model in njegov matematični opis je podrobneje opisan v mnogih knjigah, kot npr.: [5, 6], tukaj pa so podane zgolj osnove.

Standardni model uspešno matematično obravnava tri od štirih osnovnih sil v smislu kvantnih teorij polja, ki prežemajo celotno vesolje. Zapisane po vrstnem redu upadanja moči so močna, elektromagnetna in šibka sila. Gravitacijska sila kot četrta osnovna sila zaenkrat še ni zadovoljivo vključena v Standardni model.

Delci se v Standardnem modelu kažejo kot vzbujena stanja polj. Standardni model sestavlja 12 delcev snovi (fermionov) in šest delcev nosilcev sil (umeritvenih bozonov), ki so prikazani na levi oziroma desni strani Slike 1. Fermioni imajo spin 1/2, bozoni pa spin 1. Fermioni se (vodoravno na sliki) delijo na kvarke in leptone, odvisno od njihovih temeljnih lastnosti. Kvarki imajo delni električni naboj, medtem ko imajo leptoni celoštevilske vrednosti. Poleg tega lahko fermione (vertikalno na sliki) razdelimo tudi na tri generacije, ki imajo med seboj enaka kvantna števila, razen njihovih mas. Vse stvari, ki jih srečamo v naravi, so sestavljene iz prve generacije fermionov, medtem ko so za nastanek preostalih potrebni posebni pogoji. Obstaja šest okusov kvarkov, od tega imajo trije kvarki tipa “gor” električni naboj +2/3 in trije kvarki tipa “dol” električni naboj -1/3. Vsi kvarki imajo tudi barvni naboj. Nabiti leptoni imajo električni naboj -1 in jih spremljajo njihovi brezmasni in električno nevtralni partnerji, nevtrini. Vsak fermion ima svoj antidelec z nasprotnim električnim nabojem in drugimi kvantnimi števili.

Vsako od sil posreduje izmenjava umeritvenih bozonov, ki so na Sliki 1 prikazani z rumeno barvo. Ti so odgovorni za interakcije fermionov. Osem brezmasnih gluonov, ki nimajo električnega naboja, posreduje močno silo. Ker gluoni posedujejo barvni naboj, poleg kvarkov interagirajo tudi z drugimi gluoni, kar povzroči nastanek tri- in štirigluonskih vozlišč, zaradi česar je kvantna kromodinamika (QCD) bolj zapletena kot kvantna elektrodinamika (QED). Elektromagnetna sila se manifestira preko izmenjave virtualnih fotonov. Ti so prav tako električno nevtralni in brez mase, kar omogoči neskončen doseg elektromagnetne sile. Ker vseh dvanajst fermionov nosi naboj šibke interakcije, znan kot šibki izospin, vsi sodelujejo v šibkih interakcijah. Bozoni W (Z) so odgovorni za nabite (nevtralne) šibke interakcije. Bozon Z je električno nevtralen, medtem ko obstajata dva bozona W, eden z negativnim in eden s pozitivnim električnim nabojem. Ker so šibki bozoni masivni, je doseg šibke interakcije zelo kratek. Zadnji delec, ki sta ga leta 2012 odkrili kolaboraciji ATLAS [21] in CMS [22], je Higgsov bozon, s katerim je Standardni model postal kompletna in konsistentna teorija. Za razliko od vseh drugih delcev je to skalarni delec s spinom 0, ki zagotovi mehanizem, s katerim vsi drugi delci pridobijo svoje mase. Poleg tega

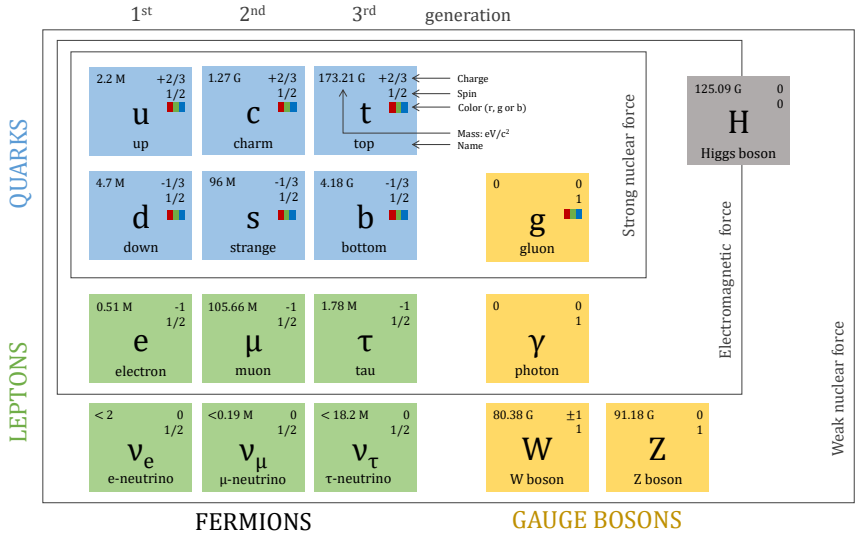

Slika 1: Osnovni delci v Standardnem modelu skupaj z njihovimi lastnostmi in tri osnovne sile, preko katerih med seboj interagirajo.

se od vseh drugih delcev razlikuje po svoji neničelni vakuumski pričakovani vrednosti. Ko delci, ki so prvotno brez mase, interagirajo z neničelnim Higgsovim poljem, dobijo svoje mase. Nosilec gravitacije, graviton, še ni bil odkrit in zato ni prikazan na Sliki 1. V nasprotju z drugimi nosilci sil naj bi imel spin 2.

Kljub natančnemu opisu številnih temeljnih zakonov narave Standardni model še vedno ne velja za končno teorijo vsega, saj ne more ustrezno razložiti nekaterih fizikalnih pojavov, med drugim temne snovi, temne energije, nevtrinskih mas in neravnovesja med snovjo in antisnovjo v vesolju. Zaradi teh pomanjkljivosti je predlaganih veliko teoretičnih rešitev, ki nadgrajujejo Standardni model, tako da bi bil skladen z obstoječimi podatki. Žal po letu 2012 niso bili opaženi nobeni namigi o še neznanih delcih. Poleg tega še ni bilo nobenega eksperimentalnega rezultata, ki bi dokončno nasprotoval Standardnemu modelu na statistični ravni 5σ, ki v splošnem velja kot prag za odkritje. To je morda posledica razmeroma majhnih produkcijskih sipalnih presekov ali velikih mas potencialnih novih delcev.

V tej doktorski disertaciji se osredotočamo na razširitve Standardnega modela, ki ustvarjajo mase nevtrinov in uvajajo dvojno nabite skalarne bozone, ki so osnova za analizo. Mase nevtrinov so za velikostne rede nižje od mas drugih delcev Standardnega modela, kar nakazuje na možnost, da bi jih lahko generiral neki drug mehanizem. V smislu gugalničnega mehanizma lahko majhne mase neposredno pripišemo obstoju težkih prostostnih stopenj in kršitvi leptonskega števila. Če minimalno razširimo vsebino Standardnega modela, tj. le z enim multipletom, so možni le trije modeli, znani kot:

- **Gugalnični mehanizem tipa I** [2, 48, 49], ki uvede dodaten fermionski singlet, desnoročni nevtrino, ν_R.

- **Gugalnični mehanizem tipa II** [49–51], ki uvede $\mathrm{SU}(2)_L$ skalarni triplet, Δ, ki se sklaplja z levoročnim leptonskim dubletom in s tem krši ohranitev leptonskega števila.

- **Gugalnični mehanizem tipa III** [52], ki doda $\mathrm{SU}(2)_L$ fermionski triplet, Σ. Je podoben tipu I z dodatnimi težkimi leptoni, ki so električno nabiti.

Ettore Majorana je leta 1937 predstavil idejo [47], v kateri desnoročni nevtrini niso potrebni za pojasnitev njihove mase. Tako imenovani Majoranovi nevtrini, definirani kot $\nu = \nu_L + \nu_L^C$, so sami sebi antidelci, njihov masni člen v Lagrangeovi gostoti pa se zapiše kot $\mathcal{L}_M = -M/2\left(\bar{\nu}_L^C \nu_L + \bar{\nu}_L \nu_L^C\right)$. V gugalničnem mehanizmu nevtrini lahko pridobijo komponentno Majoranove mase.

V nasprotju z vsemi drugimi osnovnimi silami je šibka interakcija popolnoma asimetrična med levo in desnoročnimi polji. Ta kršitev parnosti je eksperimentalno dejstvo, ki je pomagalo oblikovati Standardni model, vendar je njen izvor ostal nepojasnjen. Naravno je, da iščemo teorijo z višjo simetrijo in ohranjeno parnostjo na neki višji energijski skali, ki se na neki točki spontano zlomi. To zamisel so prvi predstavili Pati, Salam, Mohapatra in Senjanović v sedemdesetih letih prejšnjega stoletja in je znana kot levo-desno simetrični model [53–59]. Minimalna levo-desno simetrična teorija poleg simetrijske grupe Standardnega modela uvede še lokalno simetrijo $\mathrm{SU}(2)_R$, pod katero se levosučna polja transformirajo kot singleti, desnosučna polja pa kot doubleti. Kvarki in leptoni na ta način postanejo popolnoma simetrični, hkrati pa zlom simetrije generira mase pripadajočim desnoročnim umeritvenim bozonom $W_R^{\pm}$ in Z_R. Dodatno se Higgsov sektor razširi z bi-dubletom Φ ter z levo in desnoročnim $\mathrm{SU}(2)$ tripletom $\Delta_{L,R}$, ki imata eno nevtralno komponento in po dve enojno nabiti in dvojno nabiti komponenti. Ko vse nevtralne komponente Higgsovih skalarnih polj zavzamejo pozitivne neničelne vakuumske pričakovane vrednosti (vev) se zgodi spontani zlom simetrije v dveh korakih. Najprej se razširjena umeritvena grupa levo-desno simetričnega modela zlomi do grupe Standardnega modela, ko nevtralna komponenta tripleta Δ_R zavzame neničelen vev, v_R, ki generira mase desnoročnim nevtrinom. Kasneje se Standardni model na elektrošibki energijski skali kot običajno zlomi do $\mathrm{U}(1)_{\mathrm{EM}}$. Znotraj levo-desno simetričnega modela lahko vpeljemo kombinacijo gugalničnih mehanizmov tipa I in II, ki vsebuje tako težki desnoročni nevtrino kot interakcije s polji Higgsovega tripleta.

V disertaciji dodatno obravnavamo Zee–Babu model [62–64], ki je še ena preprosta razširitev Standardnega modela z upeljavo dveh $\mathrm{SU}(2)_L$ skalarnih singletov, enojno nabitega $h^{\pm}$ in dvojno nabitega $k^{\pm\pm}$. Ker v modelu ne nastopa desnoročni nevtrino, ni možno nevtrinom generirati Diracove mase. Poleg tega se h in k ne sklapljata z leptoni in Higgsovim dubletom, kar bi nevtrinom dalo Majoranove mase. Edini način generiranja mase nevtrinom v tem modelu je radiativno preko dvozančnega diagrama.

Analiza predstavljena v tej doktorski disertaciji, ki je bila objavljena v Referenci [199], se ukvarja z iskanjem dvojno nabitih Higgsovih bozonov, $H^{\pm\pm}$, ki se lahko sklapljajo z levoročnimi in desnoročnimi leptoni, vektorskimi umeritvenimi bozoni ali skalarji iz tripleta. Prevladujoči mehanizem produkcije $H^{\pm\pm}$ na Velikem hadronskem trkalniku (LHC) je Drell–Yanov proces, ki poteka preko izmenjave fotona ali bozona Z v kanalu s. Obe kiralnosti nista proizvedeni v enakem obsegu, saj je presek Drell-Yan produkcije $H_L^{++}H_L^{--}$ zaradi različnih sklopitev z bozonom

Z približno dvakrat večji od produkcije $H_R^{++}H_R^{--}$ [69]. Feynmanov diagram Drell-Yanovega produkcijskega procesa para bozonov $H^{\pm\pm}$ je prikazan na Sliki 2.

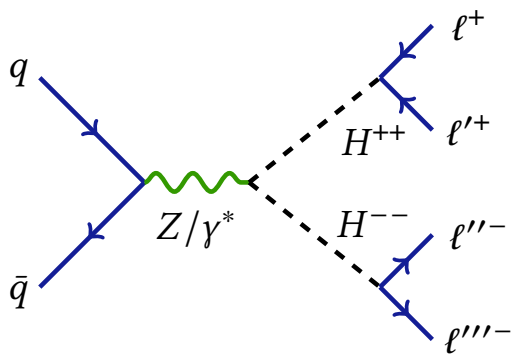

Slika 2: Feynmanov diagram Drell-Yanovega produkcijskega procesa, $pp \to H^{++}H^{--}$. V disertaciji nas zanimajo le leptonski razpadi $H^{\pm\pm}$, medtem ko druge analize posebej obravnavajo razpad v par bozonov W [79].

Ker imata $H_R^{\pm\pm}$ iz levo-desno simetričnega modela in $k^{\pm\pm}$ enaka kvantna števila, je tudi njuna elektrošibka produkcija enaka. Nedavno so pokazali, da se za Drell-Yanov produkcijski mehanizem preseki in diferencialne skalarne porazdelitve v Zee–Babuovem modelu in gugalničnem mehanizmu tipa II razlikujejo kvečjemu za normalizacijski faktor [65]. To nam omogoča, da lahko rezultate interpretiramo v okviru obeh modelov.

Dvojno nabiti Higgsov bozon lahko razpade v par bozonov W ali leptonov, odvisno od vakuumske pričakovane vrednosti, v_L, Higgsovega tripleta, Δ_L. Pri nizkih vrednostih v_L razpade izključno v leptone, medtem ko pri večjih večinoma razpade na par bozonov W. V predstavljeni analizi se osredotočamo na leptonski razpad, pri čemer se razpadna širina zapiše kot

$$\Gamma_{\mathrm{LRSM}}(H^{\pm\pm} \to \ell^{\pm}\ell'^{\pm}) = \frac{1}{1+\delta_{\ell\ell'}}\frac{h_{\ell\ell'}^2}{16\pi}m_{H^{\pm\pm}}, \quad \Gamma_{\mathrm{ZB}}(k^{\pm\pm} \to \ell^{\pm}\ell'^{\pm}) = \frac{1}{1+\delta_{\ell\ell'}}\frac{|g_{\ell\ell'}|^2}{4\pi}m_{k^{\pm\pm}}, \qquad (1)$$

kjer Kroneckerjeva $\delta_{\ell\ell'}$ funkcija poskrbi za faktor $1/2!$ faznega prostora v primeru dveh leptonov enakega okusa v končnem stanju. Faktor $h_{\ell\ell'}$ je zgoraj omejen in je odvisen od kombinacije leptonskih okusov [71, 72]. Podobno so v Zee–Babuovem modelu sklopitvene konstante $g_{\ell\ell'}$ prosti parametri modela, zaradi česar je razvejitveno razmerje za različne razpadne kanale apriorno neznano.

V splošnem model ne daje prednosti razpadom v težje leptone, saj sklopitev ni sorazmerna z maso leptona, kot velja na primer za Higgsov bozon v Standardnem modelu. Treba je poudariti, da modela dovoljujeta tudi razpade, ki kršijo ohranitev leptonskega okusa, $H^{\pm\pm} \to e^{\pm}\mu^{\pm}/\mu^{\pm}\tau^{\pm}/e^{\pm}\tau^{\pm}$. To dejstvo povezuje visokoenergijska iskanja na LHC z nizkoenergijskimi iskanji dvojnega β razpada brez nevtrinov [73, 74].

Kolaboracija ATLAS je že analizirala podatke protonskih trkov pri težiščni energiji $\sqrt{s} = 13\,\mathrm{TeV}$ na LHC, ki so ustrezali integrirani luminoznosti $36.1\,\mathrm{fb}^{-1}$ v obdobjih zbiranja podatkov med letoma 2015 in 2016. Masa dvojno nabitih Higgsovih bozonov je bila izključena do 870 GeV

za $H_L^{\pm\pm}$ in do 760 GeV za $H_R^{\pm\pm}$ pri 95% stopnji zaupanja [77]. Kolaboracija CMS je izvedla podobno analizo z uporabo $\sqrt{s} = 7$ TeV protonskih trkov, zbranih v obdobju zbiranja podatkov "Run 1" [78], in določil spodnje meje za maso $H^{\pm\pm}$ med 204 GeV in 459 GeV v scenarijih s 100% razvejitvenim razmerjem, odvisno od vsebnosti okusov v končnih dvoleptonskih stanjih. Posebna analiza kolaboracije ATLAS je iskala dvojno nabite Higgsove bozone v razpadnem kanalu $H^{\pm\pm} \to W^{\pm}W^{\pm}$ z uporabo celotnega nabora podatkov 139 fb^{-1} iz druge faze "Run 2" zajemanja podatkov LHC in izključila mase $H^{\pm\pm}$ do 350 GeV [79]. Analiza, predstavljena v tej disertaciji, nadgradi prejšnje ATLAS analize in ob zavrnitni hipoteze novih delcev postavi najmočnejše spodnje limite za maso $H^{\pm\pm}$ do sedaj.

Detektor ATLAS (A Toroidal LHC ApparatuS) [90], bistven za pridobivanje podatkov vključenih v to analizo, je večnamenski detektor delcev, ki pokriva skoraj 4π polnega kota v eni izmed interakcijskih območij pp v kompleksu LHC [87] približno 100 m pod zemljo. Dolg je 44 m in visok 25 m. Sestavljen je iz več cilindričnih poddetektorjev, postavljenih vzporedno z osjo žarka. Na Sliki 3 je prikazana shema spodaj opisanih komponent detektorja. Notranji detektor (ID), ki obdaja cev žarka, je potopljen v solenoidno magnetno polje 2 T in omogoča precizno zaznavanje prehoda nabitih delcev v območju $|\eta| < 2.5$. Od cevi žarka navzven je ID sestavljen iz silicijevega "pixel" detektorja z visoko ločljivostjo, ki običajno zagotavlja štiri meritve sledi delca, iz silicijevega "microstrip" detektorja in detektorja prehodnega sevanja (TRT), ki zajema območje do $|\eta| = 2.0$.

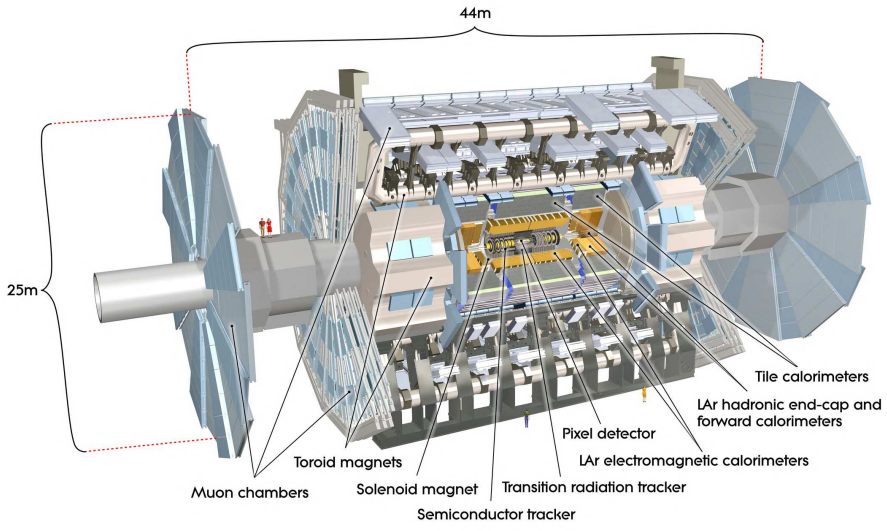

Slika 3: Shema z označenimi komponentami detektorja ATLAS. Dimenzije detektorja so 25 m v višino in 44 m v dolžino. Skupna teža detektorja je približno 7000 ton. Vzeto iz Ref. [90].

Zunaj superprevodnega solenoida kalorimeterski sistem pokriva območje psevdo-naglosti $|\eta| < 4.9$. V območju $|\eta| < 3.2$ elektromagnetno kalorimetrijo zagotavljata kalorimetra s svincem oz. tekočim argonom (LAr) z visoko ločljivostjo v centralnem predelu in dvema pokrovoma na vsaki strani valjastega ALTAS detektorja. Hadronsko kalorimetrijo omogoča kalorimeter iz zaporednih ploščic jekla in scintilatorskega materiala, ki je razdeljen na tri

centralne strukture znotraj $|\eta| < 1.7$, in dva pokrovna kalorimetra na vsaki strani.

Najbolj zunanji del detektorja ATLAS predstavlja mionski spektrometer (MS), ki pokriva območje $|\eta| < 2.7$ s tremi plastmi natančnih sledilnih komor. Mionski sistem je potopljen v magnetno polje, ki ga ustvarjajo trije veliki superprevodni toroidni magneti, vsak z osmimi tuljavami. Magnetno polje toroidov se giblje med 2.0 in 6.0 T m.

Dvostopenjski prožilni sistem izbere detektirane dogodke trkov delcev, ki so zanimivi za ATLASov fizikalni program [109]. Prva prožilna stopnja (L1) je izvedena s strojno opremo in zmanjša frekvenco dogodkov pod 100 kHz. Nato digitalni prožilec le to dodatno zmanjša na frekvenco zabeleženih dogodkov približno 1 kHz. Pri simulaciji, rekonstrukciji in analizi dejanskih in simuliranih podatkov se uporablja obsežen ATLASov programski paket [216].

ATLAS uporablja desnoročni koordinatni sistem z izhodiščem v interakcijski točki (IP) v središču detektorja in osjo z vzdolž cevi žarka. Os x kaže od IP proti središču LHC obroča, os y pa kaže navzgor. V prečni ravnini se uporabljajo cilindrične koordinate (r, ϕ), kjer je ϕ azimutalni kot okoli osi z. Psevdo-naglost je definirana glede na polarni kot θ kot $\eta = -\ln\tan(\theta/2)$. Kotna razdalja se meri v enotah $\Delta R = \sqrt{(\Delta\eta)^2 + (\Delta\phi)^2}$.

V tej analizi lahko odkrijemo $H^{\pm\pm}$ signal z iskanjem njegovih leptonskih razpadov, pri katerih nastanejo leptonski pari z enakim nabojem v končnih stanjih z dvema, tremi ali štirimi leptoni. Kategoriji z dvema in tremi leptoni sta potrebni za iskanje dogodkov, pri katerih je četrti (in tretji) lepton izgubljen zaradi omejene učinkovitosti detektorja. Visokoenergijski leptonski pari z enakim nabojem namigujejo na novo fiziko, saj takšni dogodki zelo redko nastanejo pri trkih protonov v procesih Standardnega modela. Dogodki ozadja se razlikujejo od signalnih dogodkov tako po topologiji kot po vplivu na vsa območja analize. Dogodki z dvema leptonoma večinoma izvirajo iz procesov Drell–Yan, pri čemer je naboj enega izmed elektronov napačno rekonstruiran, medtem ko so dogodki ozadja s tremi ali štirimi leptoni večinoma dogodki, ki potekajo preko nastanka dveh bozonov (WW, WZ, ZZ). V analizi smo upoštevali le lahke leptone, tj. elektrone in mione, v končnih stanjih z dvema, tremi in štirimi leptoni, pri čemer so vključeni tudi leptonski razpadi τ leptona. V analizi smo nadalje predpostavljali, da so razvejitvena razmerja vsakega od možnih leptonskih končnih stanj, $\mathcal{B}(H^{\pm\pm} \to e^\pm e^\pm / e^\pm \mu^\pm / \mu^\pm \mu^\pm / e^\pm \tau^\pm / \mu^\pm \tau^\pm / \tau^\pm \tau^\pm) = 1/6$, enaka. Da bi ocenili skladnost podatkov s pričakovanji Standardnega modela in določili spodnje limite za maso $H^{\pm\pm}$ pri 95% stopnji zaupanja, smo izvedli prileganje podatkov z metodo maksimalne zanesljivosti (angl. "binned maximum-likelihood fit"). Hkratno prilagajanje porazdelitvi invariantne mase dveh lahkih leptonov z enakim nabojem in najvišjo transverzalno gibalno količino v dogodku, $m(\ell^\pm \ell'^\pm)_{\text{lead}}$, smo izvedli v dvo- in trileptonskih območjih, medtem ko smo v štirileptonskih območjih uporabili skupno število dogodkov, ki so preživeli območne selekcije. Kanali, kjer pričakujemo tri ali štiri leptone v končnem stanju, so inkluzivni glede na leptonski okus, s čimer je dosežena najboljša občutljivost.

Dogodki so izbrani z metodo, ki temelji na individualnih, ročno izbranih rezih, kjer so zahteve za izbor kinematičnih spremenljivk izbrane ortogonalno. Opravili smo tudi začetne študije z implementacijo strojnega učenja, ki upošteva funkcijsko odvisnost kombinacije opazovanih spremenljivk. Medtem ko so definicije objektov enake za oba pristopa, so bila območja analize optimizirana za vsako metodo posebej.

V analizi so opredeljene tri različne vrste območij: kontrolna območja (CR), validacijska območja (VR) in signalna območja (SR). Normalizacijski faktorji prevladujočega ozadja se v postopku prilagajanja podatkov obravnavajo kot prosti parametri in so ocenjeni v kontrolnih območjih. Validacijska območja se uporabljajo za preverjanje modeliranja ozadja, vendar niso vključena v samo prilagajanje. Tako kontrolna kot validacijska območja so postavljena kinematično blizu območja pričakovanega signala, vendar morajo vseeno biti definirana tako, da vsebujejo le zanemarljiv delež signala. CR in VR so definirana z uporabo pravokotnih rezov glede na SR, pri čemer glavno vlogo igra signifikanca signala [32, 200], definirana kot

$$\mathcal{S} = \sqrt{2\left((s+b)\ln\left(1+\frac{s}{b}\right)-s\right)}, \tag{2}$$

kjer sta s in b skupna izkoristka pričakovanih dogodkov signala oziroma ozadja. V limiti $s \ll b$ se enačba poenostavi v $s/\sqrt{b}$.

Pred optimizacijo območij je potrebno opraviti predizbor dogodkov in paziti, da so izmerjeni podatki v SR zastrti (angl. "blinded"), s čimer preprečimo pristranskost fizikalnih rezultatov. Dogodki, izbrani v analizi, morajo izpolnjevati standardne ATLASove zahteve za kakovost podatkov [201]. Dogodki so bili zbrani z uporabo dvoleptonskih prožilcev, ki izbirajo pare elektronov, mionov ali kombinacije elektronov in mionov. Spodnje mejne vrednosti p_{T} dvoleptonskih prožilcev so se v času zajemanja podatkov dvignile zaradi naraščajoče luminoznosti trkajočih žarkov, vendar nikoli niso bile višje od 24 GeV (24 GeV) za prvi (drugi) elektron in 22 GeV (14 GeV) za prvi (drugi) mion. Nadalje zahtevamo, da ima vsak lepton v paru $p_{\mathrm{T}} > 40$ GeV, pljuski hadronov pa $p_{\mathrm{T}} > 20$ GeV.

V fiziki osnovnih delcev je potrebno zelo dobro poznati pričakovano ozadje, saj vsako neskladje z napovedjo lahko nakazuje na možnost še neodkritih delcev. Ozadja se glede na njihov izvir delijo na posredna in neposredna. Prva kategorija je ocenjena z metodami, ki temeljijo na podatkih, druga pa je pridobljena z Monte Carlo (MC) simulacijami.

Neposredni viri ozadja so procesi Standardnega modela, pri katerih v končnih stanjih nastopajo podobni leptonski pari kot pri signalu. To so večinoma razpadi bozonov W, Z, H, ter razpadi leptonov τ oz. kvarkov t. V predstavljeni analizi prevladujejo prispevki iz produkcije dvojnih vektorskih bozonov z nekaj prispevki Drell–Yan procesa, predvsem v dvoleptonskih območjih. Dogodke generiramo s pomočjo računalniško zakodiranih teoretičnih modelov, njihove interakcije z detektorjem pa modeliramo z orodjem Geant4 [116]. Po koncu simulacije dobimo digitalne podatke v enaki obliki, kot jih dobimo pri meritvi podatkov iz trkov protonov.

Dogodki, ki vsebujejo leptone, katerih naboji so bili napačno rekonstruirani, so viri posrednega ozadja. Elektroni so edini pomemben vir napačne identifikacije naboja, saj so mioni veliko težji in ne izgubljajo energije tako hitro preko zavornega sevanja. Poleg tega se njihove sledi merijo tako v Notranjem detektorju kot v mionskem spektrometru, kar zagotavlja boljšo meritev ukrivljenosti in posledično rekonstrukcijo naboja. Ker se modeliranje napačne identifikacije naboja ne ujema dobro med podatki in MC simulacijo, so normalizacijski faktorji izpeljani s tehnikami, ki temeljijo na podatkih. Procesi, pri katerih rekonstruirani leptoni izvirajo iz napačno rekonstruiranih objektov, kot so curki, iz razpadov lahkih ali težkih kvarkov ali, v primeru elektronov, iz pretvorbe fotonov, prav tako spadajo v kategorijo posrednega ozadja. Te

vrste dogodkov tako vsebujejo vsaj en lažni lepton in se zaradi velikih negotovosti pri simulaciji hadronizacije pljuskov ne ocenjujejo z MC simulacijo. Za oceno njihovega prispevka iz ozadja $W+$ jets in $t\bar{t}$ dogodkov z več curki je prav tako potreben pristop, ki temelji na podatkih.

Za oceno lažnih elektronov in mionov smo uporabili metodo *fake factor* [203], ki razdeli leptone v dve ortogonalni množici Loose in Tight. Tight so signalni leptoni, Loose pa leptoni, ki niso dosegli potrebne identifikacijske ali izolacijske ravni za Tight, so pa zadostili ohlapnejšim zahtevam. Razmerje med številom Loose in Tight je t.i. lažni faktor (angl. "fake facor"), $F_\ell = N_{\text{TIGHT}}/N_{\text{LOOSE}}$. Po navadi ga izmerimo v odvisnosti od kinematičnih spremenljivk, npr.: p_{T}, η, v kontrolnih oz. stranskih območjih in nato ekstrapoliramo v signalna območja. Število lažnih leptonov v primeru signalnega območja z dvema leptonoma se izračuna po formuli

$$N_{\text{fake}} \overset{\text{if } l=2}{=} \left[\sum_{TL} F_2 + \sum_{LT} F_1 - \sum_{LL} F_1 F_2\right]_{\text{podatki}} - \left[\sum_{TL} F_2 + \sum_{LT} F_1 - \sum_{LL} F_1 F_2\right]_{\text{MC simulacija}} . \quad (3)$$

Od števila lažnih leptonov, ocenjenega iz podatkov, je potrebno odšteti število simuliranih, ki ne zadostijo polnim Tight zahtevam, da se izognemo dvojnemu štetju istih leptonov.

Na podoben način se v posebnem $Z \longrightarrow ee$ območju izmerijo tudi popravki za napačno rekonstrukcijo leptonovega naboja. Le-ta se lahko pojavi zaradi zavornega sevanja, pri čemer se nastali foton zaradi interakcije z detektorskim materialom pretvori v par elektron–pozitron. V končnem stanju imamo tako tri elektrone, zaradi česar je določitev prvotnega naboja otežena. Poleg tega se lahko visokoenergijskim elektronom kljub močnemu magnetnemu polju znotraj detektorja smer ne spremeni dovolj, da bi na podlagi ukrivljenosti sledi nabitega delca v magnetnem polju pravilno določili njegov električni naboj.

V analizi smo obravnavali tako teoretične kot eksperimentalne sistematične negotovosti. Teoretične negotovosti izvirajo predvsem iz nekaterih predpostavk pri simulaciji procesov, kot so na primer izbira faktorizacijske in renormalizacijske skale (μ_F in μ_R), izbira partonskih distribucijskih funkcij, hadronizacijskega modela in nenazadnje vrednosti vhodnih parametrov (α_{s}, m_{t}). Eksperimentalne sistematične negotovosti so posledica neujemanja rekonstruiranih dogodkov med izmerjenimi podatki in simulacijo. Določijo se na podlagi namenskih meritev učinkovitosti in se uporabljajo za napovedi MC signala in ozadja. Lahko jih razdelimo v dve glavni kategoriji: kalibracijske negotovosti, ki so povezane z meritvami energijskih skal, medtem ko učinkovitostne negotovosti merijo sposobnost rekonstrukcije, identifikacije in selekcije rekonstruiranih objektov.

V analizi z implementacijo pravokotnih rezov je za signalna območja, neodvisno od kombinacije števila leptona in okusa, zahtevana invariantna masa vodilnega leptonskega para z enakim nabojem nad 300 GeV. Dodatne zahteve, ne glede na leptonski okus, se postavijo leptonskim parom z istim nabojem, da se poveča signifikanca. Kotna razdalja leptonov z istim nabojem v dvoleptonskem signalnem območju (SR2L) mora biti $\Delta R(\ell^{\pm}, \ell'^{\pm}) < 3.5$. Poleg tega mora vektorska vsota transverzalnih gibalnih količin obeh vodilnih leptonov,$p_{\text{T}}(\ell^{\pm}\ell'^{\pm})_{\text{lead}}$, presegati 300 GeV tako v dvoleptonskem kot trileptonskem (SR3L) signalnem območju. V signalnem območju štirih leptonov (SR4L) se signifikanca signala poveča z zahtevo, da povprečna invariantna masa dveh leptonskih parov z enakim nabojem izpolnjuje $\overline{m}_{\text{SC}} = (m_{\ell^+\ell'^+} + m_{\ell^-\ell'^-})/2 > 300\,\text{GeV}$.

Kontrolna in validacijska območja zajemajo nižji $m(\ell^{\pm}\ell'^{\pm})_{\text{lead}}$ interval ali pa zahtevajo druge ortogonalne izbire, če se uporabi enako $m(\ell^{\pm}\ell'^{\pm})_{\text{lead}}$ okno kot v signalnih območjih. V kontrolnih območjih je izmerjen normalizacijski faktor za Drell–Yan procese in produkcijo dvojnih vektorskih bozonov. Za slednjega so v dvoleptonskih območjih uporabljeni trije faktorji, glede na kombinacijo leptonskega okusa končnega stanja.

Za izboljšanje rezultatov analize na podlagi pravokotnih rezov, smo preizkusili osnovne metode strojnega učenja, ki se v fiziki visokih energij vse pogosteje uporabljajo. Pri strojnem učenju smo testirali dva algoritma, in sicer pospešena odločevalna drevesa implementirana v paketu *CatBoost* [210] in nevronske mreže, zagotovljene v knjižnici *PyTorch* [211]. Dogodki so bili razdeljeni v tri skupine za učenje, validacijo in testiranje v razmerju 50% : 25% : 25%. Za vsako posamezno leptonsko številčnost je bil naučen svoj model, pri čemer so bile vhodne količine izbrane na podlagi BDT algoritma, ki oceni pomembnost posamezne spremenljivke. V primeru dveh leptonov v končnem stanju je bilo izbranih 15 količin, v primeru treh 23 in v primeru štirih leptonov v končnem stanju 13. Odločevalna drevesa so se učila 5000 iteracij, medtem ko nevronske mreže 10, 22 in 35 epoh za posamezen model v skupinah po 128 dogodkov. Nevronske mreže sestavljajo tri skrite plasti s po 256 nevroni, ki so aktivirani s funkcijo ReLu. Boljše rezultate so vračale nevronske mreže, zato je bil v nadaljevanju analize uporabljen ta pristop.

V analizi z uporabo strojnega učenja je selekcija ohlapna kolikor je le mogoče, s čimer smo v analizi zajeli večje število dogodkov. Glavna spremenljivka je logit MVA rezultat, s katerim so definirana signalna območja. Podobno kot v analizi z uporabo pravokotnih rezov so validacijska območja definirana na obrnjenem intervalu te spremenljivke, medtem ko so kontrolna območja definirana s pomočjo drugih opazljivk. Povzetek zahtev za oba analizna pristopa je predstavljen v Tabeli 1.

Tabela 1: Povzetek regij, definiranih v pristopu analize na podlagi ortogonalnih rezov (zgornji blok) in strojnega učenja (spodnji blok). Uporaba zahteve je označena s kljukico (✓) ali *obrnjena*, če je obrnjena. Območja s tremi in štirimi leptoni v končnem stanju vključujejo vse kombinacije leptonskih okusov. Če je v ustrezni celici pomišljaj, se izbira ne uporablja. Poleg navedenih zahtev, se v vseh regijah uporablja b-jet veto.

	Kontrolna območja				**Signalna območja**			**Validacijska območja**		
	DYCR	DBCR2L	DBCR3L	CR4L	SR2L	SR3L	SR4L	VR2L	VR3L	VR4L
Kanal	e^+e^-	$e^{\pm}e^{\pm}$ $e^{\pm}\mu^{\pm}$ $\mu^{\pm}\mu^{\pm}$	$\ell^{\pm}\ell^{\pm}\ell^{\mp}$	$\ell^+\ell^+\ell^-\ell^-$	$e^{\pm}e^{\pm}$ $e^{\pm}\mu^{\pm}$ $\mu^{\pm}\mu^{\pm}$	$\ell^{\pm}\ell^{\pm}\ell^{\mp}$	$\ell^+\ell^+\ell^-\ell^-$	$e^{\pm}e^{\pm}$ $e^{\pm}\mu^{\pm}$ $\mu^{\pm}\mu^{\pm}$	$\ell^{\pm}\ell^{\pm}\ell^{\mp}$	$\ell^+\ell^+\ell^-\ell^-$
$m(\ell^{\pm}\ell'^{\pm})_{\text{lead}}$ [GeV]*	≥ 300	$[200,\ 300)$	≥ 300	$[100,\ 200)$	≥ 300	≥ 300	≥ 300	≥ 300	$[100,\ 300)$	$[200,\ 300)$
$p_{\text{T}}(\ell^{\pm}\ell'^{\pm})_{\text{lead}}$ [GeV]	-	-	-	-	≥ 300	≥ 300	-	$[200,\ 300)$	-	-
$\Delta R(\ell^{\pm}\ell'^{\pm})_{\text{lead}}$	-	-	-	-	< 3.5	-	-	< 3.5	-	-
$\overline{m}_{\text{SC}}$ [GeV]	-	-	-	-	-	-	≥ 300	-	-	-
$E_{\text{T}}^{\text{miss}}$ [GeV]	-	> 30 -	-	-	-	-	-	> 30 -	-	-
$\lvert\eta(\ell,\ell')\rvert$	-	< 3.0 -	-	-	-	-	-	< 3.0 -	-	-
Z-bozon veto	-	-	obrnjena	-	-	✓	✓	-	✓	-
	DYCR	DBCR2L	DBCR3L	CR4L	SR2L	SR3L	SR4L	VR2L	VR3L	VR4L
logit MVA rezultat	-	-	-	-	≥ 0	≥ 3	≥ 0	< 0	< 3	< 0
$m(\ell^{\pm}\ell'^{\pm})_{\text{lead}}$ [GeV]*	≥ 300	$[200,\ 300)$	-	-	≥ 300	-	-	≥ 300	-	-
$p_{\text{T}}(\ell^{\pm}\ell'^{\pm})_{\text{lead}}$ [GeV]	-	-	-	-	≥ 300	-	-	-	-	-
$\overline{m}_{\text{SC}}$ [GeV]	-	-	-	< 200	-	-	≥ 200	-	-	≥ 200
$\lvert\eta(\ell,\ell')\rvert$	-	- -	-	-	-	-	< 3.0	- -		
Z-boson veto	-	-	obrnjena	-	-	✓	-	-	✓	-

*V območju DYCR se rez upošteva na invariantni masi vodilnega leptonskega para z **nasprotnim nabojem**.

Končno statistično analizo podatkov smo izvedli z metodo največje verjetnosti, ki je produkt Poissonovih in Gaussovih porazdelitev. Poissonova verjetnost primerja izmerjeno število dogodkov s pričakovanim številom dogodkov, medtem ko Gaussova porazdelitev modelira proste parametre, ki so povezani s sistematičnimi negotovostmi. Dodatno v maksimalni verjetnosti nastopajo Poissonovi členi, ki modelirajo statistično negotovost simuliranih procesov, skupaj s prostimi parametri za normalizacijo izbranih vrst ozadja. Glavni maksimizacijski parameter v statistični analizi je sipalni presek oz. normalizacijski faktor iskanega procesa nove fizike v primeru prisotnosti signala. Po obdelavi podatkov smo ugotovili, da ni statistično pomembnih odstopanj, zato smo z metodo CL_S [208] določili zgornje meje produkcijskega sipalnega preseka za različne mase $H^{\pm\pm}$ pri 95% stopnji zaupanja. Na podlagi teh rezultatov je mogoče določiti tudi najnižje spodnje dovoljene mase $H^{\pm\pm}$ v okviru levo-desno simetričnega gugalničnega mehanizma tipa II in modela Zee–Babu.

Izmerjene spodnje masne meje bozonov $H^{\pm\pm}$ v modelu LRSM (Zee-Babu) se gibljejo med 520 GeV in 1050 GeV (410 GeV in 880 GeV), odvisno od števila leptonov v končnem stanju, pri predpostavki $\sum_{\ell\ell'} \mathcal{B}(H^{\pm\pm} \to \ell^{\pm}\ell'^{\pm}) = 100\%$. Če združimo vse tri kanale, izmerjena spodnja meja mase bozona $H^{\pm\pm}$ doseže 1080 GeV v okviru LRSM oziroma 900 GeV za Zee-Babu model. Po drugi stani je pričakovana spodnja meja 1065^{+30}_{-50} GeV za LRSM in 880^{+30}_{-40} GeV za Zee-Babu model, pri čemer so negotovosti pridobljene iz pasu $\pm 1\sigma$. Rezultati so predstavljeni na Sliki 4. Meja, pridobljena iz končnega stanja s štirimi leptoni, je najmočnejša in odločilno vpliva na kombiniran rezultat. Po preliminarnih študijah se je izkazalo, da stojno učenje da podobne rezultate in jih ne znatno izboljša.

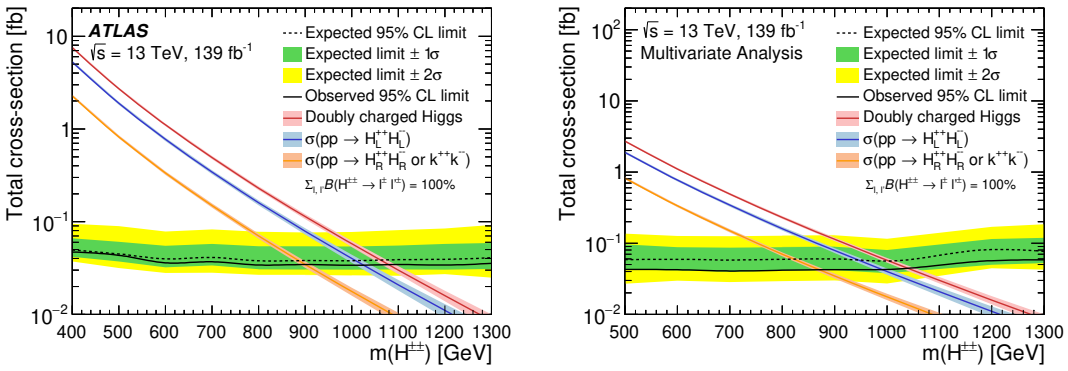

(a) (b)

Slika 4: Izmerjena (polna črta) in pričakovana (črtkana črta) zgornja meja sipalnega preseka za produkcijo para bozonov $H^{\pm\pm}$ v odvisnosti od $m_{H^{\pm\pm}}$ v analizi, ki temelji na (a) pravokotnih rezih in (b) strojnem učenju, ob predpostavki $\sum_{\ell\ell'} \mathcal{B}(H^{\pm\pm} \to \ell^{\pm}\ell'^{\pm}) = 100\%$ pri 95% stopnji zaupanja. Zeleni (rumeni) pas ustreza standardnemu odklonu $\pm 1\sigma$ ($\pm 2\sigma$) negotovosti okoli pričakovane meje. Teoretične napovedi preseka signala, podane z izračunom NLO [65, 69], so prikazane kot modra, oranžna in rdeča črta za levoročni $H_L^{\pm\pm}$, desnoročni $H_R^{\pm\pm}$ (ki je enak kot Zee–Babu $k^{\pm\pm}$) oziroma vsoto obeh kiralnosti z ustreznimi pasovi negotovosti.